A Measurement System for and the Measurement of Single Particle Energies in Quantum Dots

Kevin Lister

Submitted for the degree of Doctor of Philosophy
to the Department of Electronics and Electrical Engineering
at the University of Glasgow.

November 1999

ABSTRACT

This thesis describes the design, development, construction and performance of an instrumentation system suitable for the measurement of single electron quantum dot devices.

The inaugural measurement with this new system produced fascinating experimental data from a novel magnetic spectrometer device. This data, presented in chapter 5, suggests that it is possible to measure the single particle spacing in a 500nm quantum dot device independent of the Coulomb blockade energy and within an electron mean free path.

Devices were defined on a GaAs/AlGaAs heterostructure, the interface of which formed a 2 dimensional electron gas (2DEG). The surface was patterned with metallic surface gates. On the application of a potential to the gates, the electrons were depleted from beneath the gate and the pattern was transferred to the 2DEG. The devices were fabricated in a Hall bar geometry using standard nanofabrication techniques. Measurements were performed using a $^3He/^4He$ Kelvinox 25 dilution refrigerator unit at a lattice temperature of $T_L \approx 45mK$.

Prior to the work detailed in this thesis the lowest effective electron temperature available to quantum transport researchers at Glasgow had been 1.2 Kelvin. This was achieved with the use of a pumped ^4He variable temperature insert (VTI), for which 1.2K represented the lowest working temperature. Although a $^3He/^4He$ dilution unit had been available for some time, the unit had exhibited an effective electron temperature of $T_e > 7K$. As a direct result of the work contained within this thesis (detailed in chapter 4), the lower limit of the effective electron temperature range available was extended down to ≈250mK. This represents an improvement of more than an order of magnitude over the lowest effective electron temperature previously available and an improvement of > 20 over that previously available within the dilution unit.

In order to achieve this improvement a systems approach was adopted. The individual subsystems associated with the design of the new measurement

system were designed to work in conjunction with one another. Great care was taken with respect to referencing potentials, shielding, intrinsic noise of the electronic components used and vibration isolation in order that the measurement system imposed the minimum induced electron heating on the device under test.

Measurements were performed on quantum dot devices in the Coulomb blockade regime. Periodic peaks in the conductance of a quantum dot were observed. These conductance peaks were seen in response to an applied gate voltage, and are referred to as Coulomb oscillations. Such oscillations are a result of classical charging effects due to the addition or subtraction of a single electron to, or from, the quantum dot. These effects are a direct result of the quantisation of charge. Energy quantisation due to the confinement of the electrons wave-function, also plays a rôle in quantum dot devices. In the devices studied the classical charging energy, that gives rise to the Coulomb oscillations is generally an order of magnitude greater than the quantum mechanical effects that give rise to the single particle spectrum.

The dependence on temperature of the line shape of the Coulomb oscillations was used in order to estimate the effective electron temperature of the device. Coulomb oscillations at various temperatures were fitted to known forms and the full-width half-maximum (FWHM) derived. When the FWHM were plotted against temperature the width failed to decrease below a value corresponding to ≈250mK. A significant proportion of this residual electron heating was attributed to the excitation level imposed across the sample during the experiment.

Previously the effects of energy quantisation have been observed in small quantum dot devices as a shift from the normally periodic classical Coulomb oscillations. Measurements presented here, using a novel magnetic spectrometer device, suggested that it was possible to measure the energy quantisation effects within a quantum dot independently of the Coulomb blockade energy. The spectrometer used electron focusing techniques to measure the shift in focusing peak position for a corresponding change in dot configuration before the electron energy had been degraded by scattering events. The energy associated with this peak shift was in good agreement with the estimated single particle spacing, also presented. The most important result of this measurement was that there was no evidence of a shift in focusing peak position corresponding to the Coulomb blockade energy. This technique, therefore, was only sensitive to the much smaller single particle spacing.

ACKNOWLEDGEMENTS

During the course of this work many people have contributed to making this one of the happiest and rewarding periods of my life (although some of the actual minutes were fairly lousy!).

It was obvious that I was going have a good time here in Glasgow from the day of my interview, which began one Thursday morning in Steve Beaumont's office and ended later that evening on Byres Road with Weaver and Williamson, at which point I was considerably less than sober. It was a hell-of-a interview technique on their part.

Most of reason I have had such an enjoyable time was not the work (no, really) but the people I have worked with. These include, amongst many others:

The technical staff of the Ultra Small Structures Lab	without whom the place would fall apart and none of our stuff would work.
Beer Drinking Life-forms	David, Sarah, Brendan, Aline, Iman, Gordon, Kath. With whom I continue to enjoy the odd tasty beverage.
Sympathy Givers	Karen Mcilvaney, Kay Wray, Karen Phillips and Shona Ballantine. But most especially Carol Clugston who listened to me complain frequently and at length and was always supportive.
John Williamson	For being my supervisor, reading this manuscript and having a unique view of Physics that occasionally encompassed work contained within this thesis.
Mahfuzur Rahman	who patiently taught me fabrication and helped with experiments.

More than anybody else though I would like to thank John Weaver for freely giving of his time in order to advise, supervise, comment and make suggestions on almost every aspect of this work, but especially on the measurement system design. And just as importantly for being a beer drinking life-form and a good friend.

I would also like to thank my family for their support and encouragement over the years. More recently I would like to thank my girlfriend Mimi who has only known me during the last part of my Ph.D. and despite this has stayed with me!

Kevin Lister

November 21, 1999

1 INTRODUCTION

The way we view and understand the world has been determined, to a large extent, by those things around us of comparable size. We evolved to understand the world that we could see, touch, hear and therefore analyse. More recently in our history we have gained the ability to build machines that enable us to "see" over many more length scales and into a much broader range of phenomena. The advent of the optical microscope and telescope has opened whole new fields of understanding. More recently, with the invention of measurement tools such as the electron microscope and particle accelerator, we have been able to probe astonishing extremes of dimension.

With the increased capability we have learned, however, that the physical laws that hold true on our scale break down when applied to the very large or very small scale. Newton's laws, which work so precisely on our scale, fail when we move to both the very large (interstellar), when the dominant interactions are described by general relativity, and the very small (microscopic) when the dominant interactions are described by quantum mechanics.

On the very small length scales (of the order of 1nm) classical laws fail to describe the physical processes completely, or even at all. Electrons for instance, must be described by the laws of quantum mechanics. Here the electrons nature as both a wave and a particle need to be understood. In the quantum mechanical world things are truly bizarre. Objects may pass through seemingly solid walls (tunnelling) or may take several paths leading to the same point simultaneously (interference).

Mesoscopic systems exist somewhere between the microscopic and the macroscopic world. The intriguing aspect of mesoscopic systems is that sometimes they behave classically and sometimes they show quantum mechanical behaviour. Indeed the same device can be made to exhibit both classical and quantum effects.

The recent study of mesoscopic phenomena has used, almost exclusively, semiconductor nanostructures. An important aspect of these structures that makes them suitable to study quantum effects is the ability to control the electron density. When the number of conduction electrons in a structure is zero the material is insulating. In metals, each atom in the lattice gives up one or two electrons to conduction. This leads to enormous numbers of free electrons ($\approx 10^{23}$ electrons per cubic mm), and this is the reason we can describe them classically. In semiconductor materials, it is possible to control the number of free electrons by adding a precise number of donor atoms. With low electron density, it is possible to observe quantum mechanical effects as a smaller electron density leads to a larger Fermi wavelength.

Until recently the transport of electrons within small semiconductor devices were viewed in terms of tiny classical self-contained "seas" each containing at least a few thousand electrons. As devices shrink, this view breaks down. For instance when the separation between devices on an integrated circuit becomes less than a critical length scale, electrons may tunnel between devices and data can be corrupted. Similarly, as the devices get smaller they are no longer able to average out the variation in potential caused by the random distribution of donor atoms. This may lead to a situation where the bias potential that may switch on one device in one part of a circuit fails to do so in another[1].

Obviously, these are major problems for the future of conventional electronic devices, but may also be viewed as an opportunity as devices can now be made that work only on the length scales at which conventional devices break down.

Components that work classically on the single electron level may one day form the basis of integrated circuits and hence computers of the future, with exceptionally high packing density and low heat dissipation. Whilst room temperature operation of such devices has been demonstrated[2-5] the yield and route to mass integration of complete single electron systems has yet to be proved viable.

Devices that exploit the unique properties of quantum mechanics in order to perform computational tasks may be realised in semiconductor quantum dot structures. This research area of quantum computation is of much interest and speculation presently[6]. The practical realisation of a quantum computer is, at best, many years away.

The semiconductor single electron devices (quantum dots), the subject of investigation in this thesis, may be considered tiny solid state laboratories in

which quantum mechanics and the effects of electron-electron interaction may be studied. In the past few years, these studies have advanced our understanding of the nature of these interactions enormously.

Another reason that a low electron density makes quantum mechanical behaviour of electrons observable is that it alters critical length scales over which the electron retains certain information. Quantum effects may only occur if the distance the electron travels before interfering is shorter than the phase coherence length, $l_{ø}$, the length over which the electron wave-packet retains phase information. This length is limited by the inelastic mean free path or inelastic scattering length; l_i. Scattering events can also occur that do not cause a loss of phase information, but do change the direction of the electron; this is the elastic mean free path or elastic scattering length; l_e. By comparing the elastic scattering length with the sample dimensions, different transport regimes may be distinguished.

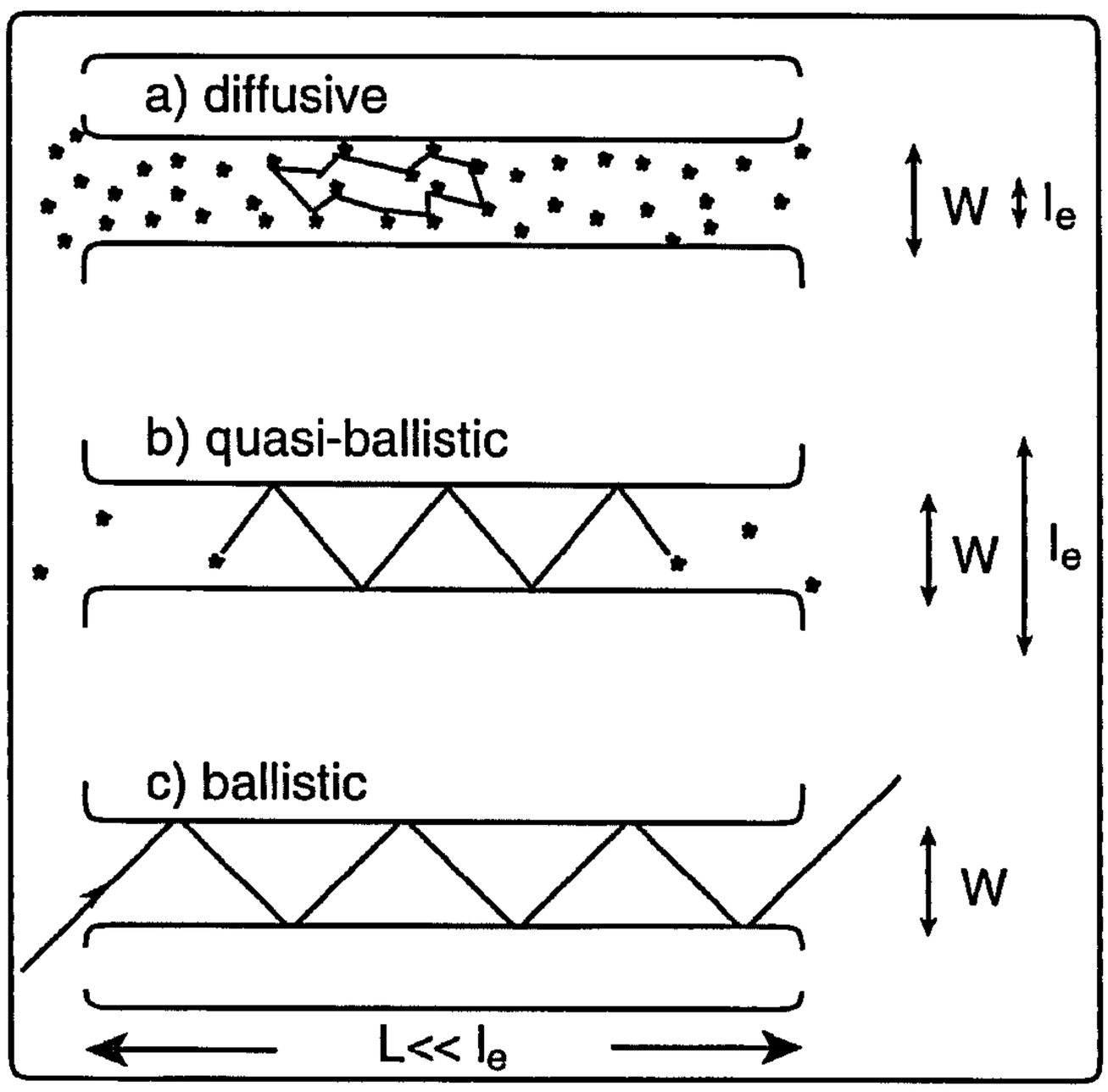

Figure 1.1 Representative electron trajectories in different transport regimes; a) the diffusive (l_e<<L,W), b) quasi-ballistic (W<l_e<L) and c) ballistic (L,W<<l_e)(7)

Figure 1.1 a) is the diffusive regime in which l_e is much smaller than the sample dimensions. Here the general behaviour can be understood classically. When l_e is less than the width but greater than the length the regime is said to be quasi-ballistic Figure 1.1 b). The ballistic regime, Figure 1.1 c), is defined when the electron passes through the sample without elastic scattering; l_e > L,W.

The effect of phase coherence has been neglected in the above definitions of transport regimes. Quantum interference effects may become observable if l_ϕ is of the same order as the sample dimensions.

Quantum confinement effects can occur when the sample length is of the same order as the Fermi wavelength. This is a result of the wave properties of the electron. When the electron is confined in a structure in this way, it can be described in terms of quantum mechanical standing waves. Figure 1.2 shows the effect of increasing the degrees of confinement on an electron.

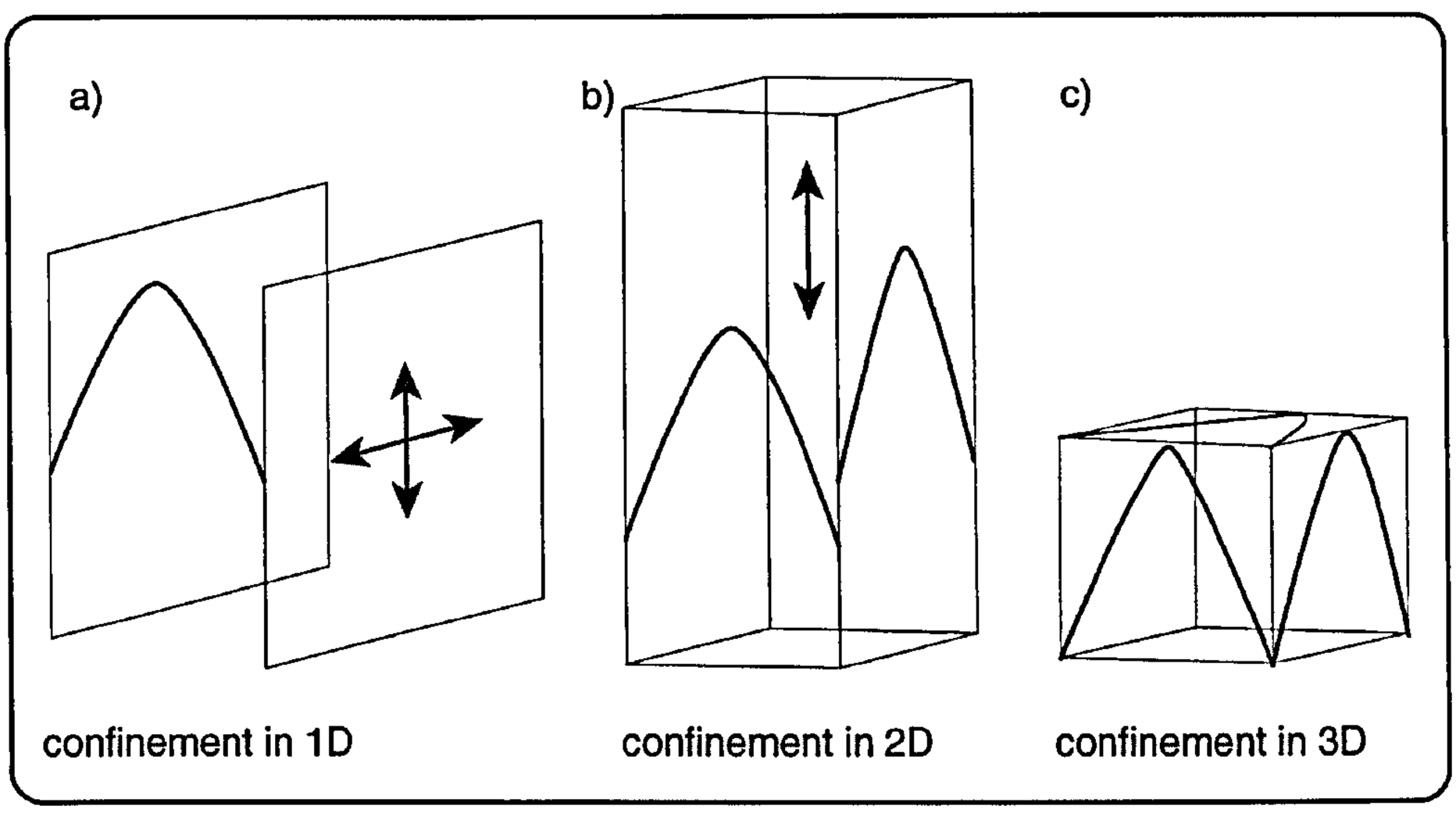

Figure 1.2 Three confined solids. a) shows a representation of an electron density wave bound in one direction but free to propagate in the other two, b) shows confinement in two directions with one remaining degree of freedom, in c) the electron is confined in all three directions and is unable to propagate[8].

As the electrons are confined, they are often referred to as losing dimension. This is a short hand phrase used to denote the electrons inability to propagate in one or more dimensions. Figure 1.2 shows that increasing the confinement reduces number of directions the electron wave can propagate. For each propagating direction lost the behaviour of the electron in that direction is described by quantum mechanical standing waves.

Historically the capability of the quantum transport group at Glasgow to perform low temperature measurements has never been fully realised. High impedance samples have always exhibited relatively high temperature characteristics even within a fully functioning dilution refrigeration unit reading a base temperature of approximately 100mK. As will be discussed in chapter 4, this implies that there were one or several major sources of noise contributing to the effective electron temperature seen by the device. Figure

1.3 shows the relevant energy scales that are important when discussing single electron devices.

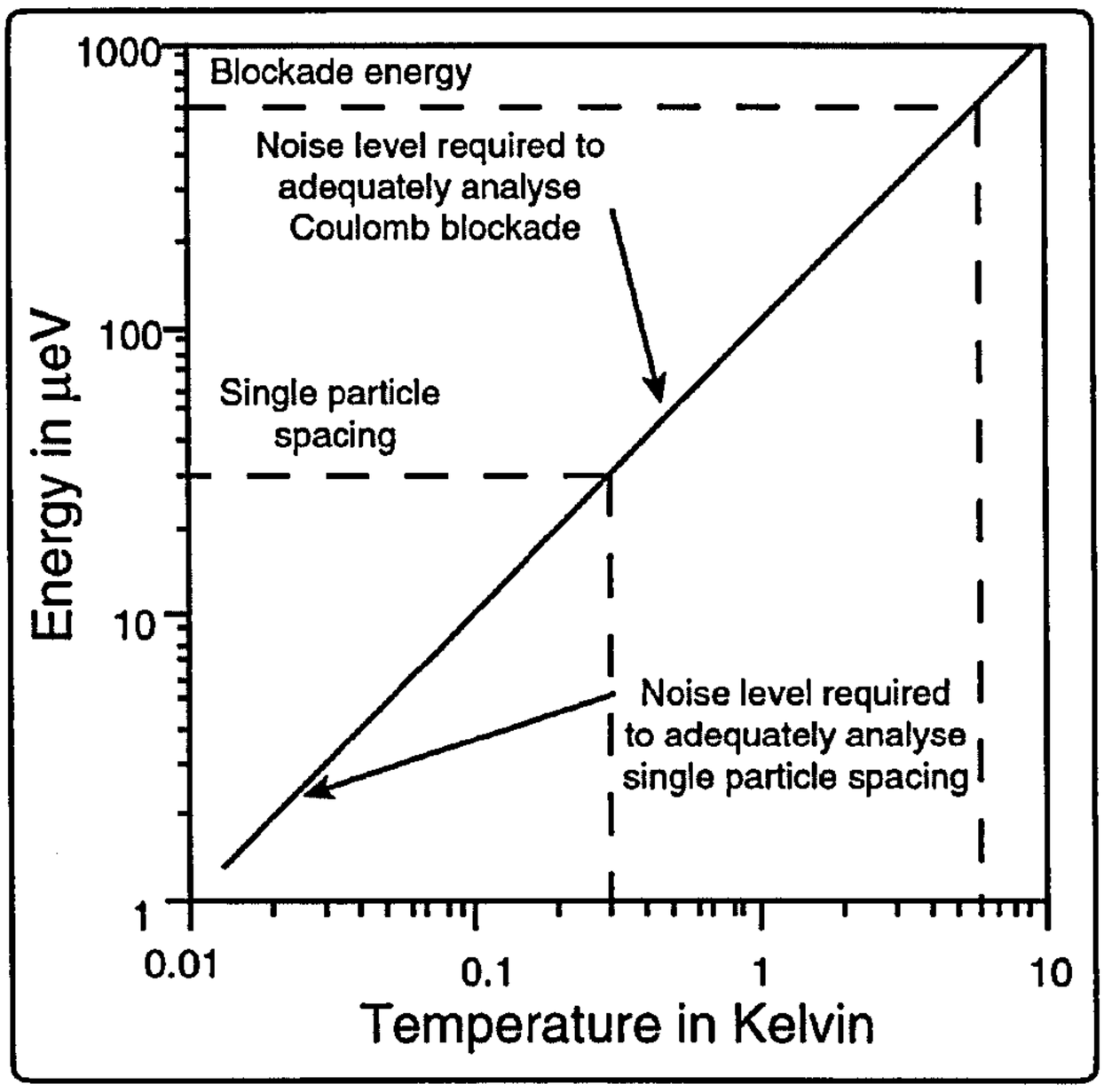

Figure 1.3 Graph of temperature versus energy for a quantum dot of nominal diameter =500nm. Indications of notable energy scales relevant to the design of a measurement system for single electronic devices are shown.

The graph simply shows temperature versus energy, but with annotated reference to the energy levels associated with both Coulomb blockade and the discrete quantum state (dashed lines) for an electron within a quantum dot of approximately 500nm. In order to resolve fine features and be able to analyse data with confidence at this energy scale it is desirable to have an instrumentation system capable of measuring energies an order of magnitude below the smallest feature of interest. These points are indicated by the arrows in Figure 1.3. The graph shows that for this to be the case, for this size of dot, a noise level incident on the sample of the order a few μeV is required.

Without the capability to make measurements at this level, an investigation into new and exciting phenomena is made all but impossible. The vast majority of the time and effort of the authors work for the past four years, detailed in chapter 4, has been concerned with a major upgrading of the measurement capability within the Quantum Transport group at Glasgow.

This thesis is divided into five chapters, this introduction being the first. The subsequent two chapters provide a general overview of mesoscopic physics and an introduction to the techniques necessary to fabricate and measure such devices. Chapters 4 and 5 deal with the work that has been undertaken and the results that have been forthcoming. Chapter 4 details the design, analysis

and implementation of the new measurement system. Chapter 5 deals with the experimental results obtained from a novel magneto-spectroscopy device.

1.2 References

(1) A. Asenov, "Random Dopant Induced Threshold Voltage Lowering and Fluctuations in sub-0.1 μm MOSFET's: A 3-D "Atomistic" Simulation Study" IEEE Transactions On Electron Devices 45 (12), 2505-2513 (1998).

(2) H. Ishikuro, T. Fujii, T. Saraya *et al.*, "Coulomb Blockade Oscillations At Room Temperature In A Si Quantum Wire Metal-Oxide-Semiconductor Field-Effect Transistor Fabricated By Anisotropic Etching On A Silicon-On-Insulator Substrate" Applied Physics Letters 68 (25), 3585-3587 (1996).

(3) R. P. Andres, S. Datta, M. Dorogi *et al.*, "Room Temperature Coulomb Blockade and Coulomb Staircase from Self-Assembled Nanostructures" Journal of Vacuum Science & Technology a-Vacuum Surfaces and Films 14 (3 Pt1), 1178-1183 (1996).

(4) L. Clarke, M. N. Wybourne, M. D. Yan *et al.*, "Fabrication And Near-Room Temperature Transport Of Patterned Gold Cluster Structures" Journal of Vacuum Science & Technology B 15 (6), 2925-2929 (1997).

(5) C. Schonenberger, H. Van Houten, and H. C. Donkersloot, "Single-Electron Tunneling Observed At Room-Temperature By Scanning- Tunneling Microscopy" Europhysics Letters 20 (3), 249-254 (1992).

(6) A. Barenco, "A Short Introduction to Quantum Computation" (1996) http://eve.physics.ox.ac.uk/NewWeb/Research/Tutorial/recherche.html

(7) C. W. J. Beenakker and H. Van Houten, "Quantum Transport In Semiconductor Nanostructures" Solid State Physics Advances In Research And Applications 44, 1-228 (1991).

(8) Thesis, L. P. Kouwenhoven, "Transport of Electron-Waves and Single-Charges in Semiconductor Nanostructures" , Delft University Of Technology, 1992.

2 MESOSCOPIC PHENOMENA

This chapter provides an overview of physical principles involved within mesoscopic devices. A number of quite diverse phenomena are described all of which are studied most readily at the nanometer scale. Although all the sections have relevance, the sections on charge quantisation in 0-dimensional devices is the most pertinent to the work presented elsewhere in this thesis.

Quantum transport in mesoscopic semiconductor systems is reviewed thoroughly in references[1,2]. Excellent reviews of quantum dots are given in[3-6] as well as the thesis' of[7] and [8]. Extensive use has been made of these texts throughout this chapter.

2.1 Properties of 2DEGs

With the advent of highly controllable semiconductor growth processes, the most notable being MBE (molecular beam epitaxy), device structures can be grown with extraordinary purity and crystalline perfection. The growth of these crystalline structures controllable down to the atomic level, together with the control of impurities has yielded materials of startling purity, with remarkable properties.

The ability to deposit different materials on consecutive atomic monolayers is of crucial importance in the construction of low dimensional electron systems. Within the Aluminium-Gallium-Arsenide (AlGaAs) material system, dealt with exclusively here, the ability to deposit lattice matched AlGaAs on a GaAs substrate creates a very narrow quantum well at the interface of the two materials. This occurs because AlGaAs has a larger band gap than GaAs. As they are joined, the electrons in the AlGaAs try to minimise their energy by falling into the GaAs and forming a conducting sheet. A major advantage of the AlGaAs system over Silicon/Silicon dioxide is that the donors can be spatially separated from the conducting electron sheet by a spacer layer of undoped AlGaAs. This significantly reduces impurity scattering caused by the random variations of potential that occurs when the donors are close to the 2DEG, and hence increases electron mobility.

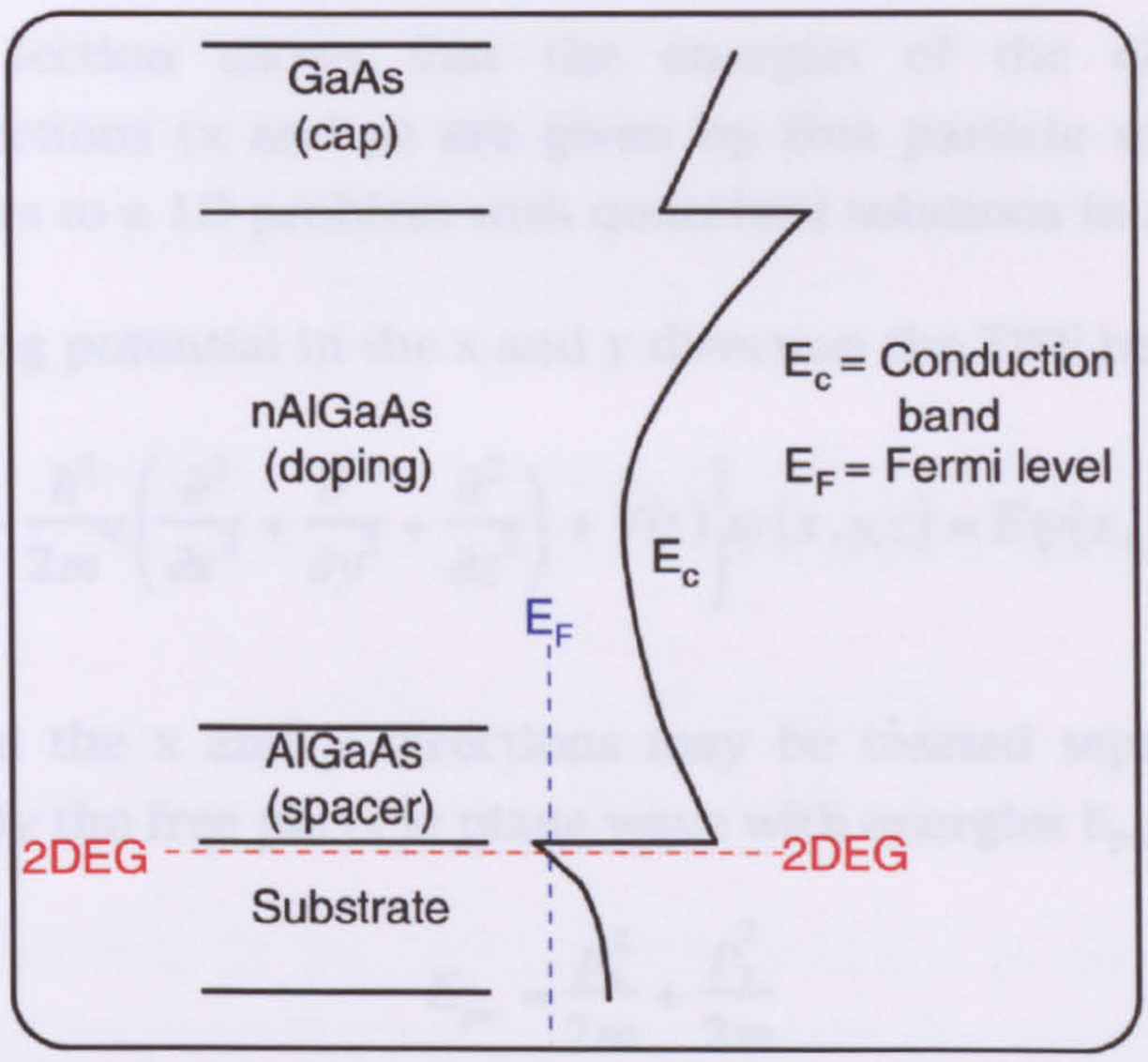

Figure 2.1 Energy band diagram of GaAs-AlGaAs heterostructure and corresponding layer structure.

Figure 2.1 shows the band diagram and layer schematic of a modulation doped AlGaAs heterostructure. The conduction property of the layer determines the

shape of the band within the heterostructure. If the layer is insulating, then the potential within the layer is given by Laplace's equation and varies linearly. If the layer is conducting, then the potential within the layer is given by Poisson's equation and varies quadratically. The bands jump discontinuously at the heterojunctions, although the electric potential must be continuous in both value and slope except at the junctions.

2.2 Electrons in 2D

Electrons can be confined at the interface of a GaAs-AlGaAs heterostructure in such a way as to make their discrete energies observable. This arises because the electrons lose the ability to propagate in one dimension.

To describe the electrons behaviour the three-dimensional time independent Schroedinger wave equation (TISE) is used as a starting point.

$$\left[-\frac{\hbar^2}{2m^*}\nabla^2 + V(r)\right]\psi(r) = E\psi(r)$$

Eqn. 2.1

Where $\hbar$ is Planks constant and m* is the effective mass. Because of the layered nature of the heterostructure the potential energy remains constant parallel to the surface, but varies perpendicular to it. Conventionally this perpendicular direction is defined as the z direction.

The following section shows that the energies of the electrons in the unconfined directions (x and y) are given by free particle solutions, the 3D TISE then reduces to a 1D problem with quantised solutions in z.

With no confining potential in the x and y direction the TISE becomes

$$\left[-\frac{\hbar^2}{2m^*}\left(\frac{\partial^2}{\partial x^2}+\frac{\partial^2}{\partial y^2}+\frac{\partial^2}{\partial z^2}\right) + V(z)\right]\psi(x,y,z) = E\psi(x,y,z)$$

Eqn. 2.2

The solutions in the x and y directions may be treated separately with the energies given by the free particle plane wave with energies E_{pw}

$$E_{pw} = \frac{p_x^2}{2m} + \frac{p_y^2}{2m}$$

Eqn. 2.3

hence equation Eqn. 2.1 becomes

Eqn. 2.4
$$\left[\frac{p_x^2}{2m^*}+\frac{p_y^2}{2m^*}-\frac{\hbar^2}{2m^*}\frac{\partial^2}{\partial z^2}+V(z)\right]\psi(z)=E\psi(z)$$

taking the plane wave energies to the RHS leaves

Eqn. 2.5
$$\left[-\frac{\hbar^2}{2m^*}\frac{\partial^2}{\partial z^2}+V(z)\right]\psi(z)=\left[E-\frac{p_x^2}{2m^*}-\frac{p_y^2}{2m^*}\right]\psi(z)$$

For convenience, a variable ε may be defined which incorporates all the energies that are not associated with the potential confinement

Eqn. 2.6
$$\varepsilon=E-\frac{p_x^2}{2m^*}-\frac{p_y^2}{2m^*}$$

then the 3D TISE becomes effectively 1D

Eqn. 2.7
$$\left[-\frac{\hbar^2}{2m^*}\frac{\partial^2}{\partial z^2}+V(z)\right]\psi(z)=\varepsilon\psi(z)$$

Equation Eqn. 2.7 defines a system that has discrete energy states in one direction. The 3D system is reduced to an equation with a 1D eigenfunction ($\psi(z)$) for the given 1D confining potential V(z).

The potential created at the GaAs-AlGaAs interface can be approximated by a triangular quantum well where the potential V(z)=eFz is a semi-infinite linear potential. With this potential confinement, solutions to the Schroedinger equation of the form of Eqn. 2.7 reduces to Eqn. 2.8

Eqn. 2.8
$$\frac{d^2}{d\xi^2}\psi_\varepsilon(\xi)-\xi\psi_\varepsilon(\xi)=0$$

where ξ is an intermediate energy-dependent variable. Equation Eqn. 2.8 is of the form of the Airy equation the solutions of which give energies levels

Eqn. 2.9
$$E_n=\left[\frac{3}{2}\pi\left(n-\frac{1}{4}\right)\right]^{\frac{2}{3}}\cdot\left[\frac{(eF\hbar)^2}{2m^*}\right]^{\frac{1}{3}}\qquad \text{where n =1,2,...}$$

The shape of the well at the GaAs-AlGaAs interface is only approximately triangular, as the potential flattens out deeper into the substrate. Higher level energies are therefore bound more weakly hence this approximation is poor above the first energy level. Also no account has been taken of electron-electron interactions which can be quite large in 2DEG systems. A more accurate picture may be obtained using self-consistent numerical methods.

2.2.1 2D Density of states

Calculation of the density of states follows a similar derivation regardless of the dimensionality constraints, but the resultant dependence on energy is quite different. The general approach is to determine the density of states in k-space and then use the free electron dispersion relation to obtain the density in energy. Essentially it is the different number of degrees of freedom of k-space that gives rise to the different energy dependence.

The free electron wavefunction cannot be normalised in a simple way such that

Eqn. 2.10
$$\int |\psi|^2 = 1$$

Periodic boundary conditions are imposed such that the value of the wavefunction and its derivative are continuous,

Eqn. 2.11
$$\psi_{x=0} = \psi_{x=L} \text{ and } \frac{d\psi}{dx_{x=0}} = \frac{d\psi}{dx_{x=L}}$$

where the system is imagined to be repeated periodically and that the wavefunction is matched within each period. As

Eqn. 2.12
$$e^{ik0} = 1$$

then

Eqn. 2.13
$$\frac{d}{dx} e^{ikx} = ike^{ikx}$$ which = ik when x=0

Eqn. 2.14
$$\therefore \psi_{x=0} = \psi_{x=L} = 1 = e^{ikL}$$

Eqn. 2.15
$$\frac{d\psi}{dx_{x=0}} = \frac{d\psi}{dx_{x=L}} = ik = ike^{ikL}$$

the above conditions are satisfied if the spacing between points in k-space is

Eqn. 2.16
$$k_n = \frac{2\pi}{L} n$$ where n=0, ±1, ±2,...

hence

Eqn. 2.17
$$\psi_x = \psi_L = e^{i\frac{2\pi}{L}nL} = e^{i2\pi n}$$

Electrons confined to a box L_x by L_y therefore have a density of states in k-space of

Eqn. 2.18
$$N(k) = 2\frac{L_x L_y}{(2\pi)^2}$$

where the prefactor of 2 allows for the spin degeneracy. Per unit area this becomes

Eqn. 2.19
$$n_{2D}(k) = \frac{2}{(2\pi)^2} = \frac{2}{4\pi^2} = \frac{1}{2\pi^2}$$

with the area of a ring between k and k+dk=2πkdk and therefore the number of states in this region is

Eqn. 2.20
$$\partial k = \frac{k}{\pi} dk$$

the number of points in energy-space must equal that in k-space,

Eqn. 2.21
$$\partial E = \frac{dE}{dk}\partial k$$

which leads to

Eqn. 2.22
$$\frac{dE}{dk} = \frac{d}{dk}\left(\frac{\hbar^2 k^2}{2m^*}\right) = 2\frac{\hbar^2 k}{2m^*} = \frac{\hbar^2 k}{m^*}$$

taking the derivative

Eqn. 2.23
$$n(E)\frac{\hbar^2 k}{m^*}\partial k = \frac{k}{\pi} dk$$

the density of states in energy becomes

Eqn. 2.24
$$n(E) = \frac{k}{\pi}\partial k \frac{m^*}{\hbar^2 k \partial k} = \frac{m^*}{\hbar^2 \pi}$$

which is independent of energy.

2.2.2 Transport Properties

An electron in an electric field E acquires a drift velocity

Eqn. 2.25 $$v_{drift} = -\mu_e E \qquad \text{where} \qquad \mu_e = \frac{e\tau}{m^*}$$

Where μ_e is the electron mobility and τ is the average time between scattering event. The conductivity can be written using the Drude model[1,9].

Eqn. 2.26 $$\sigma = \frac{e^2 n_s \tau}{m^*} = e n_s \mu_e = 2\frac{e^2}{h}\frac{k_F l}{2}$$

with the right hand side using the substitution,

Eqn. 2.27 $$n_s = 2\frac{k_F^2}{4\pi}$$

and the mean free path

Eqn. 2.28 $$l = v_F \tau$$

Only those electrons with energies near the Fermi level play a rôle in transport as the states below a few times k_bT are essentially full. More accurately the states that contribute to conduction are those that lie in the interval between the electrochemical potentials in the left (μ_1) and right (μ_2) reservoirs.

2.3 1-Dimensional Devices

Quantised energy levels, due to confinement in another dimension (x or y) may be observable if the confinement in that direction is made strong enough. Here the electron is free to move in only one direction and restricted, to the order of its wavelength, in the other two. This may be accomplished in GaAs 2DEG structures by applying a negative potential to a metallic gate electrode, which forms a Schottky barrier at the surface. The negative potential depletes the electrons from underneath the gate, confining the electron motion to the ungated region. This is commonly referred to as the split gate technique[10]. A schematic is shown in Figure 2.2. The advantage of this technique is that the conducting channel in the 2DEG can be tuned from the defined lithographic width of the written pattern to zero by the application of a bias potential.

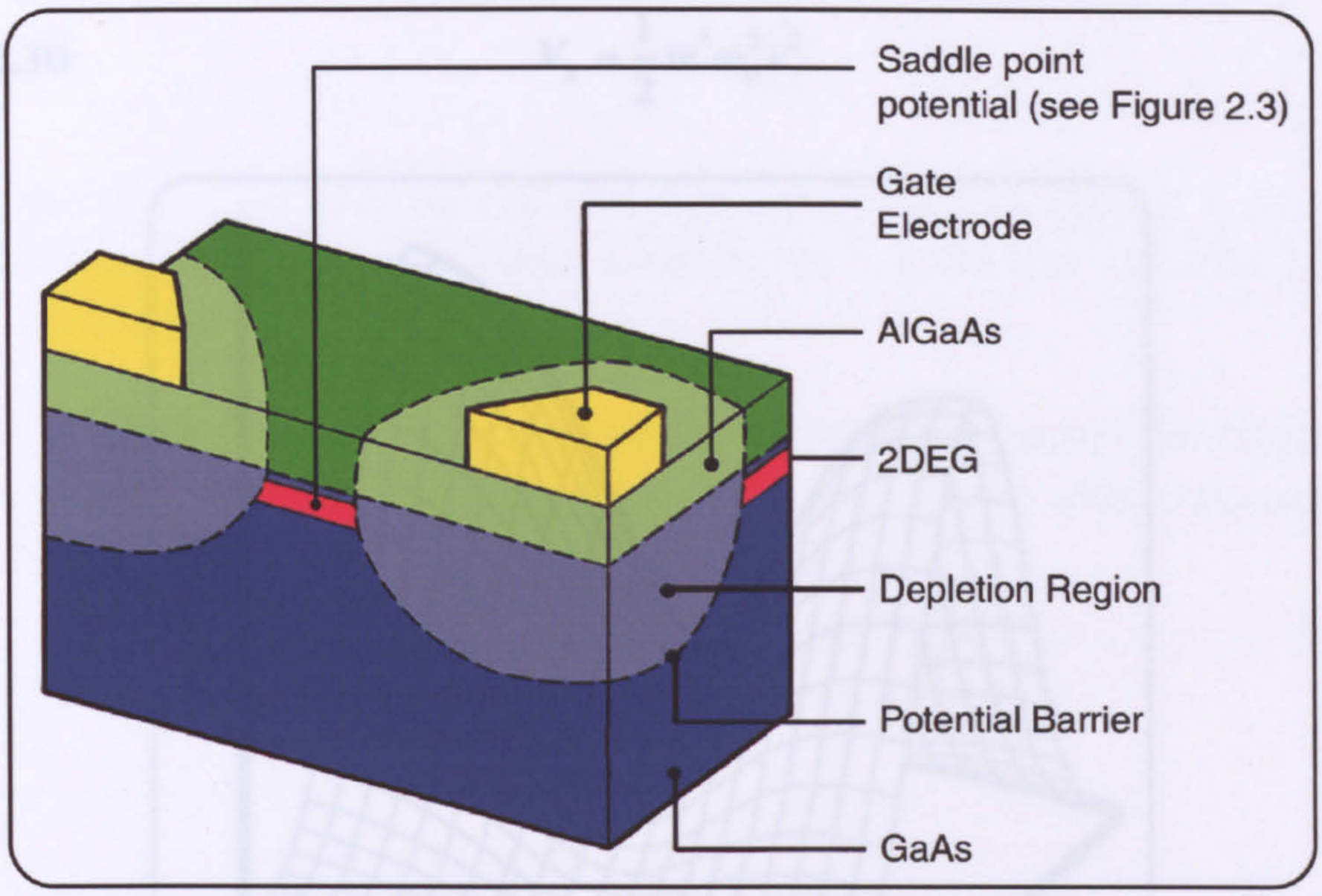

Figure 2.2 Applying a negative potential to the surface gates pushes the electrons from under the gated region and induces a pattern in the 2DEG.

Transport between the two wide 2DEG regions is dominated by the constriction. As the width of the region is made comparable to the Fermi wavelength, the conductance becomes quantised in values of $2e^2/h$ (B=0). This device is known as a quantum point contact[10,11].

2.3.1 Electrons in 1D

In order to understand the reason for the appearance of quantised conductance values in 1D structures, it is necessary to consider the effect that the loss of an additional direction of propagation (one degree of freedom) has on the mathematical description of the electron. Solutions to the TISE will lead us to quantised solutions in two directions and free particle solutions in the third.

Eqn. 2.29
$$\left[\frac{p_y^2}{2m^*} - \frac{\hbar^2}{2m^*}\frac{\partial^2}{\partial x^2} - \frac{\hbar^2}{2m^*}\frac{\partial^2}{\partial z^2} + V(x,z)\right]\psi(x,z) = E\psi(x,z)$$

The z direction is taken to be normal to the surface of the semiconductor and therefore the confinement is that of the 2DEG given in section 2.2.

A good approximation for the confinement induced by the split gates is a parabolic potential[12] at the saddle point shown in Figure 2.3. The potential then takes the form of Eqn. 2.30.

Eqn. 2.30

$$V_x = \frac{1}{2} m^* \omega_o^2 x^2$$

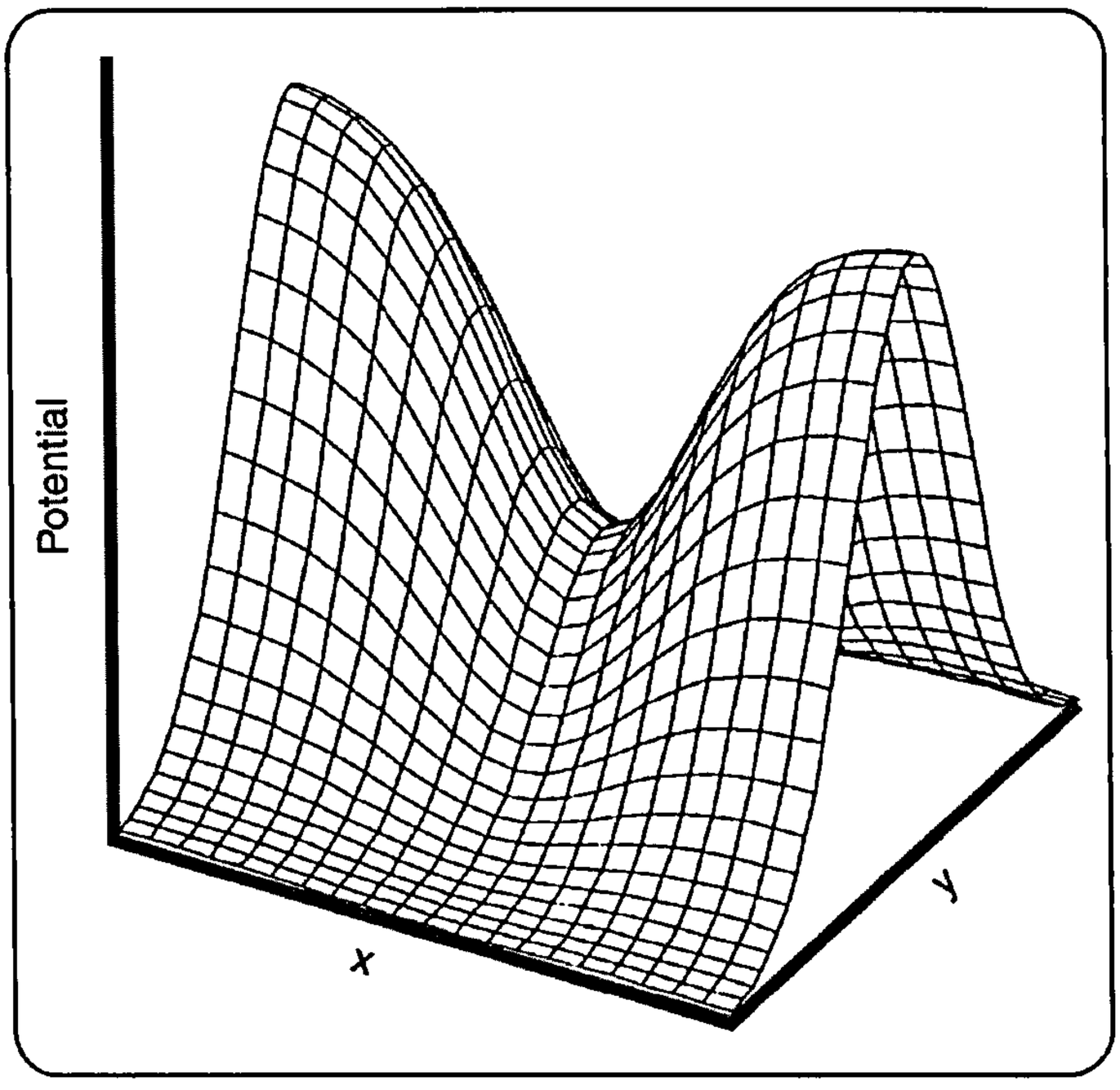

Figure 2.3 Potential landscape at a constriction induced by the split gates. The potential in both x and y is smoothly varying and can be approximated by a 2D saddle potential.

The resulting Schroedinger equation has the energy eigenvalues of the form

Eqn. 2.31

$$E_n = \left(n + \frac{1}{2}\right) \hbar\omega_o + \frac{\hbar^2 k_y^2}{2m^*} \qquad \text{where n=0,1,2,...}$$

which gives a free electron energy dispersion solution in y and quantised values separated by $\hbar\omega_0$ in x. Each value of $(n+1/2)\hbar\omega_0$ becomes the energy value at the bottom of a 1D subband.

2.3.2 1D Density of states

The same procedures that determined the 2D density of states in section 2.2.1 is followed to obtain the 1D case. Equation Eqn. 2.16 gives the separation of points in k-space; $2\pi/L$.

The number of states per unit length in k-space is

Eqn. 2.32
$$N_k = 2 \times 2 \times \frac{L}{2\pi}$$

where the first 2 accounts for the spin degeneracy and the second 2 allows for the different directions of k ($\pm k_y$). Dividing by L gives the 1D density in k-space = $2/\pi \equiv n_k$.

As in the 2D case the number of states in k-space must equal the number of energy states. The quadratic dispersion relation means that, although the points are equally spaced in k this is not the case in E.

Eqn. 2.33
$$n_k = n_E \frac{dE}{dk} \Rightarrow \frac{2}{\pi} = n_E \frac{\hbar^2 k}{m^*} \Rightarrow n_E = \frac{2}{\pi} \frac{m^*}{\hbar^2 k}$$

hence

Eqn. 2.34
$$n_E = \frac{2m^*}{\hbar^2 \pi} \frac{\hbar}{\sqrt{2m^* E}} \Rightarrow \frac{1}{\pi\hbar} \sqrt{\frac{2m^*}{E}}$$

The resulting 1D density of states has a $1/\sqrt{E}$ dependency. This means that the density at the bottom of a 1D subband is large.

2.3.3 Transport in 1D

Transport of electrons through the system originates from an electrochemical potential difference between the two wide 2DEG regions.

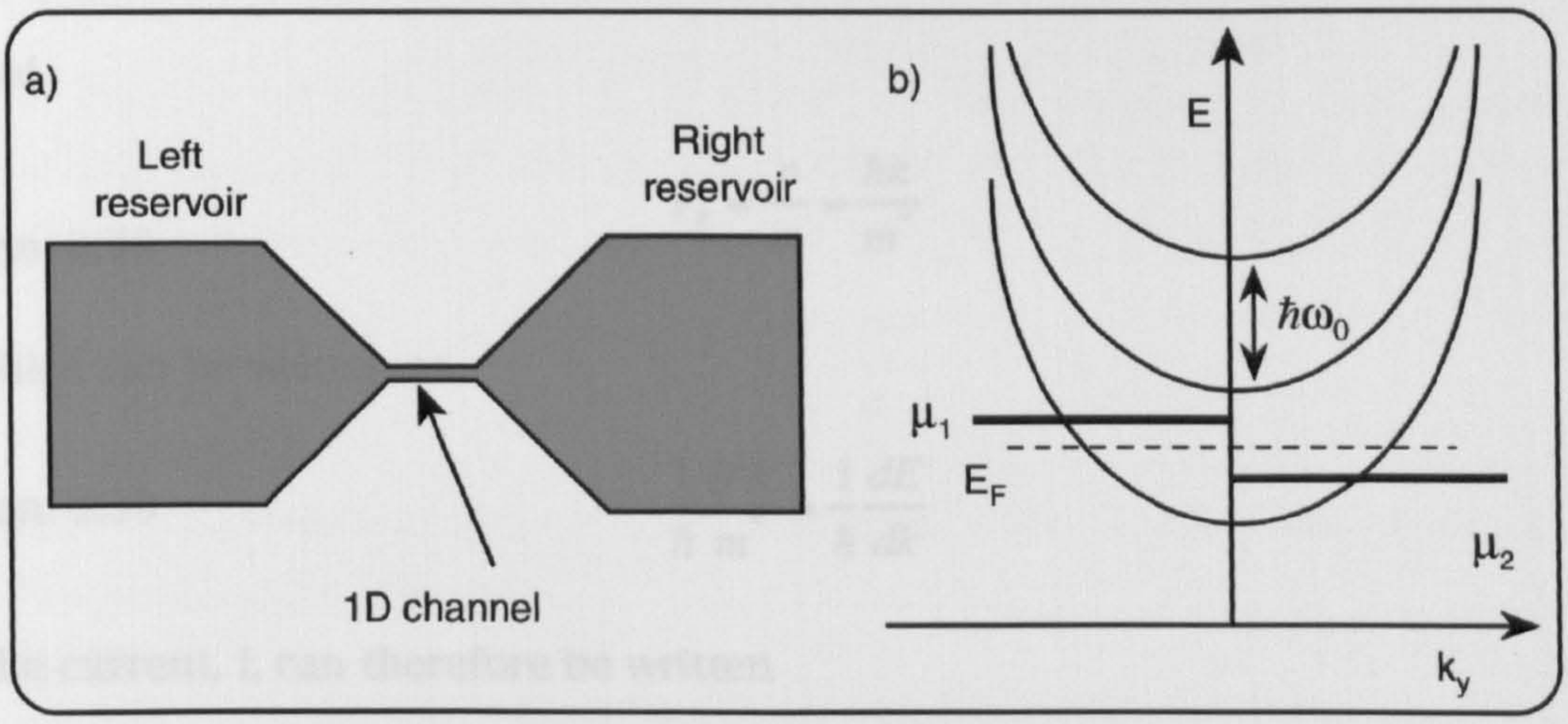

Figure 2.4 a) The left and right reservoirs of the two wide 2DEG regions linked by a 1D channel. b) Three parabolic subbands separated by $\hbar\omega_o$. Electron transport takes place with an applied bias across the sample causing a electrochemical potential difference between the two reservoirs[1,7].

Electrons in the left reservoir move to the right populating all the states up to the electrochemical potential μ_1. Similarly the left going electron states are all filled up to the electrochemical potential μ_2 of the right 2DEG region. Assuming a small electrochemical difference between them (μ_1-μ_2), so that the average velocity may be approximated by the slope of the subband, the electron velocity is

Eqn. 2.35
$$v_n = \frac{1}{\hbar}\left(\frac{dE}{dk}\right) \equiv v_F \qquad \text{for } E=E_F$$

E_F (and therefore v_F) is defined as $E_F=\mu_1=\mu_2$ at v=0, this is also assumed to be valid for small values of V.

The voltage difference $V=(\mu_1-\mu_2)/e$ between the reservoirs results in a net electron, and therefore current, flow. This current is carried by the states between μ_1 and μ_2 and can be seen as a result of having available (unoccupied) electron states within the right reservoir.

The net current flow is given by

Eqn. 2.36
$$I = \frac{1}{2}\int_{\mu_1}^{\mu_2} dE \cdot n_E \cdot v_F \cdot e$$

from equation Eqn. 2.33

Eqn. 2.37
$$n_E = \frac{2}{\pi}\frac{m^*}{\hbar^2 k} = \frac{2}{\pi}\left(\frac{dE}{dk}\right)^{-1}$$

and

Eqn. 2.38
$$v_F = \frac{p}{m} = \frac{\hbar k}{m^*}$$

which can be written as

Eqn. 2.39
$$\frac{1}{\hbar}\frac{\hbar^2 k}{m^*} = \frac{1}{\hbar}\frac{dE}{dk}$$

The current, I, can therefore be written

Eqn. 2.40
$$I = \frac{1}{2}\int_{\mu_1}^{\mu_2} \cdot \frac{2}{\pi}\frac{m^*}{\hbar^2 k} \cdot \frac{1}{\hbar}\frac{\hbar^2 k}{m^*} \cdot e = \frac{2e}{h}(\mu_1 - \mu_2)$$

An extremely important aspect of 1D transport can be seen in equation Eqn. 2.40 in which the dispersion relation dE/dk from the velocity and the density

of states cancel. This cancellation means that the current carried by a single1D subband has no dependence on energy.

Eqn. 2.41
$$I = \frac{2e}{h} eV = \frac{2e^2}{h} V$$

This is in the form I=GV and on rearrangement we obtain the quantised conductance relation

Eqn. 2.42
$$G = \frac{2e^2}{h}$$

The conductance G also depends on the number of occupied subbands (N) and a tunnelling probability factor $T_{n(E_F)}$ which allows for the possibility that only a fraction of incident electrons will get through. Hence the conductance becomes:

Eqn. 2.43
$$G = \frac{2e^2}{h} \sum_{n=1}^{N} T_{n(E_F)}$$

which is the Landauer-Buttiker[13,14] formula. Figure 2.5 shows conductance of a quantum point contact. The subbands become depopulated with increasingly negative gate voltage. The conductance changes in steps of $2e^2/h$ for each subband. This data was taken as part of the data set from the quantum dot device presented in chapter 5. Quantised conductance data taken from quantum point contact experiments rarely show conductance plateaus at exactly $2e^2/h$. This is normally as a result of T_n having a value less than 1.

The number of subbands, N, is given by the number of half electron wavelengths at the Fermi energy which will fit into the channel and hence is given by [15].

Eqn. 2.44
$$N = Int\left[\frac{k_F W}{\pi}\right]$$

Where *int* denotes the nearest integer value, K_F is the Fermi wavevector and W is the width of the channel.

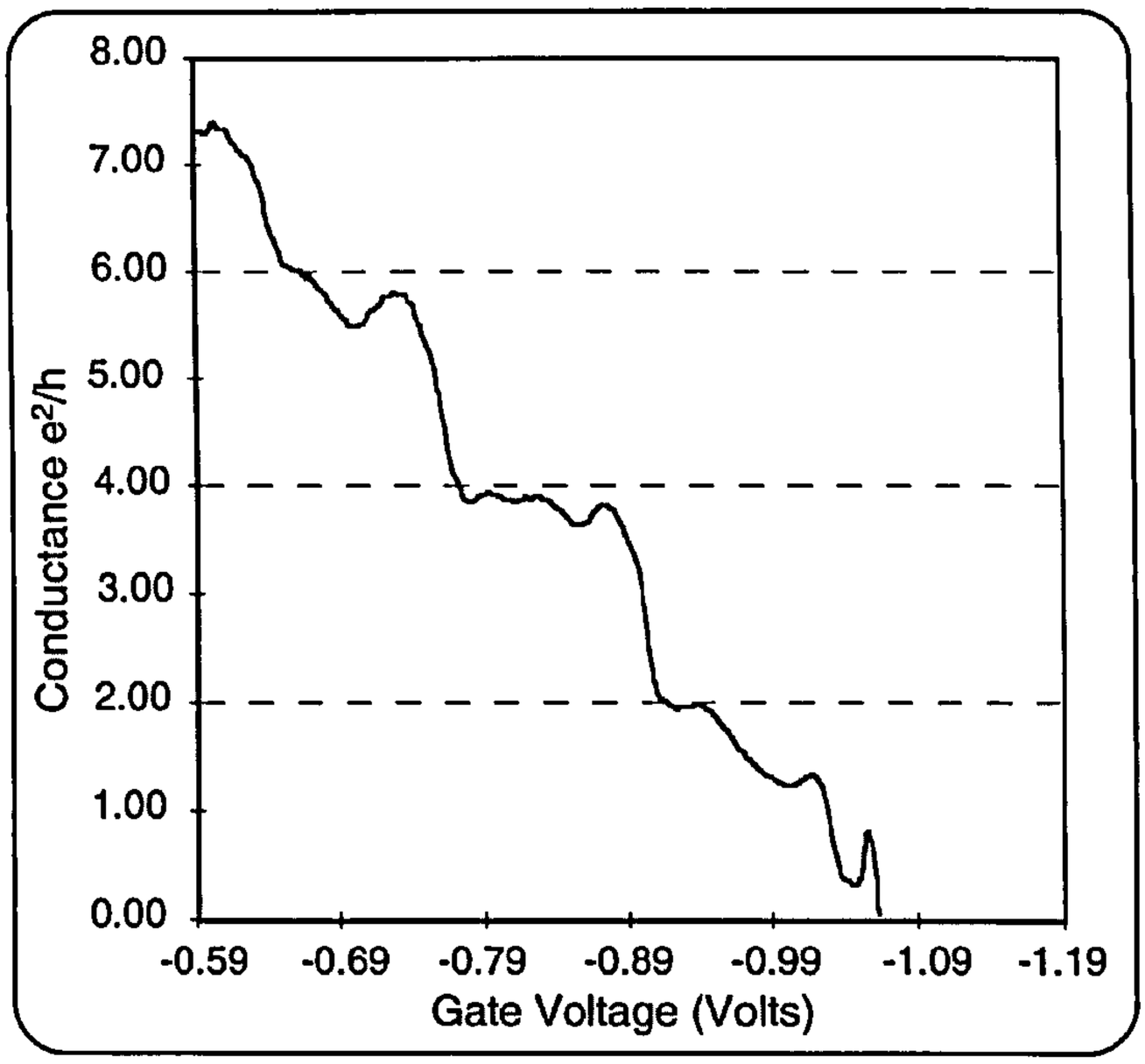

Figure 2.5 A conductance versus gate voltage plot showing steps in the conductance at multiples of $2e^2/h$.

2.4 0-Dimensional Devices

Sections 2.1 and 2.3 have detailed the effect of increasing levels of confinement on electrons. The interface confines the electrons to a plane allowing propagation in two perpendicular directions (x,y). Using the split gate technique the electrons lose another propagation direction and are confined to a line (quantum wire). In this section the effects of increasing the confinement, resulting in the inability of the electrons to propagate in any direction, are considered. This increased confinement results in the formation of an isolated island of electrons which is referred to variously as a quantum dot or single electron device.

Two regimes are distinguishable in such devices.

Firstly there is the classical blockade regime. In this regime conduction through the device is dominated by the capacitance of the island, with respect to the environment, and the fundamental electron charge. These devices are small enough that the addition or subtraction of one electron dominates the current flow through the device. The energy scales over which this regime is defined is $\Delta\varepsilon_i < kT < e^2/C$, where the thermal energy is greater than the single particle spacing $\Delta\varepsilon_i$ within the dot, but less than the charging energy associated with adding or subtracting an electron, e^2/C.

Secondly there is the quantum Coulomb blockade regime. Here, although the charge quantisation of the classical blockade regime still exists, the single

particle levels become observable. Transport through the system is still controlled at the single electron level but with the addition of an energy scale due to the quantum mechanical state of the electron within the dot. In order to observe these effects the single particle energy must be at least comparable to the other energies within the system, $kT \leq \Delta\varepsilon_i \leq e^2/C$.

2.4.1 Charge Quantisation and Coulomb Blockade

Imagine a puddle (dot) of electrons. That is, a small group of conduction electrons isolated (except via capacitance) from the rest of the world; Figure 2.6.

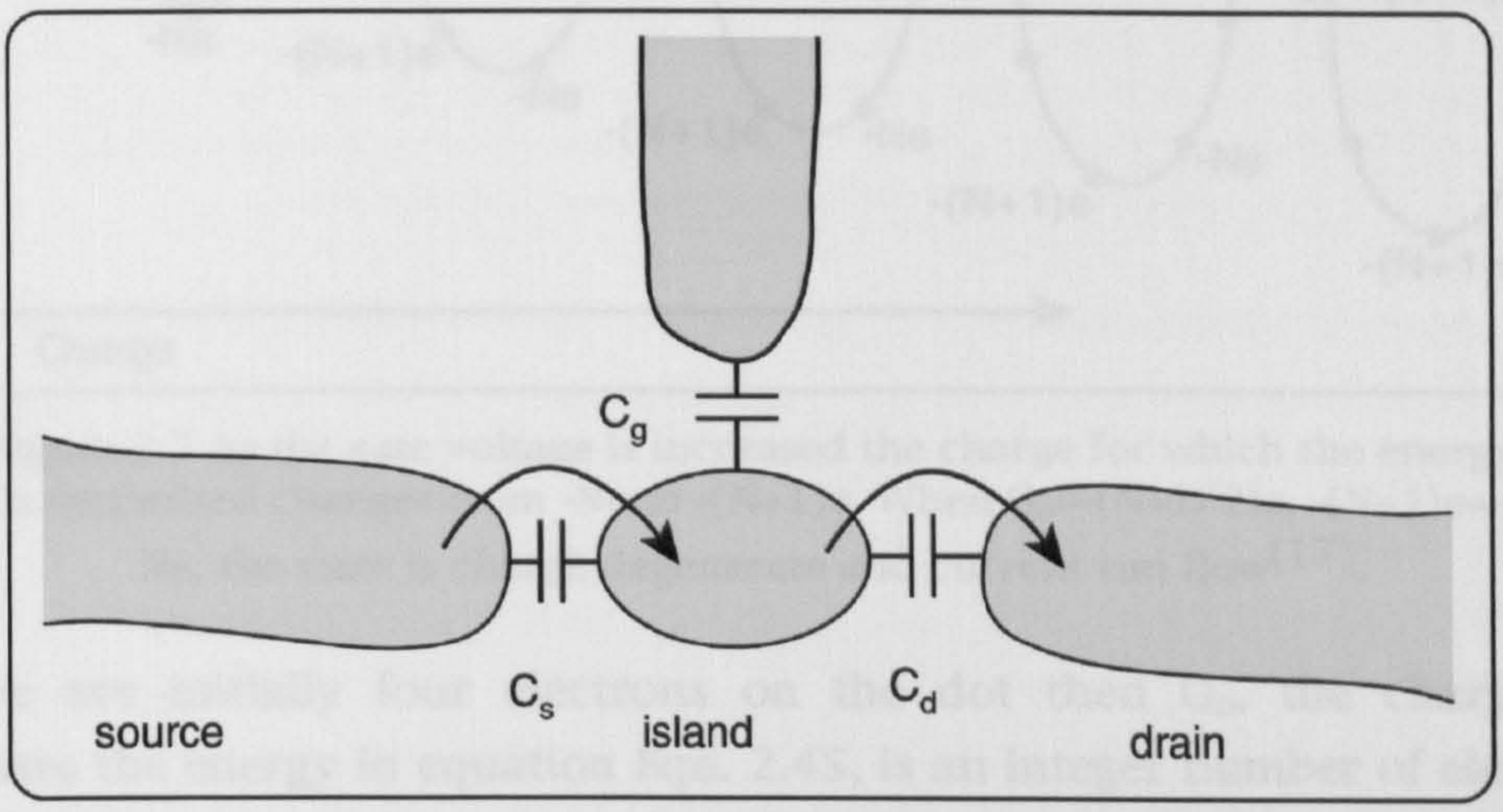

Figure 2.6. An isolated island of electrons (centre) couples to its surroundings via mutual capacitance[16].

In order to add or subtract an electron to or from the dot the energy of the dot has to change by a discrete value e^2/C_g (where e is the electron charge and C_g is the capacitance between the dot and the gate). If there is no mechanism to change the energy then no current will flow. By placing a gate electrode close to the dot, the energy of the dot may be varied continuously simply by applying a voltage, $E = QV_g$. The total energy therefore becomes the sum of the a discrete contribution, given by the integer number of electrons, and a continuous part given by the potential applied to the gates[6].

Eqn. 2.45
$$E_N = \frac{(Ne)^2}{2C_g} + eV_gC_g$$

where N is the integer number of electrons on the dot and V_g the voltage applied to the gate. In reality, the total capacitance of the dot to the outside world is a sum of many different capacitances and C_g should be replaced with C_Σ. This represents the contributions from the other defining gate electrodes

and the wide 2DEG regions to the dot. There exist two mechanisms by which the potential of the dot can be changed, either discretely by the addition or subtraction of an electron, or continuously via the gate. In order to illustrate the interaction between the discrete and continuous methods by which the dot potential is changed Figure 2.7 shows the effect of a constant increase in gate voltage on the free energy of the electrons in the dot.

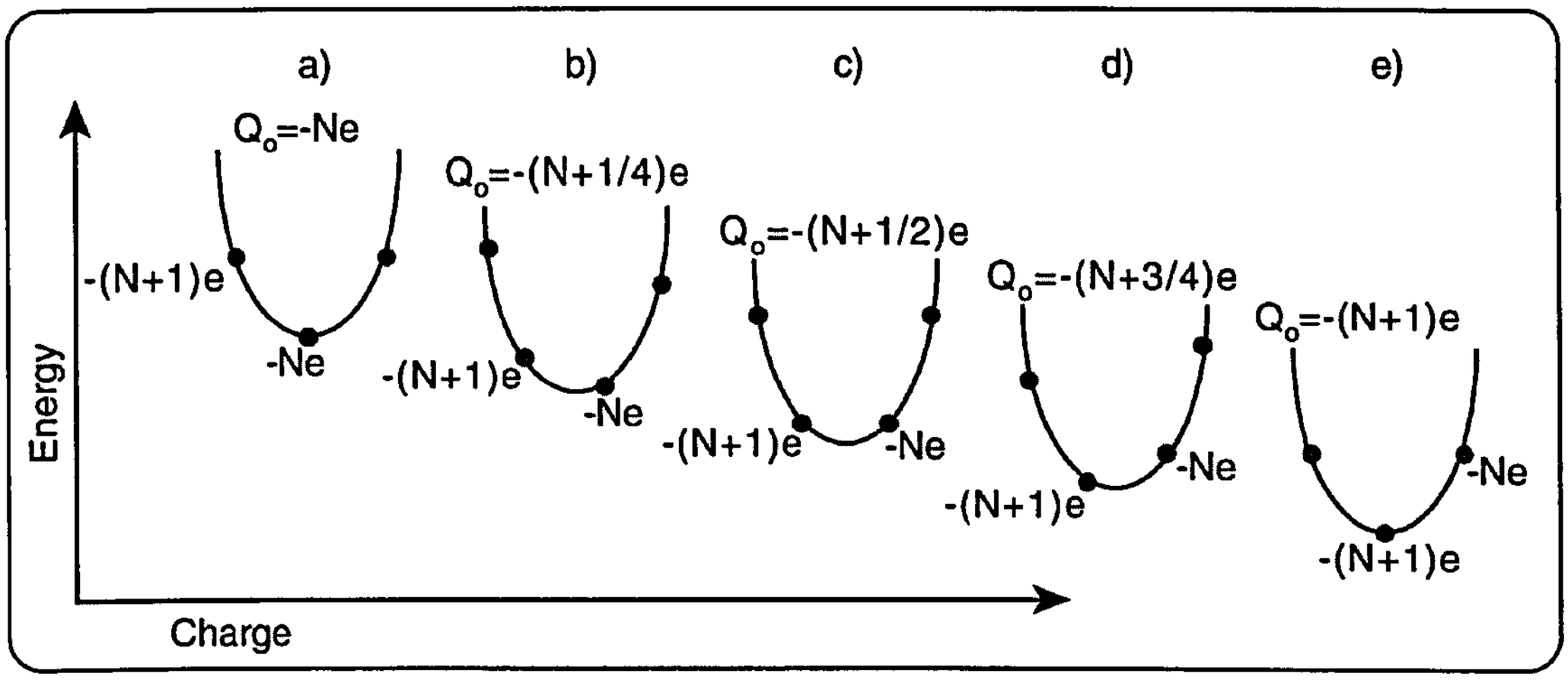

Figure 2.7 As the gate voltage is increased the charge for which the energy is minimised changes from -Ne to -(N+1)e. When Q_0=-(N+1/2)e, -(N+1)e=-Ne, the state is charge degenerate and current can flow[17].

If there are initially four electrons on the dot then Q_o, the charge that minimises the energy in equation Eqn. 2.45, is an integer number of electrons. In Figure 2.7 a) increasing the energy by a small amount leads to a situation, shown in b), where the minimum energy value is no longer an integer number of electrons, but an integer number plus the energy induced by the gate voltage. Further increase takes the potential through a half integer electron energy value, c), and eventually back to an integer value but now with an extra electron on the dot in this case five. Further increase repeats an exactly similar cycle between electron numbers five and six and so forth.

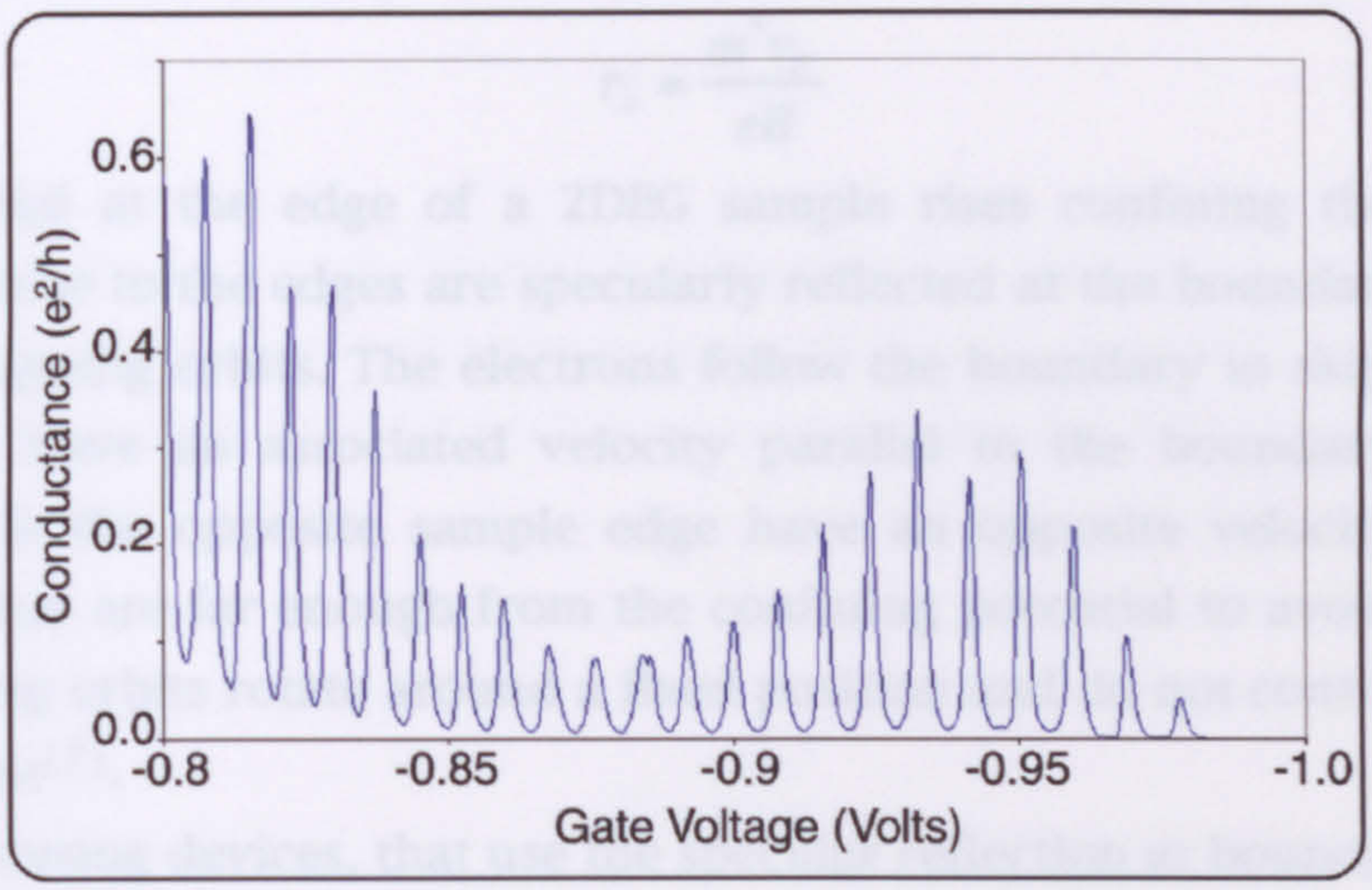

Figure 2.8. Periodic oscillations in the conductance of devices exhibiting Coulomb blockade are seen as the gate voltage is swept. The maximum of each peak is a charge degenerate point where current is flowing. The zero conductance points in between peaks are when the energy of the dot is minimised by an integer multiple of electrons.

In the small bias regime, when the energy of the dot is equal to an integer number of electrons current through the system is at a minimum and the dot is said to be Coulomb blockaded. By continuously increasing the gate voltage the conductance is made to oscillate as one electron at a time is pushed out of the dot. A typical trace is shown in Figure 2.8. This trace is taken from data presented in chapter 5.

A detailed account of the incorporation of the single particle states into the classical Coulomb blockade theory is given in chapter 5.

2.5 Magneto-transport in 2DEGS

In the classical description of motion in a magnetic field the electron follows a circular trajectory (orbital). The balance of the Lorentz force

Eqn. 2.46
$$\vec{F}_L = -e\vec{v} \times \vec{B}$$

and the centripetal force

Eqn. 2.47
$$F = \frac{m^* v^2}{r}$$

leads to a cyclotron motion of the electron with a cyclotron radius at the Fermi energy

Eqn. 2.48 $$r_c = \frac{m^* v_F}{eB}$$

The potential at the edge of a 2DEG sample rises confining the electrons. Electrons close to the edges are specularly reflected at the boundary potential, forming skipping orbits. The electrons follow the boundary in skipping orbits and hence have an associated velocity parallel to the boundary direction. Electrons on the opposite sample edge have an opposite velocity direction. Electrons that are far enough from the confining potential to avoid deflection into skipping orbits rotate around a fixed position and do not contribute to the edge current[7].

Electron focusing devices, that use the specular reflection at boundary edges as well as quantum point contact structures are described in chapter 5. Experimental results are also presented.

2.5.1 Landau Levels and Edge States

In high magnetic fields, electron motion is quantised. This arises from the requirement that the electron must interfere constructively with itself around a given cyclotron orbit. Hence for a given magnetic field the electron wavelength, λ, must be at a value that allows the electron to transverse the orbit in multiples of $n2\pi$ where n is an integer. The quantum of magnetic flux is defined as the flux enclosed by an electron in a cyclotron orbit, and takes integer multiples of

Eqn. 2.49 $$\frac{h}{e} = \phi_o$$

The quantised electron energies are

Eqn. 2.50 $$E_n = \left(n + \frac{1}{2}\right)\hbar\omega_c + eV_{x,y} \qquad n = 0,1,2,...$$

where $\omega_c = eB/m^*$ is the cyclotron frequency, n is the Landau level index and $V_{x,y}$ is some constant or slowly varying potential. The density of states in each Landau level per unit area can be approximated by

Eqn. 2.51 $$\rho = 2\frac{eB}{h}.$$

Where the 2 accounts for the two possible spin states. The field dependency of the density of states arises from the modification of the electron phase, hence wavelength and separation in k-space. This relationship can be seen more clearly by rewriting ρ_E in terms of the flux quantum $\phi_o = h/e$. In which case

Eqn. 2.52 $$\rho = 2\frac{B}{\phi_o}.$$

One flux quantum changes the phase of an electron wavefunction by 2π. Hence equation Eqn. 2.52 gives twice the number of flux quanta in B. As there is one state in each Landau level for each flux quanta equation Eqn. 2.52 can be seen to be the density of states.

By substituting

Eqn. 2.53 $$B = \frac{\omega_c m^*}{e}$$

from the cyclotron frequency into equation Eqn. 2.51 n_B, the magnetic density of states becomes

Eqn. 2.54 $$n_B = \frac{m^*}{\pi\hbar^2} \cdot \hbar\omega_c$$

this is the 2D density of states modulated by $\hbar\omega_c$. Thus each Landau level contains the states that originally filled the constant 2D density of states over a range $\hbar\omega_c$[2]. The separation between Landau levels is also $\hbar\omega_c$. This means that, when averaged over a large number of Landau levels, the magnetic field doesn't change the average density of states, but collapses each width of $\hbar\omega_c$ into a δ-function. Figure 2.9 illustrates this.

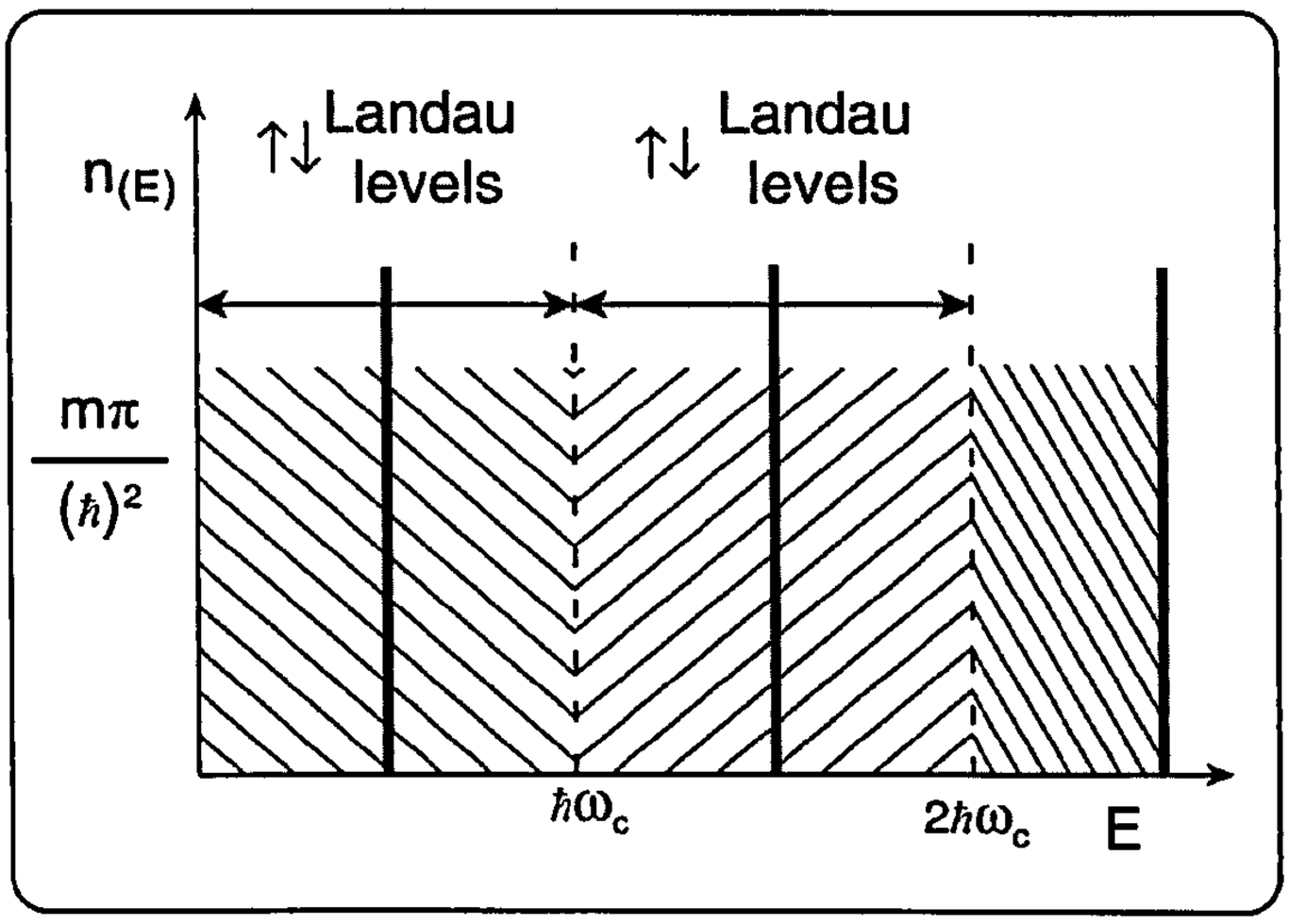

Figure 2.9 Each Landau level contains the same number of electrons that would have been contained in 2DEG at zero field within the range $\hbar\omega_c$.

For an increasing magnetic field, the density of states per Landau level increases linearly, as does the separation between Landau levels. Although the average density is unchanged, gaps appear in the energy distribution. In the

high field regime, large numbers of electrons are contained in a very few fat Landau levels.

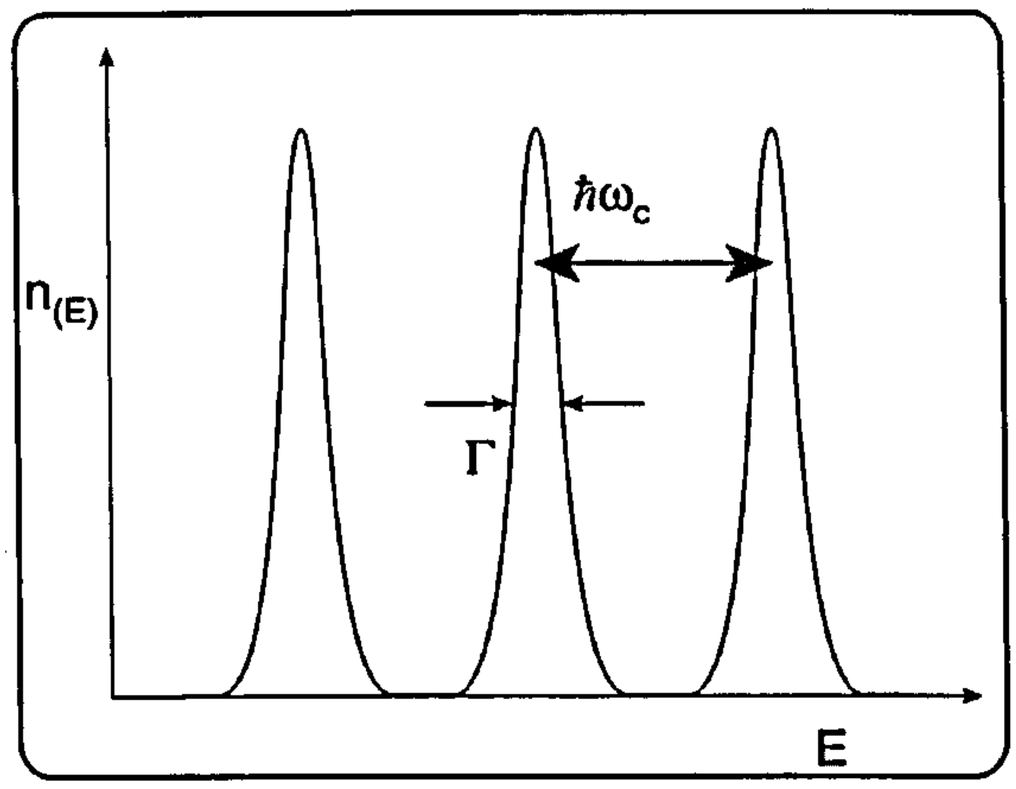

Figure 2.10 As the field increases the Landau levels can contain a larger number of electrons until eventually all are contained in a single level defined as η=1.

Figure 2.10 shows Landau levels whose spacing $\hbar\omega_c >> \Gamma$ where Γ is the non-zero width of the level. E_F is positioned at an integer filling factor where the density of electrons is zero. With the density of electrons n_{2D} roughly constant the number of occupied Landau levels must change. Raising B causes the Landau level to move up in energy and the number of states in each level grows with fewer electrons occupying the top level. The Fermi energy, E_F, also has to move with the changing density of states to keep the density of electrons constant. If the Fermi energy lies in the empty region between Landau levels when ν, the filling factor is an integer. Raising B causes the Fermi energy to fall back to the Landau level below. Raising B further when E_F is within the Landau level causes E_F to rise linearly with B until the next integer value of ν is reached.

2.5.2 Magneto-Resistance of 2DEGS

The B-dependent nature of the density of states and formation of Landau levels has important consequences in longitudinal and transverse measurements of magnetoresistance (and hence magnetoconductance).

Shubnikov De Haas

A striking effect is the oscillation of longitudinal resistivity with B shown in Figure 2.11; the Shubnikov De Haas effect.

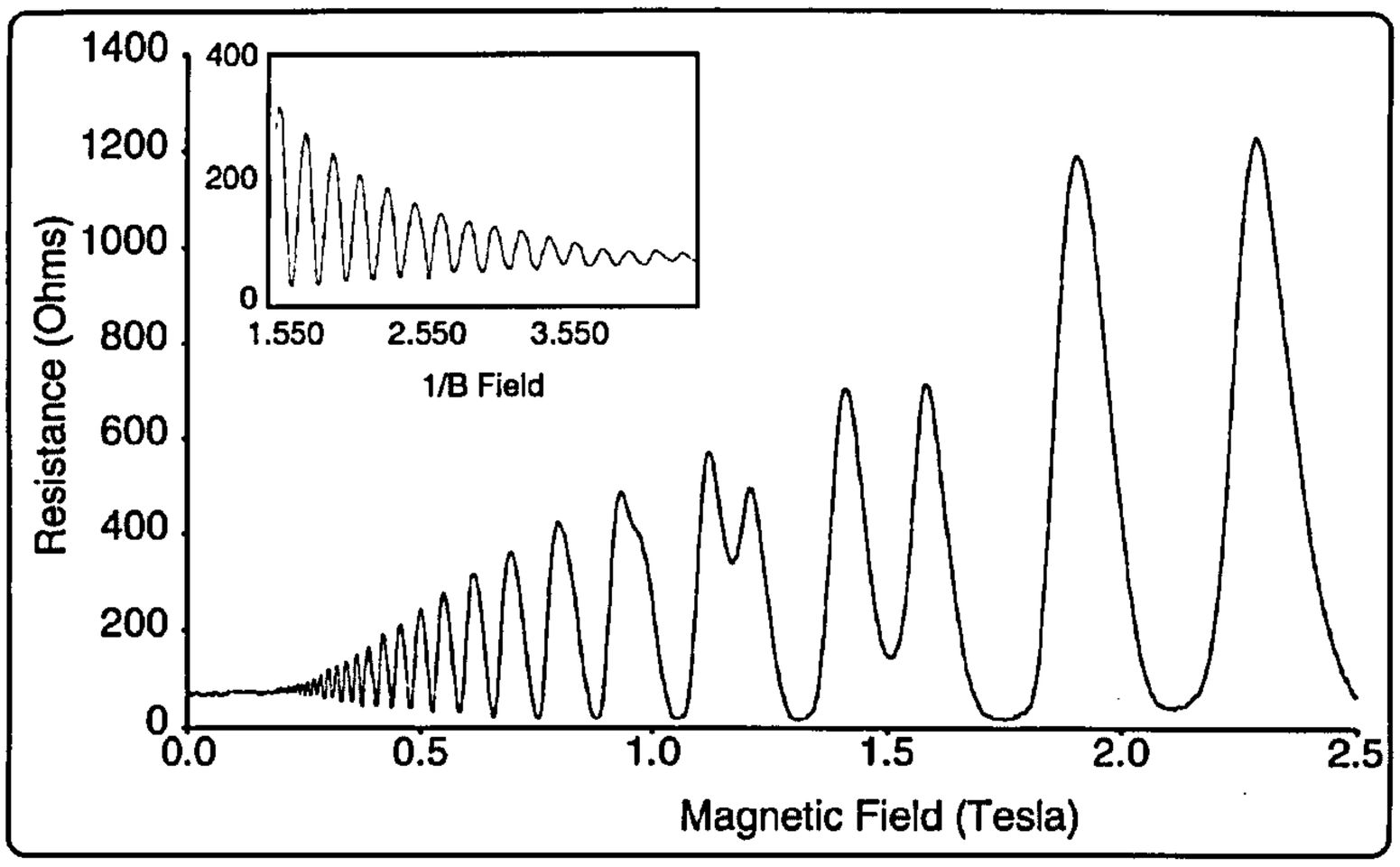

Figure 2.11 As the Fermi level oscillates in B to keep within an electron populated band so, in turn does the resistance.

These oscillations are a direct result of the oscillations in the density of states at the Fermi energy. The resistance is a minimum when the Fermi energy lies between two Landau levels where the density of states is a minimum due to fewer available states for scattering into. This occurs at integer filling factors. The oscillations are periodic in 1/B and hence

Eqn. 2.55
$$\Delta\frac{1}{B}=\frac{e}{hn_s}$$

Shubnikov De Haas is the standard means by which the electron density n_{2Ds} is determined.

Quantum Hall Effect

The quantised conductance value can be arrived at by use of the 2D electron density in the standard Hall equations

The Hall equations, in terms of conductivity, are

Eqn. 2.56
$$\sigma_{y,x}=\frac{J_y}{E_x}=\frac{1}{R_H B_Z}=\frac{en_{2D}}{B_Z}$$

substituting the 2DEG electron density (n_{2D}=NeB/h) gives the quantised Hall conductance value

Eqn. 2.57
$$\sigma_{y,x}=N\frac{e^2}{h}$$

In section 2.2.3, this same result was arrived at for the conductance of the quantum point contact. This is evidence that edge channels can be viewed as

1D current channels. The effect on the magneto-conductance, shown in Figure 2.12, is remarkable.

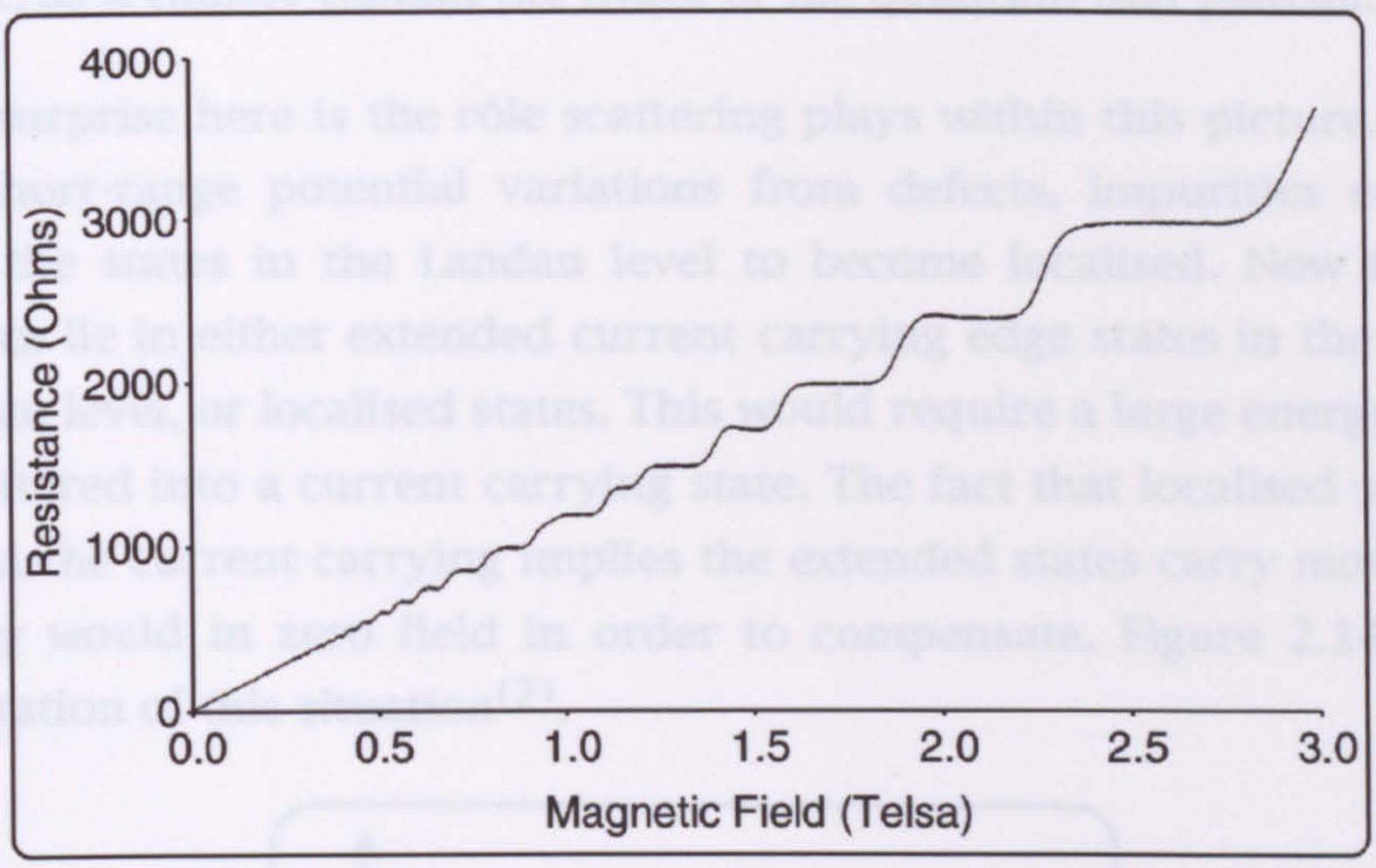

Figure 2.12 The Quantum Hall effect is obtained in 2DEG samples at low temperatures. The origins are exactly the same as the Shubnikov-De Haas effect with the Fermi energy jumping to the next available Landau level. In a Hall measurement this results in extremely well defined conductance plateus at the conductance quantum values of e^2/h.

The ease of the above derivation belies some of the subtleties within the physical picture associated with the quantum Hall effect.

The spatial separation of the different velocity directions, referred to in Section 2, is shown in Figure 2.13 for the situation where E_F is between Landau levels.

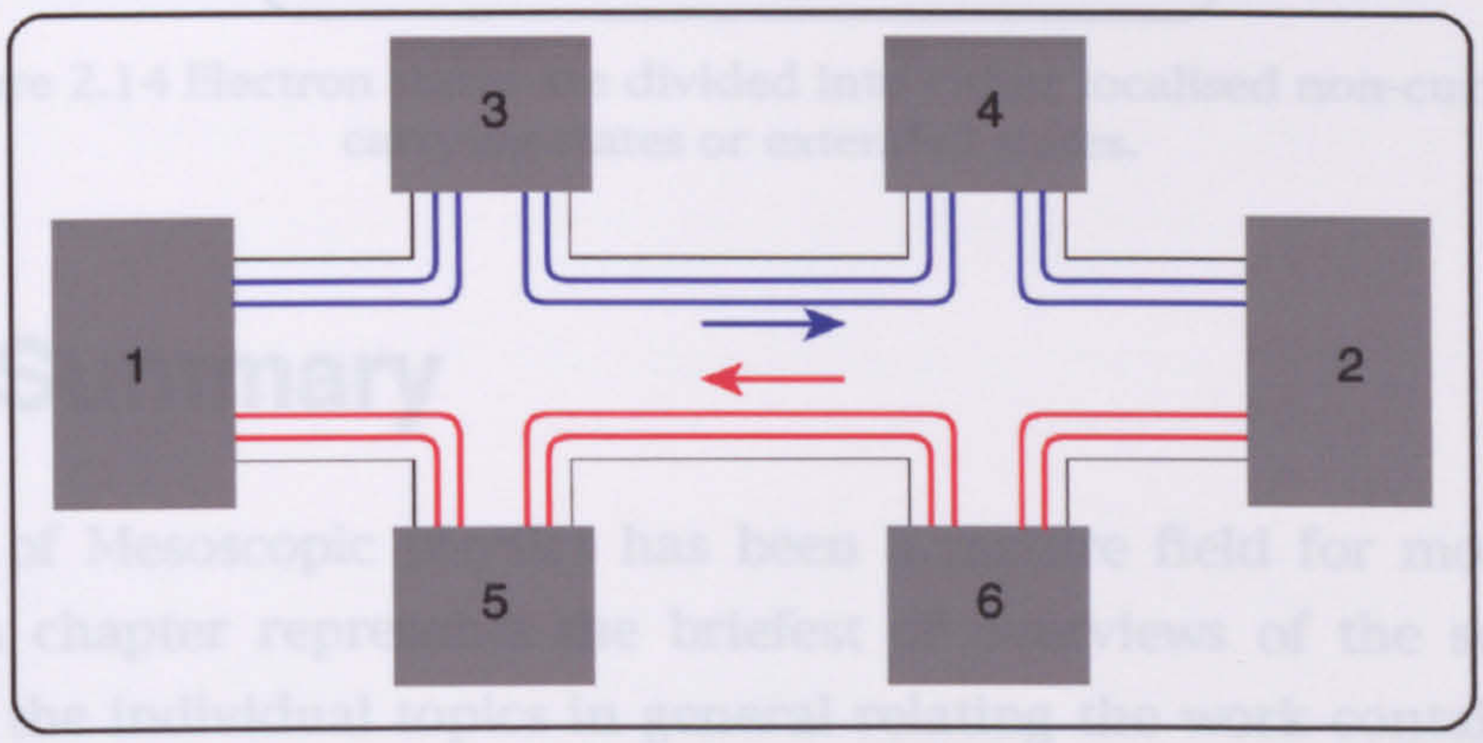

Figure 2.13 In high magnetic field the edge states travelling in opposite directions are at opposite sides of the sample.

In Figure 2.13 the states travelling from 1 to 2 are on opposite sides of the sample to those travelling from 2 to 1. This gives rise to an almost total suppression of backscattering, since this would require an electron to scatter from one side of the sample to the other.

In section 0 however it was shown that it is extremely difficult to position the Fermi energy between Landau levels. This poses a problem for the above argument, as it cannot explain the width of the quantum Hall plateau.

A major surprise here is the rôle scattering plays within this picture. Disorder due to short-range potential variations from defects, impurities etc., cause some of the states in the Landau level to become localised. Now the Fermi energy can lie in either extended current carrying edge states in the centre of the Landau level, or localised states. This would require a large energy in order to be scattered into a current carrying state. The fact that localised states play no part in the current carrying implies the extended states carry more current than they would in zero field in order to compensate. Figure 2.14 shows a representation of this situation[2].

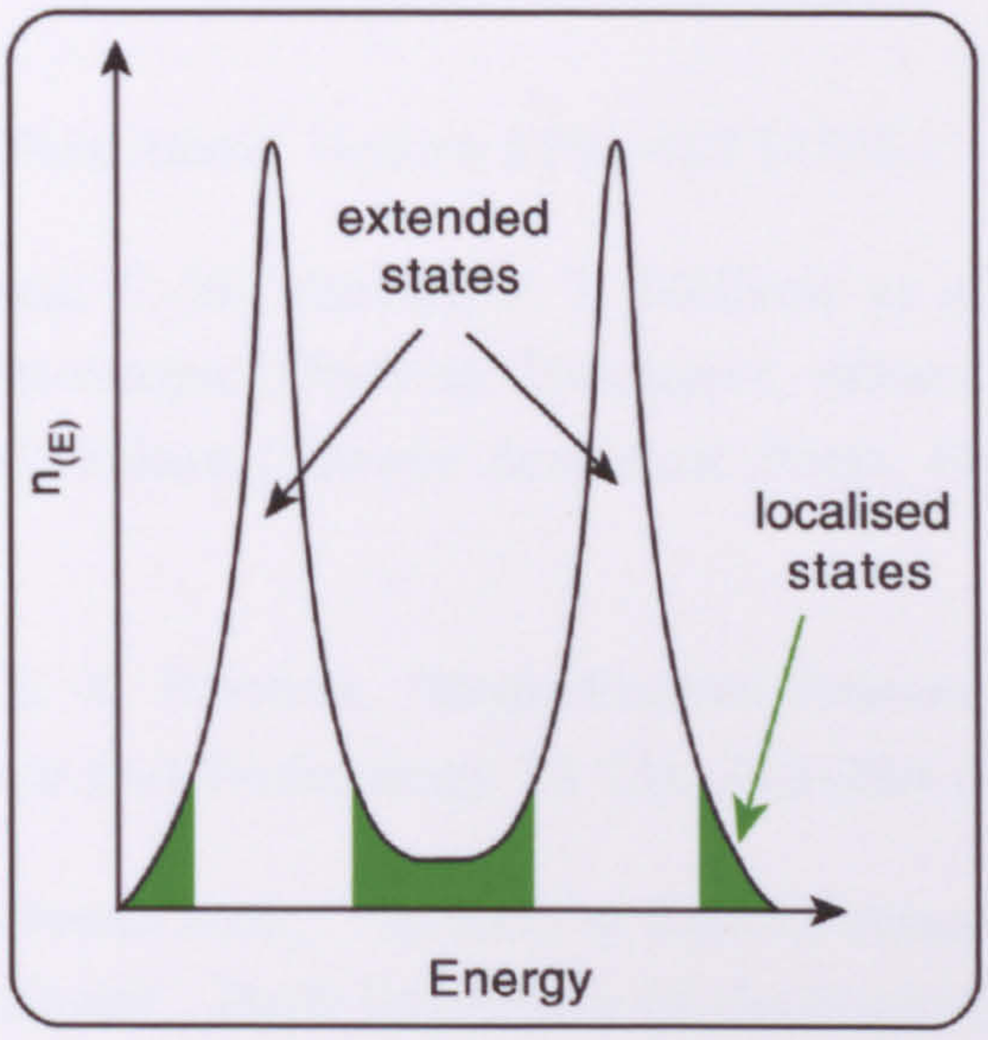

Figure 2.14 Electron states are divided into either localised non-current carrying states or extended states.

2.6 Summary

The study of Mesoscopic physics has been a mature field for more than 15 years. This chapter represents the briefest of overviews of the subject as a whole and the individual topics in general relating the work contained within this thesis. An attempt has been made to give the most physically accessible picture, at the expense of mathematical rigour, and in general, the picture presented is considered as the conventional view, held by the majority of the community.

In chapter 5, where experimental results are presented, extensions are made to the picture presented here of the interplay between single particle energy states and Coulomb blockade energy.

2.7 References

(1) C. W. J. Beenakker and H. Van Houten, "Quantum Transport In Semiconductor Nanostructures" Solid State Physics Advances In Research And Applications 44, 1-228 (1991).

(2) J. H. Davies, "Nanoelectronics Lecture Notes" (Now published as "The Physics of Low Dimensional Semiconductors", 1994).

(3) H. Van Houten, C. W. J. Beenakker, and A. A. M. Staring, "Coulomb Blockade Oscillations in Semiconductor Nanostuctures" in Single Charge Tunneling, edited by H. Grabert and M. H. Devoret (Plenum Press, New York and London, 1993), Vol. 294, pp. 167-212.

(4) R. C. Ashoori, "Artificial Atoms" Nature 379, 419 (1996).

(5) L. P. Kouwenhoven, C. M. Marcus, P. L. McEuen *et al.*, "Electron Transport in Quantum Dots" in Mesoscopic Electron Transport, edited by L. L. Sohn, L. P. Kouwenhoven, and G. Schon (Kluwer Academic Press, Dordrecht, 1997), Vol. 345.

(6) U. Meirav and E. B. Foxman, "Single-Electron Phenomena In Semiconductors" Semiconductor Science and Technology 11 (3), 255-284 (1996).

(7) Thesis, L. P. Kouwenhoven, "Transport of Electron-Waves and Single-Charges in Semiconductor Nanostructures" , Delft University Of Technology, 1992.

(8) Thesis, M. Persson, "Transport Properties of 1D and 0D Structures in GaAs/AlGaAs Heterostructures" , Chalmers University of Technology, 1994.

(9) N. W. Ashcroft and D. N. Mermin, "Solid State Physics" (Saunders College Publishing, 1976).

(10) T. J. Thornton, M. Pepper, H. Ahmed *et al.*, "One-Dimensional Conduction in the 2D Electron-Gas of a GaAs-AlGaAs Heterojunction" Physical Review Letters 56 (11), 1198-1201 (1986).

(11) B. J. Van Wees, H. Van Houten, C. W. J. Beenakker *et al.*, "Quantized Conductance Of Point Contacts In a Two-Dimensional Electron-Gas" Physical Review Letters 60 (9), 848-850 (1988).

(12) S. E. Laux, D. J. Frank, and F. Stern, "Quasi-One-Dimensional Electron-States in a Split-Gate GaAs/AlGaAs Heterostructure" Surface Science 196 (1-3), 101-106 (1988).

(13) R. Landauer, IBM J.Res.Dev. 1, 223 (1957).

(14) M. Buttiker, Physical Review Letters 57, 1761 (1986).

(15) H. Van Houten, C. W. J. Beenakker, and B. J. Van Wees, "Quantum Point Contacts" Semiconductors And Semimetals 35, 9-112 (1992).

(16) M. H. Devoret and H. Grabert, "Single Charge Tunneling: Coulomb Blockade Phenomena in Nanostructures" , edited by M. H. Devoret and H. Grabert (Plenum Press, 1992).

(17) M. A. Kastner, "Artificial Atoms" Physics Today 46 (24), 24-31 (1993).

3 METHODS

This chapter deals with the materials, methods and techniques used to design, fabricate and measure quantum dot devices. The chapter is not intended as a tutorial but as an overview of the various processes involved. None of the methods are unique, or have been developed in the course of this work, with the notable exception of the measurement system, which is dealt with, more fully in chapter 4. Specifications of material, an account of electron beam lithography, the attainment of low temperature and a brief introduction to general measurement are included.

3.1 Material

The device, for which results are presented in Chapter 5, was fabricated on an in-house grown GaAs-AlGaAs MBE heterostructure. The 2DEG was 90nm below the surface with a carrier concentration $n_s=2x10^{11}m^{-2}$ and electron mobility[1] $\mu=1.5x10^{6}cm^{-2}V^{-1}s^{-1}$ leading to an elastic mean free path of $\approx 11\mu m$. Figure 3.1 shows a schematic of the layer structure used in the experiments detailed in chapter 5.

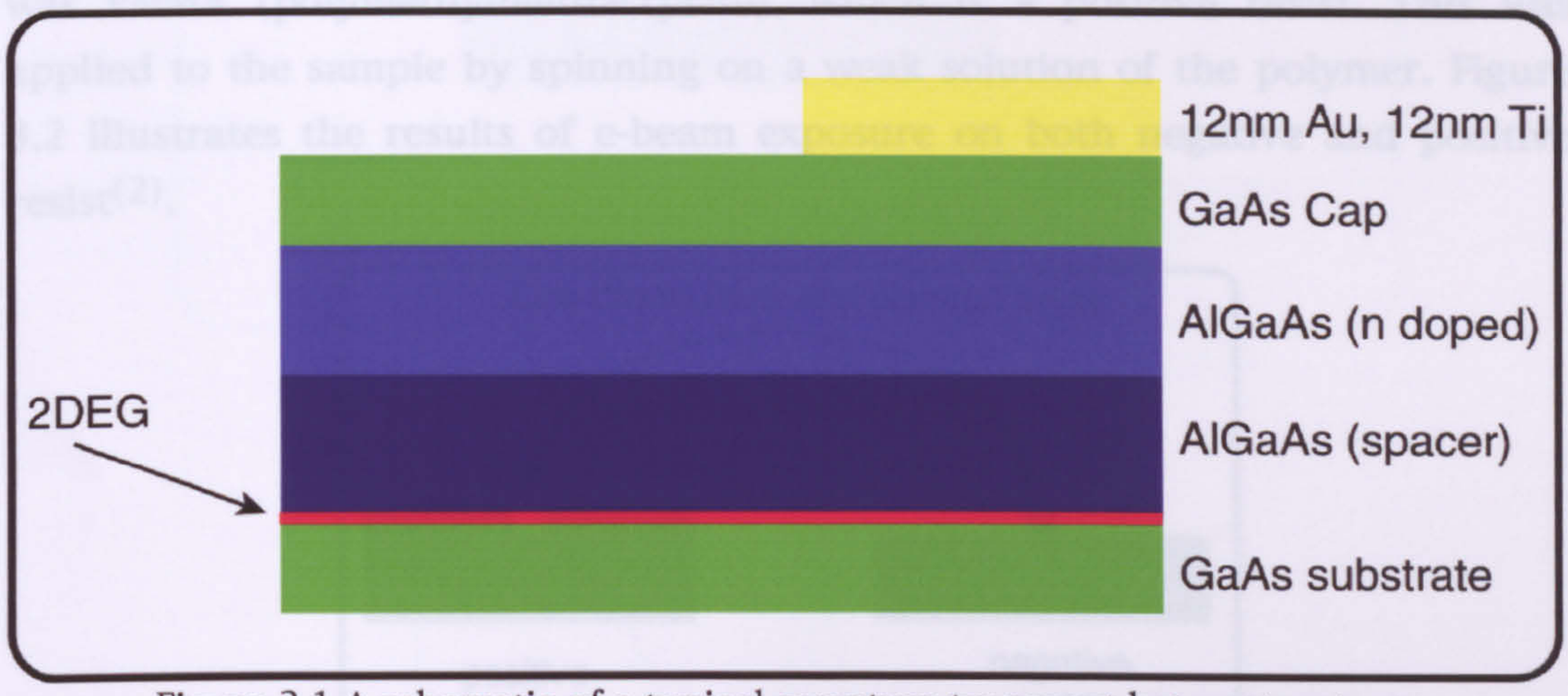

Figure 3.1 A schematic of a typical quantum transport heterostructure.

The conduction band electrons (in the 2DEG) are separated from the randomly distributed donors by an undoped spacer layer of AlGaAs. For a discussion of the band structure and properties of the electrons confined within the 2DEG see Sections 2.1 and 2.2.

3.1.1 Electron Beam Lithography

Pattern transfer using electron beam lithography (EBL) is based on the same technology as the scanning electron microscope. An electron beam may be created by heating a cathode sufficiently so that the electrons have enough energy to overcome the electron affinity of the material and hence are ejected. Subsequently they are usually accelerated to high energies by an electric field typically up to 100KeV. The electron beam can then be focused and collimated by magnetic coils in a lens system. The beam can be focused onto the substrate with a typical minimum spot size of approximately 10nm. The deflection of the beam is controlled by electric and magnetic fields making it possible to aim the

beam with high accuracy at any point on the substrate within a limited area (block size).

3.1.2 Electron Beam Resists

In order to transfer patterns onto a substrate using an electron beam the substrate is covered with EBL resist. The properties of the resist change when it is exposed to the electron beam. There are, in general, two types of resist; positive and negative. In positive resist the exposed area is removed by developer and in negative resist the unexposed area is removed by the developer. In the devices fabricated in the course of this work the EBL resist was PMMA (polymethylmethacrylate), which is a positive resist. This was applied to the sample by spinning on a weak solution of the polymer. Figure 3.2 illustrates the results of e-beam exposure on both negative and positive resist[2].

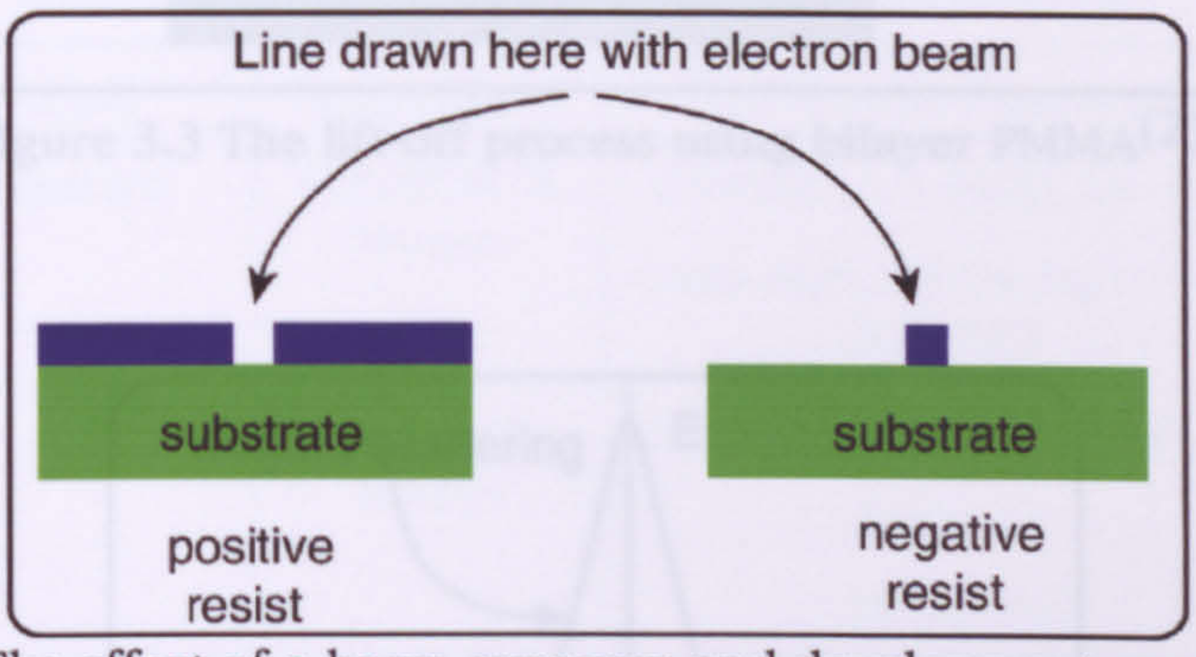

Figure 3.2 The effect of e-beam exposure and development on positive and negative resists.

Polymer resist can be thought of as being made up of long molecular chains. In positive resist these chains are broken down by exposure to electrons and hence become more soluble in developer. In negative resists the exposed regions become cross-linked, which means that the polymer chains get longer, and less soluble. The developers used for dissolving the unexposed regions of resist were mixtures of IPA (isopropanol) and MiBK (methyl isobutyl ketone). For metallic contacts (gate and Ohmic levels) the metal was deposited on the developed resist and the exposed areas of substrate. The resist (and hence metal on the resist) was then removed with a solvent (acetone). This is a standard process technique known as lift-off[3] and is illustrated in Figure 3.3.

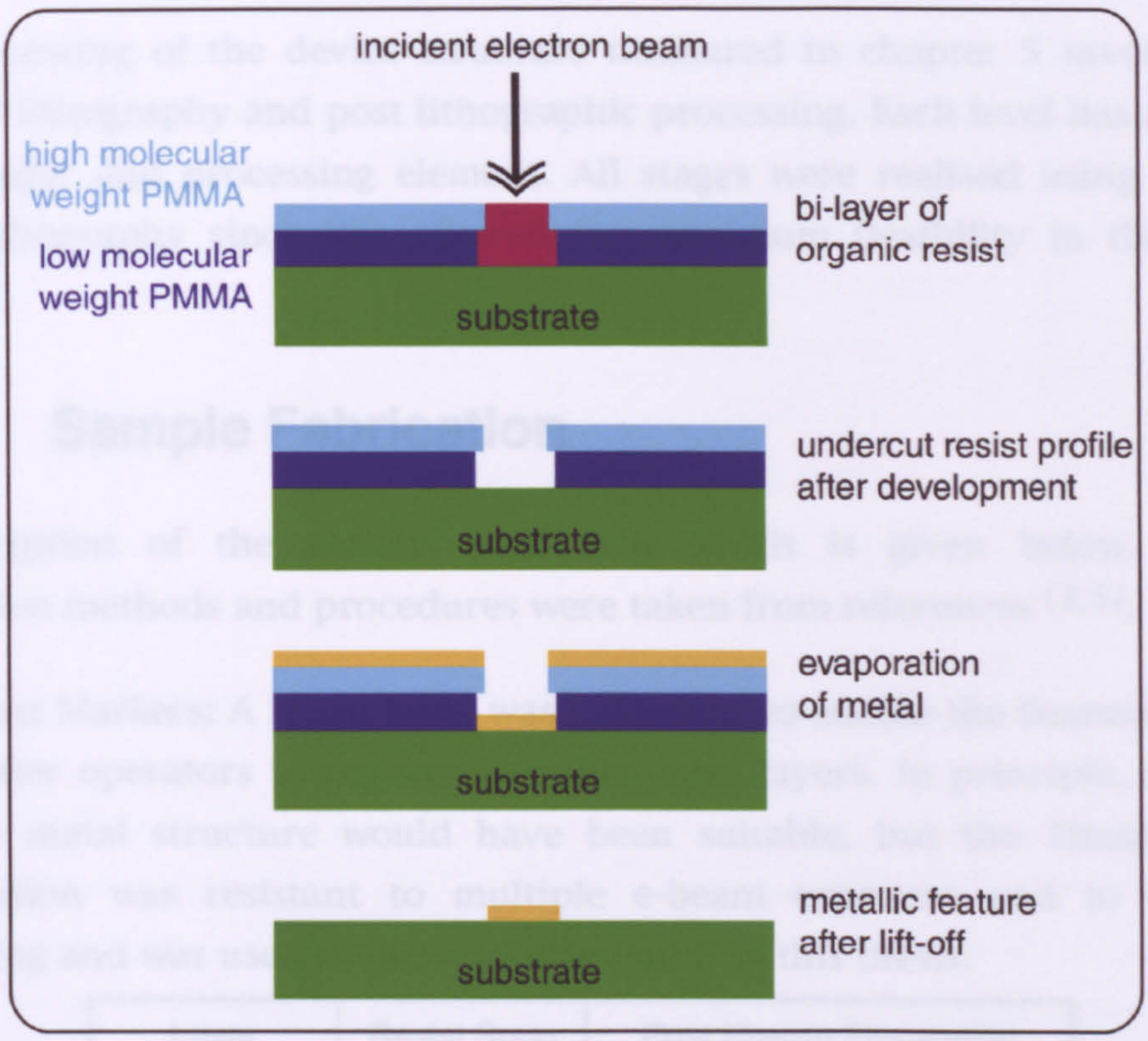

Figure 3.3 The lift-off process using bilayer PMMA[2].

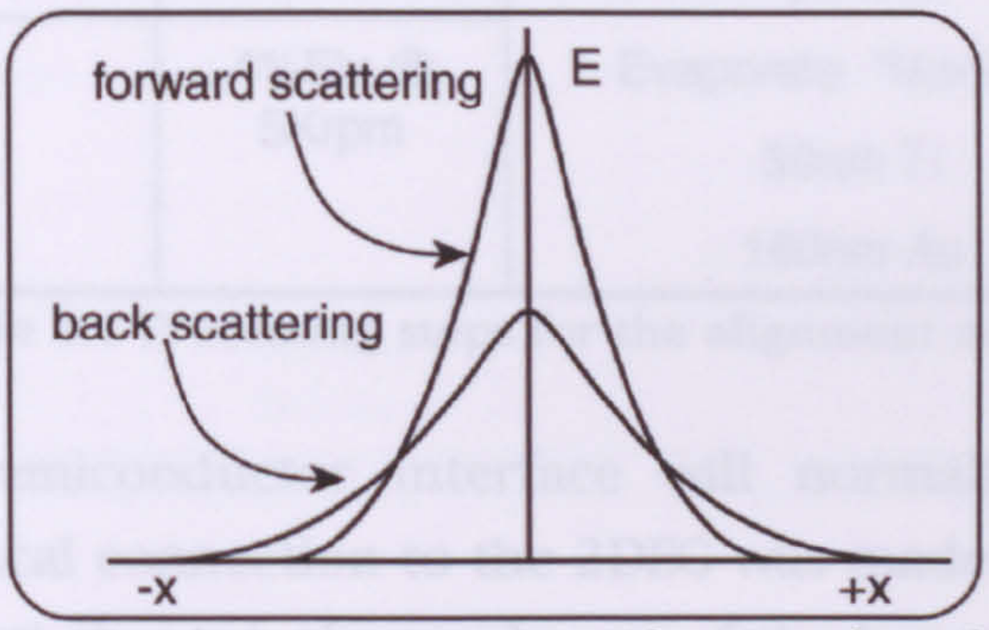

Figure 3.4 Two overlapping Gaussians showing the relative spatial distribution of forward and back scattered electrons[4].

Electrons scatter as they pass through the resist producing a flow of secondary electrons, this gives the largest contribution to resist exposure. Electrons that pass through the resist and into the substrate can be scattered from the substrate back into the resist and expose the resist several microns away from the beam. Under these conditions the absorbed dose has a distribution that consists of two superimposed Gaussians, illustrated in Figure 3.4. For isolated features this is, in general, not a problem, but when many closely packed features are exposed together the energy from the back scattered electrons add and act like a background "fog". This is referred to as the proximity effect and is of particular importance when dealing with fine or densely packed features.

The processing of the device structure measured in chapter 5 involved five levels of lithography and post lithographic processing. Each level has a design, lithographic and processing element. All stages were realised using electron beam lithography since this allowed for maximum flexibility in the design process.

3.1.3 Sample Fabrication

A description of the various processing levels is given below. General fabrication methods and procedures were taken from references [2,5].

Alignment Markers: A metal layer was deposited to enable the Beamwriter and Beamwriter operators to register to subsequent layers. In principle, any high contrast metal structure would have been suitable, but the Titanium-Gold combination was resistant to multiple e-beam exposure and to chemical processing and was used in the work presented in this thesis.

Layer	Resist Spun	Post Ebeam Processing
Markers	15%BDH @ 5Krpm	Develop; 1:1 MIBK for 60s Deox etch ; IPA→ H_20 → 4:1 H_2O:HCl
	4%Elv @ 5Krpm	Evaporate "Markers" 30nm Ti 160nm Au

Table 3.1 Processing steps for the alignment marks

Ohmics: A metal/semiconductor interface will normally form a Schottky barrier. Good electrical connection to the 2DEG was made by diffusion of high density Ge (n dopant) through the top layers of the heterostructure This then formed a very thin tunnel barrier. The barrier was small enough such that Ohmic behaviour was exhibited even at low temperatures and bias currents. Nickel (Ni) was used as a wetting agent.

Layer	Resist Spun	Post Ebeam Processing
Ohmics	15%BDH @ 5Krpm	Develop; 1:1MIBK for 60s Deox etch ;IPA → H_20 → 4:1 H_2O:HCl Evaporate "Ohmics 7" 8nm Nickel: 120nm Ge: 130nm Au: 80nm Nickel: 250nm Au; RTA recipe 9 : 380^{0}C for 90s
	4%Elv @ 5Krpm	

Table 3.2 Processing steps for the Ohmic contacts

Isolation: Isolation between structures was achieved by etching away the doped layers, thereby removing 2DEG. Devices typically showed a resistance of between ≈6KΩ and 10KΩ at room temperature between ohmic contacts that where closely or maximally spaced apart respectively. The resistance between the surface Schottky gates and the Ohmic connections was typically greater than 1GΩ.

Layer	Resist Spun	Post Ebeam Processing
Isolation	15%BDH @ 5Krpm	Develop; 1:1MIBK for 60s Isolation etch ; 4:1 H_2O:HCl
	4%Elv @ 5Krpm	

Table 3.3 Processing steps for the isolation level

Gates: The gates are metallic electrodes that form Schottky barriers at the surface. An image of the pattern the gates form is transferred to the 2DEG when a potential is applied to the gates. The smallest features were written at the beamwriters maximum resolution configuration, with a 12nm spot at 100KV and the smallest available aperture.

Layer	Resist Spun	Post Ebeam Processing
Gates	2.5%BDH @ 5Krpm	Develop; 2.5:1 MIBK for 60s Deox etch ; IPA→ H_20 → 4:1 H_2O:HCl Evaporate "Gates 5" 12nm Ti, 15nm Au
	2.5%Elv @ 5Krpm	

Table 3.4 Processing steps for the gates.

Wiring: In order to reduce beamwriter time to a minimum the gates level was written in two parts. The wiring was the larger structures of the gate electrodes and is written with a spot size of 160nm at 50KV.

Layer	Resist Spun	Post Ebeam Processing
Wiring	15%BDH @ 5Krpm	Develop; 1:1MIBK 60s Deox etch ;IPA→ H_20 → 4:1 H_2O:HCl Evaporate "Gates 1"; 33nm Ti: 160nm Au
	4%Elv @ 5Krpm	

Table 3.5 Processing steps for the large level wiring

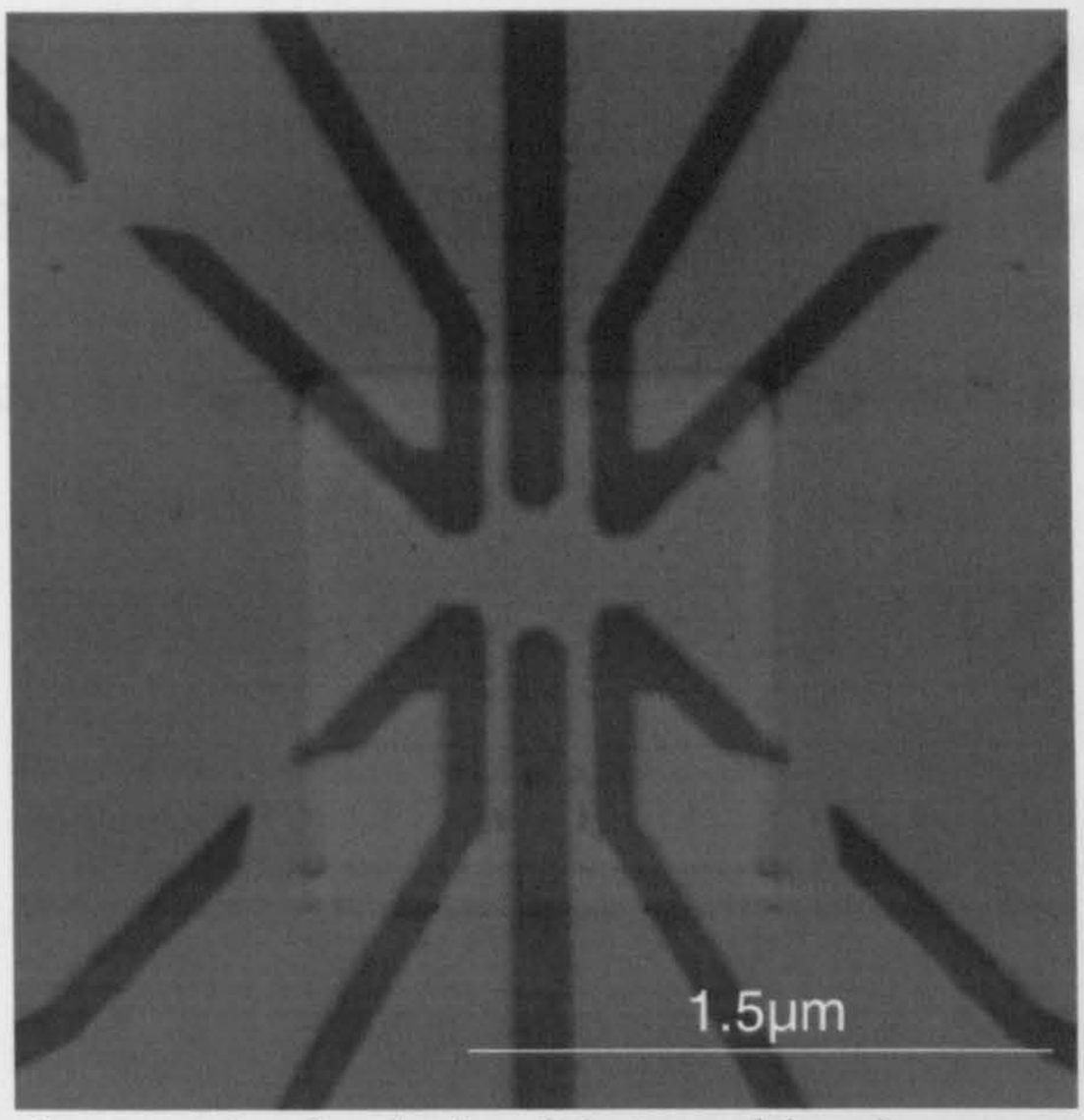

Figure 3.5 A micrograph of a device fabricated by the processes described in the text. A similar device was used in the experiments detailed in Chapter 5. The dark areas are the gate electrodes, the light areas the GaAs surface.

3.2 Dilution Refrigeration

The dilution refrigerator is the workhorse of the millikelvin regime. It uses the unique properties of ^{3}He-^{4}He mixtures to obtain temperatures well below 100mK. Liquid ^{3}He can be mixed with ^{4}He to any concentration above 0.86K but below a separation into two phases occurs. Below 2.17K the mixture is a normal liquid or superfluid depending on the concentration of ^{3}He. Below 0.86K the mixture separates into two liquid phases, one with a high concentration of ^{3}He(concentrated phase), a normal fluid, and one with a low content of ^{3}He, a dilute superfluid phase (dilute phase).

In a dilution refrigerator cooling takes place in the mixing chamber. The flow of ^{3}He across the boundary between the phases is maintained by distilling the ^{3}He off from the dilute phase. This is achieved in the still which connects to the bottom of the mixing chamber. The ^{3}He is pumped away from the liquid surface in the still and re-circulated to the concentrated phase with an external pump, keeping the system in dynamic equilibrium. Pumping the dilute phase ^{3}He from the still makes the pressure lower than in the mixing chamber thus ^{3}He is forced into the still by the pressure difference. The ^{3}He flowing from the mixing chamber to the still is used to cool the returning flow of concentrated phase in a series of heat exchanges. This ensures that the ^{3}He returning to the mixing chamber is at nearly the same temperature as the liquid already there.

When the dilution unit is started the 1K pot is used to condense the ^{3}He-^{4}He mixture. The 1K pot is cooled by evaporation of ^{4}He by constantly pumping a ^{4}He reservoir. A flow impedance, in the form of a capillary tube is used to maintain a high enough pressure in the 1K pot region for the gas to condense[6,7]. Figure 3.6 shows a schematic of a typical dilution refrigerator.

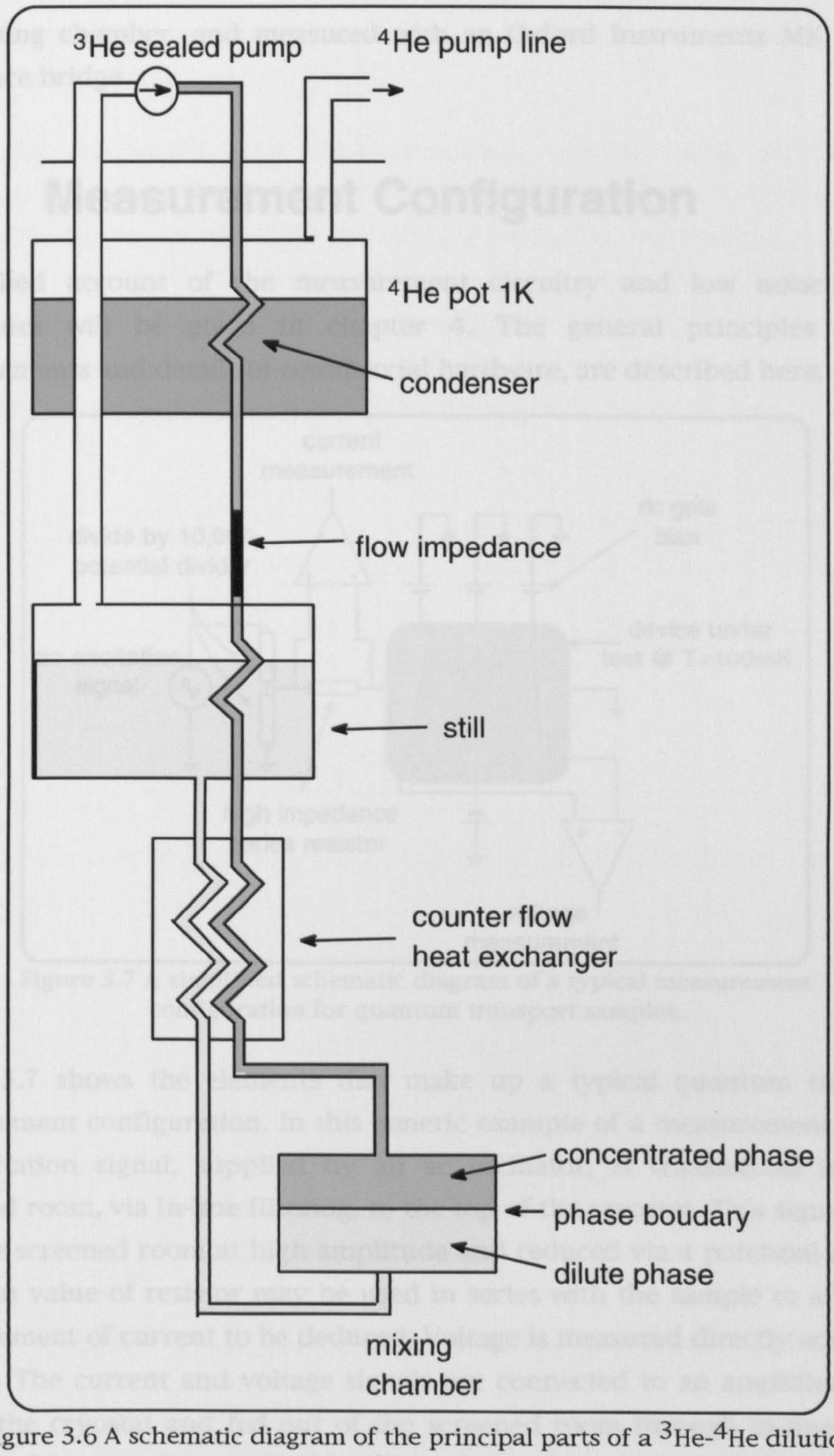

Figure 3.6 A schematic diagram of the principal parts of a ^{3}He-^{4}He dilution refrigerator.

The dilution refrigerator used at Glasgow is a KelvinOx 25 unit. The particular version used has a sliding seal assembly, which enables moderately fast sample exchange times of around 36 hours. The unit is immersed within a standard Oxford Instruments (OI) cryostat that houses a 13 Tesla superconducting magnet. Thermometry is via carbon resistors on the 1K plate, still plate and

the mixing chamber, and measured with an Oxford Instruments MK III A.C. resistance bridge.

3.3 Measurement Configuration

A detailed account of the measurement circuitry and low noise design techniques will be given in chapter 4. The general principles of the measurements and details of commercial hardware, are described here.

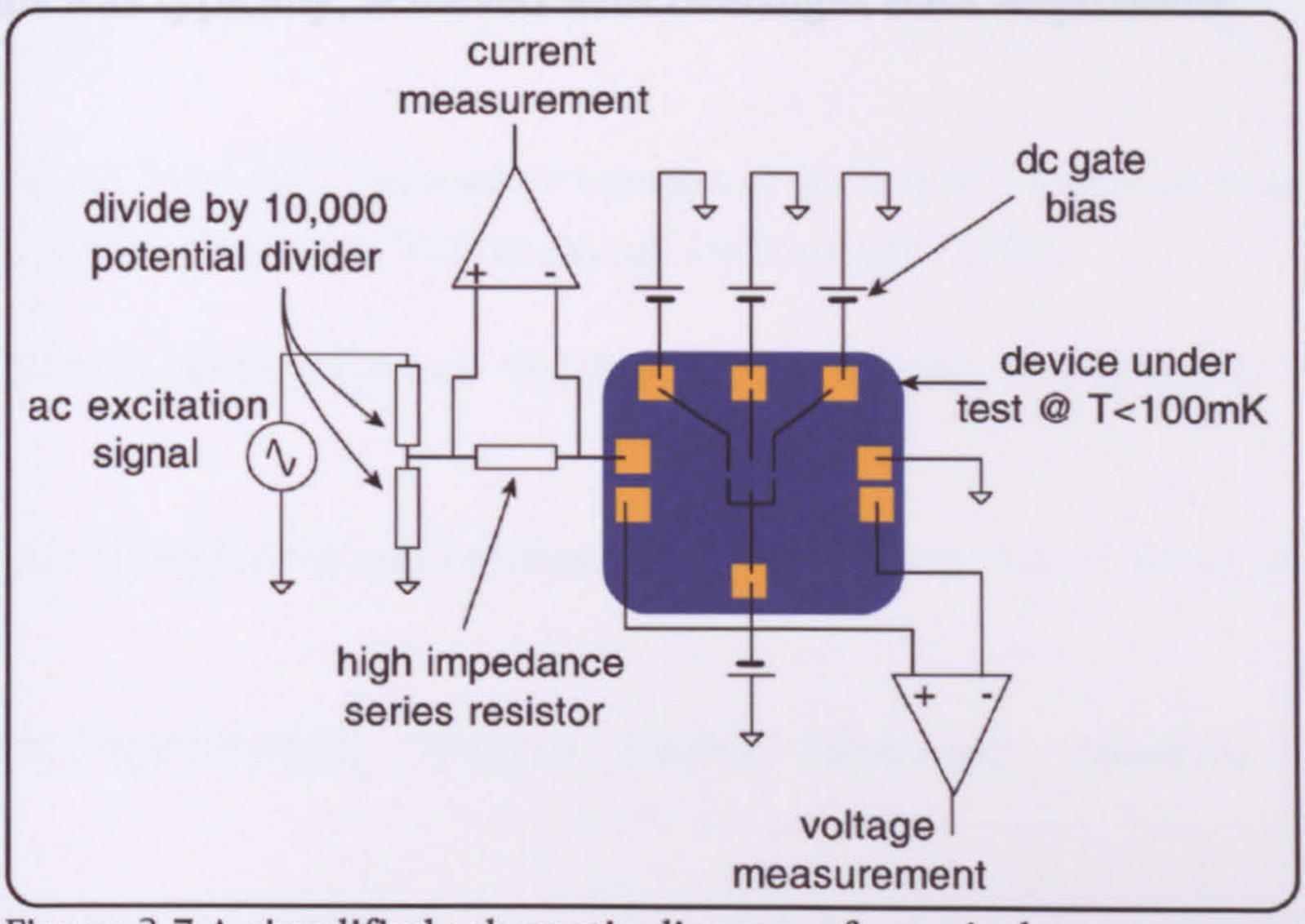

Figure 3.7 A simplified schematic diagram of a typical measurement configuration for quantum transport samples.

Figure 3.7 shows the elements that make up a typical quantum transport measurement configuration. In this generic example of a measurement system an excitation signal, supplied by an ac oscillator, is transmitted into the screened room, via in-line filtering, to the top of the cryostat. This signal is fed into the screened room at high amplitude and reduced via a potential divider. A known value of resistor may be used in series with the sample to allow the measurement of current to be deduced. Voltage is measured directly across the sample. The current and voltage signals are connected to an amplifier at the top of the cryostat and fed out of the screened room through in-line filters. The gate bias may be supplied by dc sources and is referenced to the same point as the excitation and the sample.

In the data presented in chapter 5 two EG&G 5210 lock-in amplifiers were used to measure the current and voltage signals, the outputs of which were fed directly into the measurement computer via GPIB (IEEE 488). The gate signals

were generated by Hewlett Packard 3245A Dual Channel Universal Sources with a minimum step size of $10\mu V$[8].

The data acquisition and instrumentation control were all acquired automatically using LabView© by National Instruments© on a Pentium© I PC running under the Windows 95 operating system. This system controlled gate voltage incrementation as well as the acquisition of current and voltage data and the manipulation of the superconducting magnet. The software was designed[9] for batch automation to allow extended explorations of parameter space. This was typically, achieved with overnight data acquisition.

3.4 References

(1) Personal Communication, M. Holland, "Heterostructure Specifications" (1995).

(2) S. Thoms and D. Macintyre, "Notes on EBL" (1994).

(3) M. Hatzakis, "Semiconductor Metallising Process" IBM Tech. Disclosure Bull. 10 (494) (1967).

(4) Thesis, M. Persson, "Transport Properties of 1D and 0D Structures in GaAs/AlGaAs Heterostructures" , Chalmers University of Technology, 1994.

(5) Personal Communication, M. Rahman, "A Guide to Fabrication Techniques" (1995).

(6) A. Kent, "Experimental Low Temperature Physics" (Macmillan Press Ltd, London, 1993).

(7) Oxford-Instruments, "Kelvinox Dilution Refrigerator. Operating Instructions" (1990).

(8) Hewlett-Packard, "HP 3245A Universal Source" Operating and Programming Manual (1988).

(9) B. Milton, "Quantum Transport LabView Measurement Suite" (1998).

4 THE DESIGN AND CONSTRUCTION OF A LOW NOISE MEASUREMENT SYSTEM

This chapter deals with the redesign of the quantum transport measurement facility. The chapter is divided into six major sub-sections. Firstly, noise measurements performed on the initial system are presented. Secondly a discussion of the general mechanism by which noise arises in systems is presented. Thirdly general good practice in low noise design applicable to this case is discussed. The design of the system is then described in some detail with particular reference to components, construction, and specifications. An analysis of the theoretical noise performance of the electronics within the system is presented. The measured system performance is presented in chapter 5 in the context of measurements on highly sensitive single electron devices.

4.1 Electron Temperature

Before detailing the redesign of the measurement system, it is necessary to consider the reasons that gave rise to the up-grading.

Although a samples lattice may be in thermal equilibrium with the mixing chamber of a dilution refrigerator (<100mK), without adequate noise suppression, the free electrons will not. High impedance samples, where the impedance is strongly localised, present a particular problem as nearly all the excess energy is dissipated in, or close to, the impedance, thus raising the local temperature within the active region of the device. Excess energy, due to the presence of noise sources, will excite extra conduction levels within the range kT_0 where T_0 is no longer just the lattice temperature. In addition, at increased excess energy the electron confinement within the quantum dot becomes compromised as the tunnel barriers become more transparent. Calculations have been made[1] on the level of noise reduction necessary in order to for a system to be dominated by the lattice temperature of the device. In these calculations it is extremely difficult to include the degree of coupling of the noise sources to the sample for both photon radiation coupling directly to the device or electromagnetic radiation coupling to the measurement system in any practical experimental arrangement.

4.2 Noise Spectra of Measurement System Prior to Redesign

It was already known[2] that the experimental arrangement associated with the dilution unit suffered from severe electron heating effects. Experiments had previously been performed on quantum point contact (qpc) structures both in the VTI (variable temperature insert) at 1.2K and the dilution unit at T_L<100mK where T_L is the lattice temperature of the sample. In the VTI the quantum point contact exhibited quantised conductance between temperatures of 1.2K and ≈7K. The same device, when placed in the dilution unit at a lattice temperature T_L=100mK, showed no evidence of quantised structure whatsoever[2]. The conclusion drawn was that the electron temperature of the dilution unit was in excess of 7K.

A set of experiments were performed on the measurement system in order to determine noise levels and sources. A 60KΩ resistor cooled to T_L<100mK acted

as the sample. An excitation of 3μV at between 23-33 Hz was applied, and measured in a two terminal configuration on a HP 3561A Dynamic Signal Analyser (DSA). In order to minimise the number of components in the system that could contribute to the noise, the voltage across the resistor was measured directly by the DSA. No amplification or filtering was used in the signal path. The data in Figure 4.1 to Figure 4.3 are averages of 20 measurements each using a Hanning window function with a bandwidth of ≈1Hz. Frequencies below of 20Hz were not monitored as there was little spectral content below this point. Above 100Hz the dominant spectral content were harmonics of 50Hz. The frequency of 120Hz was chosen as the upper limit monitored as this included the 100Hz mains harmonic. The approach adopted was to try to identify the contributions to the measured noise by elimination. Power supplies to various pieces of equipment were turned off systematically and their effect on the noise spectrum noted. In order to try to distinguish between electromagnetic coupling and vibrational coupling the cryostat was raised onto vibration isolators. This also provided a useful test of the effectiveness of vibration isolation in general.

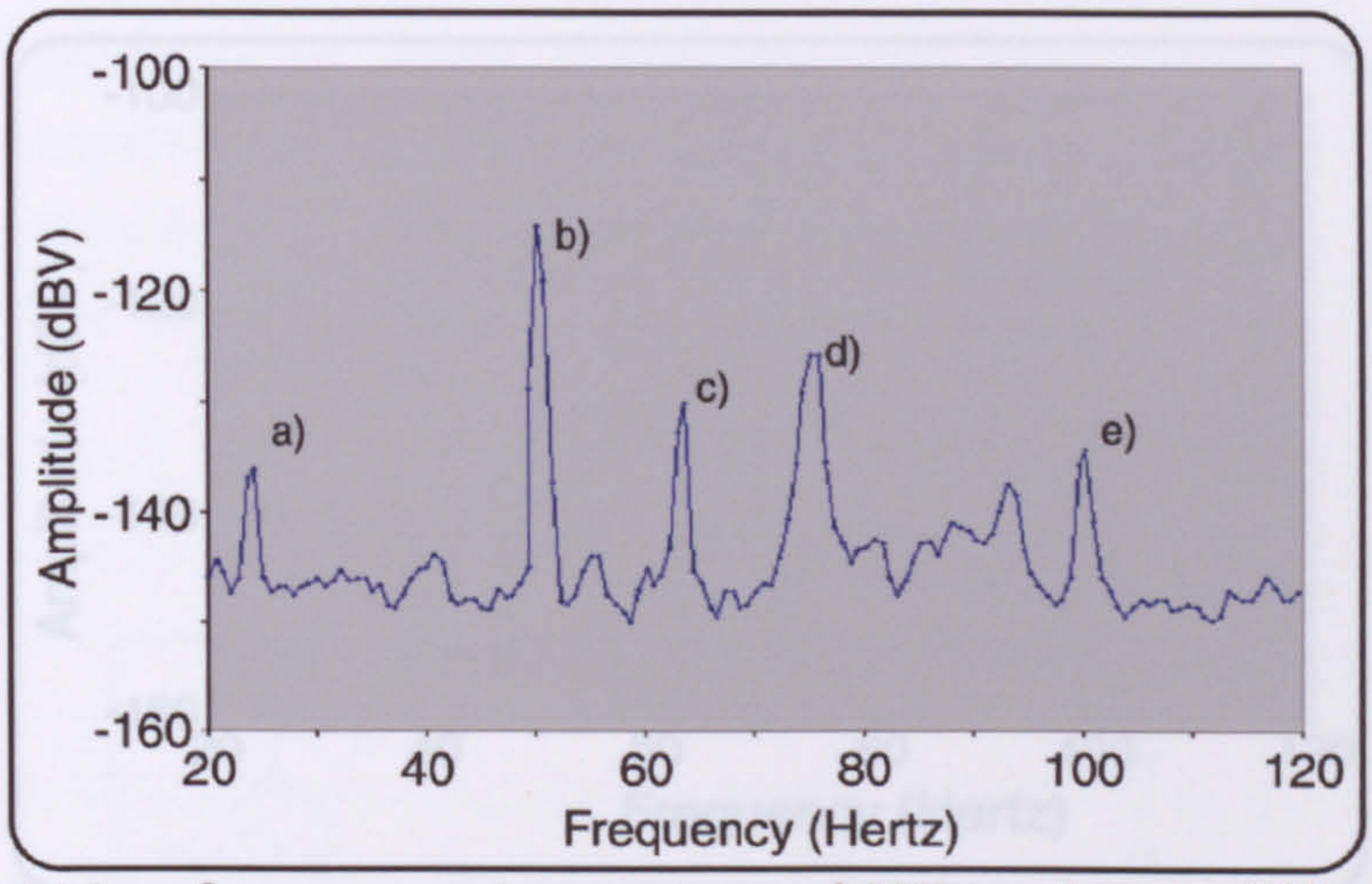

Figure 4.1 Low frequency noise spectrum of 60KΩ resistor at 100mK, with no attempt at noise reduction.

Figure 4.1 represents the spectrum obtained in the worst case. Here the mains ring on the inside of the screened room was activated and the door and hatch are open. The 50Hz mains coupling together with the 100Hz harmonic are evident at points b) and e) with the excitation at a). Point c) represents a vibrational resonance of the floor. The cause of the component at point d), as will be seen, proved a little more difficult to identify completely and it is possible that more than one source played a rôle.

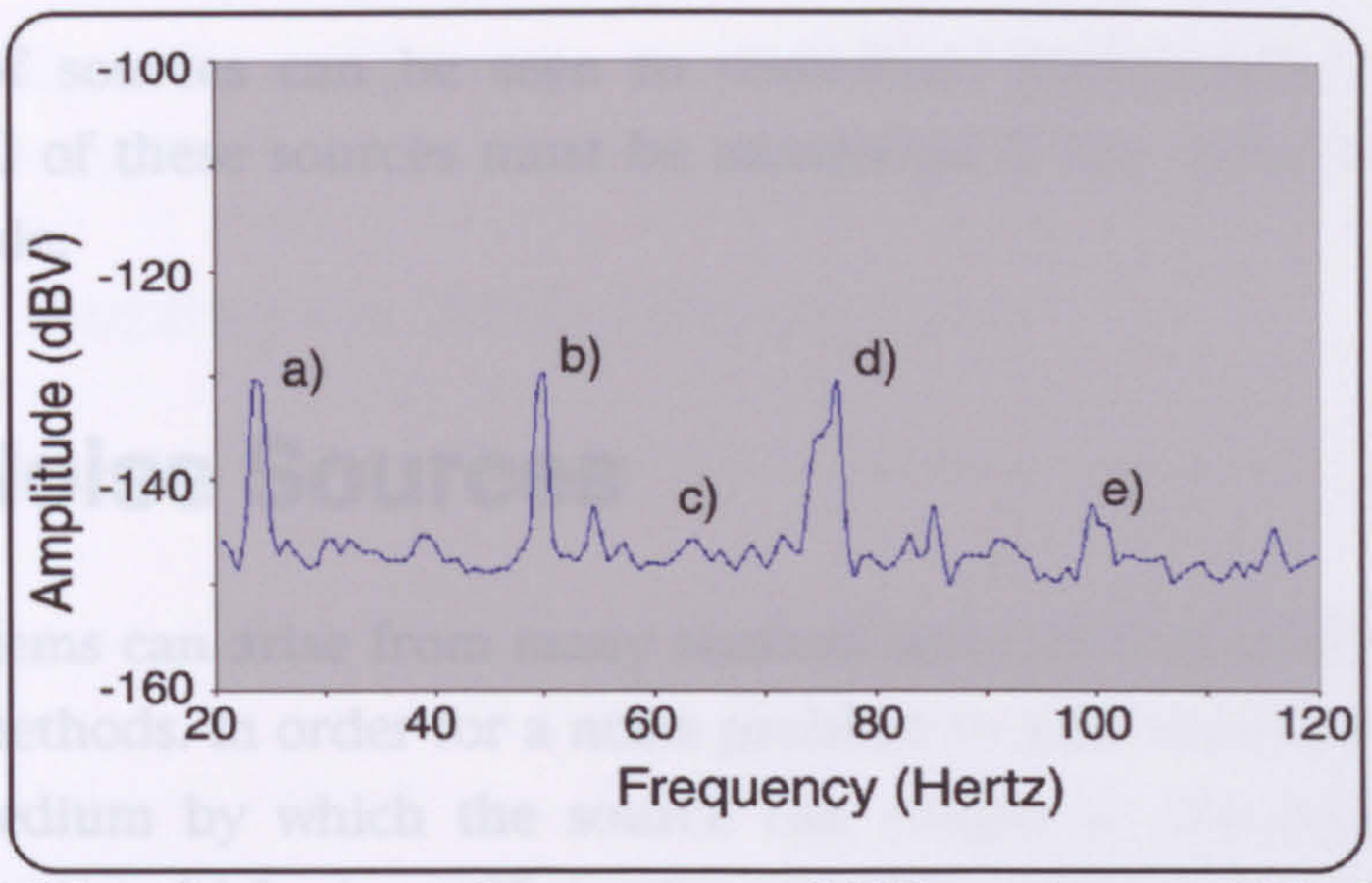

Figure 4.2 Low frequency noise spectrum of 60KΩ resistor at 100mK. Mains ring off and vibrationally isolated.

Figure 4.2 represents the spectrum with the mains ring inside the screened room switched off. The cryostat was positioned on isolation dampers, the door, and the hatch to the screened room closed. Reductions of ≈18dB in the 50Hz component at b) and ≈15dB in the vibrational contributions at c) are observed. Reductions in points d) and e) of 5dB and 7dB are also observed.

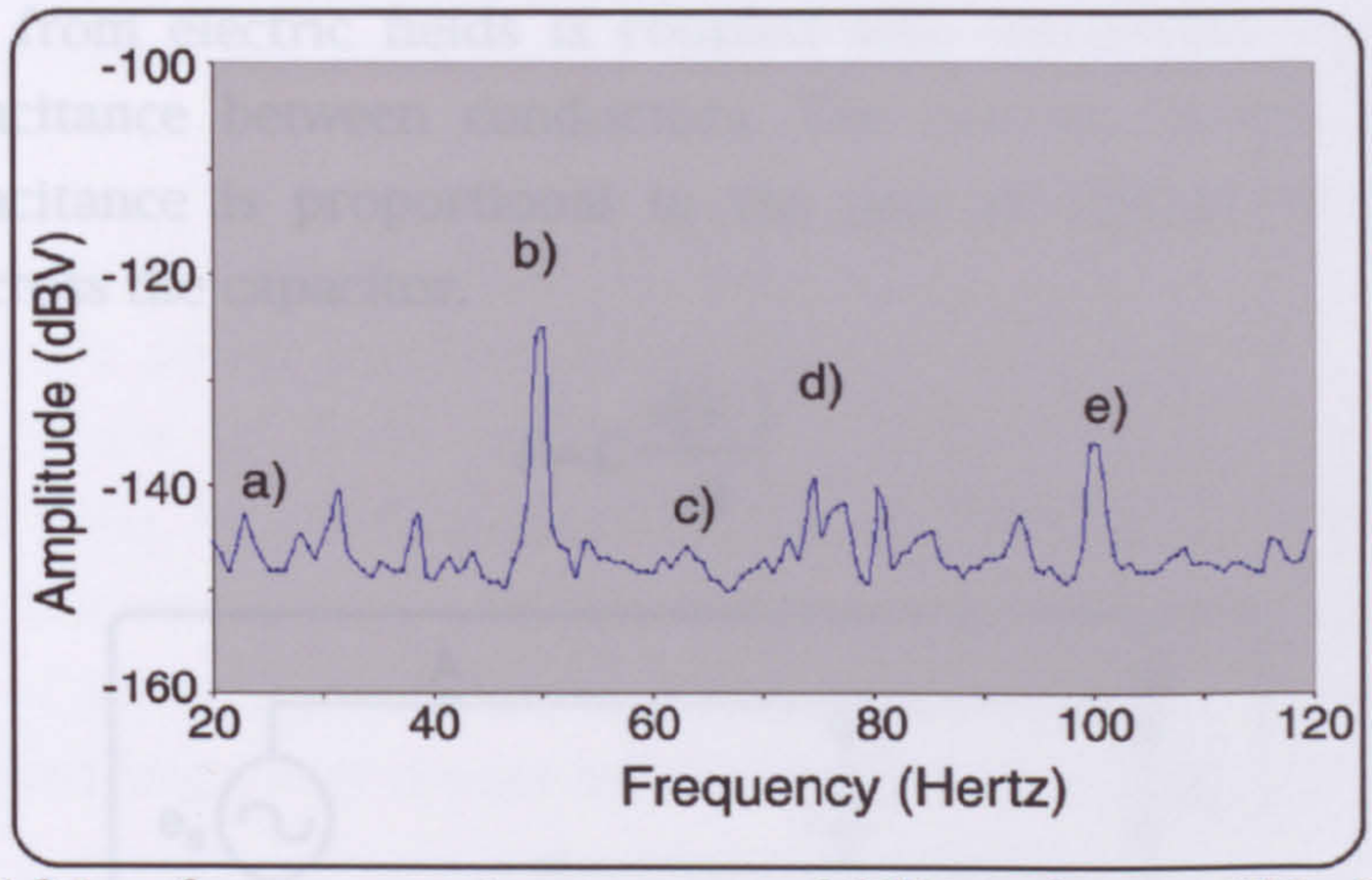

Figure 4.3 Low frequency noise spectrum of 60KΩ resistor at 100mK. Mains ring off, vibrationally isolated and heating extractor off.

Figure 4.3. represents the spectrum under similar conditions to Figure 4.2 but with the heating extractor fan above the screen room turned off. The excitation visible at point a), was reduced in this plot. This represents the lowest noise spectrum obtained in this series of experiments. The 100Hz component makes a more significant contribution than in the previous plot. The amplitude of the 100Hz component proving somewhat variable throughout the course of these experiments.

A number of sources can be seen to contribute significantly to the noise spectrum. All of these sources must be minimised if low noise measurements are to be made.

4.3 Noise Sources

Noise in systems can arise from many sources and can couple into the system by various methods. In order for a noise problem to exist there must be a noise source, a medium by which the source can couple to the specimen and a receiver circuit which is sufficiently sensitive that the noise level is problematic. This section looks at some of the major sources of noise and common coupling mechanisms.

4.3.1 Field Coupled Noise

Electric field noise via capacitative coupling

Interference from electric fields is coupled into susceptible circuits via the mutual capacitance between conductors. The current flowing through this mutual capacitance is proportional to the rate of change of the potential difference across the capacitor.

Eqn. 4.1

$$i = C\frac{d(V_c)}{dt}$$

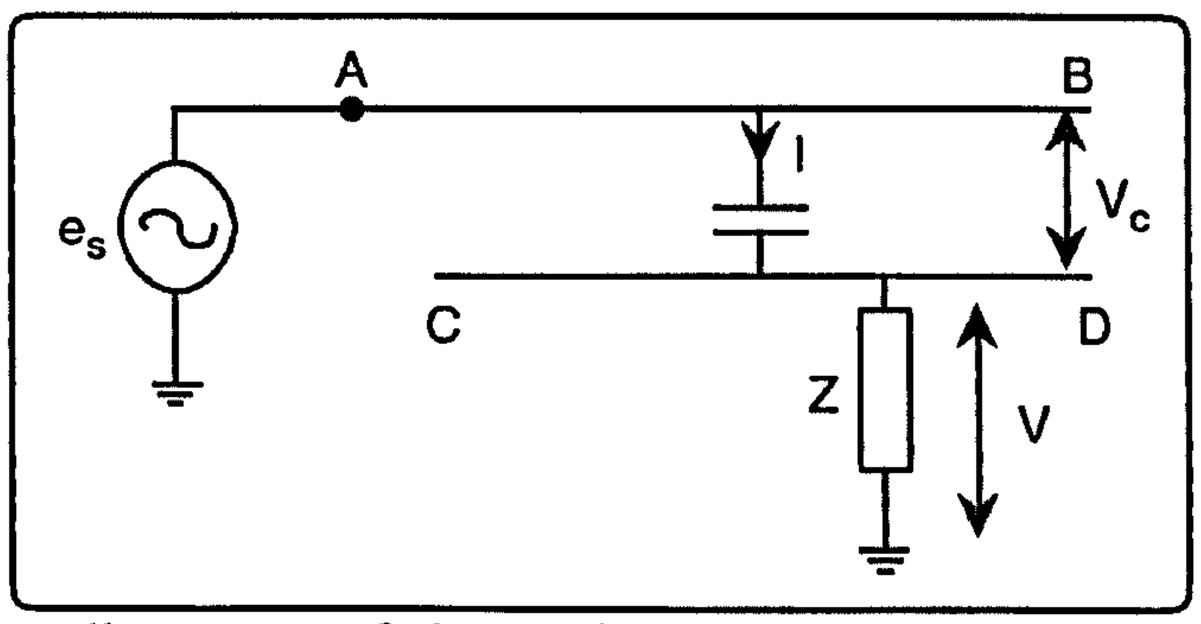

Figure 4.4 An illustration of electric field coupling via mutual capacitance between conductors[3].

In Figure 4.4 the voltage noise in Z is developed via a noise current, i. Capacitatively coupled noise will be reduced by reduction of the load impedance Z. High impedance op-amp (operational amplifier) inputs are susceptible to this type of coupling. Fast rise-time digital signals and some a.c power interference are particularly troublesome sources of this type of noise.

The former due to the rapid voltage transition times, and the latter due to the large absolute amplitude of the signal.

Magnetic Coupling via Mutual Inductance

An alternating current flowing in one circuit induces an emf in another circuit of

Eqn. 4.2 $$v_2 = -M_{21}\frac{di}{dt}$$

That is, the emf in the secondary circuit is proportional to the rate of change of current flowing in the primary circuit as illustrated in Figure 4.5.

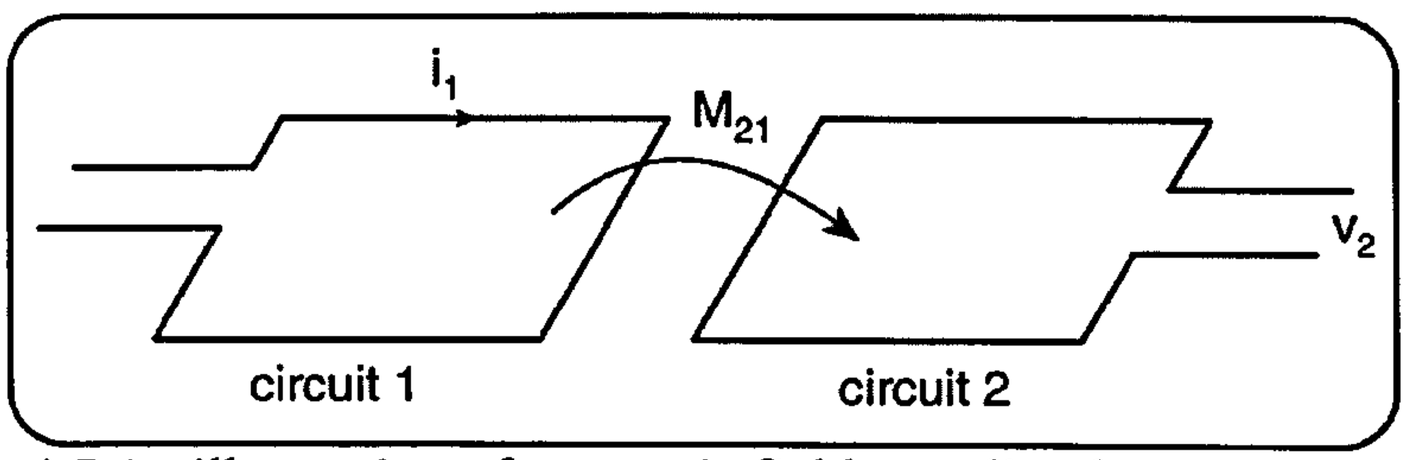

Figure 4.5 An illustration of magnetic field coupling between two closed loop circuits. The current flowing in circuit 1 produces a voltage at the output of circuit 2[3].

Common sources of magnetic field interference are mains power transformers and switch mode power supplies. In mains power transformers the fields and induced emfs are at 50Hz and, if the transformer becomes saturated, harmonics of 50Hz. In switch mode power supplies the fields and induced emfs are at 50 Hz but may also contain high frequency components corresponding to harmonic of the charging frequency of the power supply. Grounding circuits that form closed loops may couple noise into a system via this mechanism.

4.3.2 Thermal

Thermal emfs are of considerable concern in low temperature measurement systems. Emfs are generated as a result of the junction between two or more dissimilar metals individually anchored at different temperatures. Cable of the same materials was used to connect between stages of different temperatures. Where it was necessary to join cable of different materials care was taken to ensure the both materials were thermally anchored to the same temperature before joining.

4.3.3 Vibrationally Induced Noise

Electrical noise of non-electrical origin can most often be ascribed to mechanical sources. The common mechanisms by which they appear as electrical noise are described below. Measures taken to reduced the effect of vibrationally induced noise are described in section 4.5.11

Tribo-electric noise

Charge is transferred when dissimilar materials touch and separate leaving one positively and the other negatively charged. When this occurs between conductors the high electron mobility allows charge movement to compensate quickly for any energy imbalance and the effect is largely unnoticeable. If the charge transfer is intermittent between a conductor and, for example, the insulator of a cable the effect can be significant, particularly in circuits having high source impedance.

Conductors in Magnetic Fields

Faraday's law tells us that any conductor moving in a magnetic field generates an emf thereby causing a current to flow in that conductor. The emf induced is dependent on both the velocity at which the conductor vibrates and the magnetic field. In low noise systems, the vibration of low level signal carrying cables in a magnetic field can lead to significant noise. This is of particular concern in this context as the sample, and hence a part of the cabling loom, may be subjected to fields of up to 15 Tesla.

Space Charge Effects

Movement of conductors, separated by a vacuum, relative to each other induces a voltage change. A change in separation results in a variation of capacitance between the conductors. Assuming a constant charge, i.e. no leakage, then a change in separation results in a variation of capacitance between the conductors, and hence a variation in capacitor voltage. The change in capacitor voltage, δV, for a change in capacitance, δC, is[3]

Eqn. 4.3 $$\delta V = \frac{dV}{dC}\delta C = \frac{d\left(\frac{Q}{C}\right)}{dC}\delta C = \frac{Q}{C^2}\delta C$$

4.4 Low Noise Design

This section presents an outline of the techniques used and general good practice adhered to which allowed low sample noise and acceptable signal to noise ratio to be achieved.

4.4.1 Balanced Differential Configuration

Most interference noise couples into, or can be made to couple into, a system as a common mode signal; this is of great advantage. Balanced differential signals potentially allow the full common mode rejection of an op-amp to be accessed. Using a balanced system allows the use of shielded twisted pair cables for the signal. This reduces magnetic and electric field coupling and keeps the signal reference completely separate from the shielding circuit. Grounding issues are dealt with in section 4.4.3

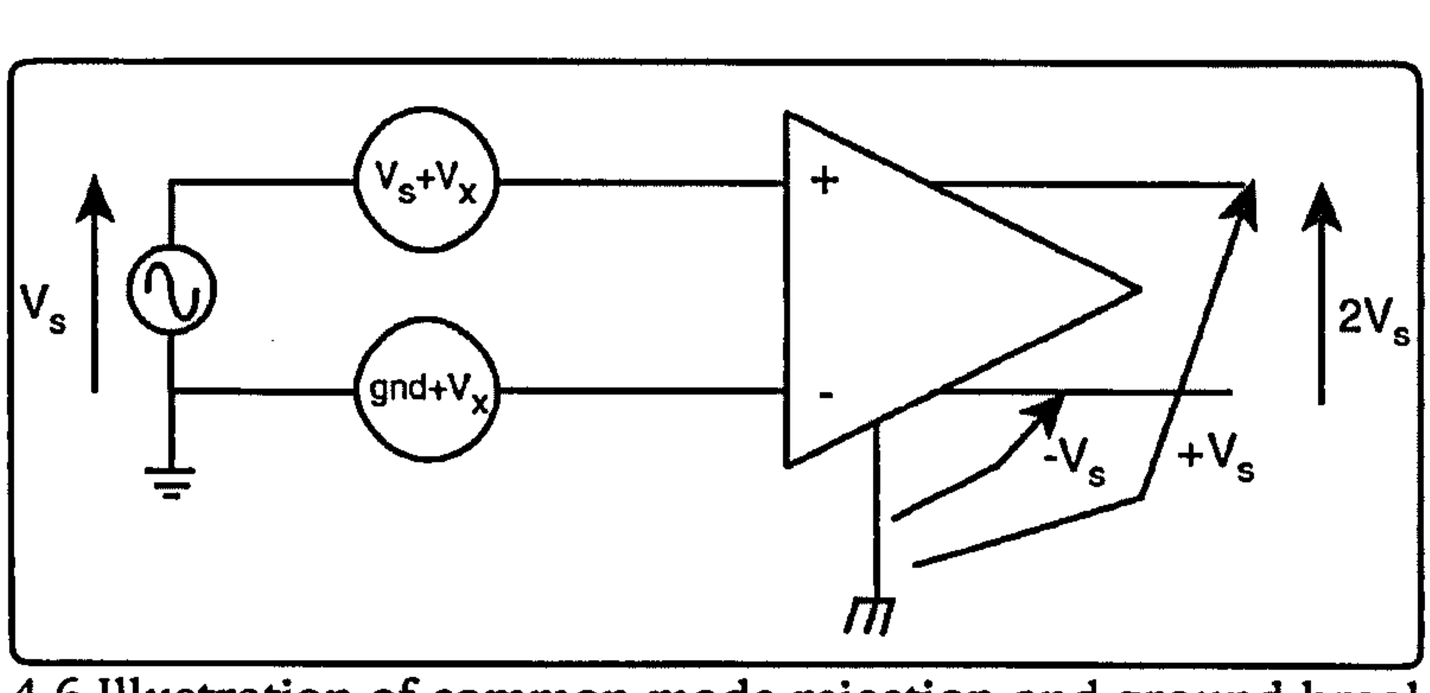

Figure 4.6 Illustration of common mode rejection and ground breaking. V_x is common to both inputs and does not appear at the output. The output signal is developed with respect to the two halves of a balanced output, this enables shielding and reference potentials to be kept separate.

Close matching of the input circuitry, especially when the circuitry is in the same package, minimises the temperature difference between the two inputs of the op-amp and hence reduces offset voltage V_{os}. The measurement system detailed here employs a balanced output, differential input circuit configuration extensively, together with twisted pair shielded cabling (see section 4.5.4). This arrangement lends itself easily to ground loop breaking, that is, separately referenced circuits can be connected together without the noise voltage appearing in the signal circuit[4]. It should be noted that

differential circuits, with differential outputs such as Figure 4.6, have a natural minimum gain of 2.

Figure 4.7 shows reference voltages that appear within the system. Some secondary references were used within the subsystems (e.g. a power reference on the PCBs (printed circuit board)) but those listed below represent the principal references for the system.

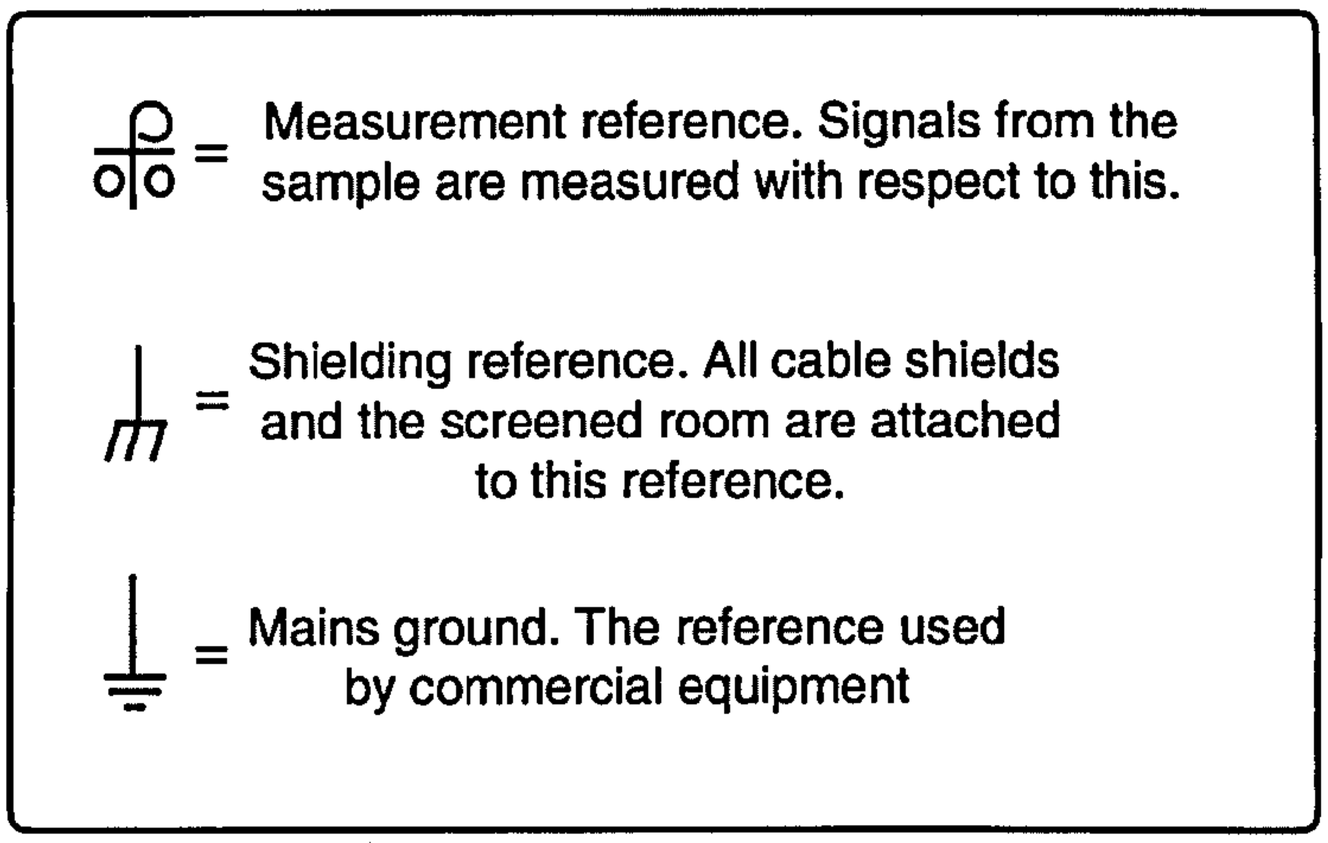

Figure 4.7 shows the three main references that appear within the system.

4.4.2 Shielding

Shielding is used to reduce electric, magnetic or electromagnetic field strengths. Either the source of noise, or the susceptible circuit into which the noise is coupling may be shielded by use of conducting and/or high permeability enclosures.

The effectiveness of these shields is extremely difficult to calculate. The effect of the fields within the shielding container depend on the amplitude, frequency and relative orientation of the field, the container and the components therein. Other factors that are of major importance are the size, shape, material, seams and aperture type used within the design of the container.

Given the complex nature of these factors and their interaction with one another, the practical implementation of shielding theory relies on adherence to general principles and good practice rather than detailed calculation. Hence, gross, and necessary simplifications are traditionally made within this subject area[3,5].

Wave impedance in the far and near field

Any circuit producing an alternating current will produce associated electric and magnetic fields. The strength of these fields depends on the current flowing in the source circuit and on both the distance and orientation of the observation point. The ratio of the electric and magnetic fields

$$Z_w = \frac{E}{H}$$

Eqn. 4.4

is called the wave impedance. When the source is far away the field can be considered a wave moving away from the source at right angles. In this case, both field components reduce[3] as 1/r where r is the distance from the source. However, if the source is in the near field the situation is more complex.

If the source generator is open circuit then the field generated is primarily electric and the wave impedance is high. In this case the near field magnetic component reduces as[3,6] $1/r^2$ and the electric component as[3,6] $1/r^3$. If the source generator is closed circuit then the field generated is primarily magnetic, and the near field magnetic component reduces as[3,6] $1/r^3$ and the electric component as[3,6] $1/r^2$.

This means that for a near electric field source the impedance reduces from a high value whilst for a near magnetic field source the wave impedance increases from a low value.

The transition from near to far field source is a function of both the wavelength of radiation of interest and the distance from the source. For a small source this would take place at about $r \approx \lambda/2\pi$ where λ is the wavelength of the radiation, for larger sources the near field extends further. The wave impedance in air for a primarily electric source in the near field is approximately[6]

$$|Z_\omega|_e = \frac{1}{2\pi f \varepsilon_o r}$$

Eqn. 4.5

and for the magnetic source in the near field[6]

$$|Z_\omega|_m = 2\pi f \mu_o r$$

Eqn. 4.6

Where f is the frequency of source field, μ_0 and ε_0 are the permeability and permittivity of free space respectively and r is the distance from the source.

Shielding Mechanisms

The effectiveness of shielding is considered here in three parts; reflection loss, absorption loss, and ducting.

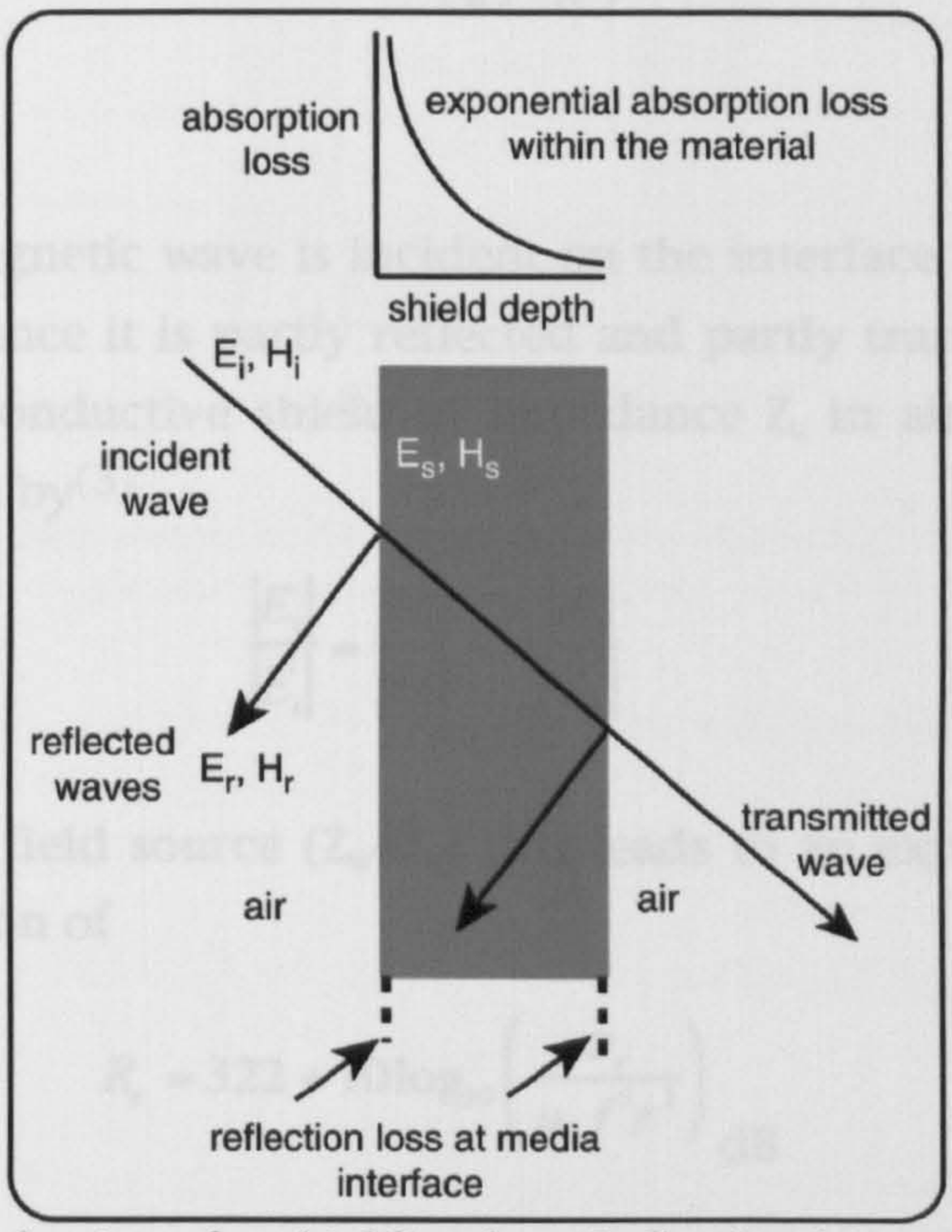

Figure 4.8 Mechanisms for shielding loss. Reflection loss at the interfaces absorption loss within the shield.

Absorption Loss

This is simply the loss the electromagnetic wave experiences as a result of passing through a resistive medium, and is given by[3,6]

Eqn. 4.7
$$E_x = E_o e^{\frac{-x}{\delta}}$$

and

Eqn. 4.8
$$H_x = H_o e^{\frac{-x}{\delta}}$$

Where E_x and H_x are the fields at distance x into the medium and δ is the skin depth. This is defined as being the depth at which the field has been reduced to 1/e of its value at x=0

Eqn. 4.9
$$\delta = \frac{1}{\sqrt{\pi f \mu \sigma}}$$

Where μ and σ is the permeability and conductivity of the material respectively. These quantities are defined as $\mu=\mu_r\mu_o$ and $\sigma=\sigma_r\sigma_c$ where μ_r is the

permeability relative to free space and σ_c is the conductivity of copper σ_r is the conductivity relative to copper. The attenuation due absorption in a shield of thickness x_s is given by[3,6]

Eqn. 4.10
$$A = 132 x_s \sqrt{f \sigma_r \mu_r}$$

Reflection Loss

When an electromagnetic wave is incident on the interface between two media of differing impedance it is partly reflected and partly transmitted. See Figure 4.8. For a highly conductive shield of impedance Z_s in air, the losses due to reflection are given by[3]

Eqn. 4.11
$$\frac{|E_t|}{|E_i|} = \frac{|H_t|}{|H_i|} = 4\frac{|Z_s|}{|Z_w|}$$

For a near electric field source (Z_w=Z_e) this leads to an expression[3,6] for the loss, due to reflection of

Eqn. 4.12
$$R_e = 322 + 10\log_{10}\left(\frac{\sigma_r}{\mu_r f^3 r^2}\right) \text{dB}$$

and for a near field magnetic source (Z_w=Z_m) the loss due to reflection is[3,6]

Eqn. 4.13
$$R_m = 14.6 + 10\log_{10}\left(\frac{\sigma_r f r^2}{\mu_r}\right) \text{dB}$$

Near Field, Low Frequency Magnetic Sources

For near field, low frequency magnetic sources absorption losses are greater than reflection, but the attenuation is small for both mechanisms and so other methods need to be found in this regime.

The most common approach is to divert the magnetic field by making the shield out of high permeability materials. This is referred to as ducting and is illustrated in Figure 4.9. With the outside assumed to be air and the shield constructed from ferromagnetic material having μ_r>>1 the magnetic field will tend to take the path of least impedance.

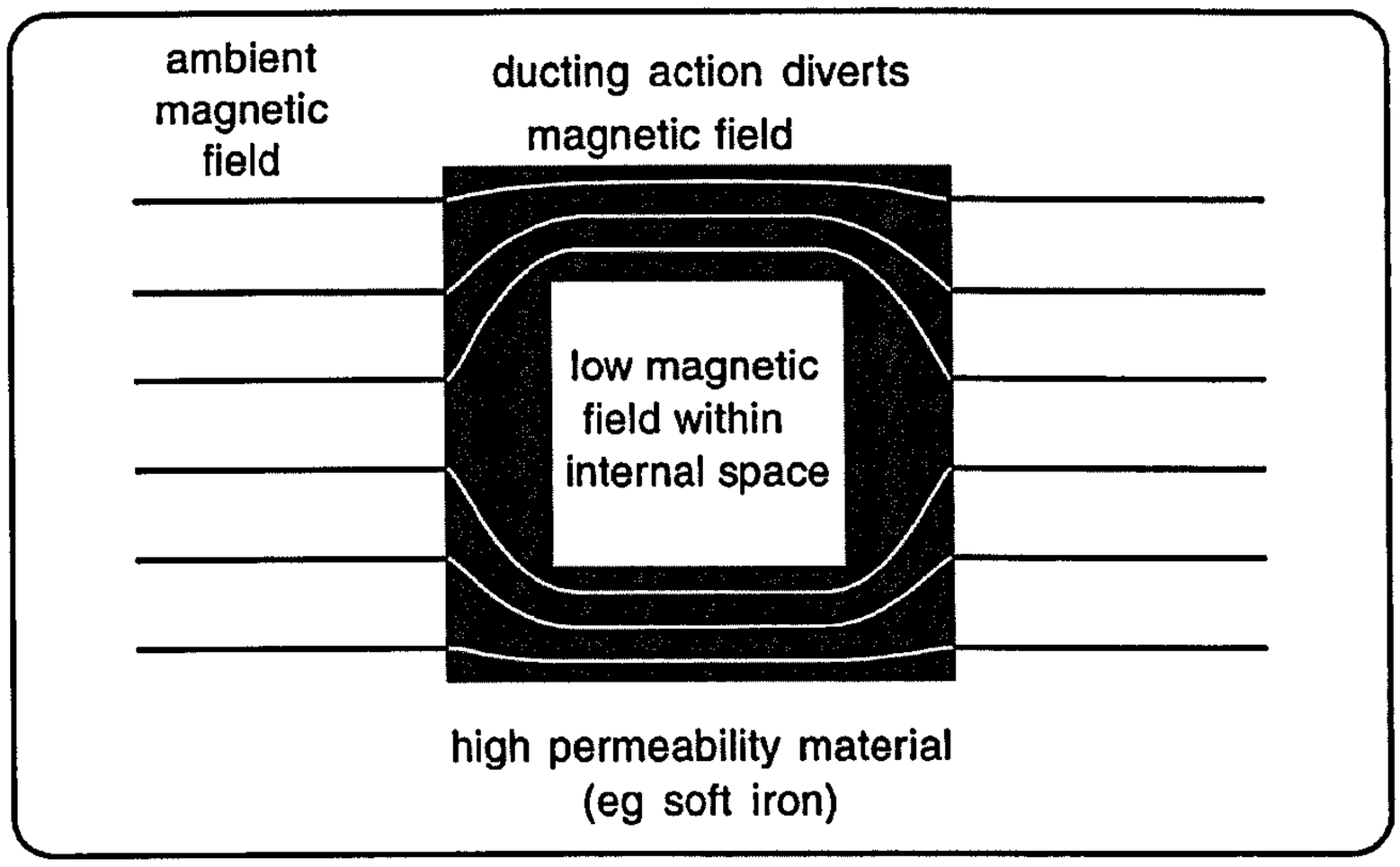

Figure 4.9 High permeability material gives the magnetic field a low impedance alternative path round the sensitive circuit.

This effect has been calculated[3] for a hollow sphere and its contribution to loss is given by

$$Z_D = 20\log_{10}\left|1 + 0.67\left(\frac{(\mu_r - 1)^2 x_s}{\mu_r a} + j\pi f \mu_o \sigma a x_s\right)\right|$$

Eqn. 4.14

Where X_s= wall thickness and a= radius of the sphere. Such high permeability materials tend to saturate at low field strengths and so it is only possible to shield small magnetic fields effectively.

4.4.3 Single Point Grounding

Grounding in low noise circuit design is a difficult and important issue. Noise can be coupled into a sensitive circuit by sharing a common connection with a noise signal. This noise is typically developed across an impedance common to several circuits, usually in the ground path. The problem of common impedance sources often stems from the failure to take into account the finite impedance of wires (including PCB tracks).

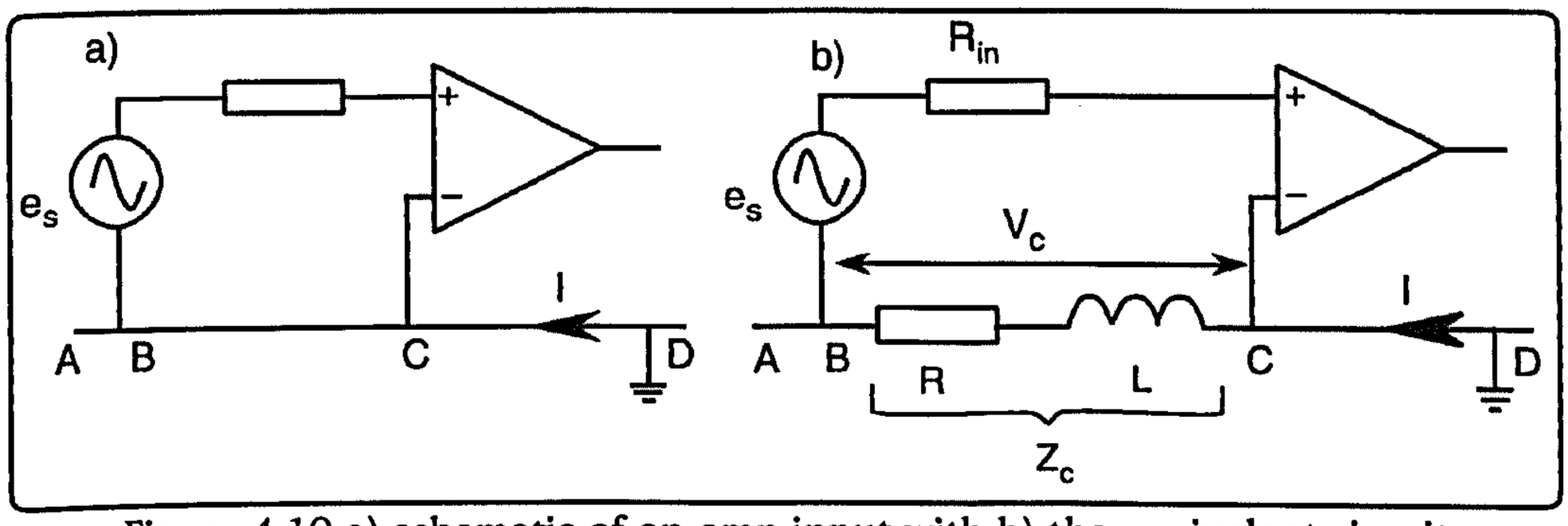

Figure 4.10 a) schematic of op-amp input with b) the equivalent circuit showing the parasitic impedances.

Figure 4.10 illustrates a typical case with b) giving the equivalent circuit showing the parasitic elements. The connection between B and C has a non-zero impedance, which for a current flow of I_{BC} gives a volt drop of V_c at the amplifier input. The current I_{BC} could well have a small but significant noise component. For a 10cm length of 1mm diameter copper the resistance R at DC is R_{DC}=2.2mΩ, rising to 26.2mΩ at 10MHz due to skin effects[3]. The inductance, L, of a similar wire is 0.1μH. This leads to an inductive reactance at 50 Hz of 31μΩ and at 10MHz of 6.3Ω at 10MHz. At low frequencies (≈50Hz) the reactance of L is negligible compared to R_{DC}, hence a noise current of I_{BC} leads to a noise voltage, due to R_c, of 2.2μV. At 10MHz, where L_c is no longer negligible, the same current leads to a noise voltage of 6.3mV[3]. Connecting to one point eliminates the path length BC and reduces the common impedance noise.

In low frequency applications (f<1MHz), single point grounding is the optimum configuration[3]. Here common ground connections are avoided by using separate leads connected to one point.

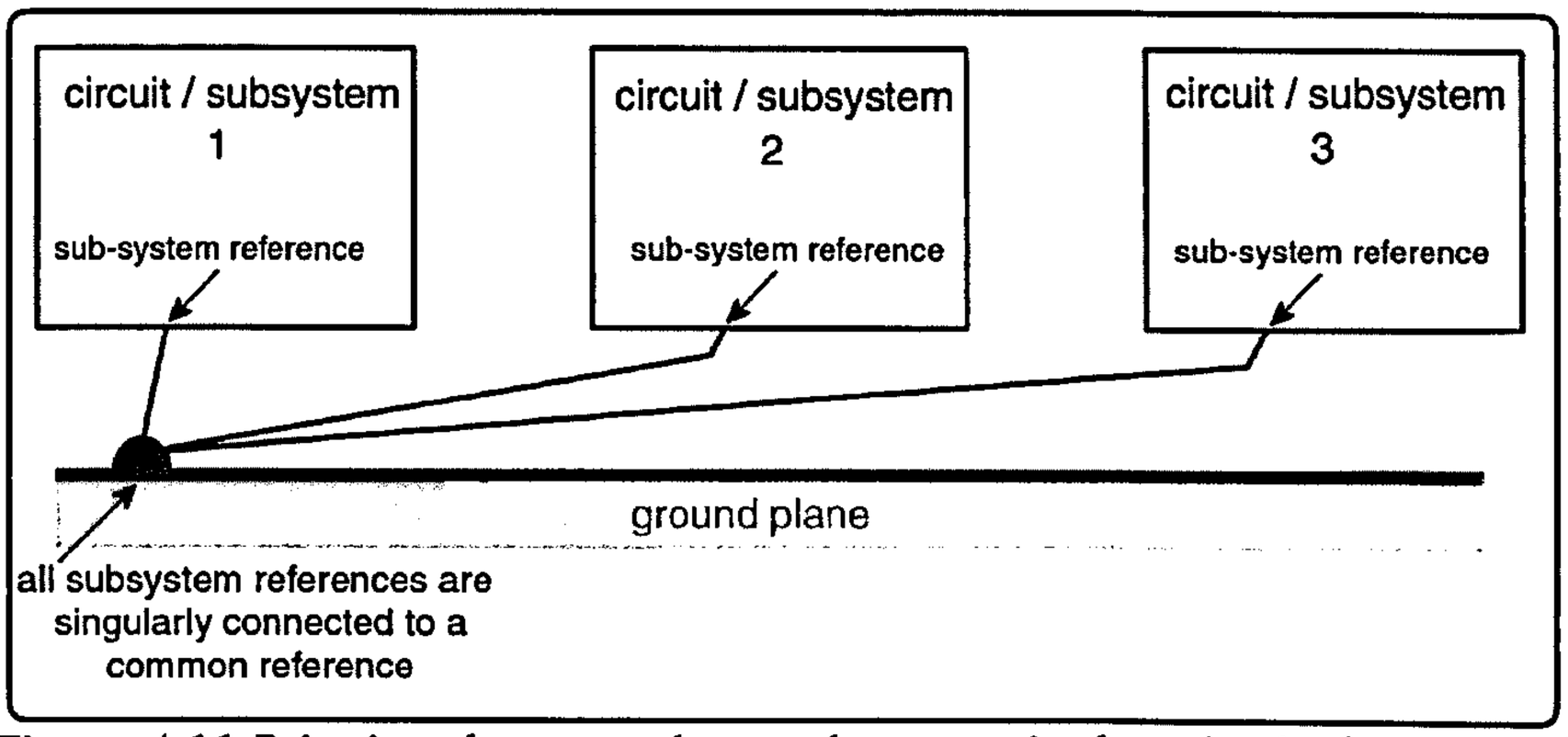

Figure 4.11 Bringing the grounds together to a single point is the optimal solution to common impedance grounding problems at low frequency[3].

Connecting circuits together in the manner of Figure 4.11 reduces common impedance noise.

Several signal leads need to be connected together in this way. These include the power supply reference, the shielding potentials including the screened room, and a reference potential for the measurement. See Figure 4.7.

Single point grounding also helps to reduce magnetic pickup by reducing or eliminating the loop area that magnetic fields have to couple into, discussed in section 4.3.1.

External Source	Typical Magnitude
50Hz	100pA
100Hz ripple	3μV
150Hz magnetic pick-up from saturated 50Hz transformers	0.5μV
radio broadcasts	1mV
switch arcing	1mV
vibration	10pA
cable vibration	100pA

Table 4.1 Typical contributions to noise from various sources[7].

Table 4.1 shows some typical values for extrinsic noise. They provide a useful guide but without a knowledge of the particular system the magnitudes given are only a rough indication of the contributions of any particular source.

4.5 The Measurement Sub-systems in Detail

Within this section the system design is examined in detail, where necessary at the component level. Component choices are discussed and the mechanisms by which they effect the noise performance of the system examined.

Most measurements in quantum transport are conductance plots and, at any instant in time, can be viewed as a simple measurement of resistance. In order to achieve this at the noise levels indicated in Figure 1.1 the problem becomes quite substantive.

Figure 4.12 and Figure 4.13 show a schematic of the physical layout of the system and a block diagram of the electronic signal paths respectively.

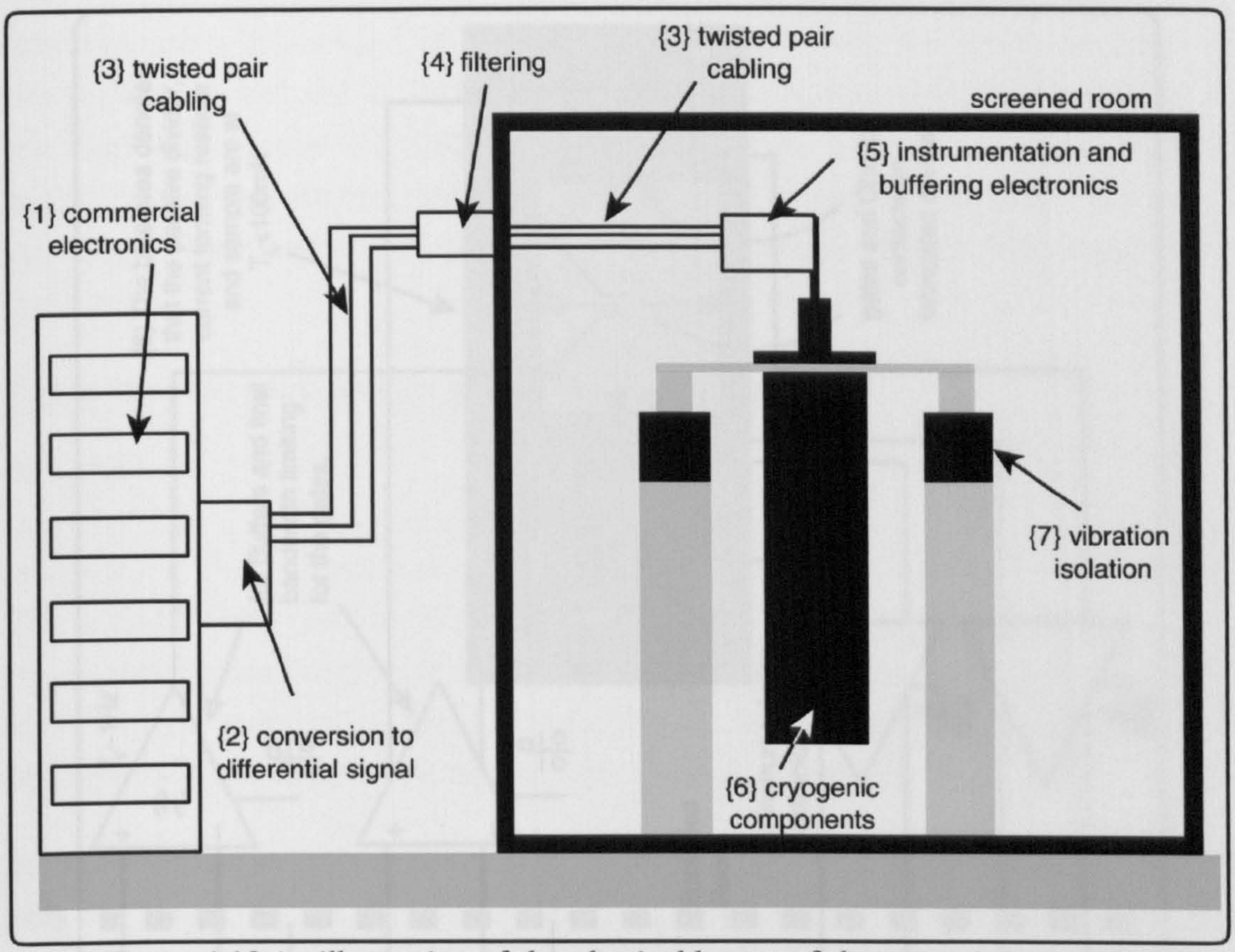

Figure 4.12 An illustration of the physical layout of the new measurement system.

All signals originate and terminate in a 19' rack unit that houses the commercial electronics (d.c sources, lock-ins etc.), shown at Figure 4.12 {1}. Input signals are converted from a single ended output to a balanced differential signal {2} transmitted via twisted pair cabling {3} to filtering at the screened room which bandwidth limits the inputs and outputs to approximately 200Hz {4}. The signals are then transmitted to a stainless steel box mounted on the dilution unit which houses systems of electronics that are accessed simultaneously and independently. Additionally it incorporates a "telephone exchange" patching system {5} that allows the different signals to be re-routed at will. The electronics within this box consists of three different systems. Firstly the excitation buffers providing buffering electronics for the a.c measurement input signal being impressed across the sample. Secondly, gate filters, which provide buffering and extreme bandwidth limiting (less than 1Hz) for the gate leads and finally, the electronics that measure I and V through and across the sample. The incoming excitation signals pass down into the dilution unit to a resistive network {6}. The I and V signals are the only outputs from the system and pass back out through the filter box. The whole cryostat assembly is suspended on a vibrationally isolated frame {7}.

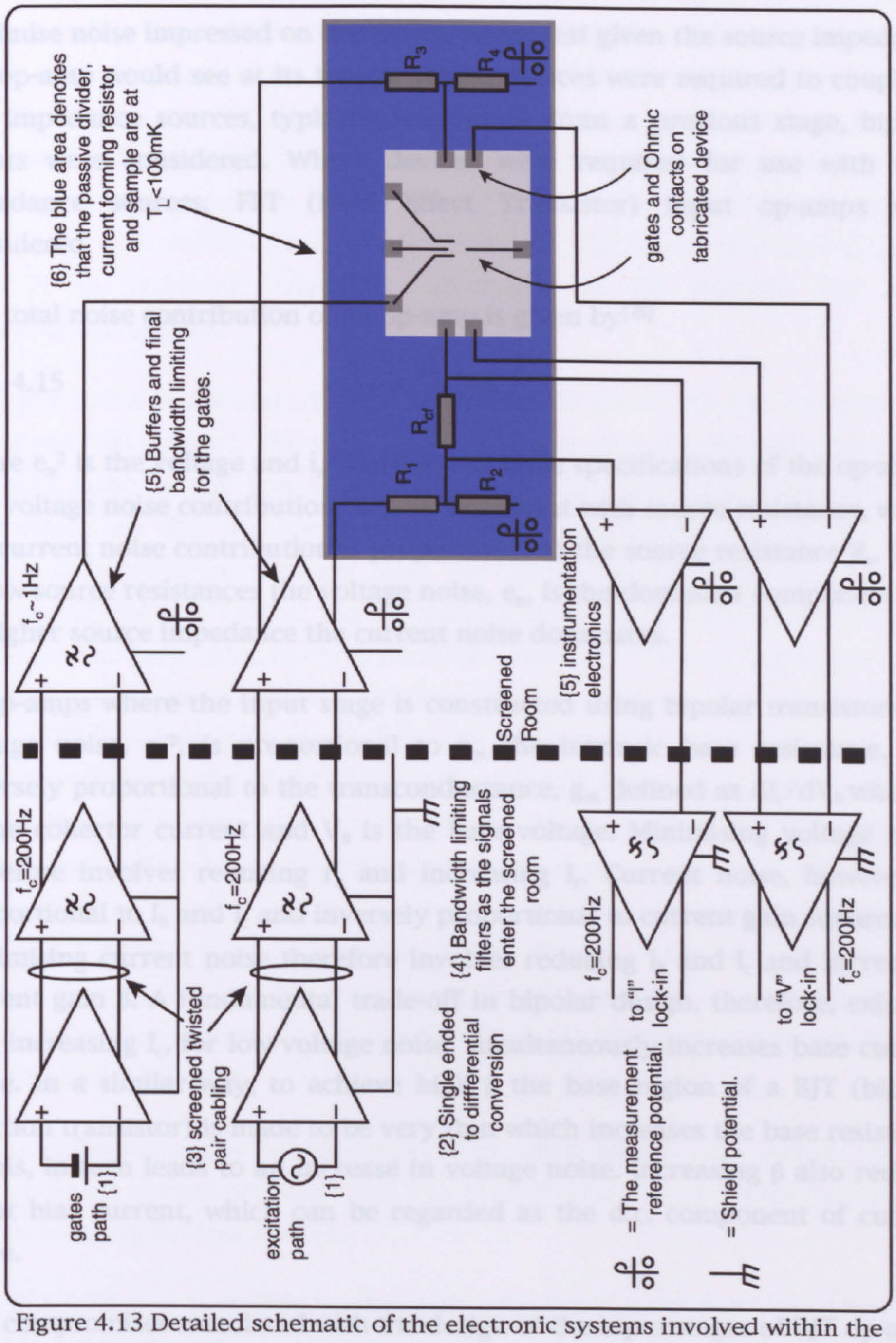

Figure 4.13 Detailed schematic of the electronic systems involved within the new quantum transport measurement system.

4.5.1 Choices in Low Noise Op-amps

The choice of op-amp types for this work was determined by the intrinsic noise performance.

It was important to assess device noise specifications in the context of their placement within the system. Specifically, op-amps were chosen in order to

minimise noise impressed on the device under test given the source impedance the op-amp would see at its inputs. Where devices were required to couple to low impedance sources, typically the output from a previous stage, bipolar inputs were considered. Where devices were required for use with high impedance sources, FET (Field Effect Transistor) input op-amps were considered.

The total noise contribution of an op-amp is given by[8]

Eqn. 4.15 $$e_T^2 = e_n^2 + (i_n R_s)^2$$

where e_n^2 is the voltage and i_n^2 the current noise specifications of the op-amps. The voltage noise contribution to e_T is a constant with source resistance, whilst the current noise contribution is proportional to the source resistance R_s. Thus at low source resistances the voltage noise, e_n, is the dominant component and at higher source impedance the current noise dominates.

In op-amps where the input stage is constructed using bipolar transistors the voltage noise, e_n^2, is proportional to r_b, the intrinsic base resistance, and inversely proportional to the transconductance, g_m defined as dI_c/dV_B where I_c is the collector current and V_B is the base voltage. Minimising voltage noise therefore involves reducing r_b and increasing I_c. Current noise, however, is proportional to I_b and I_c and inversely proportional to current gain squared, β^2. Minimising current noise therefore involves reducing I_b and I_c and increasing current gain β. A fundamental trade-off in bipolar design, therefore, exists in that increasing I_c, for low voltage noise, simultaneously increases base current noise. In a similar way, to achieve high β the base region of a BJT (bipolar junction transistor) is made to be very thin which increases the base resistance r_b this, in-turn leads to an increase in voltage noise. Increasing β also reduces input bias current, which can be regarded as the d.c. component of current noise.

The compromises associated with the design of the input stages of BJT op-amps result in low values of voltage noise and relatively high values of current noise and input bias current. This makes bipolar input op-amps a good choice for low source impedance applications, but an inappropriate choice when used with high source impedances.

Op-amps with FET input stages are a more appropriate choice when used with high source resistances. These hybrid devices have FET input stages fabricated on the same substrate as the remaining bipolar circuitry. The voltage noise of a FET is inversely dependent on g_m. FETs generally have lower g_m than BJTs and

hence tend to have higher voltage noise for similar operating conditions. Unlike BJTs the voltage noise in JFETs have a significant 1/f component which may be important at low frequencies. The current noise of JFETS is typically 1 or 2 orders of magnitude less than BJTs, and at low frequencies is determined by the gate leakage current, which is small in FETs. The input bias current can be as much as 5 orders of magnitude smaller in JFET input op-amps than BJTs. This is an extremely important advantage in d.c coupled low noise measurement systems.

Similarly CMOS input and wholly CMOS op-amps have very low current noise and input bias current. The small amount of current noise present arises from the shot noise in the gate leakage current whilst the input bias current is determined by the leakage current of the gate-channel capacitor[9]. The voltage noise contributions are from the thermal noise of the channel and, most significantly, 1/f noise. The 1/f noise is inversely proportional to the area of the device. Large area devices, therefore, reduce 1/f noise. Large area CMOS op-amps still have significantly higher 1/f noise corners than the best low-noise JFET op-amps. This stems from the difference in construction of these devices and the origin of 1/f noise. 1/f noise is due to the random nature of free carrier generation and recombination. This is particularly apparent at a surface or interface where the crystal structure is non-uniform. In JFET devices the conducting channel and the gate region are both semiconductors and the interface between them is accurate on an atomic scale. In CMOS devices, though, the channel and the gate region are separated by an oxide layer. The interface is non-uniform, as the oxide layer is not lattice matched to the semiconductor channel.

Three different types of op-amps were used within the design of the measurement system detailed here. The INA105 and OPA637 from Burr-Brown, and the Analog Devices AD743.

The INA 105 is a monolithic unity gain differential amplifier, consisting of a precision op-amp and on-chip metal film resistors. The resistors are laser-trimmed for accurate gain and, more importantly in this context, high common mode rejection and low input bias current. As the resistor network is integrated with the op-amp module, and accurately matched, this results in a low offset voltage of typically 50μV with a temperature coefficient of typically 5μV/^{0}C. This figure includes the input bias and offset currents of .the amplifier. The broadband noise performance of 60nV/$\sqrt{Hz}$ is quoted with reference to the output, as the circuit is defined as unity gain, and includes the amplifiers input current noise and thermal noise contributions from the

resistor network[10]. This op-amp is used extensively throughout the electronic design in buffering and ground breaking applications.

The AD743 is a hybrid FET-bipolar (BiFET) construction that has low noise performance across a wide range of source impedances. This op-amp is used in the filtering circuit (section 4.5.5, item {4} Figure 4.12). The source resistance seen by the op-amp is dominated by the 10KΩ resistor in the passive filter structure of Figure 4.18. Above a source resistance of ≈2KΩ the source resistance dominates the noise contribution of the AD743. At 18Hz the input voltage noise spectral density is 4nV/√Hz and the input noise current noise ≈30fA/√Hz[11].

The most critical part of the system is the instrumentation circuitry that connects directly to the cryogenic components, including the device under test. The all-round noise performance of the op-amp attached to the device under test had to be good, as the impedance of a sample could range between essentially zero, in magneto-resistance experiments, to >100MΩ when in strong Coulomb blockade. The device chosen as the front end of the instrumentation circuit was the OPA637. This is a JFET input hybrid device that uses Burr-Browns Dielectric Isolated FET technology (DiFET). This technique allows the JFET input stage to be fabricated on a substrate dielectrically isolated from the remaining bipolar circuitry. At 18Hz the input voltage noise spectral density is 8nV/√Hz and the input current noise spectral density is ≈1.6fA/√Hz. As the 1/f corner is at approximately 200Hz these noise specifications are raised from the lowest values quoted. The unit provides a low input bias current of typically 1pA[12].

4.5.2 Power Supply and Layout Considerations

All the electronics within the system design were powered by sealed lead-acid batteries. This eliminated the possibility of direct injection of power supply noise. The batteries were chosen in order that the system could measure continuously for 4 days without the need for recharging. This allowed for the implementation of long data collection routines, which in turn, allowed the mapping of large areas of parameter space. All op-amps power supplies were decoupled as shown in Figure 4.14. The 51Ω resistor was included as a precaution against resonances on the power supply line and can be viewed as a damping element. The 1μF capacitor to ground decoupled high frequency interference components on the power supply line. All power supply decoupling references seen in Figure 4.14 were brought back to the same point on the circuit board separately connected at a single point.

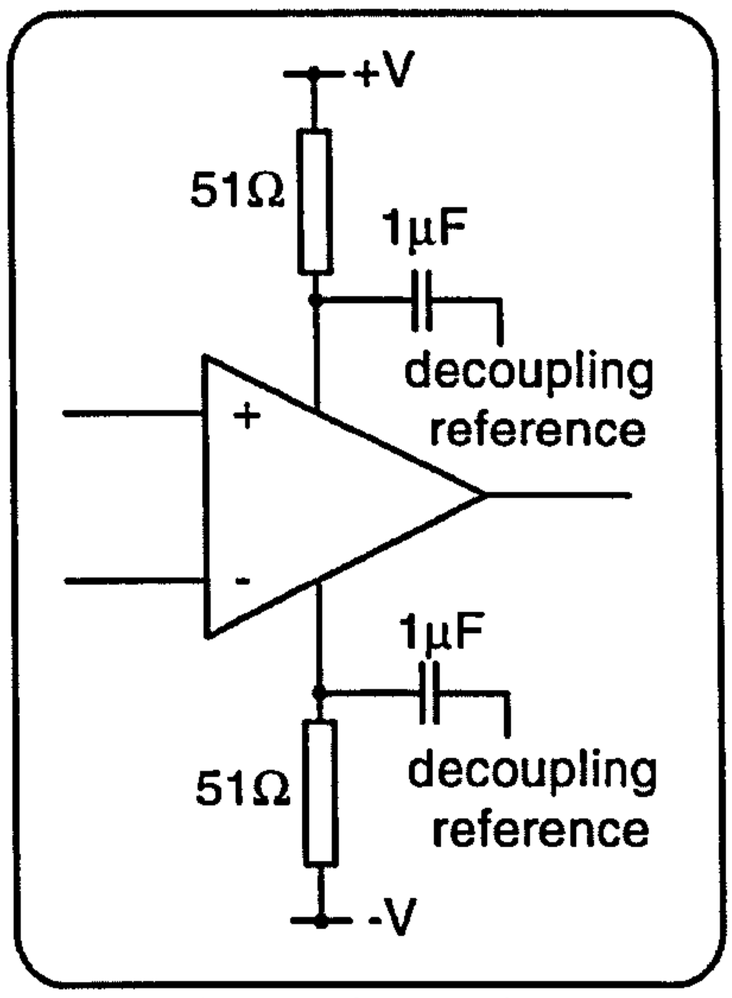

Figure 4.14 Power supply decoupling scheme used for all electronics associated with this work.

In order to reduce leakage currents between printed circuit board (PCB's) tracks, especially to the input bias pins of the op-amps, ground planes were used on both sides of the PCBs. These ground planes on opposite sides of the board were singly connected to the same point as the decoupling reference. This was standard procedure for all PCB designs associated with this work.

4.5.3 Single Ended to Differential Conversion

One of the practical problems with designing a fully balanced system is that almost all commercial electronic test equipment are fitted with BNC connectors, thus offering a single ended (grounded shield) output. In this case, it is assumed that the shield forms part of the reference potential for the circuit. In some cases, there is the option to float the ground connection thus enabling an external reference to be used. The problem is then that the outer shield is also being used as a signal and is therefore subject to interference.

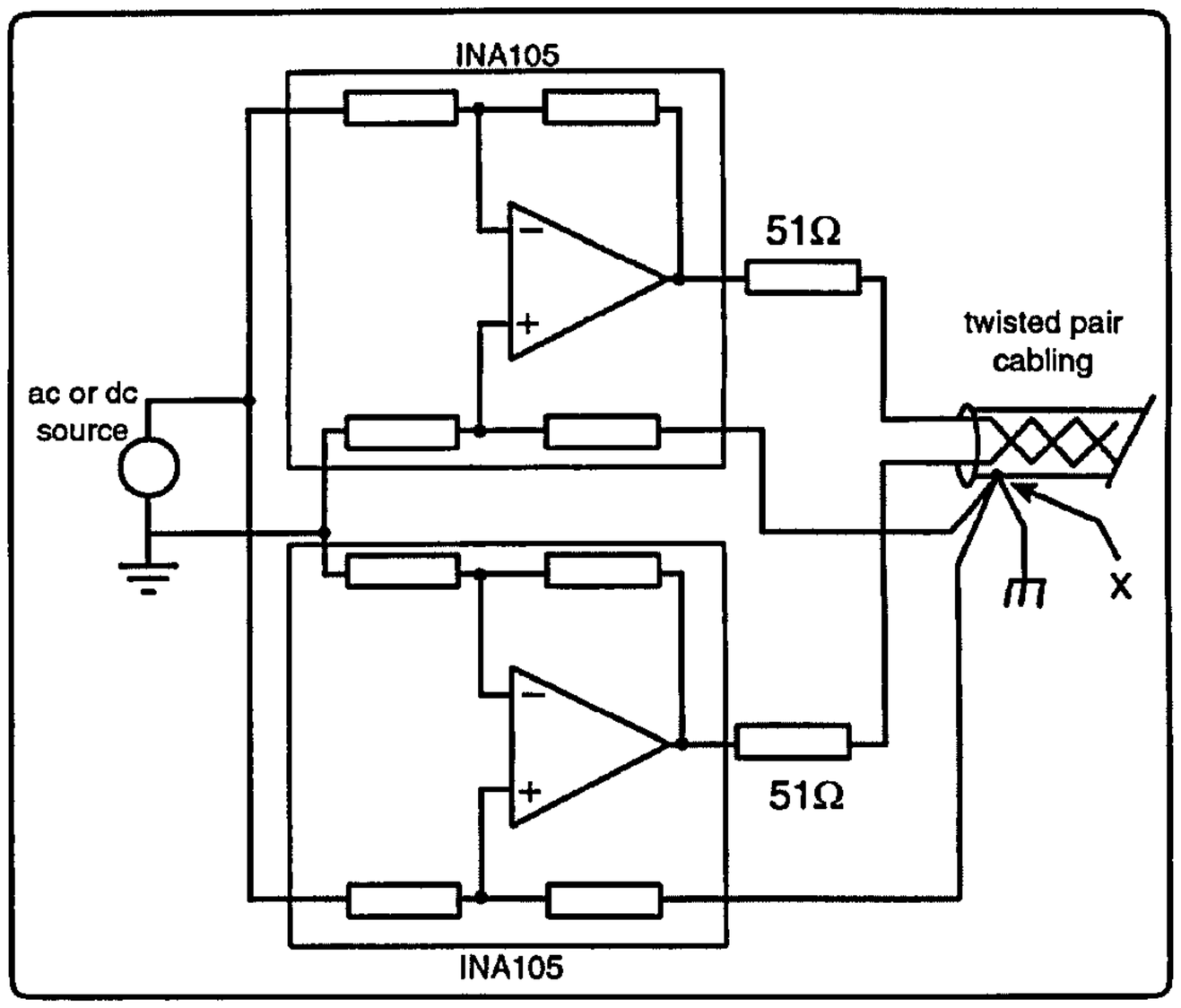

Figure 4.15 Input stage to the measurement system for both a.c and d.c sources.

The solution to this problem adopted here, was to use a differential input, differential output op-amp configuration designed to fit directly onto the front of this equipment this then provided the appropriate differential output for subsequent circuitry. Figure 4.15.a) shows such an arrangement for a signal transmitted toward the sample (either the excitation or a gate voltage). The signals at point X were connected to the shield to ensure that the shield potential was equal to the mean of the two signal levels. The inclusion of the 51Ω resistors at the outputs of the INA105s ensured that there was damping in the circuit, created by the output of the op-amp and the cable capacitance, and hence prevented this circuit from oscillating. It should be noted that there was no direct connection between references from the input side in this circuit to the output. This is an example of "ground breaking" discussed in section 4.4.1.

A noise analysis of the system as a whole is presented in section 4.6 and shown Figure 4.34

4.5.4 Cabling

Shielded twisted pair wires were used in the system to provide interference shielding from both capacitive and inductive field sources.

Twisting wires together in pairs reduces magnetically coupled interference. The flux coupling the wire induces alternate polarity emfs in each adjacent loop, hence these emfs tend to cancel. Figure 4.16 illustrates this.

The screen reduces electric field noise and, if used together with a balanced circuit, will tend to induce any residue field as a common mode signal on the

twisted pair, which will be rejected by the CMRR (Common Mode Rejection Ratio) of the amplifier. For this to work effectively the system must maintain a balanced output source and differential input. This cabling configuration (with its associated balanced circuitry) was used both inside and outside the screened room (Figure 4.12 points {3}).

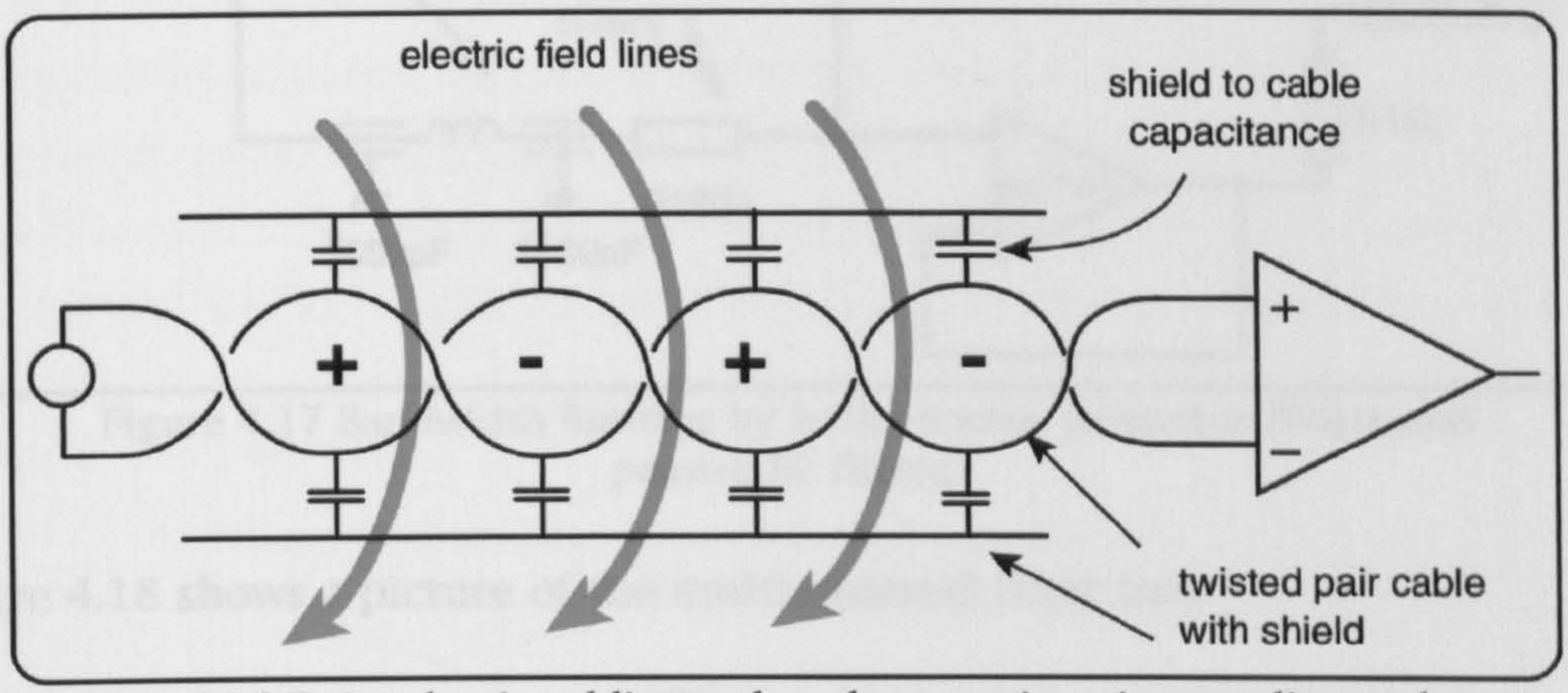

Figure 4.16 Twisted pair cabling reduced magnetic noise as adjacent loops have opposite polarity. Any electric field noise tended to couple equally to both core conductors and was therefore seen as common mode, and rejected by subsequent circuitry.

4.5.5 Filtering

The output from the circuit of Figure 4.15 was fed to a filter on the side of the screened room shown in Figure 4.17. This circuit comprised of a ceramic Pi-section filter and a single pole passive filter with a buffered output for each signal line. The Pi-section filter had an insertion loss of 20dB at 10MHz and the passive filters had a cut-off off approximately 200Hz. The Pi-section filter was used to eliminate high frequency components that may otherwise have by-passed the passive filter circuit via the stray capacitance. These filters were general to the system and had to pass both the a.c excitation signals as well as the d.c gate voltages. A cut-off of 200Hz was chosen to ensure the low frequency a.c excitation signal (typically 18 Hz) was sensibly free from phase distortion.

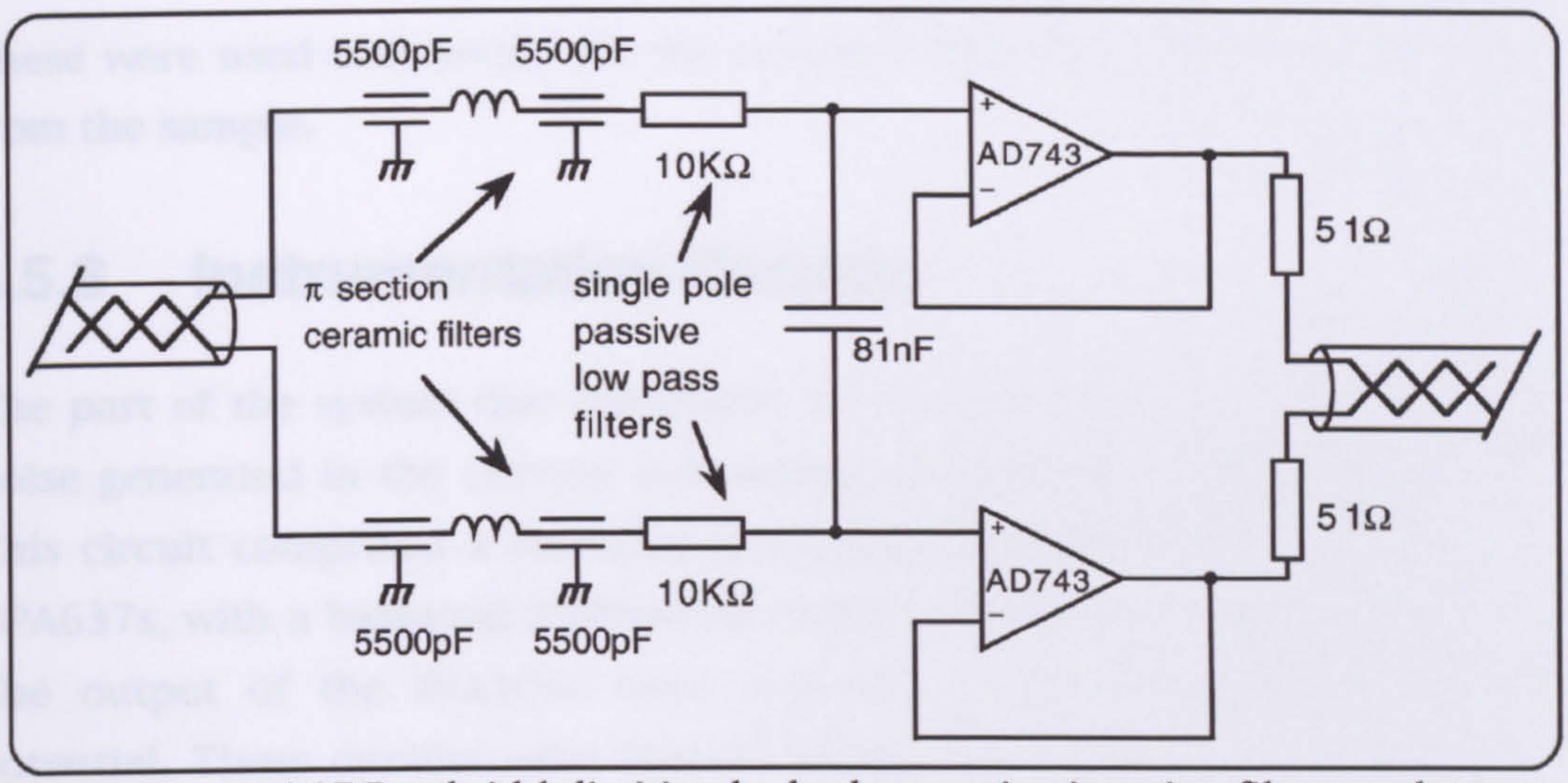

Figure 4.17 Bandwidth limiting by both ceramic pi-section filters and passive RC filters.

Figure 4.18 shows a picture of the multi-channel filter box.

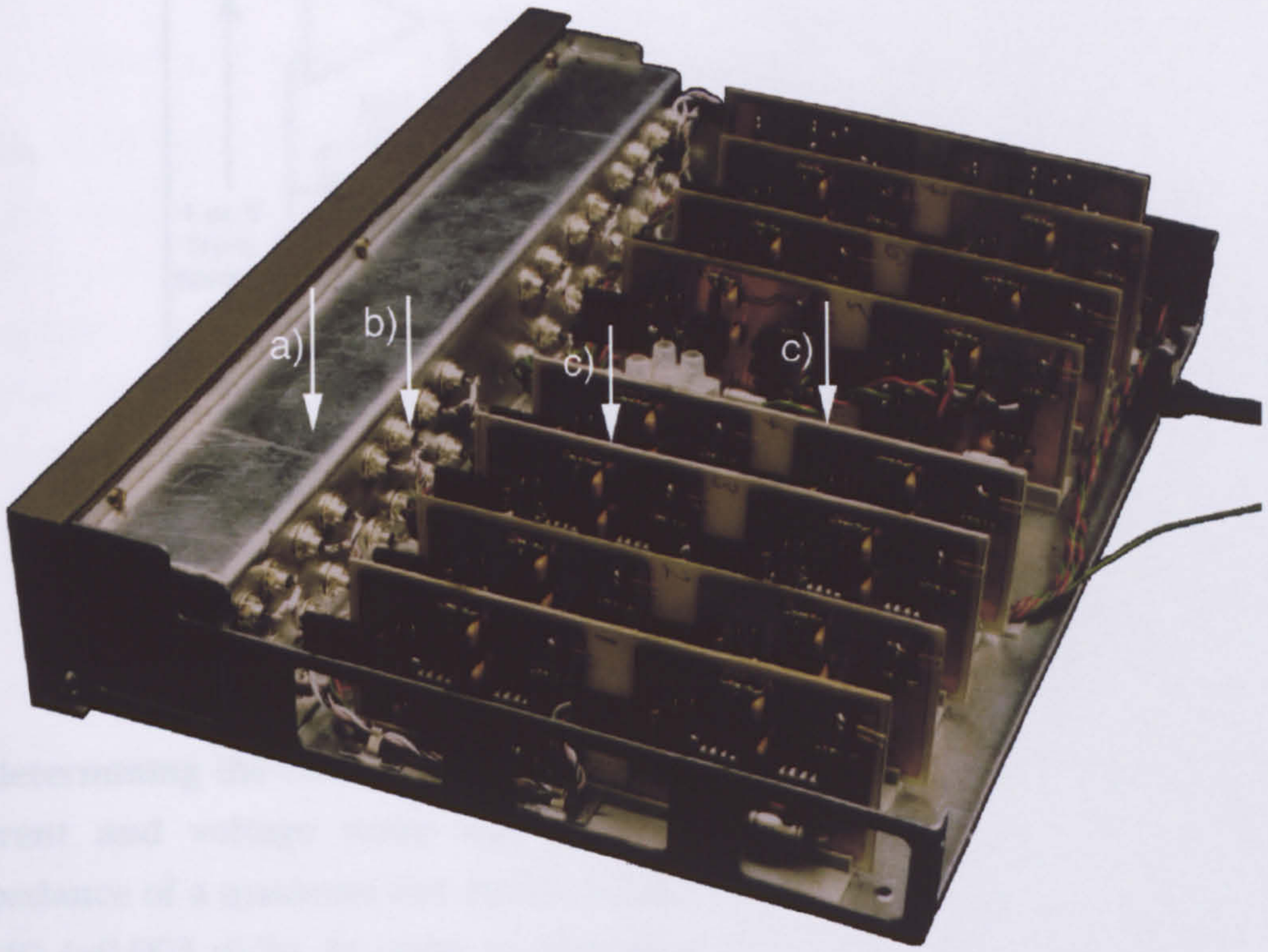

Figure 4.18 shows the multi-channel filter system; at a) the internal shield is shown b) is the pi-section filters and c) shows the PCB's with two channels per circuit board.

The pi-section filters were mounted within an internal screen in order to minimise stray fields coupling into the filter circuitry. Each circuit board consisted of two filter channels. The filter box supported 16 independent channels. The circuit board containing the two channels at the top of the picture was configured to allow signals to pass out from the screened room.

These were used exclusively for the current and voltage measurement signals from the sample.

4.5.6 Instrumentation Circuits

The part of the system that dominates the overall signal to noise ratio is the noise generated in the current and voltage measurement circuit, Figure 4.19. This circuit comprised a standard instrumentation amplifier, formed around OPA637s, with a balanced differential output formed around the two INA105s. The output of the INA105s were referred to the measurement reference potential. These circuits were housed within the enclosure at the top of the cryostat, point {5} Figure 4.12.

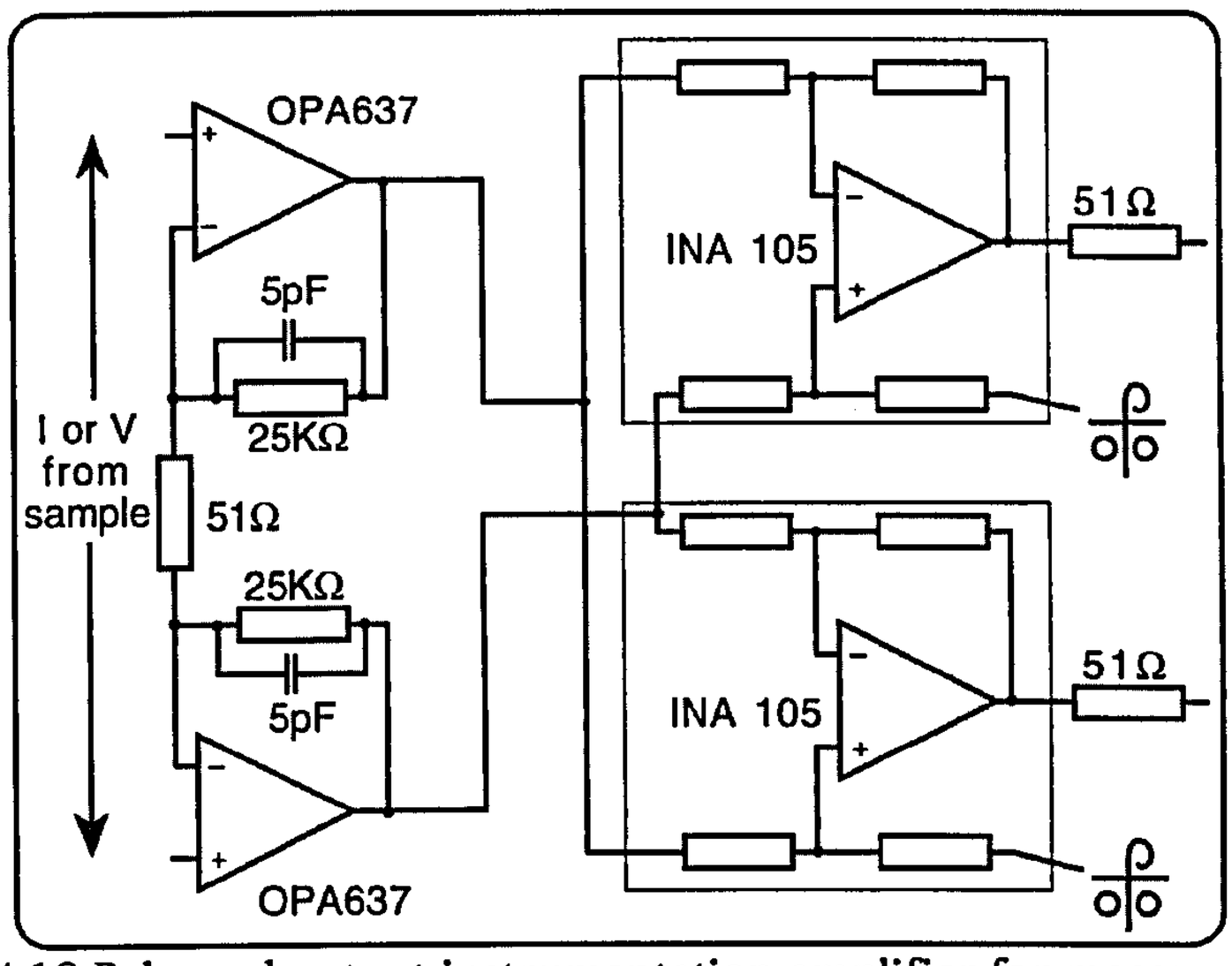

Figure 4.19 Balanced output instrumentation amplifier for measurement of I and V signals.

In determining the correct op amp for use with a high impedance source, both current and voltage noise was taken into account. Typically the source impedance of a quantum dot device ranges from ≈ 25KΩ (e^2/h) to greater than 10MΩ (≈0.003 e^2/h). In order to determine which op-amp is most suitable for measuring such devices, the impedance of the quantum dot is assumed ≈1MΩ. A suitable choice of op-amp therefore needs to exhibit low intrinsic noise performance up to ≈1MΩ.

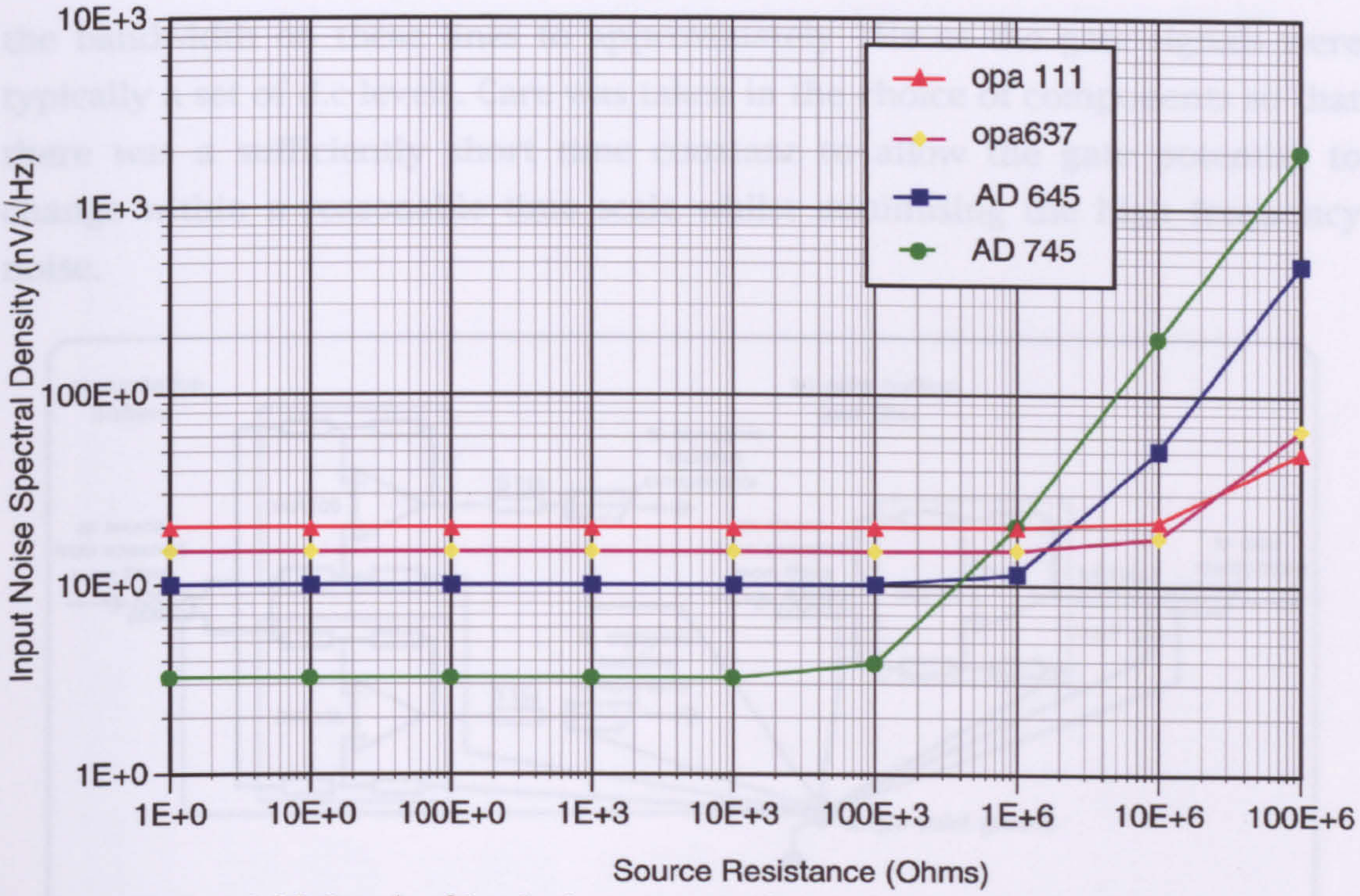

Figure 4.20 Graph of intrinsic op-amp noise against source impedance.

Figure 4.20 shows that the AD745 has the lowest voltage noise for the lower source impedance. However, as the source impedance increases to above 100KΩ current noise dominates. Current noise doesn't affect the OPA111 until the source impedance is greater than 10MΩ but it has a higher voltage noise spectral density than all of the other devices. Both the AD645 and OPA637 have acceptable and similar performance, with the AD645 having lower noise up to 1MΩ, but increasing rapidly thereafter and the OPA637 remaining virtually constant to 10MΩ, for this reason the OPA637 was chosen over the AD645.

4.5.7 Excitation and Gate Buffers

The box on the dilution unit (Figure 4.12 {5}) also contained the final stage of electronics before the incoming signals were imposed across the cryogenic components.

For the excitation signal this consisted of a differentially configured buffer that provided a high impedance input for the previous stage to work into, and a well balanced, low impedance output which was presented to the resistive network at the base of the dilution unit.

The gate buffers, although providing similar functions in terms of impedance conditioning, had single ended outputs, as they were intended to drive into a single Schottky gate. A passive filter stage was positioned on the output to limit

the bandwidth on these lines to approximately 1Hz as the gate signals were typically a set of d.c levels. Care was taken in the choice of components so that there was a sufficiently short time constant to allow the gate potential to change within a reasonable time scale whilst minimising the high frequency noise.

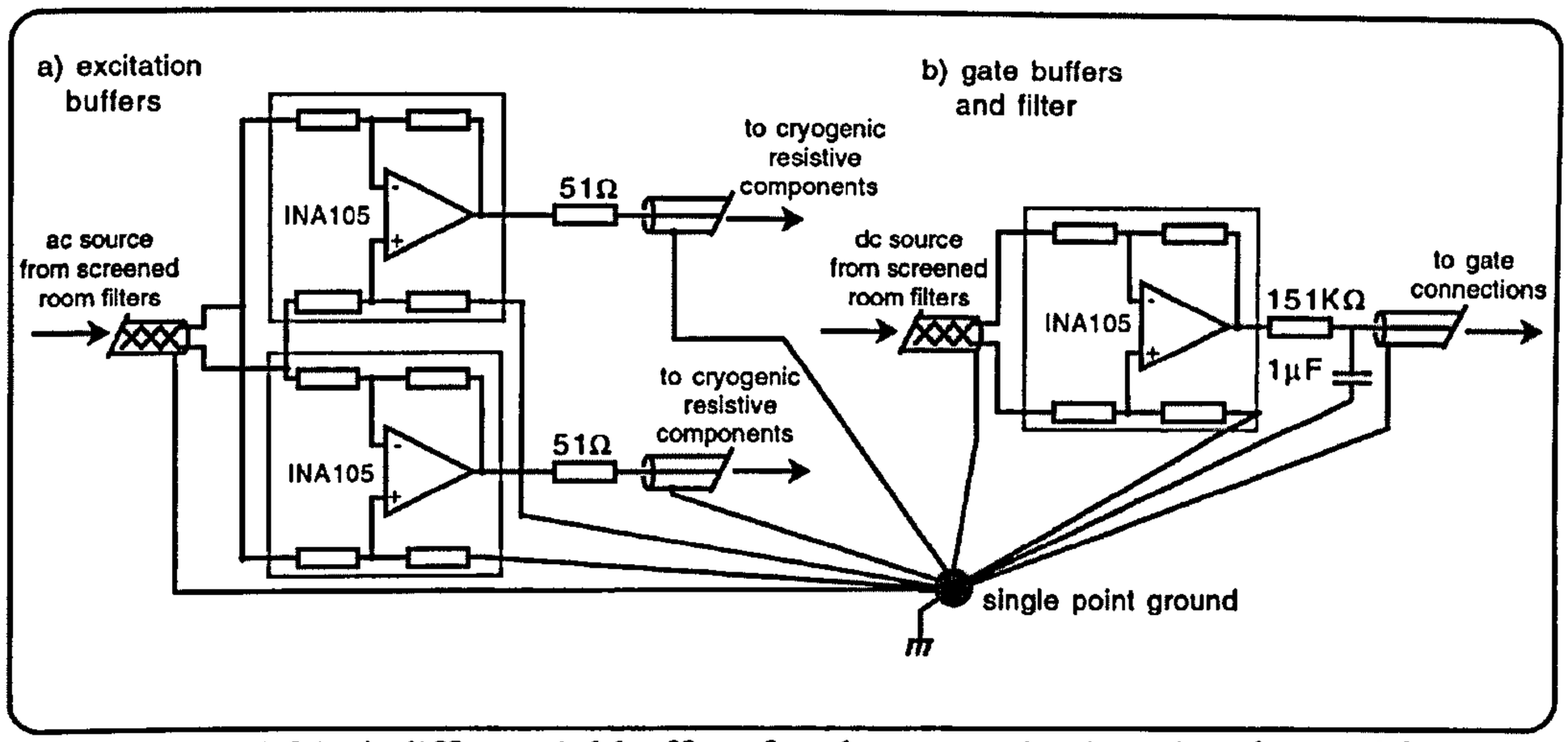

Figure 4.21 a) differential buffers for the a.c excitation signal, provides impedance matching and common mode rejection of the incoming signal. b) differential to single ended conversion and bandwidth limiting for the gate signals as well as impedance matching and common mode rejection.

4.5.8 Signal Routing (Patching)

The system allowed 11 independent signals to be applied to the sample (14 leads as some signals required 2 leads for differential configuration); eight gate leads, two current measurement leads, two voltage measurement leads and two leads to apply the excitation signal. During the course of a typical set of measurements, however, it was necessary to reconfigure these signals to observe different physical phenomena exhibited by the sample e.g. quantum Hall, Shubnikov de Haas, Coulomb blockade etc. In order to allow the maximum flexibility in signal reconfiguration a "telephone exchange" system was used. The arrangement of this system can be considered in two halves. The array of 24 (3x8) connections on the left-hand side of Figure 4.22 a), were directly connected to the sample. The two groups on the right of Figure 4.22 b) and c), were the input and output signals. Any connection from the input/output side was assigned to a sample connection by patching leads between the relevant sockets. The patching leads were constructed from RG316 cable with LEMO 00 series coaxial connections.

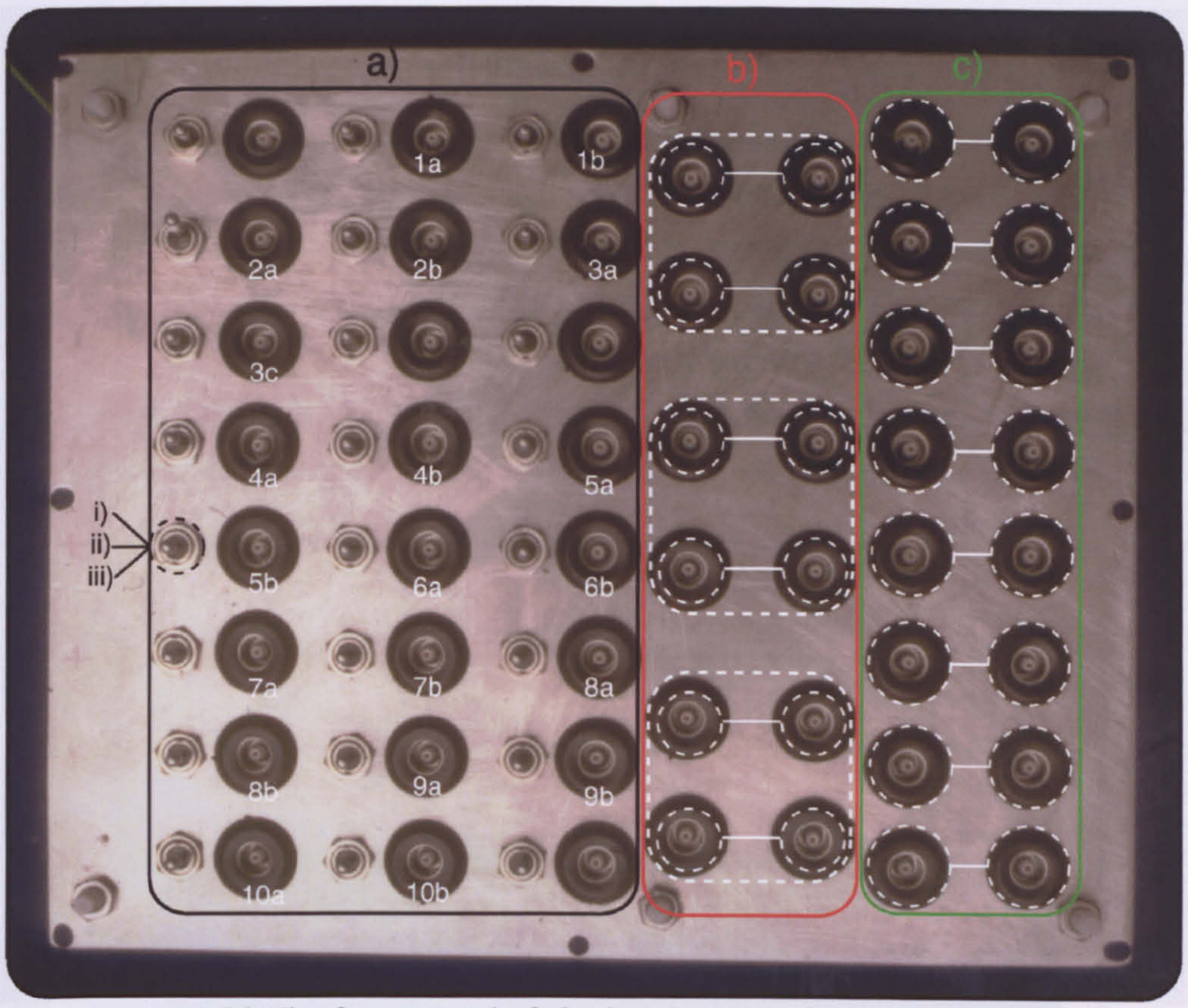

Figure 4.22 The front panel of the box housing the instrumentation electronics and buffering circuit acted as a signal routing panel. Section a) attached directing to the cabling entering the cryostat whilst b) and c) accessed the instrumentation amplifiers and gate buffers respectively.

The two columns of eight connections of Figure 4.22 c) were for connection to the gates. Each group of two were identical outputs and allowed two different gates on the sample, which require identical potentials, to be driven by a single voltage source. Section b) Figure 4.22 consisted of 3 groups of 4 connections. The top two groups were identical and are used for differential measurement of either current or voltage, simultaneously and independently. The lower group was for the connection of the excitation signal to the sample. The array of 24 connections in section a) each had a three position switch to enable the sample to be connected to i) the incoming signal, ii) no connection (floating) or iii) reference potential (0V). During measurement reconfiguration, these switches were used to protect the sample from electrostatic discharge.

In general the wires in section a) were identified in pairs (1a and 1b, 2a and 2b, etc) in order to indicate the wires that were twisted together, and hence should be used together to minimise noise (see section 4.5.4). There were 7 stainless steel micro-coax wires and 17 Constantan alloy (Cu55/Ni45) that made up the cryogenic wiring loom. Each twisted pair was thermally anchored to the 4K plate, 1K plate, the still and the mixing chamber.

4.5.9 Cryogenic Components

Rather than regarding the necessity of measuring at below liquid Helium temperatures as a problem, it was used to advantage. Figure 4.23 shows a schematic of the arrangement of resistors mounted at the base temperature of the refrigerator. The excitation signal imposed across the device was fed into the system at a relatively high amplitude (typically 10s of mV) and passively reduced by a factor of 10,000 via R_1 and R_2. R_{CF} was a high resistance providing an approximation to a constant current that flows though the sample.

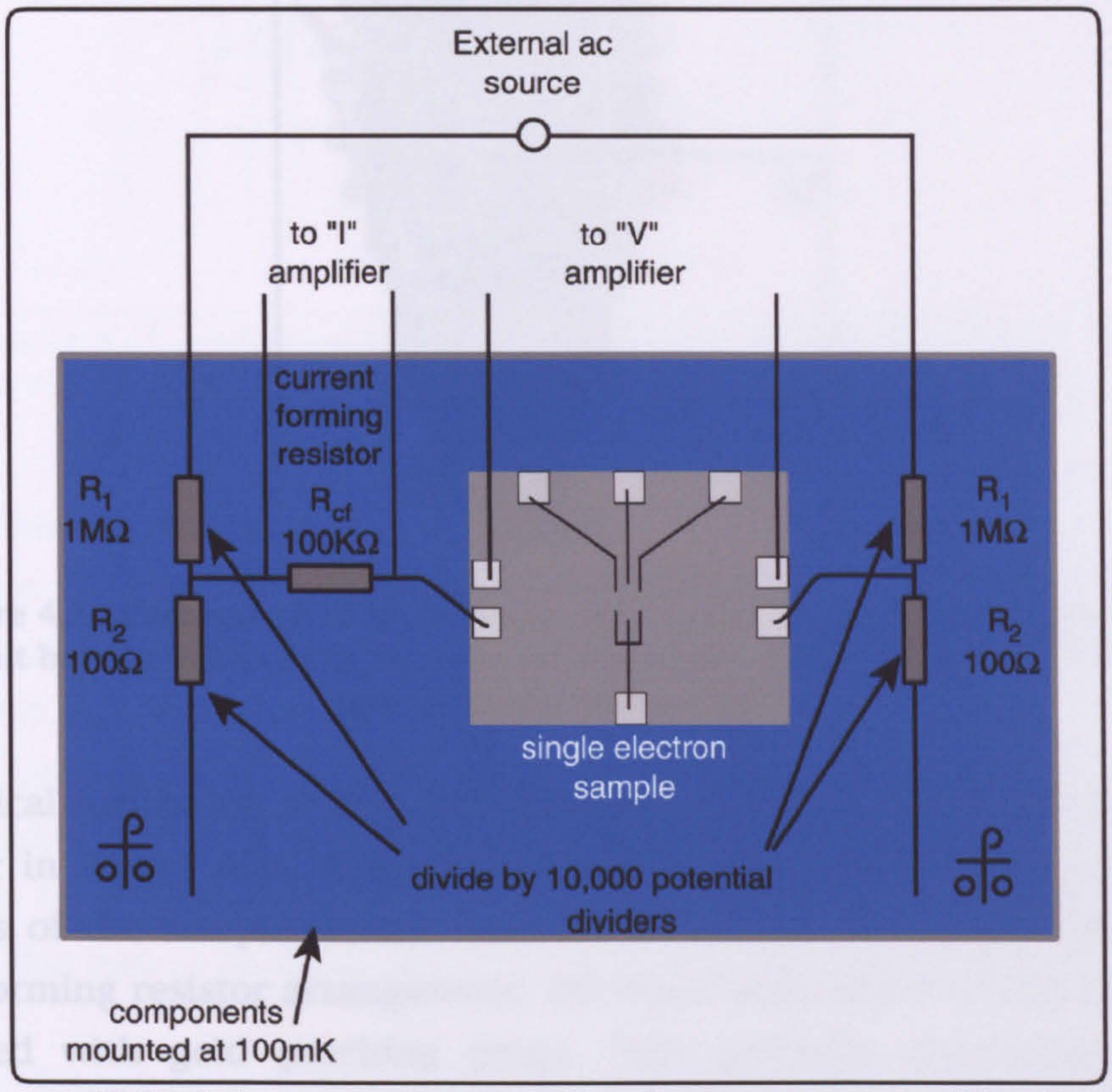

Figure 4.23 Resistive network mounted at base temperature. The dividing network (R_1 and R_2) on either side of the sample reduced the magnitude of the incoming signal whilst maintaining the balanced nature of the system. R_{cf} formed a series circuit with the sample. A measurement of voltage across R_{cf} gave the current through the sample.

The current, I, was measured as a voltage across R_{CF} and the voltage, V, across the sample was measured directly. By placing these passive components (R_1, R_2 and R_{CF}) at base temperature, the Johnson noise associated with the resistors was effectively eliminated. By mounting these resistors next to the sample, at base temperature, the very low signal levels (in the order of μV's) that needed to be expressed across the sample only had to appear over a few centimetres. This was vitally important as it gave the minimum excess noise expressed across the device. For quantum dot devices this is not simply a case of increased signal-to-noise ratio as excess noise leads to a heating of the electron

gas which may thermally smear out fine structure information. A reduction in excess noise, therefore, may have a large effect on the device performance.

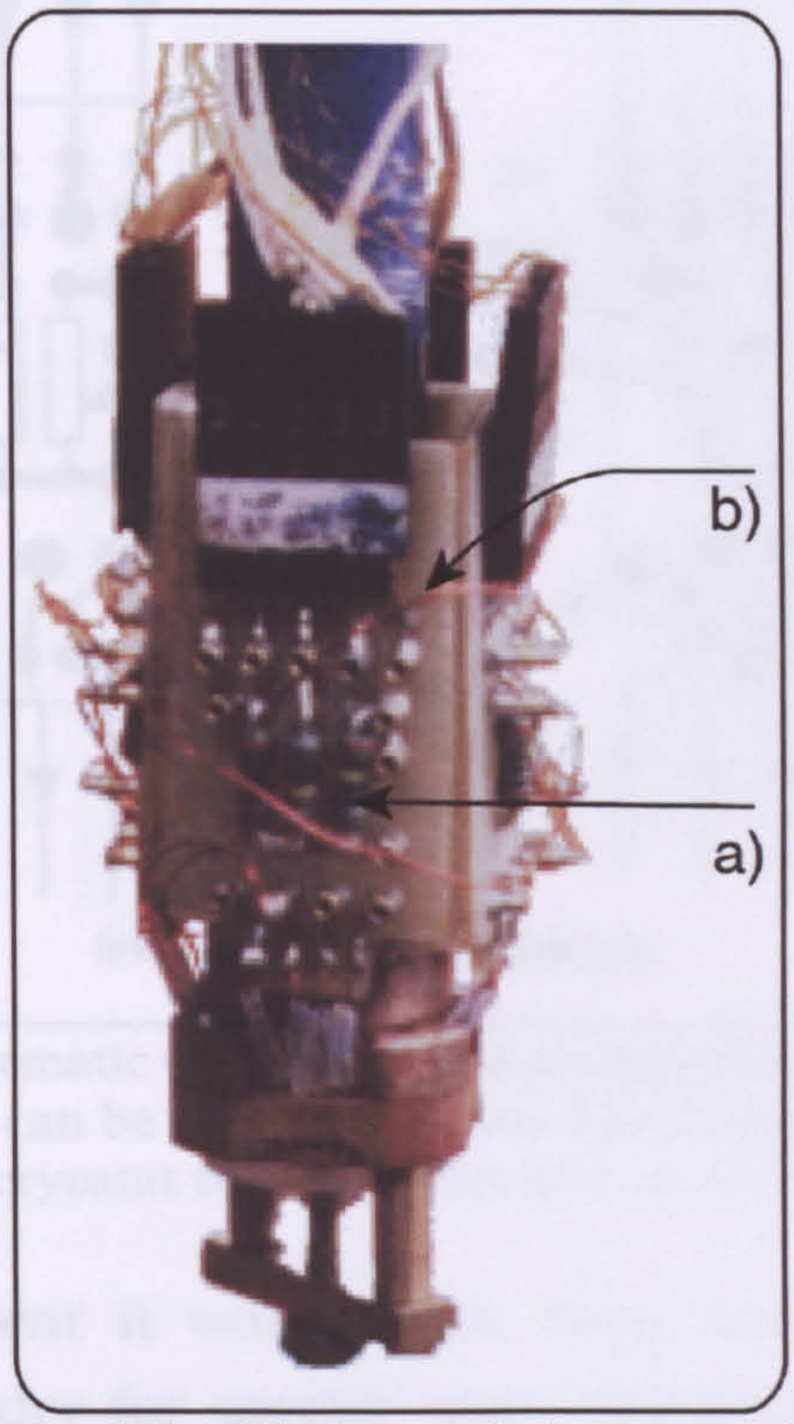

Figure 4.24 Photograph of the dilution unit foot with the sample holder and circuit boards. With a) the resistive networks and b) the wires that route the gate or Ohmic connections.

The physical realisation of this arrangement can be seen in Figure 4.24 with a schematic in Figure 4.25. Four circuit boards were used one on each of the four faces of the sample mount. On each board was a potential divider and current forming resistor arrangement, the input and output terminals were left unspecified with gold patching plugs. This patching arrangement at low temperature allowed the user of the system freedom when bonding devices within the ceramic headers.

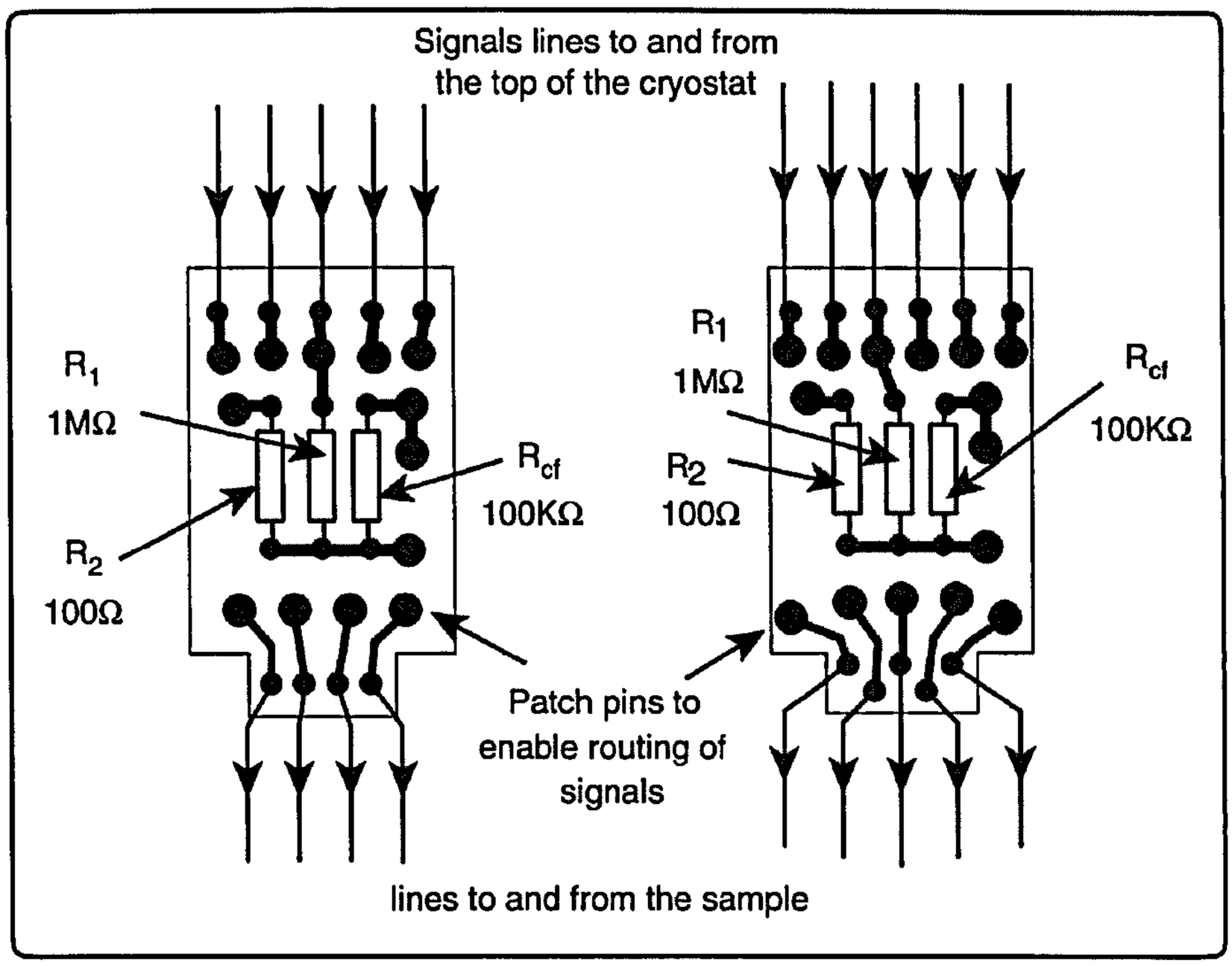

Figure 4.25 A schematic of the physical arrangement of the cryogenic components. Signals can be routed from any line coming down from the top of the cryostat to any connection on the sample.

Without this arrangement it would have been necessary to prescribe the connections on the header for specific uses. The circuit boards were used in pairs with one pair configured with the current forming resistor in circuit and one without. Four boards (two pairs) allowed two independent excitation paths and therefore two samples to be mounted in the system per measurement run. One drawback of this design was that once these connections were made they could not be altered without removing the dilution unit insert from the cryostat. This had to be done, however, in order to exchange samples.

4.5.10 Analysis of Measurement System Shielding

The most sensitive path of the measurement system were the low-level current and voltage signals that returned from the sample at base temperature to the instrumentation amplifiers at the top of the dilution unit insert. Typically, the signal levels were of the order of 1nV for low impedance and 1fA for high impedance samples. The cryostat consisted of approximately four layers of concentric stainless steel cylinders and was housed in a screened room.

The measurement electronics were housed in a stainless steel box that attached directly to the dilution unit insert approximately 1 meter away from the screened room walls. A plan view diagram of the screened room is shown in Figure 4.26 with a cross-section view of the screened room wall (inset).

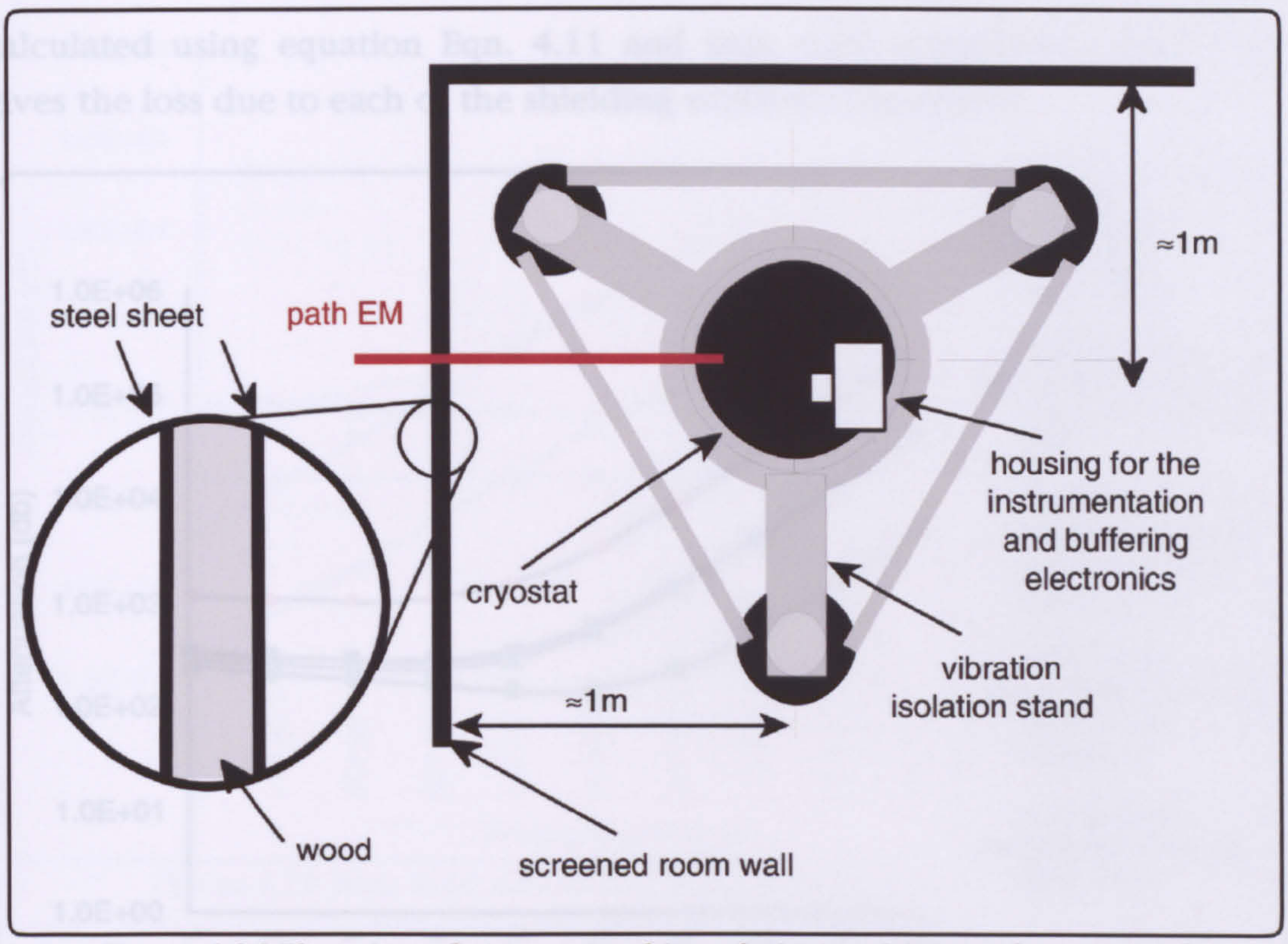

Figure 4.26 Plan view of cryostat and its relative position to the screened room. The inset shows detail of internal construction of the screen room wall.

There were four shields between the source and the electronics, the outer and inner faces of the screened room, the box and a glassy alloy cladding around the box. The glassy alloy (Co66/Si15/B14/Fe4/Ni1) was high permeability material, μ_r=200x10^3 as cast[13], and was used to provide a low impedance path for near field magnetic sources. The distance from the source to these shields, r, was taken to be 1x10^{-2}, 5x10^{-2} and 1m respectively.

Shield Effectiveness from Electric Fields

The total field effectiveness, S, from electro-magnetic fields is a sum of all the contributing shielding mechanisms[3,14].

Eqn. 4.16 $$S = R + A$$

Where R is the reflection loss and A is the absorption loss.

Figure 4.27 shows the combined reflection and absorption loss a near electric field source would experience for each surface as it propagated along path EM in Figure 4.26. The total shield effectiveness, a sum of the effectiveness of the individual shields, is also shown. The electric field source is considered to be in the near field. The contribution of reflection and absorption loss was

calculated using equation Eqn. 4.11 and Eqn. 4.10 respectively. Each curve gives the loss due to each of the shielding surfaces considered.

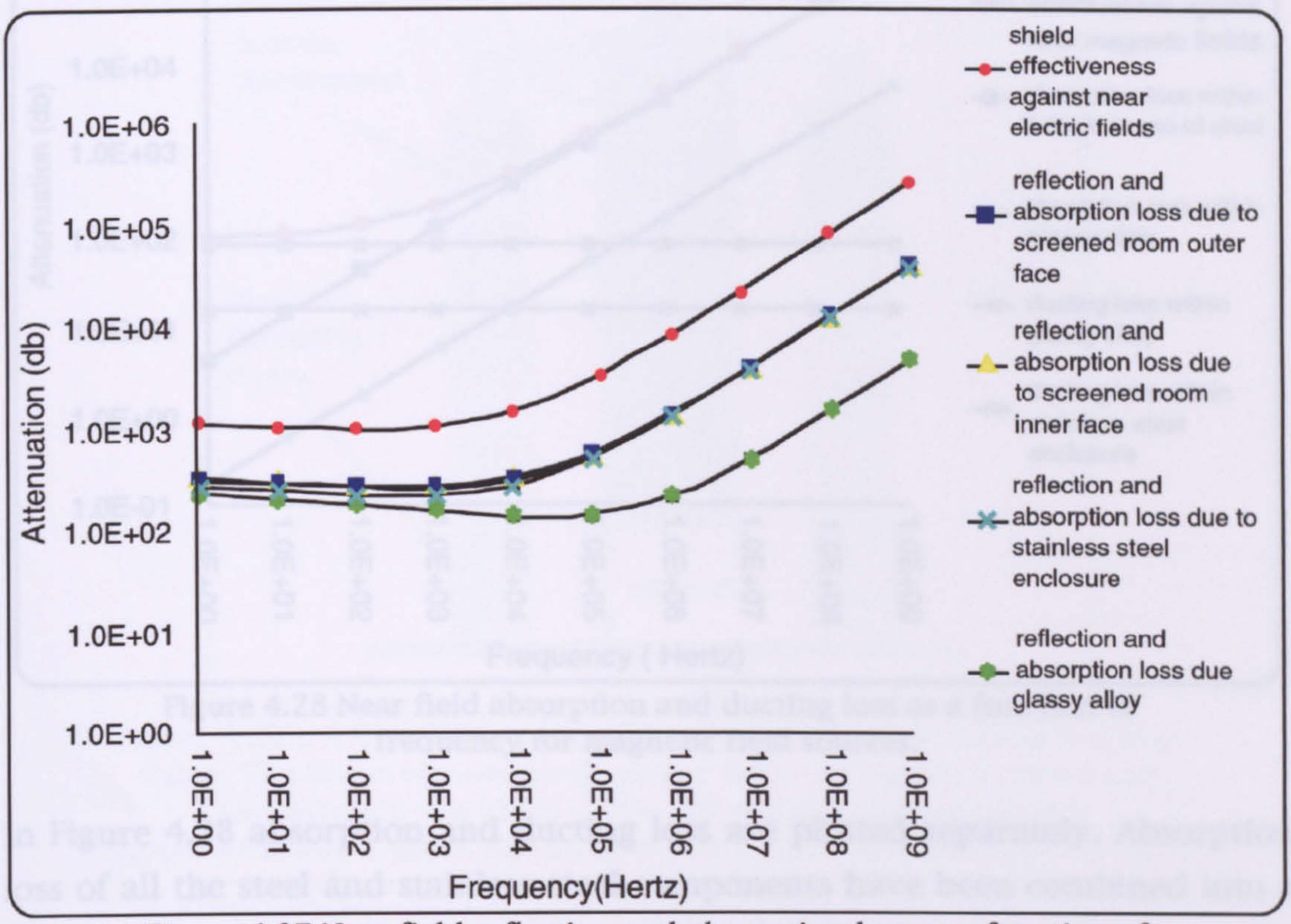

Figure 4.27 Near field reflection and absorption loss as a function of frequency for electric field sources.

Electric field sources are attenuated strongly by reflection loss from both the steel and stainless steel shields at low frequencies, while at higher frequencies absorption dominates.

Shield Effectiveness from Magnetic Fields

A major contribution to the noise spectrum of the system prior to redesign, seen in section 4.2, was low frequency magnetic fields from the mains supply on the outside of the screened room. Higher frequency switch mode power supplies in computer equipment are also sources for magnetic interference.

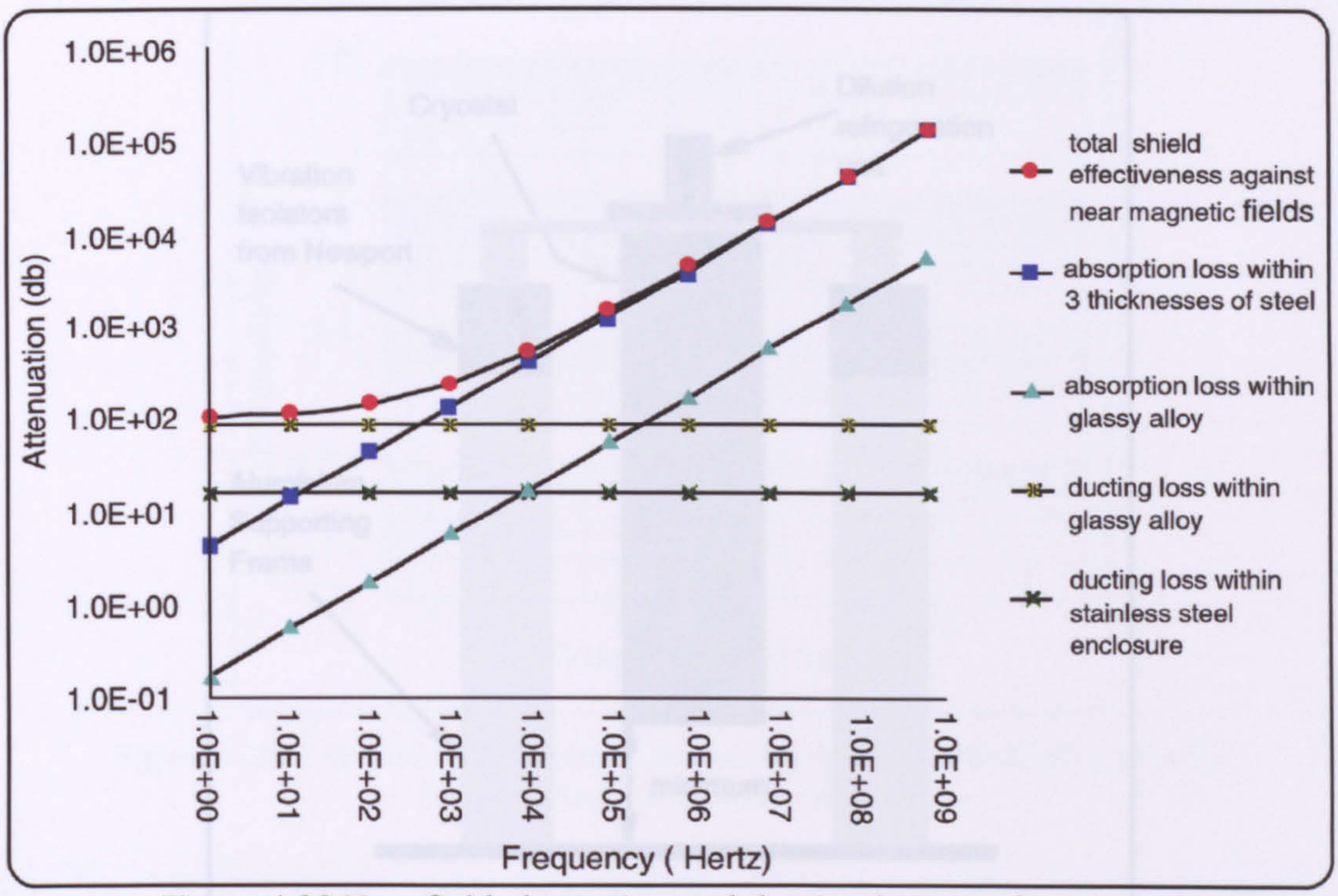

Figure 4.28 Near field absorption and ducting loss as a function of frequency for magnetic field sources.

In Figure 4.28 absorption and ducting loss are plotted separately. Absorption loss of all the steel and stainless steel components have been combined into a single curve, with the glassy alloy absorption loss considered separately. Ducting loss has been considered for the stainless steel box and glassy alloy only. Absorption loss is again calculated using Eqn. 4.10. Ducting loss has been calculated using Eqn. 4.14. taking the sphere radius, a, to be such that the volumes the sphere and the stainless steel housing are similar and X_s to be the thickness of the stainless steel.

Reflection loss plays an insignificant role in attenuating near magnetic field sources and has been neglected.

Ducting remains constant with frequency and is seen to be by far the most significant shielding mechanism at low frequency, with absorption loss being dominant above about 1KHz.

4.5.11 Vibration Isolation

From Figure 4.2 it is clear that the inclusion of vibration isolators in the system results in a significant reduction in noise. The most effective isolators available, are based on pneumatic systems where a sealed air reservoir supports the equipment to be isolated.

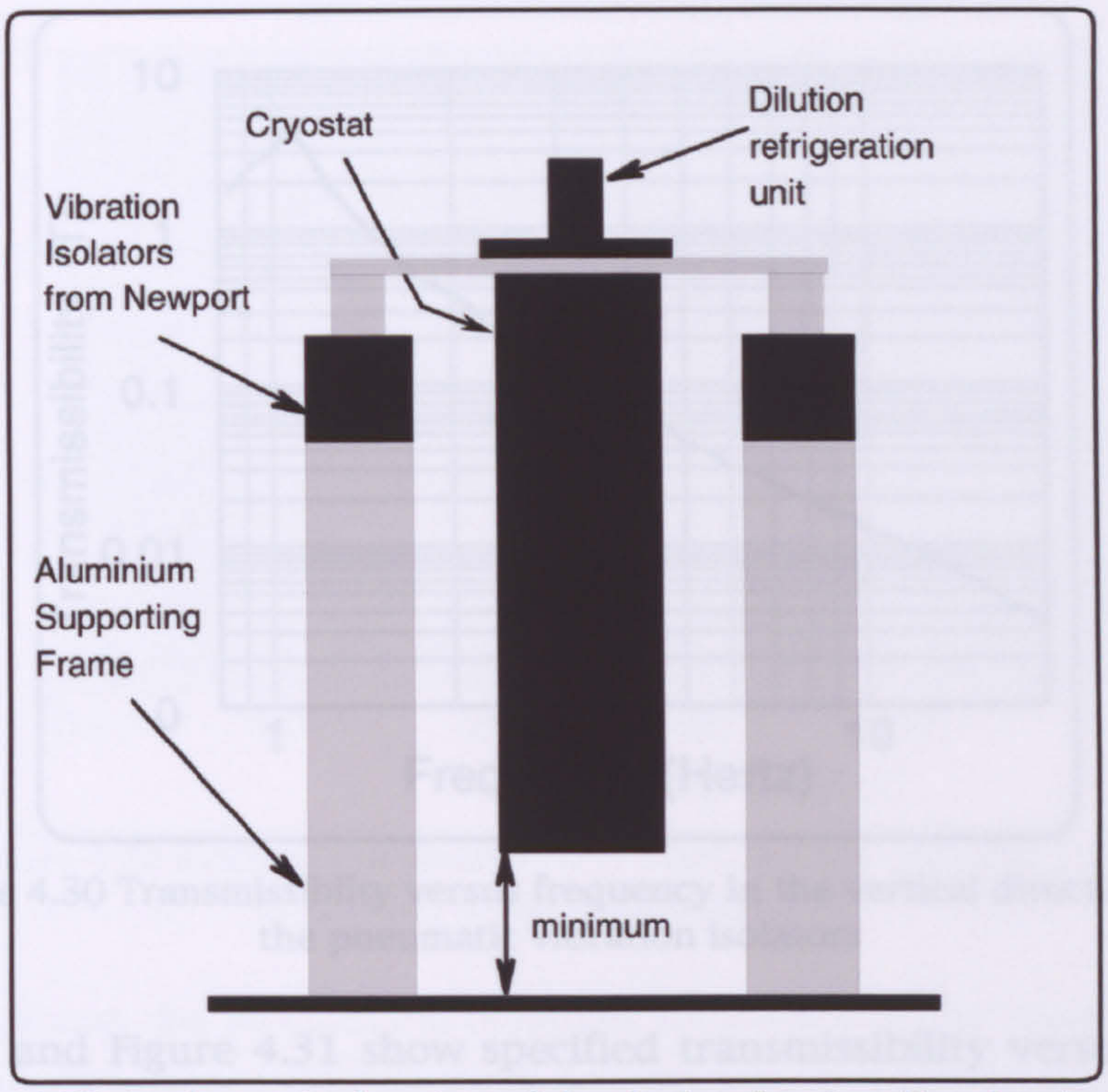

Figure 4.29 A schematic drawing of the design for the vibration isolating frame. The frame was designed around three pneumatic isolators and consideration was given to the safe working distance for the superconducting magnet. The magnet was suspended a minimum distance from sheet steel floor to prevent damage to the cryostat.

Figure 4.29 shows a schematic of the support frame design for the cryostat with vibration isolators. A critical consideration in the design was to take into account the field produced by the 12 Tesla superconducting magnet and ensure that only non-magnetic materials were used within close proximity to the magnet. Although the legs of the support were specified as Aluminium, as it is both non-magnetic and lightweight, there was no guarantee that the isolator units themselves were free from magnetic material. It was for this reason the isolators were positioned toward the top of the supporting frame. For similar reasons the cryostat was raised a minimum distance (≈ 35cm) from the sheet steel floor of the screened room to prevent damage to the cryostat.

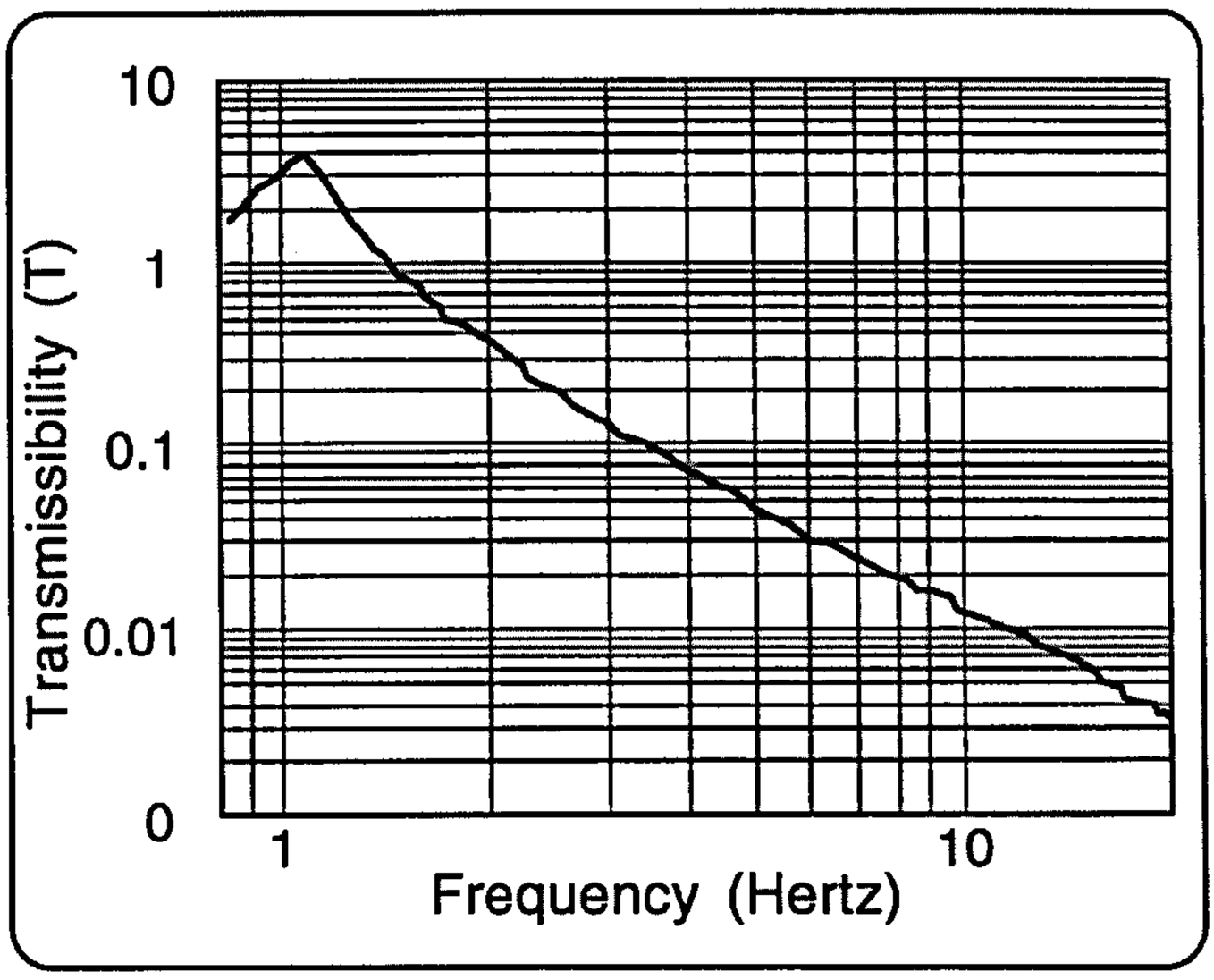

Figure 4.30 Transmissibilty versus frequency in the vertical direction for the pneumatic vibration isolators

Figure 4.30 and Figure 4.31 show specified transmissibility versus frequency data[15]. At a frequency of 11Hz and above, the resonant frequency of the insert, the transmission to the load in the vertical direction is reduced by a factor of 100; Figure 4.30. Whereas horizontal coupling is reduced by a factor of more than 10; Figure 4.31.

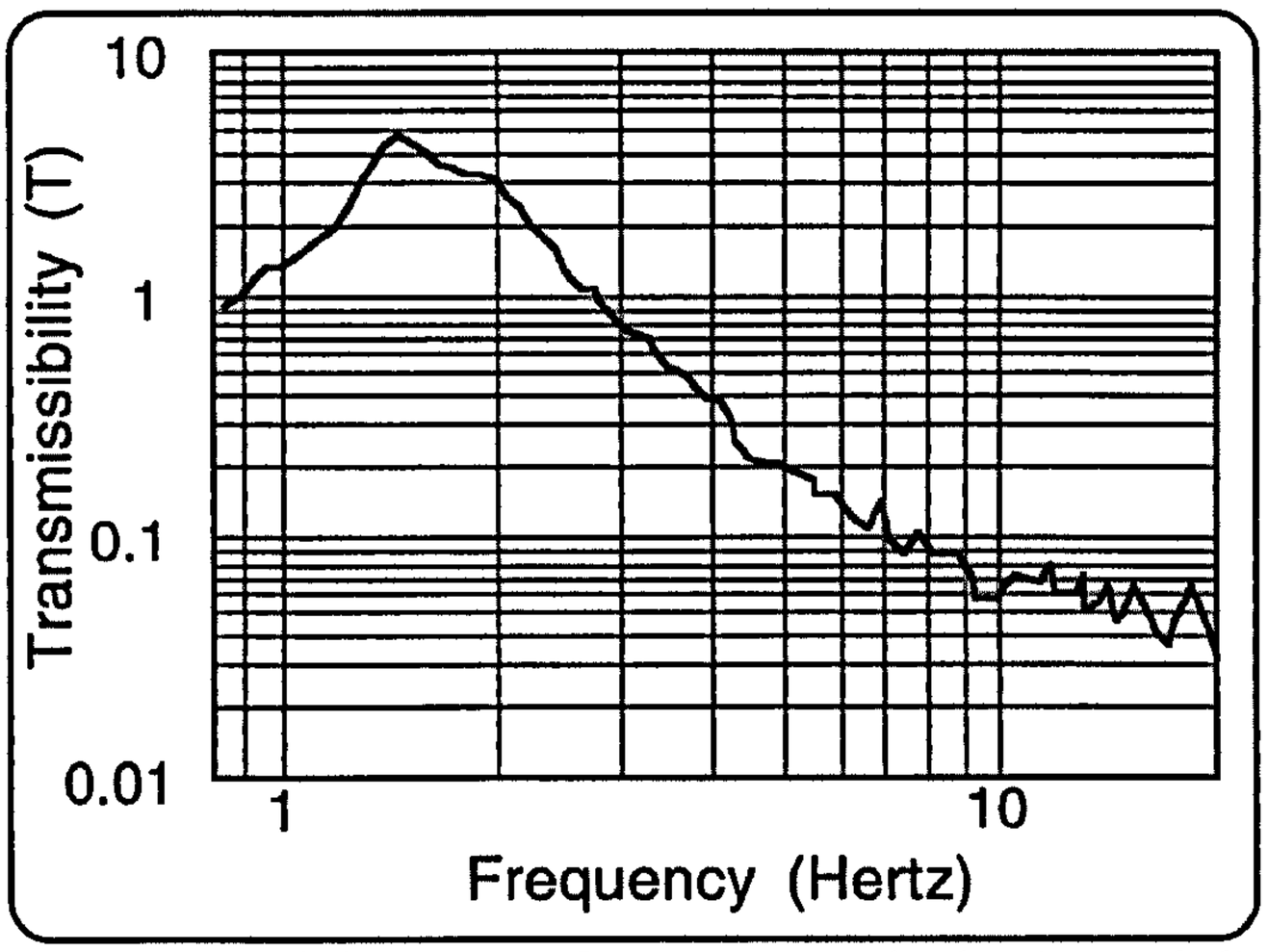

Figure 4.31 Transmissibilty versus frequency in the horizontal direction for the pneumatic vibration isolators

One of the suspected reasons that vibration contributes to the excess noise is the design of the dilution unit insert is fundamentally weak. The Kelvinox 25 was developed by Oxford Instruments as an entry level Dilution refrigeration system with a very low cooling power (25μW). Consequently the unit was made with the minimum amount of heat loading, as a result much of the mechanical strength, associated with more expensive systems was sacrificed.

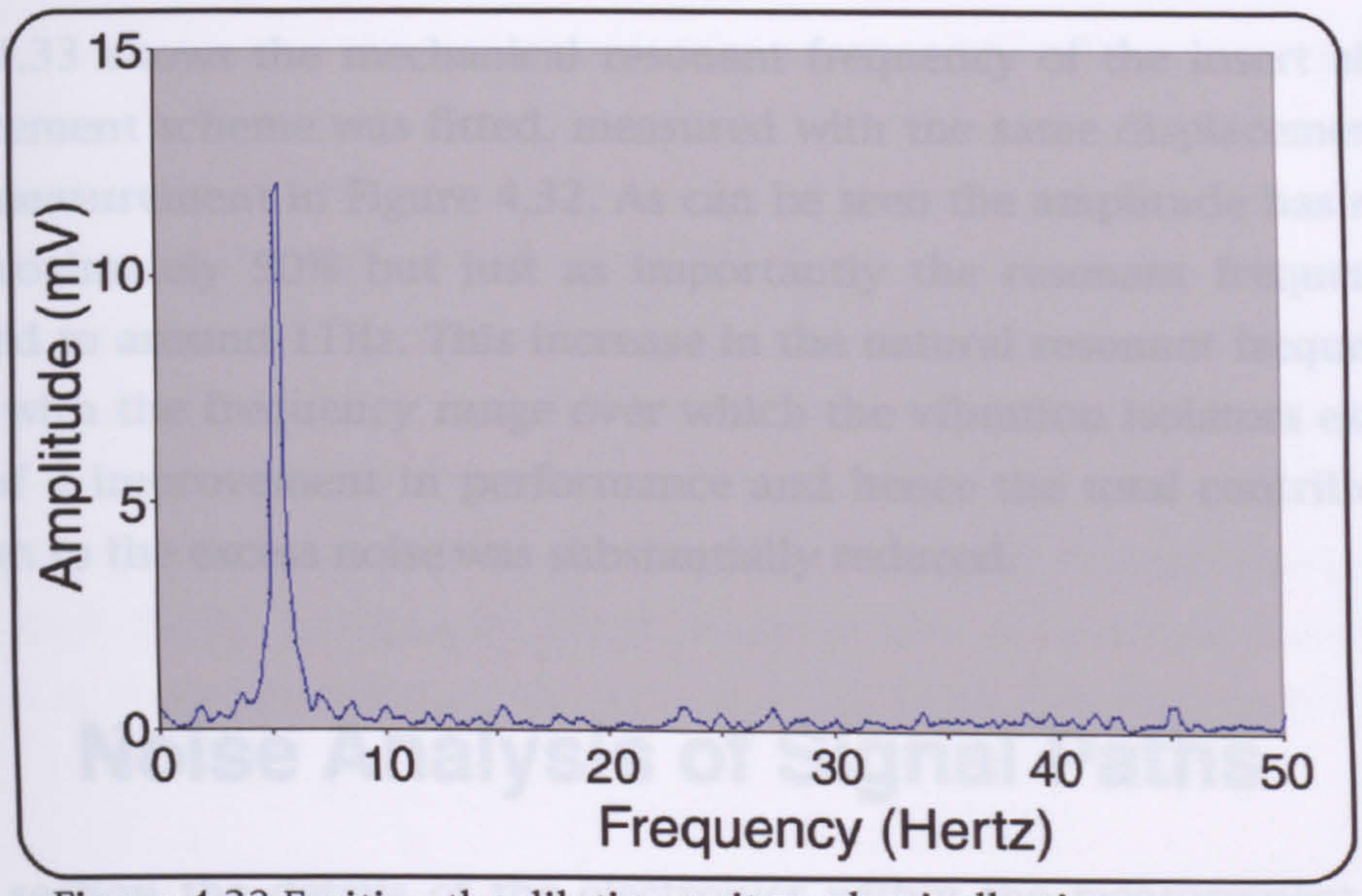

Figure 4.32 Exciting the dilution unit mechanically give a resonant frequency of approximately 6Hz.

Figure 4.32 shows the mechanical resonant frequency of the insert as measure from the sample holder using an Analogue Devices ADLX05 accelerometer. The ADLX05 unit was attached to the sample mount of the dilution unit and a force applied. The output of the accelerometer was measured on the HP 3561A Dynamic Signal Analyser.

In order to increase the stiffness of the dilution unit insert, Oxford Instruments, in collaboration with Glasgow, developed a reinforcement scheme that tied together several levels of the insert with thin walled stainless steel rods thermally isolated with Tufnol bushes.

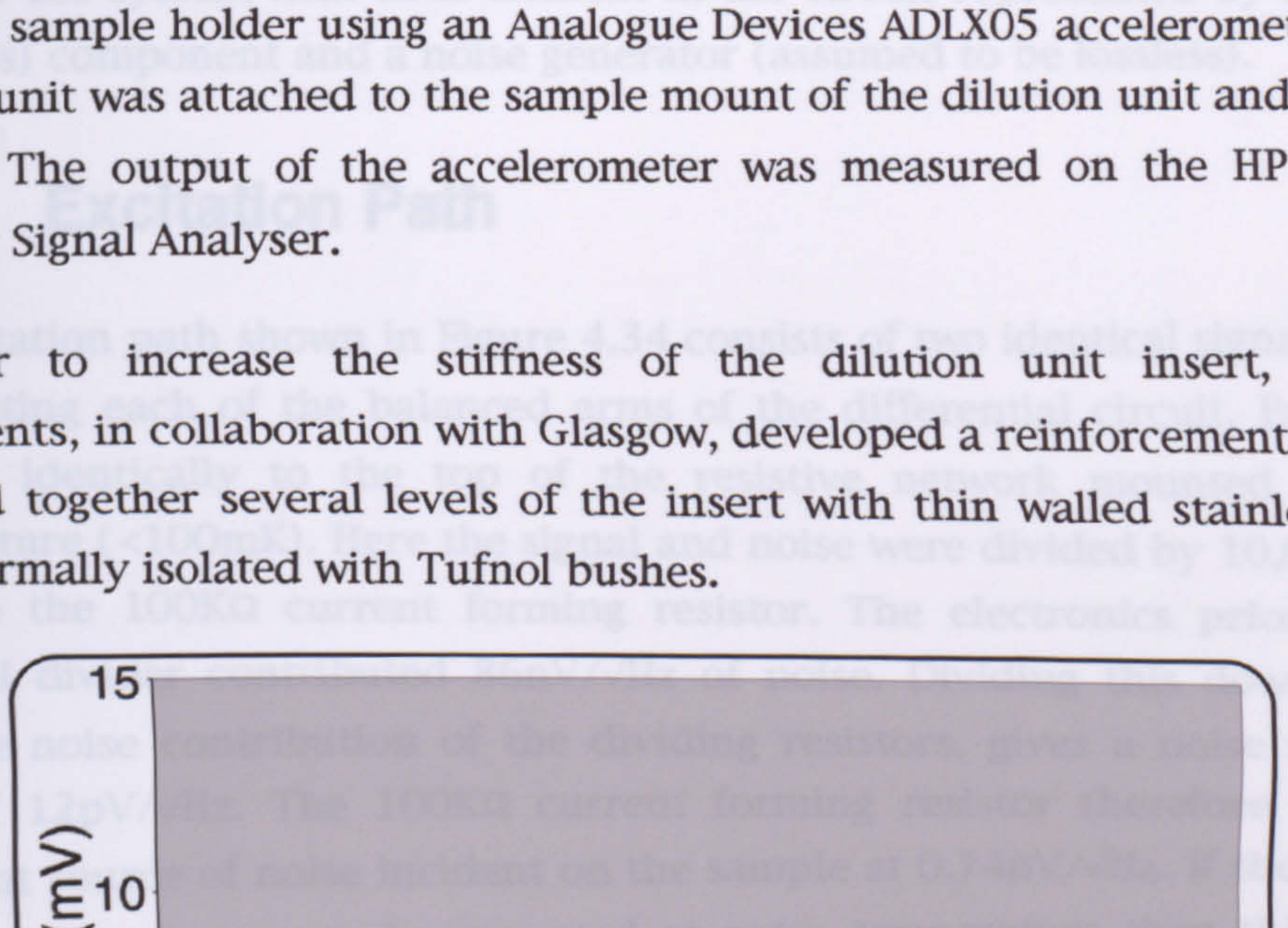

Figure 4.33 With the inclusion of the supporting structure the amplitude at resonance has halved whilst the frequency has risen to 11Hz.

Figure 4.33 shows the mechanical resonant frequency of the insert after the reinforcement scheme was fitted, measured with the same displacement force as the measurement in Figure 4.32. As can be seen the amplitude has reduced by approximately 50% but just as importantly the resonant frequency has increased to around 11Hz. This increase in the natural resonant frequency co-incides with the frequency range over which the vibration isolators exhibits a factor of 2 improvement in performance and hence the total contribution of vibration to the excess noise was substantially reduced.

4.6 Noise Analysis of Signal Paths

In this section the details of the electronics within the measurement system, seen in the previous section, are analysed and the contribution to noise, as seen by the sample, determined. Figure 4.34 shows a detailed noise equivalent circuit of the system with each element in the circuit represented by an ideal (noiseless) component and a noise generator (assumed to be lossless).

4.6.1 Excitation Path

The excitation path shown in Figure 4.34 consists of two identical signal paths, representing each of the balanced arms of the differential circuit. Each arm was fed identically to the top of the resistive network mounted at base temperature (<100mK). Here the signal and noise were divided by 10,000, and fed into the 100KΩ current forming resistor. The electronics prior to the potential divider contributed 86nV/√Hz of noise. Dividing this down, along with the noise contribution of the dividing resistors, gives a noise for both arms of 12pV/√Hz. The 100KΩ current forming resistor therefore was the dominant source of noise incident on the sample at 0.74nV/√Hz. If the passive resistor network were to be mounted at room temperature then this figure would rise to 40nV/√Hz.

In order to estimate an effective temperature the sample saw, it is necessary for a bandwidth to be included. The filters within the excitation path, outside the screened room, had a well-defined bandwidth of 200Hz. After this there was no deliberate bandwidth limiting, however cable capacitance and stray capacitance will have tended to limit the available bandwidth. Typical cable capacitances are between 100-200pF/M[16] with nominal cable lengths in this system of ≈2m. Cables terminated into a minimum resistance of 51Ω, included at the output of all sub-circuits. This leads to an upper cut-off frequency of ≈15MHz. For the purposes of calculation, a bandwidth of 10MHz has been

chosen. The inclusion of an appropriate bandwidth leads to a total noise voltage after the potential divider of 38nV. The noise voltage incident on the sample due to the 100KΩ current forming resistor at 100mK in a bandwidth of 10MHz is 2.3μV. This shows that even with the inclusion of the bandwidth the dominant noise is that associated with the current forming resistor at 100mK. The noise voltage of 2.3μV may be expressed as an energy by multiplying by the electron charge (e) which gives $3.7\text{x}10^{-25}$J and then as a temperature by dividing by Boltzman's constant (k); E_T=eV/k. The noise voltage expressed as a temperature therefore becomes 27mK. Again if the cold resistor network were mounted at room temperature this would result in an effective temperature of 470mK.

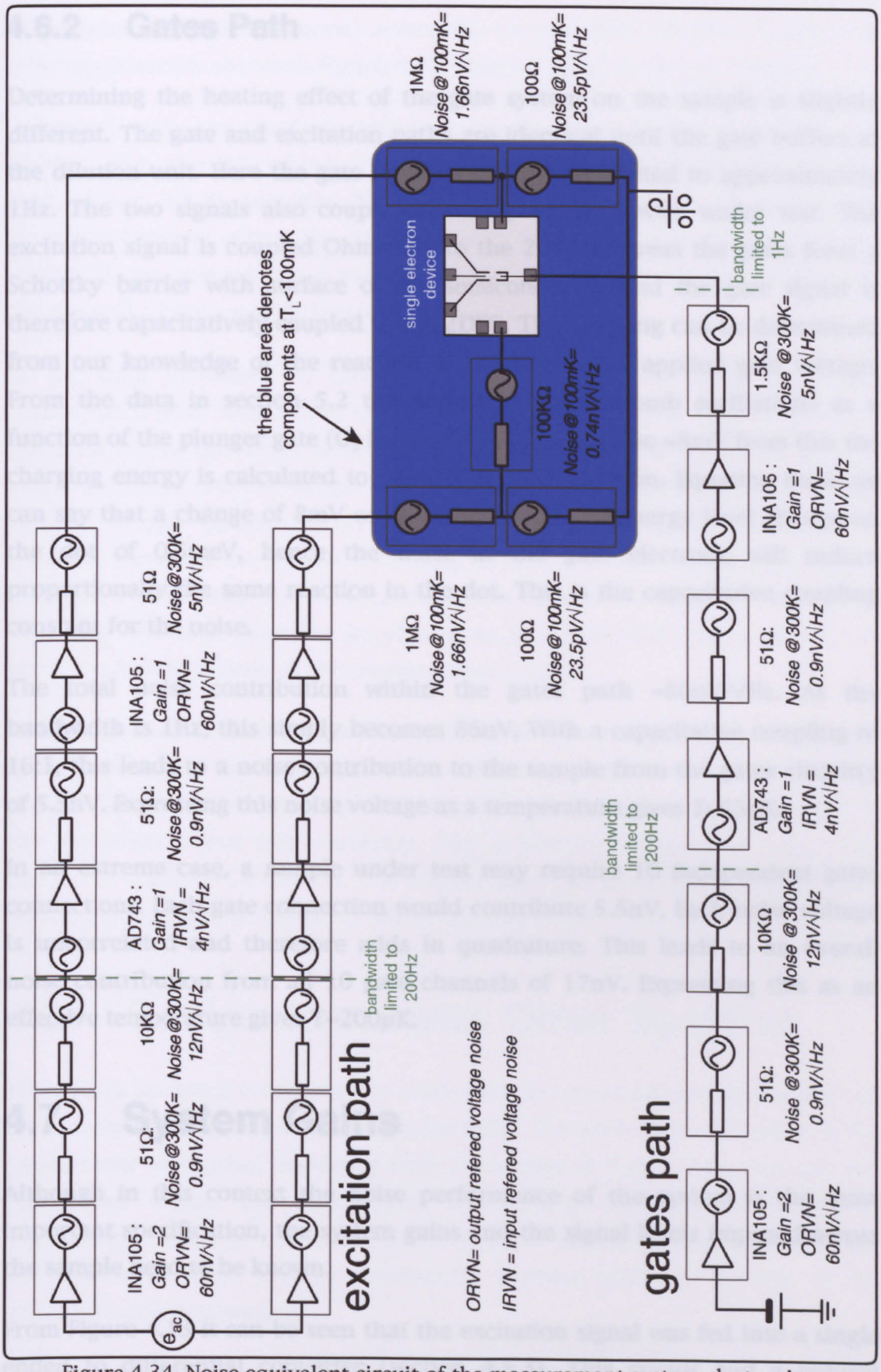

Figure 4.34. Noise equivalent circuit of the measurement system electronics.

4.6.2 Gates Path

Determining the heating effect of the gate system on the sample is slightly different. The gate and excitation paths are identical until the gate buffers at the dilution unit. Here the gate signal is bandwidth limited to approximately 1Hz. The two signals also couple differently to the device under test. The excitation signal is coupled Ohmically to the 2DEG whereas the gates form a Schottky barrier with surface of the semiconductor and the gate signal is therefore capacitatively coupled to the 2DEG. The coupling can be determined from our knowledge of the reaction of the dot to the applied gate voltage. From the data in section 5.2 the period of the Coulomb oscillations as a function of the plunger gate (G_5 Figure 5.1) was seen to be ≈8mV from this the charging energy is calculated to be ≈0.5meV per electron. Equating these we can say that a change of 8mV on the gates causes an energy level change on the dot of 0.5meV, hence the noise at the gate electrode will induce proportionally the same reaction in the dot. This is the capacitative coupling constant for the noise.

The total noise contribution within the gates path =86nV/√Hz. As the bandwidth is 1Hz, this simply becomes 86nV. With a capacitative coupling of 16:1, this leads to a noise contribution to the sample from the gates circuitry of 5.5nV. Expressing this noise voltage as a temperature gives T=65μK.

In an extreme case, a sample under test may require 10 independent gates connections. Each gate connection would contribute 5.5nV. Each noise voltage is uncorrelated and therefore adds in quadrature. This leads to an overall noise contribution from all 10 gate channels of 17nV. Expressing this as an effective temperature gives T=200μK.

4.7 System Gains

Although in this context the noise performance of the system is the most important specification, the system gains and the signal levels imposed across the sample need to be known.

From Figure 4.13 it can be seen that the excitation signal was fed into a single ended to differential converter (section 4.5.3). This circuit had a natural minimum gain of 2 as the signal was converted from +V to ±V. The screen room filters (section 4.5.5) and the excitation buffers (section 4.5.7) both had unity gain, as the signals entered and existed in differential mode. The

differential signal was imposed across the two potential divider networks at base temperature, shown in Figure 4.23, where it was divided by 10,000.

A typical excitation level as indicated on the front of the oscillator, was 100mV. After the gain of two from the single ended to differential converter (See section 4.5.3) and the division of 10^4, a signal level of $\pm 10\mu V$ was therefore imposed across the series network comprising the current forming resistor R_{cf} and the sample. A maximum current of 200pA was applied through the network at zero sample impedance.

In the data presented in chapter 5 the quantum dot exhibited typical conductance peak magnitudes of $0.3e^2/h \approx 90K\Omega$. This data was taken with a potential across the series network of $\pm 16\mu V$ which led to a current through and a voltage across the sample of 172pA and $15.5\mu V$ respectively. A voltage level of $15.5\mu V$ equates to an induced electron heating of ≈180mK. This potential exceeded the optimal operating level as it heated the electrons above the lattice temperature. It was, however, low enough for physics experiments to proceed on large quantum dot structures, as reported in chapter 5 and was not a fundamental limit of the measurement system.

The temperature stability specifications for all the op-amps used within the system was good. The maximum offset voltage variation with temperature for any of the amplifiers used is $5\mu V/^0C$ (INA105; this figure includes the effects of the amplifiers input bias currents). The maximum variation of input bias current is $0.25nA/^0C$ (AD743). The INA105 also quotes a figure for gain error versus temperature of $1ppm/^0C$, which equates to $1\mu V$ error in 1V per ^0C.

4.8 Comparisons with Other Systems

Within this section a comparison is made with the measurement systems of two other outstanding groups working in the field. The semiconductor group in the Department of Applied Physics at Delft University of Technology, Holland and the group within the Department of Physics, Chalmers University of Technology, Sweden. Both of these groups use in-house custom built electronics, as there are no commercial systems available capable of the required noise performance.

The measurement system at T.U. Delft has produced many of the most significant results in mesoscopic physics. It is a sophisticated custom design that features the extensive use of optically coupled linear isolators and the constant current source.

The isolation amplifiers used are the Burr-Brown ISO100. Opto-isolators often suffer from serious non-linearity over the input range of the device. The IS100 avoids this by the use of a matched pair of photodiodes, one in the output and one in the input circuitry. The photodiode in the input circuit receives light from the LED in a feedback arrangement that cancels the non-linearities in both the LED and photodiode. The sample is measured differentially with an Analog Devices AD624 precision instrumentation amplifier. The inputs of the amplifier can be switched to allow the use of Burr-Brown OPA111 op-amps as input buffers. These are FET input op-amps using Burr-Brown's DiFET technology (see section 4.5.1) and are presumably for use with high impedance source such as quantum dot devices.

Many of the design considerations within this chapter have obviously been addressed within the Delft system. Much attention has been given to signal referencing and grounding. Shielded twisted pair cabling is used extensively. One important area in which the design presented in this chapter has superior specification is the stability with temperature variation with the gates path. The ISO100 have a specified gain error versus temperature of 0.03%/^{0}C. A typical gate voltage magnitude of 1V therefore leads to an error of 3mV/^{0}C. Devices measured on this system have been seen to exhibit Coulomb oscillations of periods, in gate voltage, of 3.6mV[17]. A temperature variation of $\approx$1^{0}C would therefore cause a change in the number of electrons on the dot by 1. Bandwidth limiting is achieved by the IS0100s which have a bandwidth of 60KHz and cryogenic copper powder filters.

In the measurement system of Chalmers University, a schematic of which is shown in Figure 4.35 two bias resistors R_b form a current divider network with respect to IA1 and IA2.

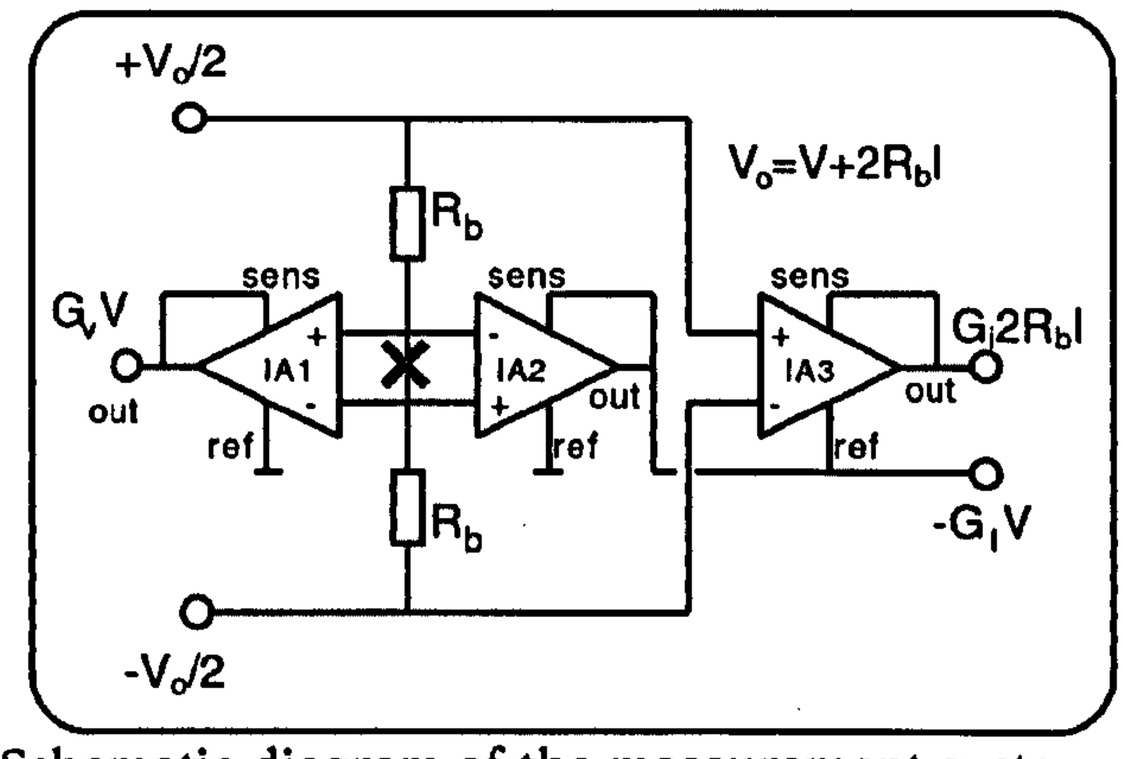

Figure 4.35 Schematic diagram of the measurement system designed and used by Chalmers University [18].

As R_b is selected to be large enough to act as an effective constant current source it is the current (not voltage) noise from these resistors that is significant. Maximum power transfer occurs when there is an impedance match between the source and receiver. Here the impedances are deliberately mismatched by a factor of 90%, $R_b \approx 10$ times greater than the maximum sample impedance. Hence, only 10% of the total thermal power of a matched system is available to couple into the sample. The contribution to voltage noise due to the current noise of IA3 is given by $(i_n R_s)^{1/2}$ where R_s is the resistance of the sample and the bias resistors R_b and in is the current noise spectral density of the input amplifiers of IA3. The input of IA3 are OPA111s and have an input current noise spectral density at 3Hz of 0.4fA/$\sqrt{Hz}$. This leads to a noise voltage of 800nV/$\sqrt{Hz}$. The biasing network ensures that the sample sees only $\approx$10% of this = 80nV/$\sqrt{Hz}$. The input voltage noise of the OPA111 is 60nV/$\sqrt{Hz}$ leading to an total voltage noise of $e_{T3}=((80nV/\sqrt{Hz})^2+(60nV/\sqrt{Hz})^2)^{1/2}=$ 100nV/$\sqrt{Hz}$. This compares with a figure of 0.74nV/$\sqrt{Hz}$, calculated in section 4.6.1, for the system presented here, a difference of $\approx$3 orders of magnitude. For IA1 and IA2 the source resistance R_s is that of the sample $\approx$30MΩ. The current noise of the amplifier contributes a voltage noise of $(i_n R_s)$=12nV/$\sqrt{Hz}$. The total noise voltage e_{T12} is therefore the addition in quadrature of the voltage noise e_n and the contribution of the current noise $i_n R_s$, therefore e_{T12}=61nV/$\sqrt{Hz}$.

The dilution refrigerators associated with both of the institutions described above are much more powerful than was available in Glasgow. The primary measurement systems at both institutions are capable of sub 10mK performance with cooling powers at 100mK of in excess of 30mW. This compares with a cooling power of the Kelvinox 25 of 20μW at 100mK.

4.9 Summary

At the start of this work single electron, devices were being measured at a lattice temperature of 1.2K as this high temperature experimental arrangement offered a substantial reduction in electron temperature, induced by noise, over the dilution unit. The estimated electron temperature of the dilution unit prior to improvement >7K[2]. Following construction of the system described here, the temperature dependent data, presented in chapter 5, suggests that the effective electron temperature was of the order of 250mK. As the excitation level induced an electron heating of $\approx$180mK, subtracting these numbers in quadrature leaves an excess electron heating of $\approx$170mK unaccounted for. An electron temperature of the order of 250mK was low enough for well-defined

single particle states to exist in a quantum dot of lithographic diameter 500nm, as presented in the results of chapter 5.

Initial noise measurements of the system identified a number of problem areas that needed to be addressed in order to improve measurement performance. A systems approach was adopted with respect to the electrical signals to and from the sample i.e., the various subsystems were designed to work together, particularly with respect to grounding and signal referencing.

Painstaking attention to detail in the design and construction of the new measurement system has resulted in a 20 fold improvement in resolution.

Since the completion of the system, it has been used extensively, particularly as an integral part of the research into strained layer superlattices. It has proved to be a highly accurate and precise measurement tool, without which the results presented in chapter 5 and the recent publications[19] as well as future proposed work would not be possible.

This system has been completely optimised throughout to reduce excess heating effects from external noise sources and hence allow genuinely low temperature measurements of single electron samples. The novelty of this system arises from the extent to which the various elements of low noise design have been incorporated. The extensive use of twisted pair cabling, balanced input electronics and the care taken in the choice of components is understood by the author to be unique. Placement of the so many passive components at base temperature is novel, other measurement systems have, at best, located the current measuring resistor below room temperature.

4.10 References

(1) D. Vion, P.F. Orfila, P. Joyez *et al.*, "Miniature Electrical Filters For Single Electron Devices" pre-print (1994).

(2) Personal Communication, M. Rahman, "Electron Temperature of Dilution Refrigerator" (1995).

(3) P. J. Fish, "Electronic Noise And Low Noise Design" (Macmillan, 1993).

(4) Internal Report, J. M. R. Weaver, "Grounding Breaking Circuits" (1995).

(5) A. Rich, "Shielding and Guarding. How to Exclude Interference-type Noise What To Do and Why to Do It." Analog Devices Application Notes 1 (20), 85-90 (1984).

(6) P. J. Clayton, "Introduction to Electromagnetic Compatibility" (John Wiley & Sons, Inc., 1992).

(7) L. Smith and D. H. Sheingold, "Noise and Operational Amplifiers" Analog Dialogue 3 (1) (1969).

(8) P. Horowitz and W. Hill, "The Art Of Electronics" 2nd ed. (Cambridge University Press, 1989).

(9) S. Franco, "Design with Operational Ampliiers and Analog Intergrated Circuits" (McGraw-Hill Book Co., Singapore, 1988).

(10) Burr-Brown, "INA 105 Precision Unity Gain Difference Amplifier" (1985).

(11) Analog Devices, "AD743 Ultralow Noise High Speed BiFET Op-Amp" .

(12) Burr-Brown, "OPA637 Precision High-Speed Difet Operational Amplifier" (1989).

(13) Goodfellow, "Goodfellow Catalogue" (Cambridge, 1997).

(14) R. B. Schulz, V. C. Plantz, and D. R. Brush, "Shielding Theory and Practice" IEEE Transactions on Electromagnetic Compatibilty 30 (3), 187-201 (1988).

(15) Newport Corporation, "Stabilizer Vibration Isolators" in The 1994 Newport Catalog (1994), pp. 16.34-16.41.

(16) A. Rich, "Understanding Interference-Type Noise. How to Deal with Noise Without Black Magic" Analog Devices Application Notes 1 (20), 81-84 (1984).

(17) Thesis, L. P. Kouwenhoven, "Transport of Electron-Waves and Single-Charges in Semiconductor Nanostructures" , Delft University Of Technology, 1992.

(18) Thesis, Pers Delsing, "Single Electron Tunnelling in Ultrasmall Tunnel Junctions" , Chalmers University of Technology, 1990.

(19) B. Milton, C. J. Emeleus, K. A. Lister *et al.*, "Modulation of Landau levels by a one-dimensional periodic potential" Physica E (To Be Published).

5 EFFECTIVE ELECTRON TEMPERATURE AND MAGNETIC SPECTROMETRY OF A QUANTUM DOT

The performance of the measurement system described in the last chapter is investigated using a large quantum dot structure. Analysis of conductance peak line width as a function of temperature allows a determination of the effective electron temperature.

Results of experiments on the probing of energy states within a quantum dot using a novel magnetic spectrometer are reported. Electron focusing techniques are used to allow the measurement of the single particle states within an elastic scattering length of the quantum dot.

5.1 Introduction

A micrograph of one of the devices studied is shown in Figure 5.1. The device was fabricated on an in-house grown GaAs-Al_x $Ga_{1-x}As$ heterostructure with a 2DEG 90nm below the surface. The 2DEG had a mobility of $1.5x10^6 cm^2V^{-1}s^{-1}$ at 4.2K[1]. The quantum dot was defined by split gates[2] and formed in region R_2 by applying a negative bias with respect to the 2DEG to gates G_1 and G_4-G_6. Probe C_1 was defined as the high current side I_{high} and probe C_4 the low current I_{low}. Applying a potential between gates G_1, G_4 and G_1, G_6 with respect to the 2DEG formed the entrance and exit point contacts respectively. Gate G_5 acted as a plunger gate and was used to vary the size of the dot.

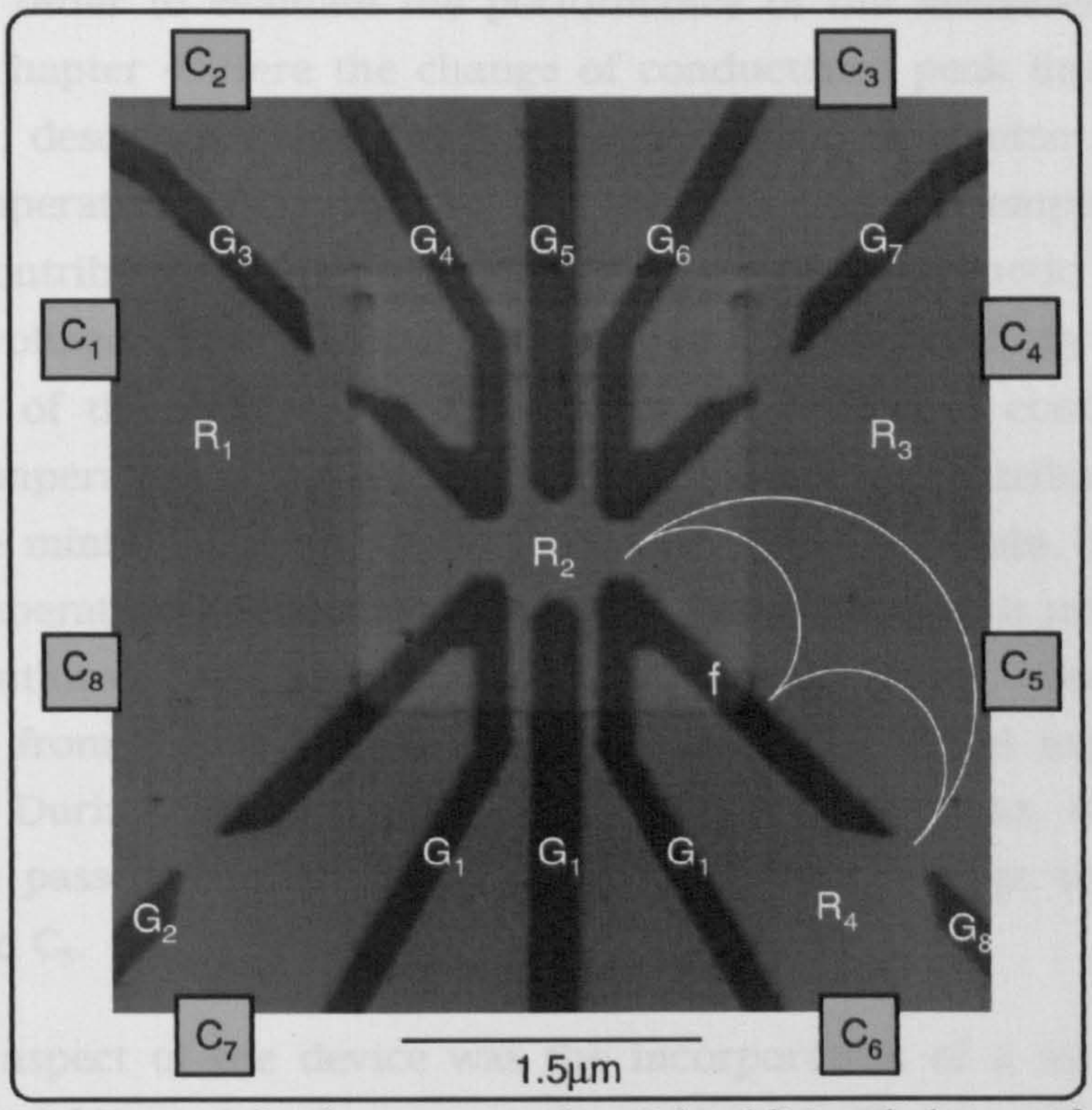

Figure 5.1 Micrograph of a quantum dot with additional electron focusing facility. Probes C_1-C_8 form Ohmic contacts to the 2DEG. G_1-G_8 are surface gates and R_1-R_4 different regions of 2DEG referred to in the text.

When the entrance and exit point contacts were biased in the strong tunnelling regime the plunger gate, G5, was swept to induce the periodic conductance oscillations seen in Figure 5.7

In addition to the bias applied to the gates that formed the dot, a bias was also applied to G_8. This gave rise to a quantum point contact external to the dot. In the tunnelling regime regions R_3 and R_4 were connected via this tuneable

barrier. The element at f was used as the focusing boundary and was fabricated as part of the exit point contact structure. Electrons leaving the dot from R_2 into R_3 were specularly reflected along f and into R_4 when an appropriate magnetic field was applied. The configuration for measurement of the differential focusing signal was such that current was passed through C_1 and C_4 whilst voltage was measured across C_5 and C_6.

Three other boundaries similar to f can be seen around the dot. This allowed for both redundancy, in case of gate failure, and the probing of a substantial area of the environment around the dot with the selection of the appropriate current, voltage and magnetic field combinations.

A similar device to that shown in Figure 5.1 was used for two purposes.

i) Conductance measurements were performed on the large quantum dot structure in order to evaluate the performance of the measurement system detailed in chapter 4. Here the change of conductance peak line shape with temperature, described in section 5.3.1, was used to determine the effective electron temperature of the device. The effective electron temperature arose from the contributions from thermal energy, electromagnetic energy and excitation voltage. The thermal energy was determined by the lattice temperature of the substrate and, assuming good thermal contact, was the operating temperature of the dilution unit. With no other contributing sources, this was the minimum temperature the electrons could attain. The effective electron temperature however, was normally raised above this minimum limit by contributions from excess energies arising from electromagnetic interference from the environment and the excitation signal imposed across the sample. During measurements of the conductance peaks, the excitation current was passed through probe C_1 and C_4 whilst voltage was measured across C_8 and C_5.

ii) Another aspect of the device was the incorporation of a novel magnetic spectrometer fabricated in close proximity to the dot. Electrons leaving the dot were deflected due to an applied magnetic field and reflected at the boundary seen at f in Figure 5.1. When the distance between focusing point contacts was a multiple of the cyclotron diameter more electrons entered the region R_4 due to the focusing effect of the magnetic field. This raised the potential within R_4 relative to R_3. A measurement of a peak in the voltage V_{34} corresponds to a determination of the cyclotron diameter and hence the electron energy and is directly analogous to a mass spectrometer. This arrangement therefore allowed a measurement of the energy of electrons leaving the dot before scattering.

The behaviour of the magnetic spectrometer will be detailed more fully in section 5.4.1.

5.2 Determination of Device Properties

Several characteristic properties and energies of the device are determined within this section. These characteristics set the energy scales for the device and allow the data to be quantified.

The single particle spacing is an important characteristic energy as it provides information about the quantum mechanical state of electrons within the quantum dot. In order to observe the energy separation associated with the quantum mechanical states within a quantum dot, this energy must be of the same order or greater than the other energies associated with noise within the system. The thermal energy, kT, at typical dilution refrigeration temperatures of ≈100mK is ≈9μeV. A largish quantum dot typically has a charging energy of approximately an order of magnitude greater than the energy separation, which is in turn 3 times greater than kT. In this case the energy separation would not be large enough to observe fine structure or for detailed line shape analysis to be carried out. The energy separation is approximately proportional to $1/r^2$, where r is the dot radius, and hence a reduction of 2 in the dot radius leads to a four fold increase in energy separation. It is therefore advantageous to fabricate smaller devices in order to see the effects of the single particle states of the electrons.

5.2.1 Energy Level Quantisation

Conventionally the single particle energy separation is incorporated into the standard Coulomb blockade model, described in section 2.4.1 by assuming that the quantum dot energy is fully described by the sum of the Coulomb charging terms, from the classical Coulomb blockade model, plus the energies associated with a discrete set of quantum levels, shown in Eqn. 5.1.

Eqn. 5.1
$$E_n = \frac{(Ne)^2}{2C} - eV_gC_g + \sum^{N} \varepsilon_i$$

where ε_i represents the energy of the ith eigenstate relative to the Fermi energy in the dot, and the summation is over the set of occupied states[3].

The incorporation of the single particle spectrum into the classical Coulomb blockade model theory gives a simple and elegant model. Whilst the classical

model is clearly and rigorously defined, the excitation model relies on at least one assumption that needs consideration. In the classical case, when the dot contains in the order of 100's of electrons the addition or subtraction of an electron causes only a minor perturbation on the interaction of the electrons within the dot. In small dots, where there are far fewer electrons these interactions cannot be ignored. Indeed, it is reasonable to expect that the addition or subtraction of an electron will generate a completely new single particle spectrum[4]. The assumption that the single particle spectrum is independent of the number of electrons is clearly wrong[3]. The nature of this correlation is still an open issue, and will be discussed further in section 5.2.2

5.2.2 Estimation Of The Single Particle Spacing

The energy necessary to add an extra electron to the dot is, in general, the sum of a number of different energies. The charging energy is usually dominant in these devices but for small devices at low temperature the single particle and spin interaction energy can play a significant rôle.

The accurate estimation of single particle spacing is a difficult problem because of the different energies involved and their mutual interaction. The addition (or subtraction) of an electron to the dot results in not only an energy increase of e^2/C but may also change the shape of the confining potential, the screening effect between electrons and the tunnelling probability for electrons entering and leaving the dot[4,5].

Normally the single particle spacing would be determined experimentally by applying a dc bias across the sample. A large source drain bias (V_{ds}) is applied to the device such that $\Delta\varepsilon_i < eV_{ds}$. Where $\Delta\varepsilon_i$ is the energy separation between discrete levels. As V_{ds} is increased more levels in the dot exist between the Fermi level in the left reservoir and that in the right. Coulomb blockade peaks split from the classical single peak, $eV_{ds} < \Delta\varepsilon_i$, into double, $\Delta\varepsilon_i < eV_{ds} < \Delta 2\varepsilon_i$, and triple peaks, $\Delta 2\varepsilon_i < eV_{ds} < \Delta 3\varepsilon_i$. In this way, the spacing between single particle energies can be investigated.

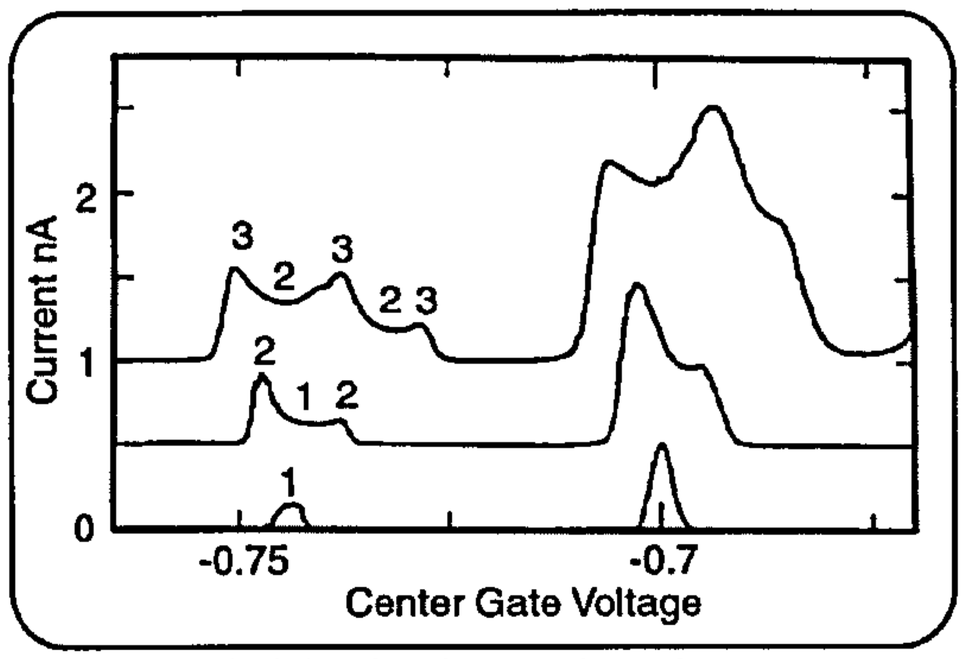

Figure 5.2 A single Coulomb blockade peak splits up in multiple peaks as dc bias is increased and extra tunnelling states contribute to the current[4].

Figure 5.2 shows the differential conductance ($G \equiv dI/dV_{ds}$) as a function of the source-drain bias. Here a single blockade peak can be seen to split into multiple peaks as the dc bias is increased. This can be understood in terms of the model shown in Figure 5.3. In this picture V_{ds} has opened up a "window" of transport between μ_l and μ_r, which in this case is $\Delta\varepsilon_i < eV_{ds} < \Delta 2\varepsilon_i$.

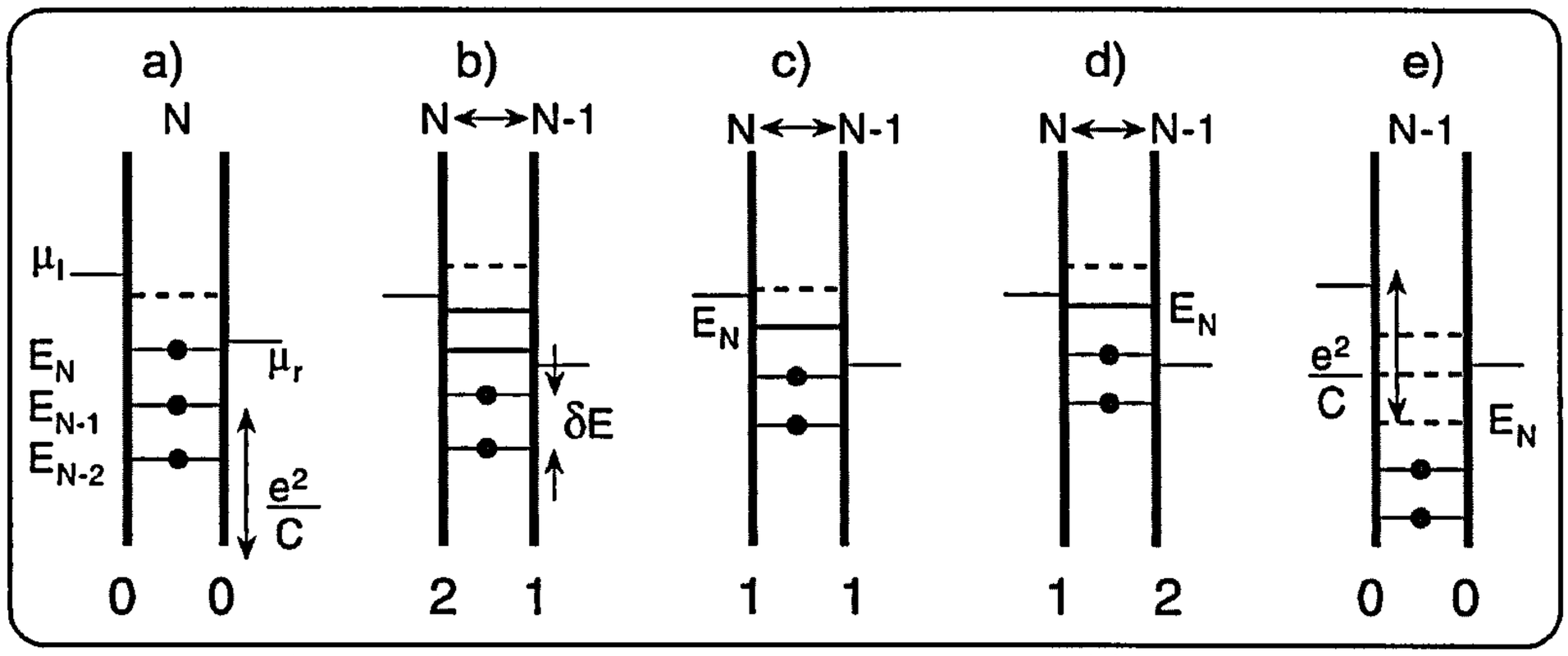

Figure 5.3 The non linear transport regime is accessed by applying a dc bias voltage across the device. This increases the states that contribute to the tunnelling current through the device.

As the blockade condition is lifted, this window spans a different number of possible tunnelling states within the dot. This varies between 0,1 and 2. As can be seen from the diagram the sequence of available tunnelling states follows the pattern 0-2-1-2-0. The more available tunnelling exists within the window, the larger the current. In this way, the observed negative differential conductance (lowering of conductance for increased gate voltage) is explained[5-7].

During the experimental work described in this thesis the instrumentation was not configured to allow a dc bias measurement of the dot. This, therefore, did not allow the single particle energies to be investigated as described above. As a result, the remainder of this section is concerned with estimations of the energy spacing between single particle states. In order for the single particle

energy spacing to be estimated, the number of electrons on the dot must be approximated.

Two methods for the estimation of the single particle spacing are used. Firstly, a simple scaling of the 2D electron density in the 2DEG is made to the size of the dot. From this the average single particle spacing is estimated[4]. Secondly, experimental data is examined to determine the span in gate voltage over which the dot exhibited Coulomb blockade. From this, the number of electrons on the dot is approximated. A model, based on wavelength, is then employed to estimate the single particle energy spacing.

In order to scale the electron density in the wide 2DEG to the dot size, the electron density in the wide 2DEG needs to be determined. This can be extracted from Shubnikov de Haas data.

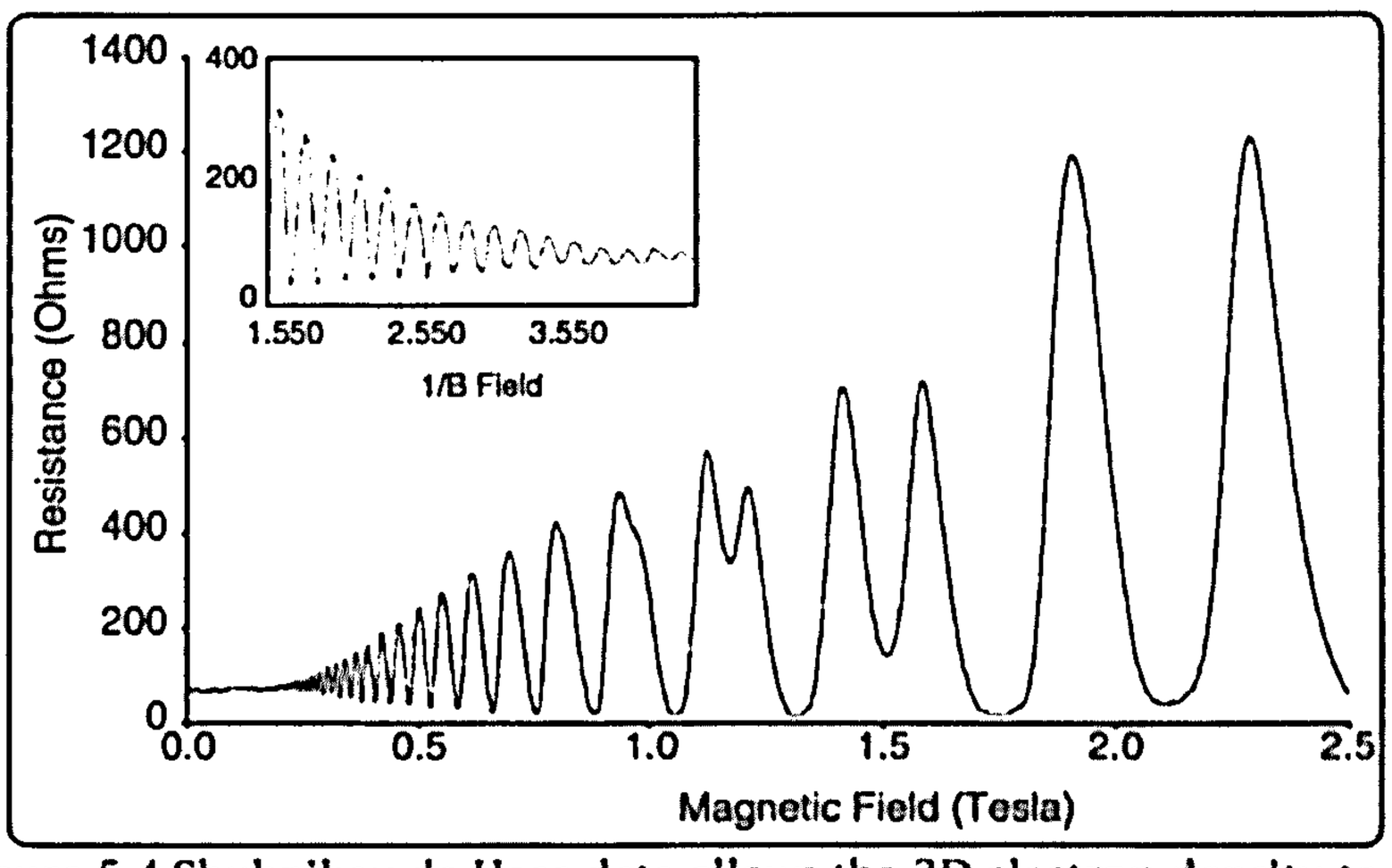

Figure 5.4 Shubnikov de Haas data allows the 2D electron density to be derived. Periodic oscillations in 1/B are related to the electron density through the flux quantum as described in section 2.5.

Figure 5.4 shows a Shubnikov de Haas trace taken at the beginning of the experiment, with the insert showing the 1/B trace. The electron density was extracted from this data using Eqn. 2.64; $n_{s2D}=2.66\times10^{15}m^{-2}$. This implied a Fermi energy of 9.5meV.

The electrostatic potential applied to the gates confined the electrons to a smaller area than the lithographic separation between the gates. Hence, for the device in Figure 5.1 the size of the dot (R_2) was taken to be 350nm which leads to a nominal area of $a=9.6\times10^{-14}m^2$. Using the 2D electron density $n_{s2D}=2.66\times10^{15}m^{-2}$ the number of electrons in the area a is $N\approx250$. This sets the upper limit on the number of electrons on the dot. The single particle spacing, ΔE, can then be scaled from the Fermi energy, with a correction for spin degeneracy, resulting in an energy spacing $\Delta E=2E_f/N \approx 75\mu eV$.

A major problem with this estimate is that it assumes that the dot extends to the same depth as the lead reservoirs, shown schematically in Figure 5.5 a). A more realistic potential is shown in Figure 5.5 b). Here the bottom of the well is raised by the electrostatic potential induced by the gates.

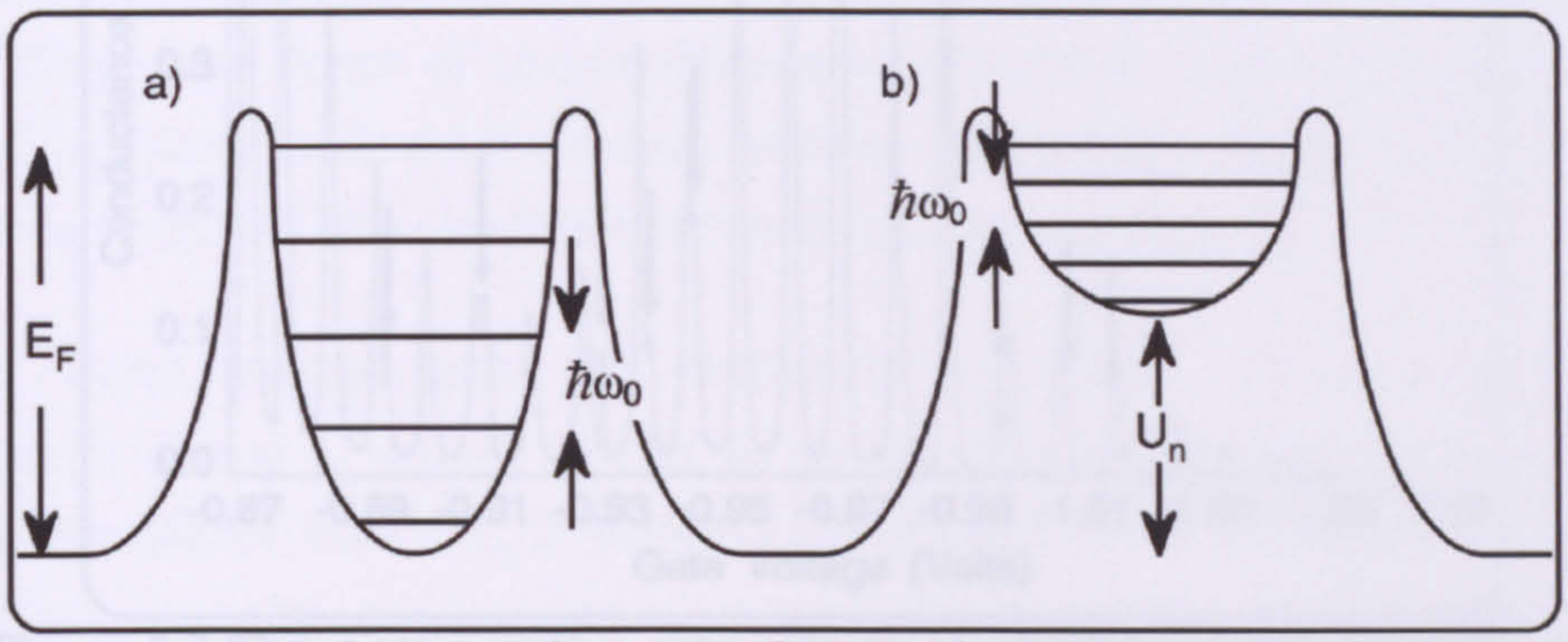

Figure 5.5 a) shows a schematic of a quantum dot with the confining potential extending from 0 to the Fermi energy E_F .in b) the bottom of the well is raised by the electrostatic potential and the well is much shallower.

A better estimate of the number of electrons on the dot than that obtained from the nominal dot size may be obtained from an examination of the experimental data. Figure 5.6 a) and b) shows the entrance and exit quantum point contacts as they approached cut off.

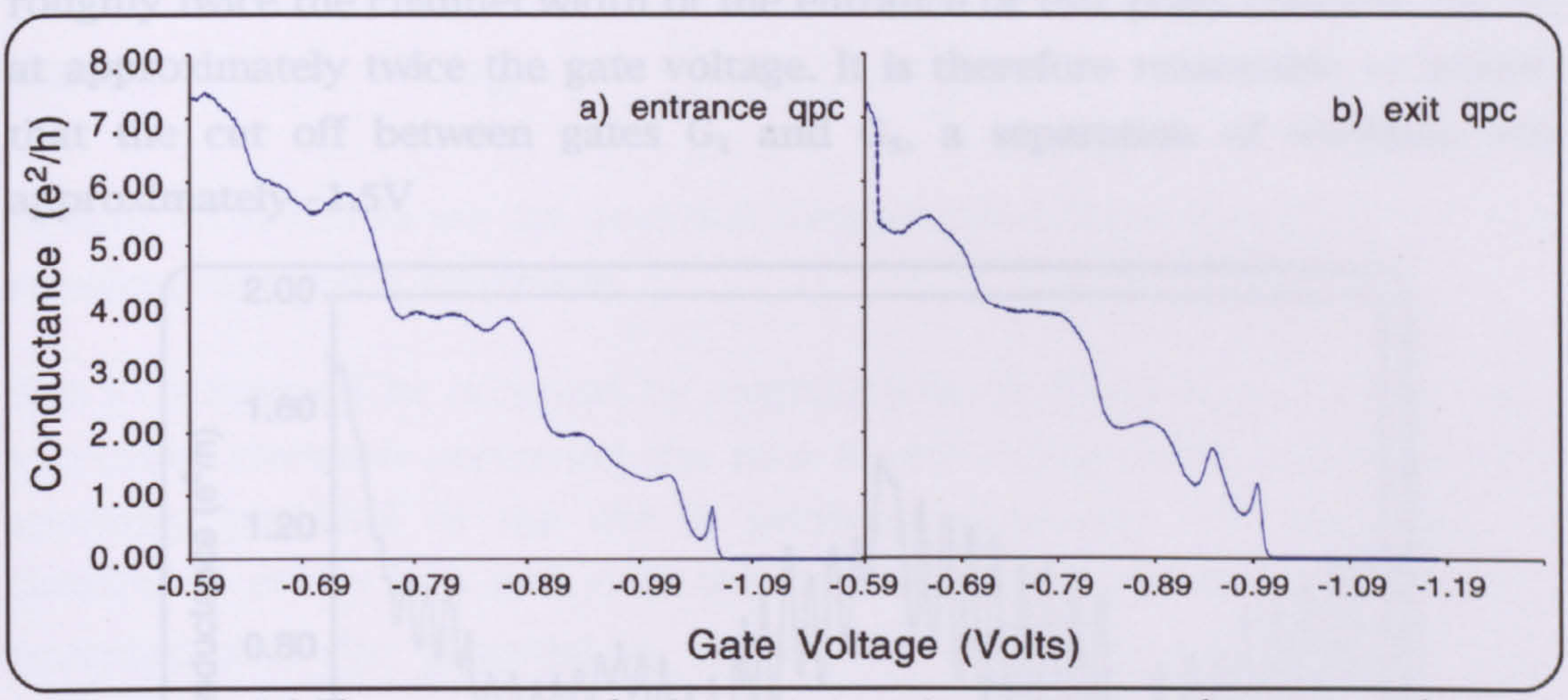

Figure 5.6 The entrance and exit quantum point contacts as they approach cut-off.

Both quantum point contacts cut off at approximately -1V. Figure 5.7 shows a trace of the Coulomb blockade where the final blockade peak prior to the device cutting off is seen at -1.055V. It is unlikely that this was the last electron in the dot, but rather represents the cut-off point of one of the quantum point contacts.

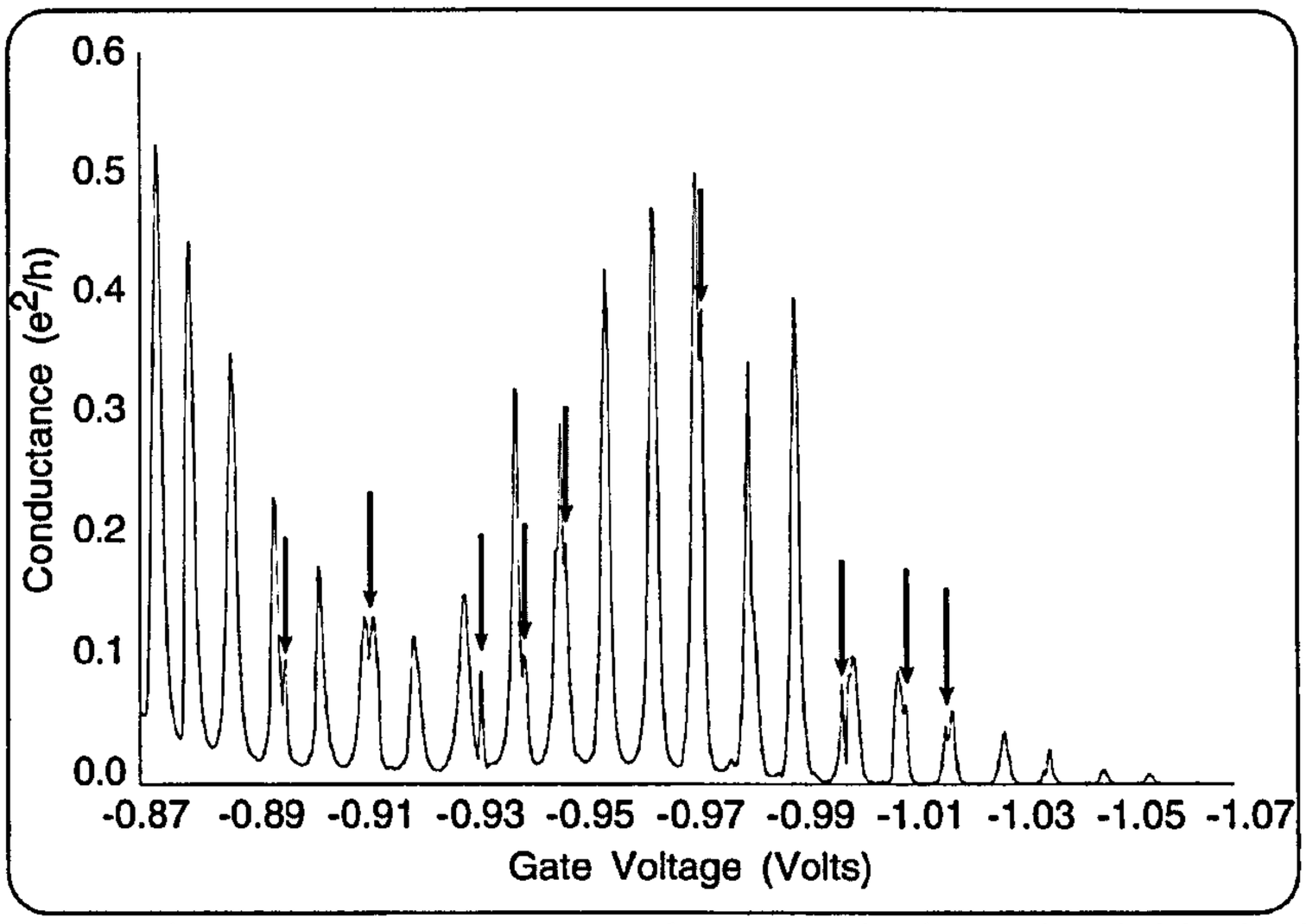

Figure 5.7 The most negative gate voltage at which Coulomb blockade is observed is just above -1.05 volts. The arrows indicate the effect of traps close to the dot charging and discharging.

The device measured differed from that shown in Figure 5.1 as the width of the focusing point contact into R_4 was ≈600nm, twice that of the entrance or exit quantum point contacts. Experimentally this focusing point contact was found to cut-off independently by -1.9V. The focusing point contact, at roughly twice the channel width of the entrance or exit point contacts, cut off at approximately twice the gate voltage. It is therefore reasonable to assume that the cut off between gates G_1 and G_5, a separation of ≈500nm, was approximately -1.5V

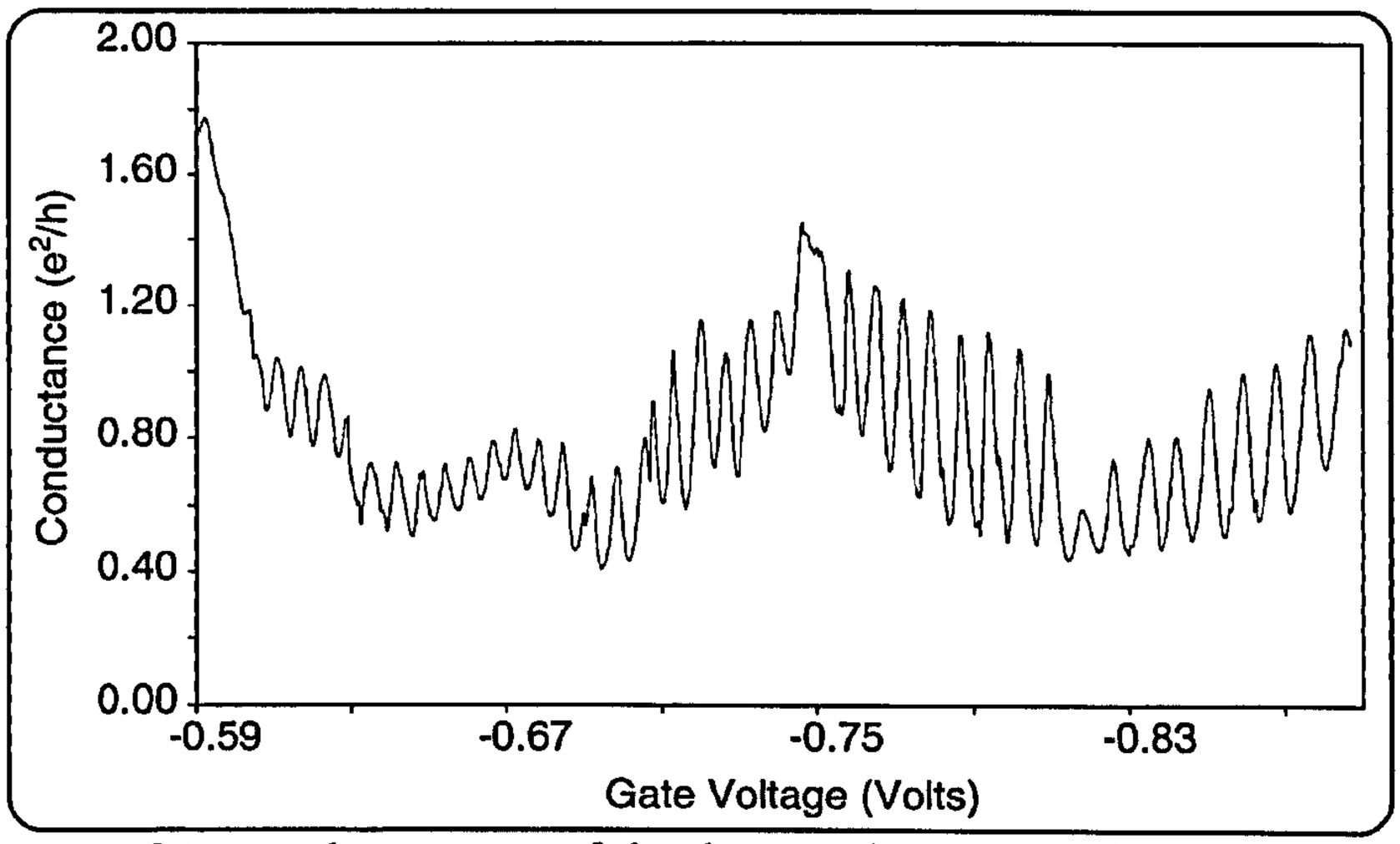

Figure 5.8 Gate voltage sweep of the dot. Conductance peaks are no longer visible below ≈-0.6V. This trace is not directly comparable to Figure 5.7 as the quantum point contacts are not biased identically.

Figure 5.8 shows that at below a gate voltage of -0.6V the conductance rises above e^2/h and the dot no longer exhibited Coulomb blockade. This gives a span in gate voltage over which the device exhibited single electron behaviour

of 0.9V. The period of the Coulomb oscillations = $\Delta V_g \approx 8mV$ as seen in Figure 5.7. Using these two limits, the number of electrons on the dot may be estimated to be 0.9V/8mV= 110.

The precise energy spectra of the single particle states will depend on the precise shape and form of the confinement potential. This is not known[8] as the random distribution of surface states and donor atoms gives rise to a random variation in the confinement potential of the dot.

To gain some insight into the evolution of single particle spacing with confinement shape a simple model is invoked. For each dimension electrons may occupy states every $\lambda_e/2$ where λ_e is the electron wavelength. Each $\lambda_e/2$ equates to a spin degenerate energy level. From the analysis of the experimental data, above, the number of electrons on the dot was approximated to be 110, which implies, roughly, 55 spin degenerate energy levels.

A two dimensional parabolic confinement is assumed with the energy of any level given by Eqn. 5.2. In the third dimension the electrons at the heterojunction interface are assumed to be confined to a single subband.

Eqn. 5.2
$$\varepsilon_{nm} = \left(n - \frac{1}{2}\right)\omega_x\hbar + \left(m - \frac{1}{2}\right)\omega_y\hbar$$

In Eqn. 5.2 n and m are the quantum numbers describing the number of half wavelengths in each dimension.

The 55 states will be occupied by combinations of electrons in x and y, with successive electrons occupying the next lowest energy state available. If the confining potential of the dot is perfectly symmetric the states will be distributed evenly in x and y. In this case ω_x and ω_y are equal. If the dot is squeezed and the potential is asymmetric the electrons with the same wavenumber in x and y will not have the same wavelength and hence energy.

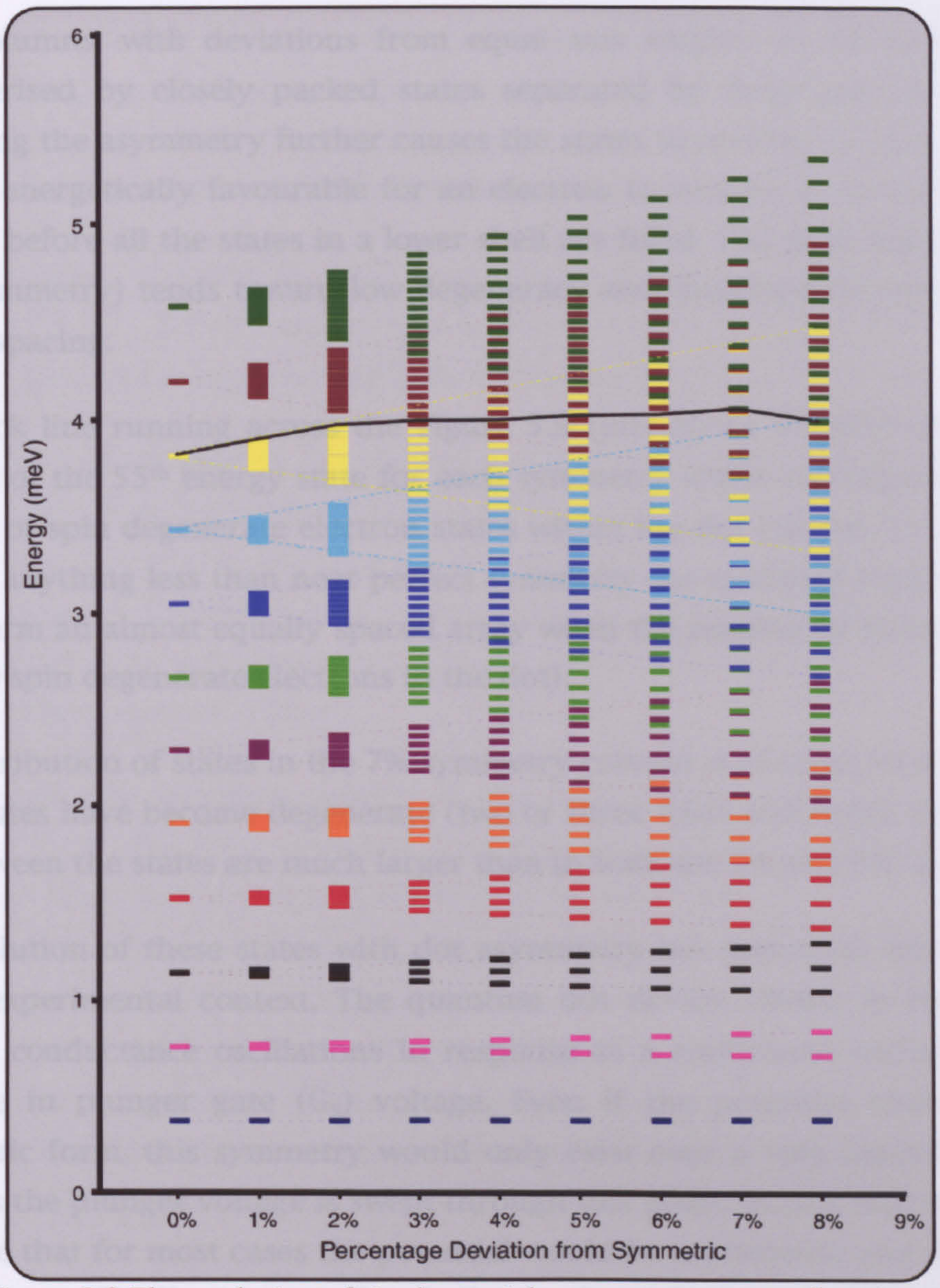

Figure 5.9 The evolution of single particle energy states as a function of quantum dot symmetry. Each subsequent column from the left represents an increase in the x-axis and decrease in the y-axis of 1%.

In Figure 5.9 the evolution of available energy states for this model is shown as a function of dot symmetry. The dot is nominally assumed to be 350nm x 350nm, and occupied by a maximum of 110 electrons. Column one (0%) represents the case where the potential is symmetric. The wavelength is the same for each wave-number in both x and y and hence ω_x and ω_y are equal. This leads to a high level of degeneracy as all the combinations of the quantum numbers n and m that represent a particular shell (n+m=x where x is an integer >2) results in the same value of ε_{nm}. Hence, the highest energy value of ε_{nm}, in column 1 (green marker), represents a 12 fold degenerate energy state. Each successive column in Figure 5.9 increases the length of the x-axis and decreases the length of the y-axis by 1%. As the dot is made increasingly asymmetric in this way the degeneracy of the states is lifted. The second and

third columns, with deviations from equal axis lengths of 1% and 2% are characterised by closely packed states separated by large gaps in energy. Increasing the asymmetry further causes the states to overlap. In these cases it may be energetically favourable for an electron to occupy an increased shell number before all the states in a lower shell are filled. The right hand column (8% asymmetry) tends toward low degeneracy and therefore an even, closely packed spacing.

The black line running across the Figure 5.9 (just above 3.5meV) marks the position of the 55^{th} energy state for each symmetry which corresponds to the number of spin degenerate electron states within the dot studied. It is evident that for anything less than near perfect symmetry the modelled single particle states form an almost equally spaced array when the number of states exceeds ≈ 20 (40 spin degenerate electrons in the dot).

The distribution of states in the 7% symmetry column is of some interest. Here some states have become degenerate (two or three fold) and hence the energy gap between the states are much larger than in both the 6% and 8% columns.

The evolution of these states with dot asymmetry has important implications in the experimental context. The quantum dot device, shown in Figure 5.1, exhibits conductance oscillations in response to a continuous increase in or decrease in plunger gate (G_5) voltage. Even if the potential could take a symmetric form, this symmetry would only exist over a very limited voltage range as the plunger voltage is swept through this point. In practical terms it is probable that for most cases the potential would be asymmetric and the single particle state distribution may be similar to the right hand column of Figure 5.9.

From Figure 5.9 it is possible to estimate a range of energies over which single particle states may be distributed. In column 1 (0%) for the symmetric case, the energy spacing between shells $\approx 350\mu$eV, however an asymmetric potential is more likely. The energy range of the most asymmetric case, seen in the column representing 8% asymmetry, is between 40-120μeV. The upper limit of 120μeV applies in the low electron regime, before the shells have started to overlap. More typically the range is $\approx$40-80μeV. These estimates are consistent with those reported elsewhere [9-11].

Equation Eqn. 5.2 used n and m as the quantum numbers that described the states. It is more conventional to solve this problem using polar co-ordinates, with the quantum numbers then being given by r,φ. This, however, would have an implied circular symmetry, which would be inappropriate for an

asymmetric dot. The context here is to set approximate limits on the energies that the single particle states can take and to gain insight into one of the factors that may effect the evolution of single particle states. As such the model presented here is considered sufficient.

More detailed theoretical work on shell filling has been performed elsewhere[12,13]. Recent experimental work has confirmed the shell like structure that quantum dots exhibit in the low electron limit[14].

The single particle spacing, an important characteristic energy of the device, was estimated. Two approximations were employed. Firstly, a simple scaling of the electron density to the size of the dot, yielding an energy spacing of 75μeV. Secondly the number of electrons in the dot was estimated from the experimental data and a model was used to place limits on the single particle spacing of between ≈40-100μeV.

An energetically accurate model of the single particle states and their evolution with changing potential is a complex problem. A more accurate model for the value of single particle spacing would require a self-consistent solution of Poisson's and Schrodinger's equation. Here the change in confining potential due to addition or subtraction of each electron would be taken into account as well as the electron-electron interaction. Since the precise form of the confinement potential of the dot was not known no attempt was made, in the model presented here, to incorporate a self-consistent compensation of the confinement potential due to the change in the number of electrons on the dot.

The numerical similarity between the two estimates is of interest as the two approaches are quite different. In the first, rather crude method, the depth of the confining potential was unrealistically large; twice the Fermi energy. However, scaling to the electron density in the reservoirs results in many more electrons in the dot than is reasonable. These two unrealistically large numbers cancel to give a quite reasonable value for the single particle spacing.

The more realistic approach takes some account of both the raising of the potential due to gate bias and the wavelike nature of the electrons in the dot. The single particle spacing predicted by this model is relatively insensitive to changes in the number of electrons within the dot. A ±10% change in electron (99-121 electrons) number results in a less than ±5% change in single particle spacing. Thus the original estimate of 110 electrons on the dot has some margin for error before significantly effecting the single particle spacing.

One aspect of the behaviour of the quantum dot device that caused a certain degree of trouble was its extreme sensitivity to telegraph noise. This may be expected as single electron devices are capable of astonishing charge resolution. This effect manifested itself in the data of Figure 5.7 as discontinuities within the conductance oscillations, and can be seen at the positions marked with arrows. This behaviour may be attributed to traps close to the dot charging and discharging. These traps may be on the surface of the wafer or impurities within the donor layer. When the trap has a net negative charge with respect to the dot, it acts as if an extra potential applied to the gate and hence shifts the peaks to a higher negative gate voltage. In an attempt to combat this problem multiple data sets were taken. In this way enough conductance peaks, unaffected by the behaviour of the traps, were analysed.

5.3 Temperature Dependence

In this section the performance of the measurement system, described in chapter 4, is assessed. As will be shown below the lineshape of the conductance oscillations exhibited by quantum dot devices in the Coulomb blockade regime is dependent on temperature. Analysis of the temperature dependent data allowed an estimation of the effective electron temperature and the total device capacitance to be made.

5.3.1 Coulomb Blockade Lineshape

The two regimes within Coulomb blockade can be distinguished by their effect on lineshape[4]:

1). classical blockade where $\Delta\varepsilon_i < kT < e^2/C$ in which many discrete quantum levels are excited.
2). quantum blockade where $kT < \Delta\varepsilon_i < e^2/C$, and transport is via one discrete quantum energy level.

In the classical blockade regime the line shape of an individual conductance peak is given by[3,4,15]

Eqn. 5.3
$$G = \frac{e^2}{2\Delta\varepsilon}\frac{\Gamma^l\Gamma^r}{\Gamma^l+\Gamma^r}\frac{\frac{\delta}{kT}}{\sinh\frac{\delta}{kT}} \approx \frac{e^2}{2\Delta\varepsilon}\frac{\Gamma^l\Gamma^r}{\Gamma^l+\Gamma^r}\cosh^{-2}\left(\frac{\delta}{2.5kT}\right)$$

where Γ^l and Γ^r are the tunnelling rates for the left and right barriers and

Eqn. 5.4
$$\delta = e\frac{C_g}{C}\left|V_{g(res)} - V_g\right|$$

This measures the distance of the centre of the peak in units of energy. $V_{g(res)}$ is the gate voltage at a conductance peak. The peak widths are linear with temperature, the maximum peak height, G_{max}, being temperature independent in this regime. Figure 5.10 shows the calculated temperature dependence of Coulomb oscillations in the classical blockade regime.

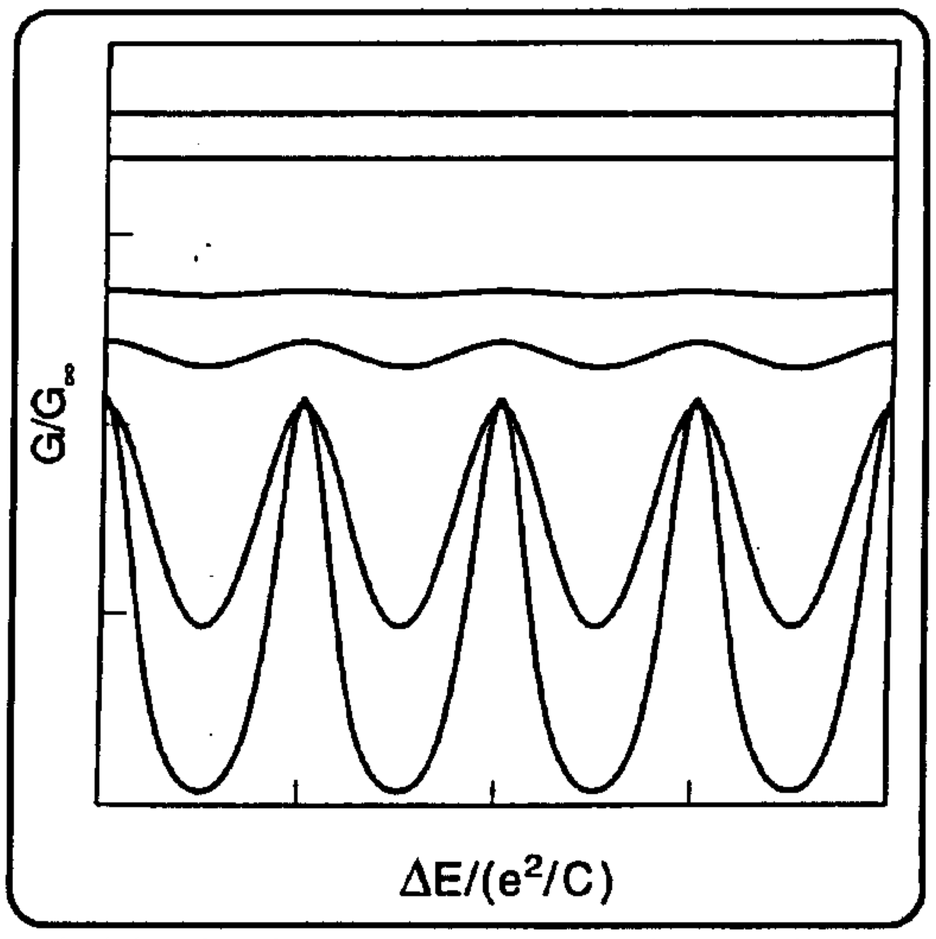

Figure 5.10 Coulomb blockade temperature dependence. The conductance (normalised to the maximum unblockaded value) versus Fermi energy (normalised to charging energy)[16].

In the quantum Coulomb blockade regime tunnelling occurs through a single level. The single peak conductance is given by[3,4,15]

Eqn. 5.5
$$G = \frac{e^2}{4kT}\frac{\Gamma^l\Gamma^r}{\Gamma^l + \Gamma^r}\cosh^{-2}\left(\frac{\delta}{2kT}\right)$$

here Γ^l and Γ^r are the tunnelling rates through the particular single level in question.

The line shapes in both the classical and quantum blockade regimes are virtually identical. However, in the quantum regime the peak amplitude scales as 1/T but it is constant in the classical regime. This behaviour distinguishes a quantum peak from its classical counterpart.

The temperature dependence of the peak height is shown in Figure 5.11. This shows that the peak height has a minimum value at intermediate temperatures, within classical blockade regime with greater heights within both the quantum and the unblockaded regimes. In the unblockaded regime, transport is dominated by the two tunnel barriers.

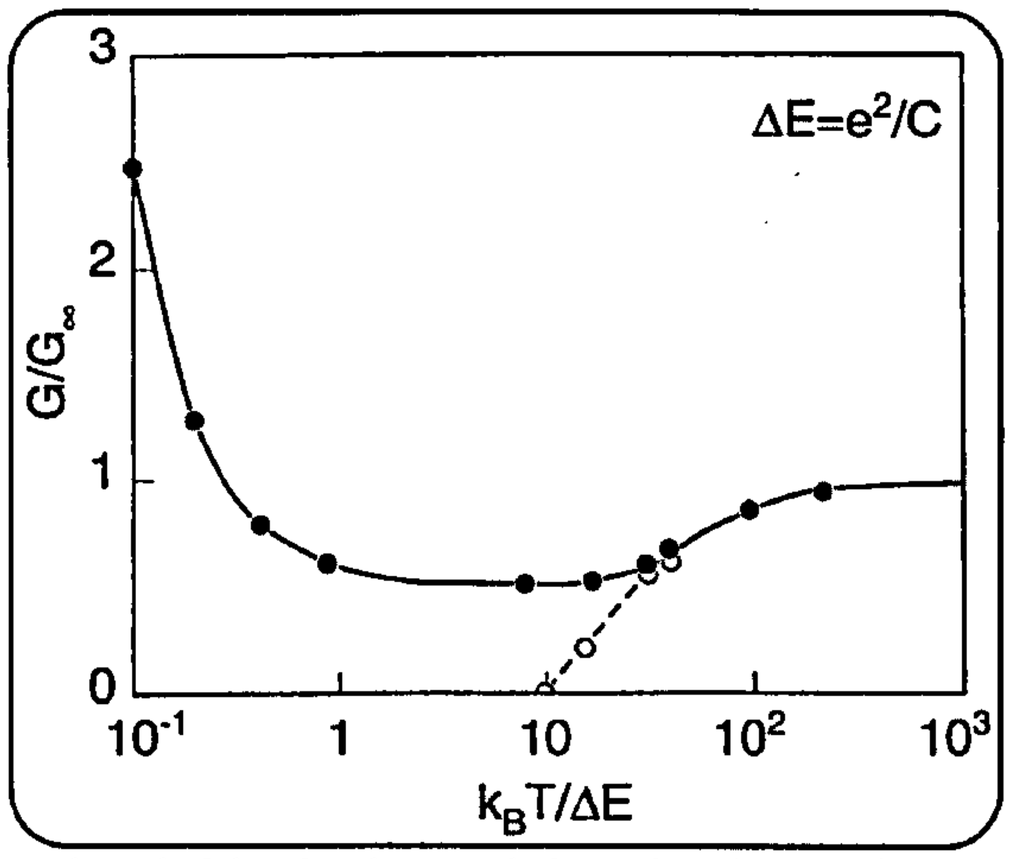

Figure 5.11 Coulomb blockade peak height dependence; conductance (normalised to the maximum unblockaded value) versus thermal energy (normalised to single particle spacing). Three regimes are defined showing that both at high and low temperature the peak height is greater than in the intermediate regime[16].

At low temperatures, when $kT < \Delta\varepsilon_i$, the conductance of any peak is dominated by the tunnelling rates through one specific single particle state. Large amplitude peaks are associated with states that couple strongly to the leads, whilst low amplitude peaks with are associated with weakly coupled states.

Increasing the temperature allows more discrete states to contribute. Although there is a 1/T dependence of tunnelling through a single particle state, this is cancelled, on average, by the T dependence of the number of levels participating in the conduction ($kT/\Delta\varepsilon_i$). The peak amplitude increases again at high temperature as the blockade begins to break down and coupling between the leads becomes stronger.

The above discussion has ignored the width of the energy levels, $\hbar\Gamma$.

5.3.2 Analysis of Experimental Temperature Dependent Data

Temperature dependent data was taken at base temperature 100mK and 100mK intervals to 400mK. A representative set is shown in Figure 5.12.

Three regimes were identified by peak height within the data of Figure 5.12

Regime 1, seen in Figure 5.12 panel a), where the conductance peak magnitude was greater in comparison to the rest of the data.

Regime 2, seen in Figure 5.12 panels b)-e), where there were only minor variations between the data.

Regime 3 seen in Figure 5.12 panel f), where much less variations in conductance peak magnitude and a rise in valley conductance was observed.

Conductance peak magnitude is strongly related to the coupling of the single particle state to the lead reservoirs[10,11], with an increase in magnitude in general reflecting a strong coupling to a single state. Conductance peak magnitude can therefore act as an indicator as to the degree of coupling between the conductance and the single particle state. Quantitatively, the magnitude is unreliable as, although the peak magnitude behaves distinctly as a function of the coupling, the individual conductance peaks exhibit different behaviour from one another. Kastner et al[11] found that the peak magnitudes for three conductance peaks within the same data set acted differently in response to temperature variation. The highest peak decreased monotonically with T, the lowest peak increased monotonically, and the one with intermediate height first increased and then decreased. This behaviour differs from the theoretical model given in section 5.3.1 where an individual peak is predicted to exhibit greater peak magnitude at the higher and lower temperature range as illustrated in Figure 5.11.

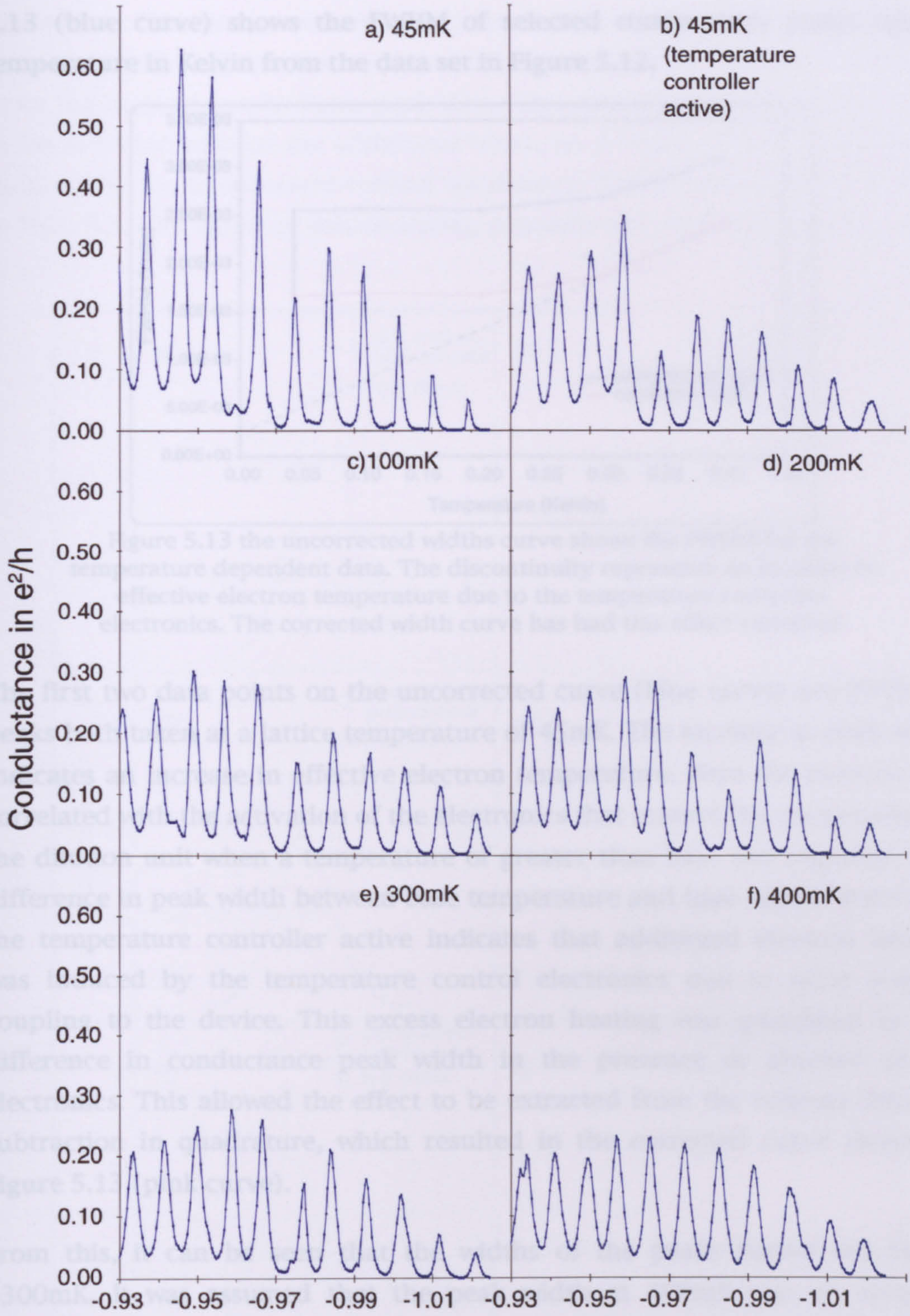

Figure 5.12. Temperature dependent behaviour of Coulomb blockade peaks. A clear difference in peak height is evident between the lowest temperature and subsequent peaks. Only minor difference can be seen between traces b)-e), but trace f) at 400mK has even peak heights and raised valley conductance values.

Conductance peak width, however, has been seen experimentally to be a reliable quantitative indicator of effective electron temperature[11]. Figure

5.13 (blue curve) shows the FWHM of selected conductance peaks against temperature in Kelvin from the data set in Figure 5.12.

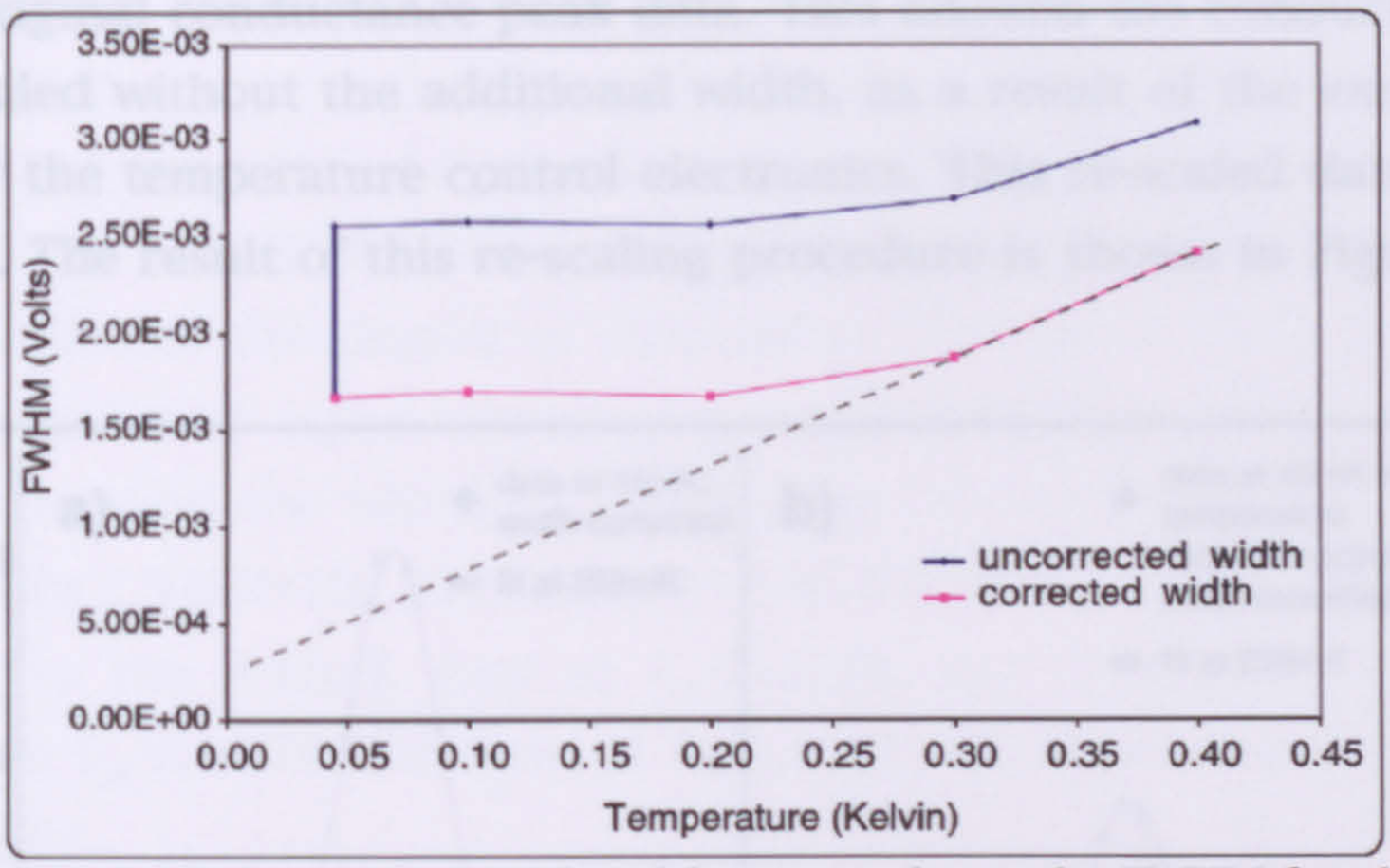

Figure 5.13 the uncorrected widths curve shows the FWHM for the temperature dependent data. The discontinuity represents an increase in effective electron temperature due to the temperature controller electronics. The corrected width curve has had this effect extracted.

The first two data points on the uncorrected curve (blue curve) are FWHM of peaks both taken at a lattice temperature of 45mK. The increase in peak width indicates an increase in effective electron temperature. Here the increase was correlated with the activation of the electronics that control the temperature of the dilution unit when a temperature of greater than base was required. This difference in peak width between base temperature and base temperature with the temperature controller active indicates that additional electron heating was induced by the temperature control electronics due to noise sources coupling to the device. This excess electron heating was quantified by the difference in conductance peak width in the presence or absence of the electronics. This allowed the effect to be extracted from the original data, by subtraction in quadrature, which resulted in the corrected curve shown in Figure 5.13 (pink curve).

From this, it can be seen that the widths of the peaks flatten out below ≈300mK. It was assumed that the peak width at 400mK was an accurate reflection of both lattice and effective electron temperature. Although there may not be enough data to justify this assumption it may be supported by the straight line fit (dashed line) to the last two points of the corrected width curve seen in Figure 5.13. This fit shows that an extrapolation of the 300 and 400mK data points would take the straight line close to the origin. Physically this would suggest that as the temperature approaches absolute zero, the conductance peak width reduces to zero.

The effect of the temperature control electronics was quantified and extracted from the FWHM values above. Additionally it was possible to extract the effect from the original conductance peak data. This allowed the conductance peaks to be re-scaled without the additional width, as a result of the excess heating induced by the temperature control electronics. This re-scaled data was fitted to Eqn. 5.3. The result of this re-scaling procedure is shown in Figure 5.14 a)-f).

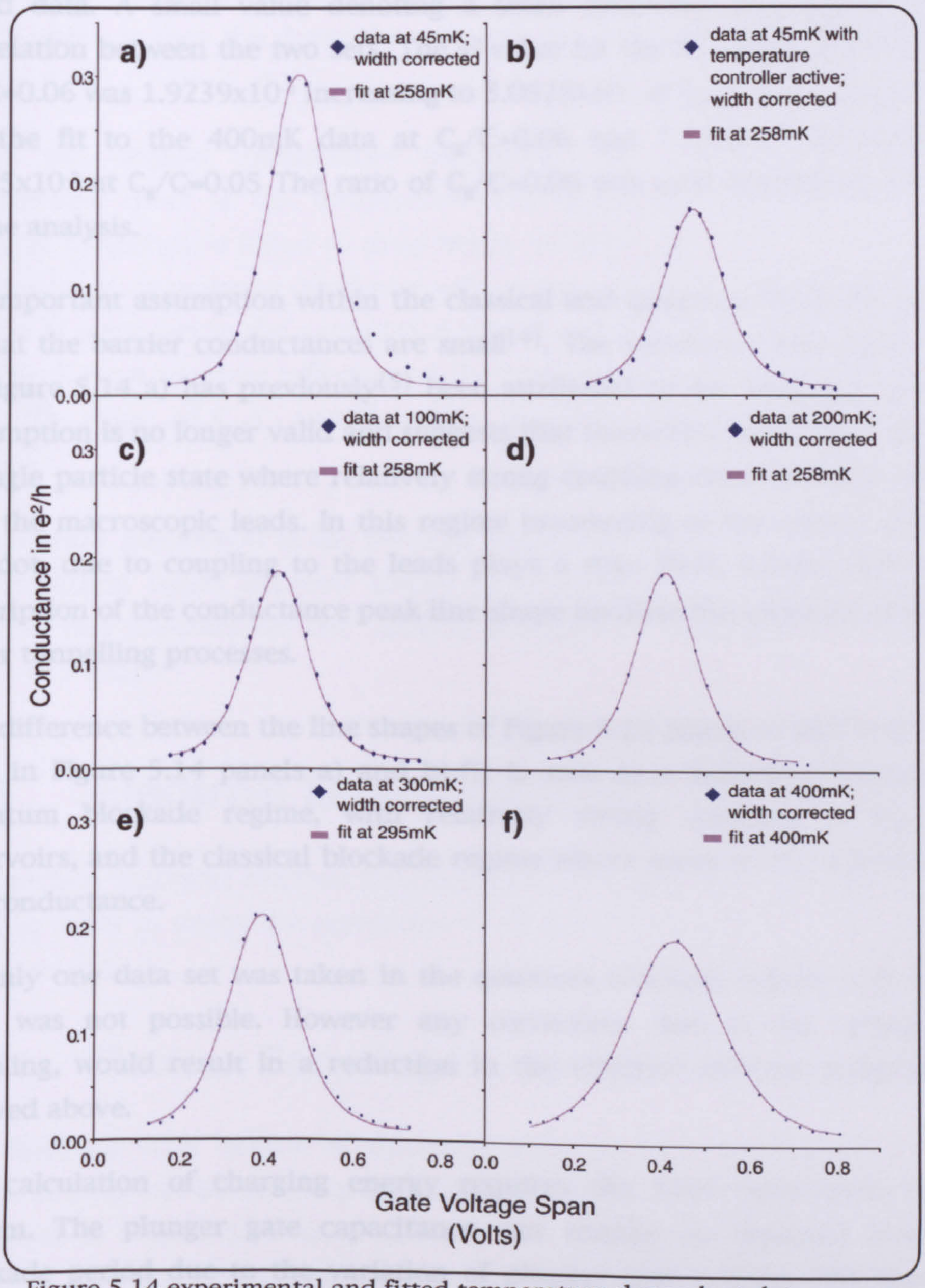

Figure 5.14 experimental and fitted temperature dependent data curves. The experimental data has been corrected for the additional electron heating induced by the temperature controller electronics.

As a measurement of total capacitance was not taken directly, an estimate can be derived from fitting the temperature dependent data. Fitting the 400mK data at T=400mK leaves the ratio of gate to total capacitance (C_g/C) as the free parameter. Setting C_g/C to 0.06 gives the fit seen in Figure 5.14 f). A change of ±0.01 (16%) to the value of C_g/C results in a minimum change in the χ^2 value of 160% for the 45mK fit and a maximum of over 7000% for the 400mK. Where χ^2 indicates the degree of correlation between the experimental and fitted data. A small value denoting a small difference and hence a high correlation between the two sets. The χ^2 value for the fit to the 45mK data at C_g/C=0.06 was 1.9239×10^{-3} increasing to 5.0525×10^{-3} at C_g/C=0.05. The χ^2 value for the fit to the 400mK data at C_g/C=0.06 was 7.333×10^{-5} increasing to 5.525×10^{-3} at C_g/C=0.05 The ratio of C_g/C=0.06 was used throughout the rest of the analysis.

An important assumption within the classical and quantum blockade regimes is that the barrier conductances are small[4]. The Lorentzian line shape, seen in Figure 5.14 a) has previously[5] been attributed to the signature that this assumption is no longer valid and suggests that tunnelling takes place through a single particle state where relatively strong coupling exists between the dot and the macroscopic leads. In this regime broadening of the energy levels in the dot, due to coupling to the leads plays a rôle. Here, $k_bT\approx h\Gamma$, and a full description of the conductance peak line shape involves the inclusion of higher order tunnelling processes.

The difference between the line shapes of Figure 5.13 panels a) and b)-f), (also seen in Figure 5.14 panels a) and b)-f)) is seen as a transition between the quantum blockade regime, with relatively strong coupling to the lead reservoirs, and the classical blockade regime where many levels contribute to the conductance.

As only one data set was taken in the quantum blockade regime a fit to the data was not possible. However any correction, due to the strong lead coupling, would result in a reduction in the effective electron temperature, derived above.

The calculation of charging energy requires the total capacitance of the system. The plunger gate capacitance can readily be obtained from the blockade period due to the variation of plunger gate voltage. The blockade period ΔV_g=8.182mV led to a gate capacitance $C_g=e/V_g$=20aF. Using the fit parameter, C_g/C, from Eqn. 5.4 the total capacitance was $C_\Sigma=C_g/0.06$=333aF, and the charging energy for the dot was $E_n=e^2/C_\Sigma=480\mu$eV.

The values of capacitance, estimated from the fitted temperature dependence data, resulted in good agreement with the literature[9]. Assuming these values to be appropriate, the effective electron temperature at T_L=45mK was 260mK (=22μeV).

Figure 5.12 f) is distinguished by the equality between conductance peak magnitudes. This is usually attributed[11] to a signature that $kT \geq \Delta\varepsilon$ and that the energy levels adjacent to E_F begin to be thermally populated. The conductance is then the thermal average of the conductance of the populated levels.

When the original temperature dependent data was corrected for the quantifiable effect of the temperature controlling electronics, the effective electron temperature failed to drop below ≈250mK. Without an experimental evaluation of capacitance this figure will contain a certain degree of error. One source of error lies in the assumption that the width of the conductance peak at 400mK is an accurate reflection of the lattice temperature. This assumption fixes the value of C_g/C and therefore the total capacitance and charging energy.

A significant proportion of the electron temperature may be accounted for by the excitation signal imposed across the sample during these experiments. Without this contribution the electron temperature would have been of the order of 170mK.

5.4 Electron Spectrometry

This section describes electron focusing and details how these techniques were used in order to probe the separation of single particle energy states within a quantum dot.

5.4.1 Electron Focusing

The skipping orbit motion of electrons along a 2DEG boundary in a small magnetic field was observed in an electron focusing experiment. The geometry is shown in Figure 5.15 with two adjacent point contacts separated by a distance L=2μm. These experiments were performed prior to the other experiments presented in this chapter on a device similar to that shown in Figure 5.1. Gates G6, G1 and G8 only were biased leaving the dot area R_2 open. This data was taken at a lattice temperature of 1.2K.

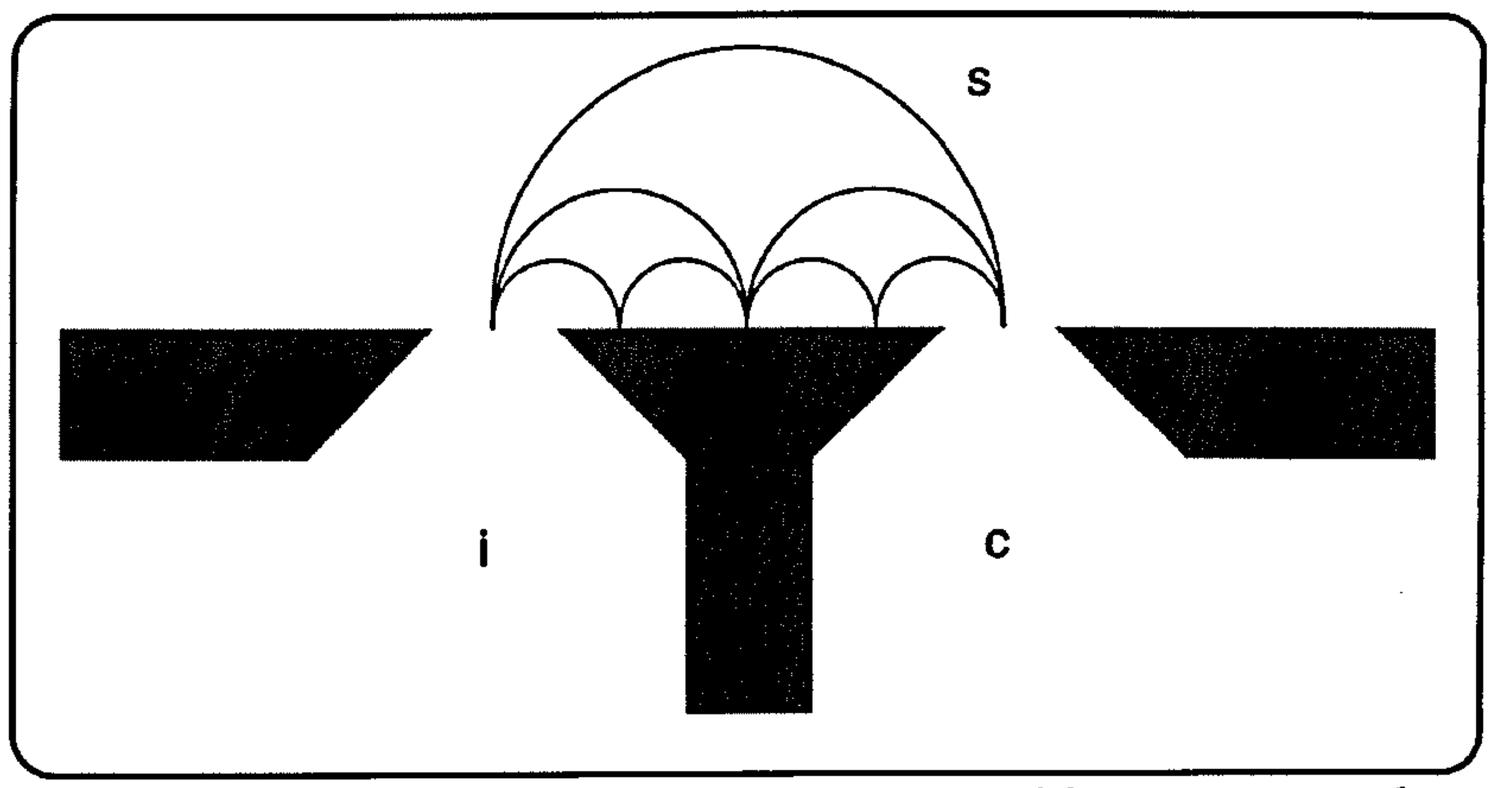

Figure 5.15 Two quantum point contacts separated by a common boundary. Separation between the qpcs is 2μm.

Electrons were injected from region i of the 2DEG through a qpc into region s. The second qpc was used as a collector as the electrons passed from s into c. The focusing points intersected the boundary at multiples of the cyclotron diameter from the injector. Increasing the magnetic field caused the focal points to shift past the collector, this led to periodic oscillations in the collector signal shown in Figure 5.17. These measurements are normally associated with electrons injected at the Fermi energy which, in Figure 5.17, is represented by the green line (0mV).

Focusing experiments demonstrate that the collisions at the boundary are highly specular, since diffusive boundary scattering would tend to average the oscillations[9].

By adding a dc bias to the excitation signal electrons were given excess energy and hence injected above the Fermi level. This yielded information about the energy environment local to the quantum point contacts. Electrons injected above the Fermi level are known as hot electrons. The effect of dc bias, in terms of the Fermi velocity occupation of one dimensional subbands may be understood from Figure 5.16.

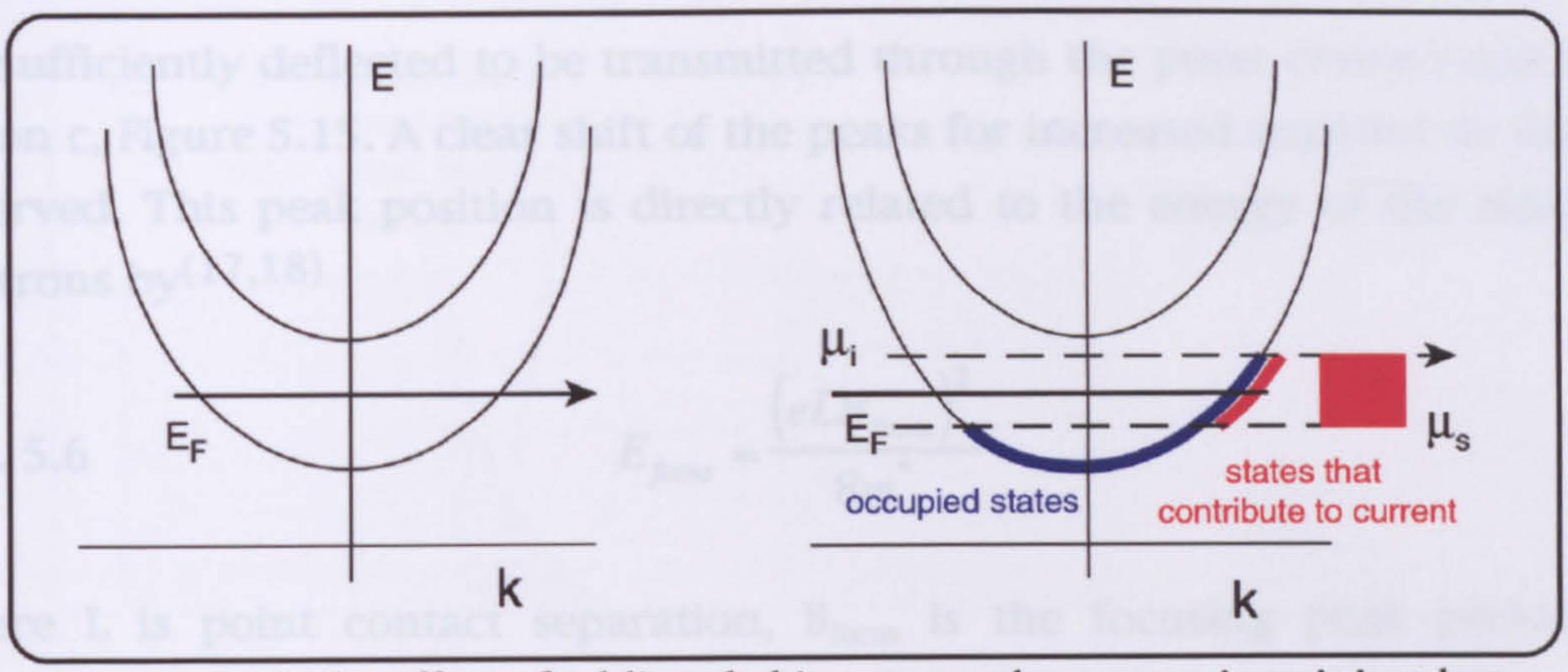

Figure 5.16 The effect of adding dc bias across the system is to inject hot electrons. Energies at the top of the excess distribution are selected, indicated by the arrows.

Differential ac measurement techniques were used to extract $\delta V_c/\delta I_i$. This technique selects primarily only those electrons with maximal injection energy. A large dc bias signal was modulated with a small ac signal. Peaks were observed in the differential conductance due to the transport of ac electrons, which had the highest energies. The red shaded area indicates the energy range of the injected hot electrons and the arrow the energies extracted by differential measurement[17,18].

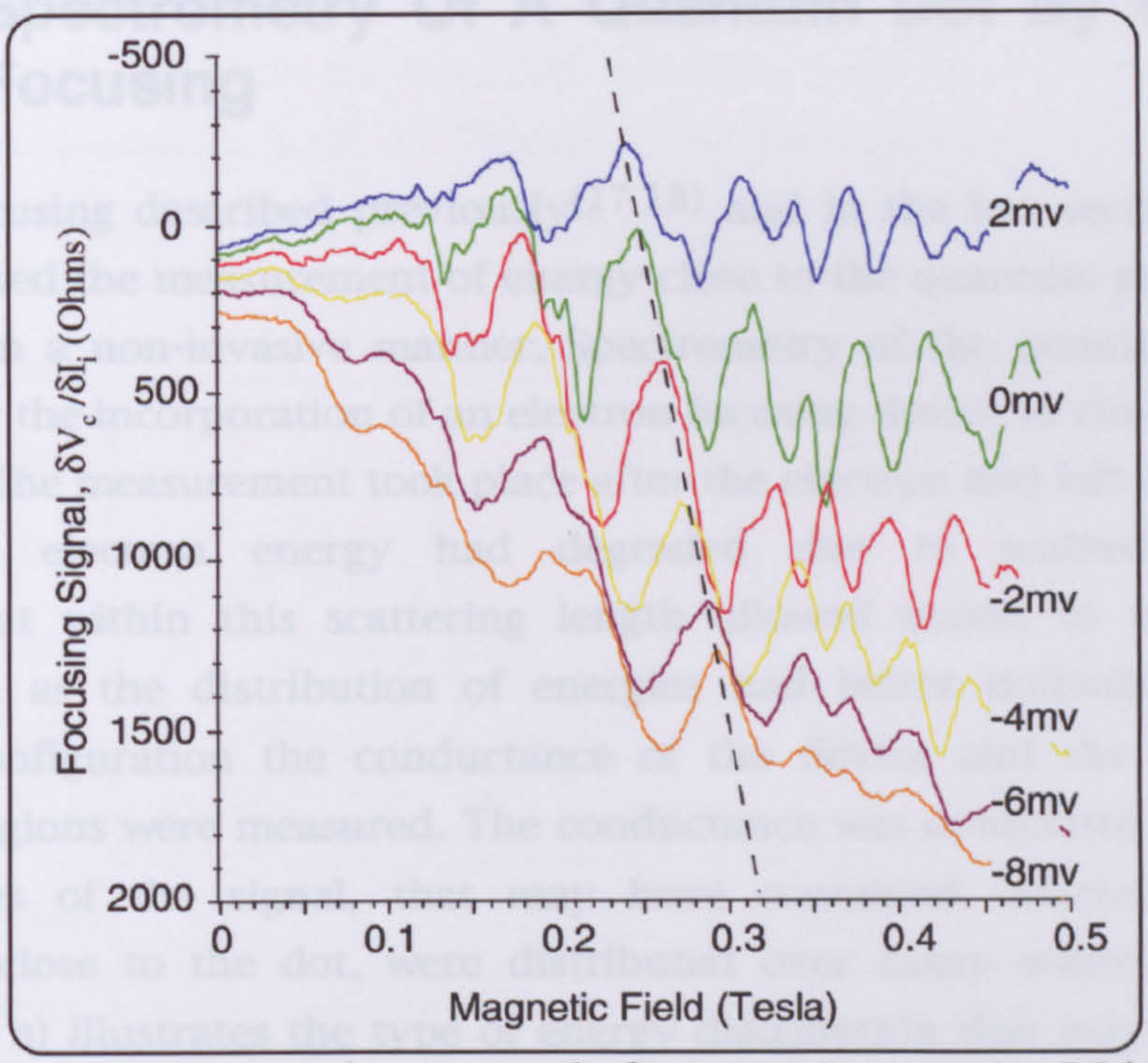

Figure 5.17 Electron focusing peaks for increasing negative DC bias

Figure 5.17 shows the differential electron focusing signal against magnetic field. Each of the six lines represents a different value of dc injection bias. The magnetic field was swept from 0 to 0.5 Tesla for each bias point. The peaks in focusing signal represent the values of magnetic field at which the electrons

are sufficiently deflected to be transmitted through the point contact and into region c, Figure 5.15. A clear shift of the peaks for increased negative dc bias is observed. This peak position is directly related to the energy of the injected electrons by[17,18]

Eqn. 5.6
$$E_{focus} = \frac{\left(eLB_{focus}\right)^2}{8m^*}$$

Where L is point contact separation, B_{focus} is the focusing peak period in magnetic field and m* and e have their usual meanings.

An important feature of this technique was that the measurement was effectively performed close to the device. More conventional resistance (conductance) measurements, from which energies can be derived, are global quantities and give little insight into the energy distribution close to the device under test. The different magnetic fields required for electrons of different energies to pass from one point contact to the other, allowed a determination of energy before degrading by scattering events.

5.4.2 Spectrometry Of A Quantum Dot By Electron Focusing

Electron focusing described previously[17,18] and in the last section (section 5.4.1), allowed the measurement of energy close to the quantum point contact structures in a non-invasive manner. Spectrometry of the quantum dot was achieved by the incorporation of an electron focusing device in close proximity to the dot. The measurement took place after the electron had left the dot, and before the electron energy had degraded due to scattering events. Measurement within this scattering length allowed access to more subtle information as the distribution of energies had better definition. In a 4-terminal configuration the conductance of the device and the wide 2DEG reservoir regions were measured. The conductance was dominated by the dot, but features of the signal, that may have contained information about conditions close to the dot, were distributed over many scattering events. Figure 5.18 a) illustrates the type of energy distribution that may occur after many scattering events. A measurement within an elastic scattering event maintained an energy distribution that was better defined, as seen in Figure 5.18 b).

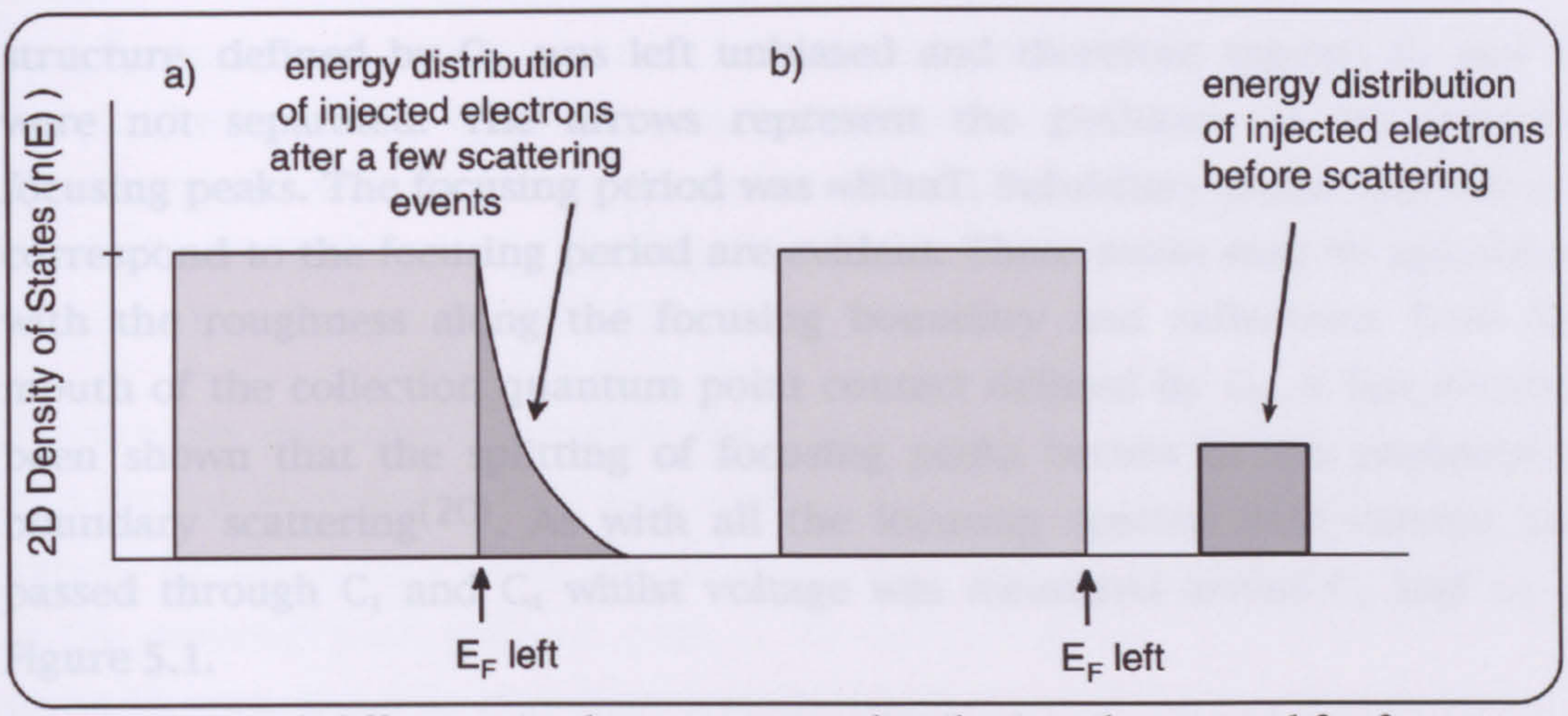

Figure 5.18 difference in electron energy distribution close to and far from the dot. The energy distribution shown in a) shows the energy distribution of electrons after several scattering events, whilst b) shows the distribution before scattering.

The need for measurement information made locally to mesoscopic structures has long been understood[19], but has been difficult to attain.

Figure 5.19 shows an electron focusing trace taken at T_L<100mK. This data was taken in a different experimental run than the data presented in section 5.4.1. The exit quantum point contact of the device, defined between gates G_1 and G_6 of Figure 5.1, was used as the injection quantum point contact in an electron focusing configuration seen in Figure 5.15. The collector quantum point contact was defined between G_1 and G_8, with electrons entering region R_4 at integer multiples of the cyclotron diameter.

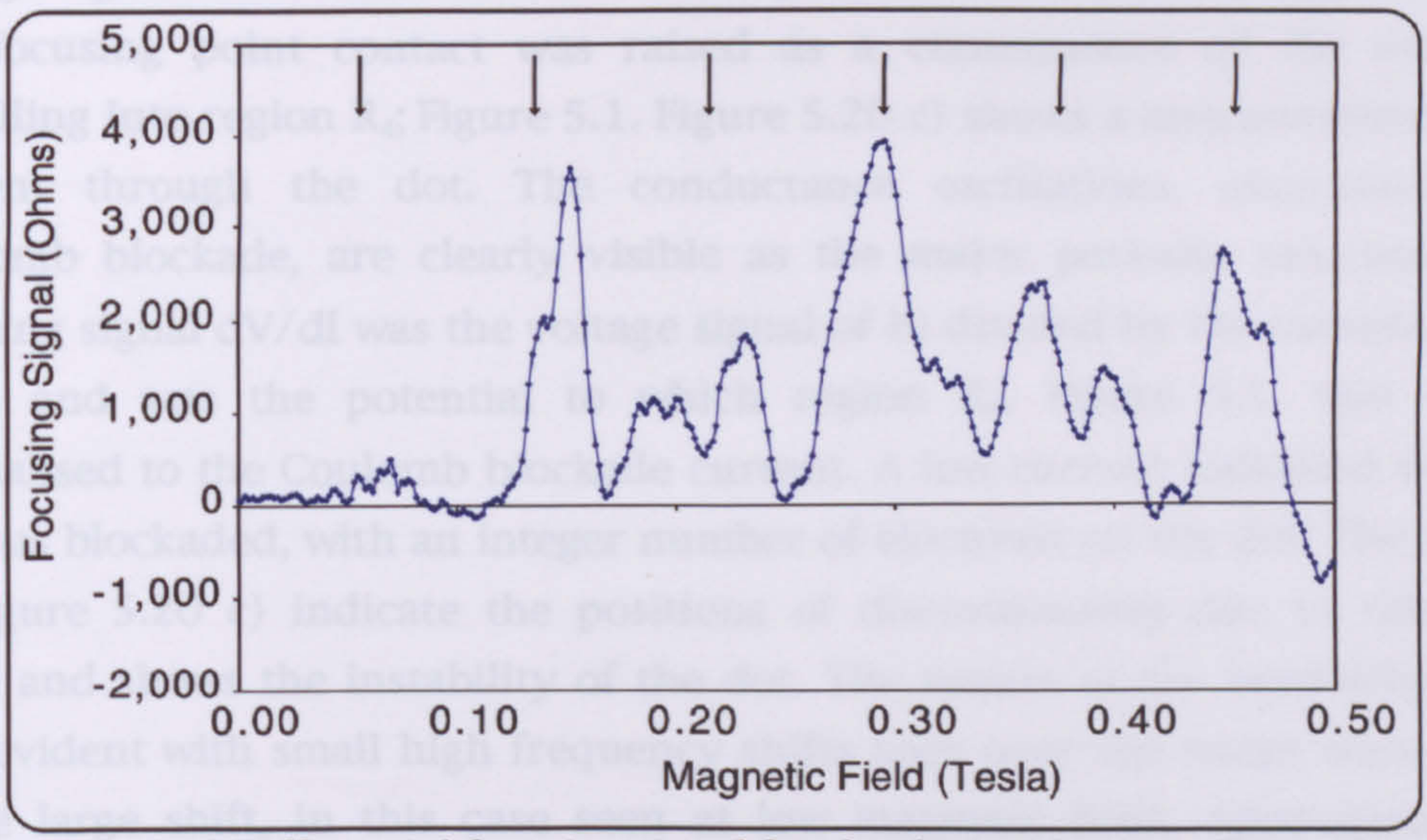

Figure 5.19 Differential focusing signal for the device shown in Figure 5.1. The entrance quantum point contact of the dot was left unbiased (G_4=0V) and hence the dot was not formed.

Figure 5.19 shows the focusing signal for electrons leaving region R_2 and entering R_4. The entrance quantum point contact of the quantum dot

structure, defined by G_4, was left unbiased and therefore regions R_1 and R_2 were not separated. The arrows represent the positions of the periodic focusing peaks. The focusing period was ≈80mT. Subsidiary peaks that did not correspond to the focusing period are evident. These peaks may be associated with the roughness along the focusing boundary and reflections from the mouth of the collection quantum point contact defined by G_8. It has recently been shown that the splitting of focusing peaks occurs in the presence of boundary scattering[20]. As with all the focusing spectra data current was passed through C_1 and C_4 whilst voltage was measured across C_5 and C_6 of Figure 5.1.

In order to investigate the effect of the quantum dot on the focusing spectra, gates G_4 and G_5 were also biased negatively and the dot formed in region R_2.

Focusing spectra data of the quantum dot was taken in two different experimental modes. The centre gate plunger was swept to induce a number of conductance peaks for small increments of magnetic field, or the gate voltage was adjusted to sit at a particular position on a conductance peak, and the magnetic field swept.

Figure 5.20 shows data taken in the first mode on the second focusing peak. The figure shows three 3-dimensional surface plots, the focusing dV_{R34}/dI_{R23} a), the voltage b) and the current signals c). On the focusing plot, Figure 5.20 a) the Coulomb blockade period is seen at those points marked with arrows. The voltage signal was a measurement of the potential to which the region behind the focusing point contact was raised as a consequence of the electrons travelling into region R_4; Figure 5.1. Figure 5.20 c) shows a measurement of the current through the dot. The conductance oscillations, associated with Coulomb blockade, are clearly visible as the major periodic structure. The focusing signal dV/dI was the voltage signal of b) divided by the current signal of c) and was the potential to which region R_4, Figure 5.1, was raised, normalised to the Coulomb blockade current. A low current indicated that the dot was blockaded, with an integer number of electrons on the dot. The arrows in Figure 5.20 c) indicate the positions of discontinuities due to telegraph noise and shows the instability of the dot. The nature of the instabilities was also evident with small high frequency shifts seen over the entire trace and a single large shift, in this case seen at low magnetic field. Approximately 5 different magnitudes of shift were observed. These may have been associated with traps at various distances from the dot. Large jumps in conductance peak position would then be associated with traps close to the dot and small jumps with traps further away.

The fine structure, which was seen in both the voltage and focusing traces, was due to the instability of the dot, and roughness along the focusing boundary. There was no evidence in this data of a shift in peak position due to Coulomb blockade or single particle spacing. The instability of the dot makes detection of subtle focusing peak shifts difficult.

There were also instrumentation limitations with this method of data taking. The minimum magnetic field step size was 1mT. This was limited by the power supply for the super-conducting magnet. This step size was of the same order as the expected peak shift, on peak 2, for the estimated single particle spacing given in section 5.2.2. This therefore does not provide high enough magnetic field resolution to see energy shifts of the order of the single particle energy level spacing.

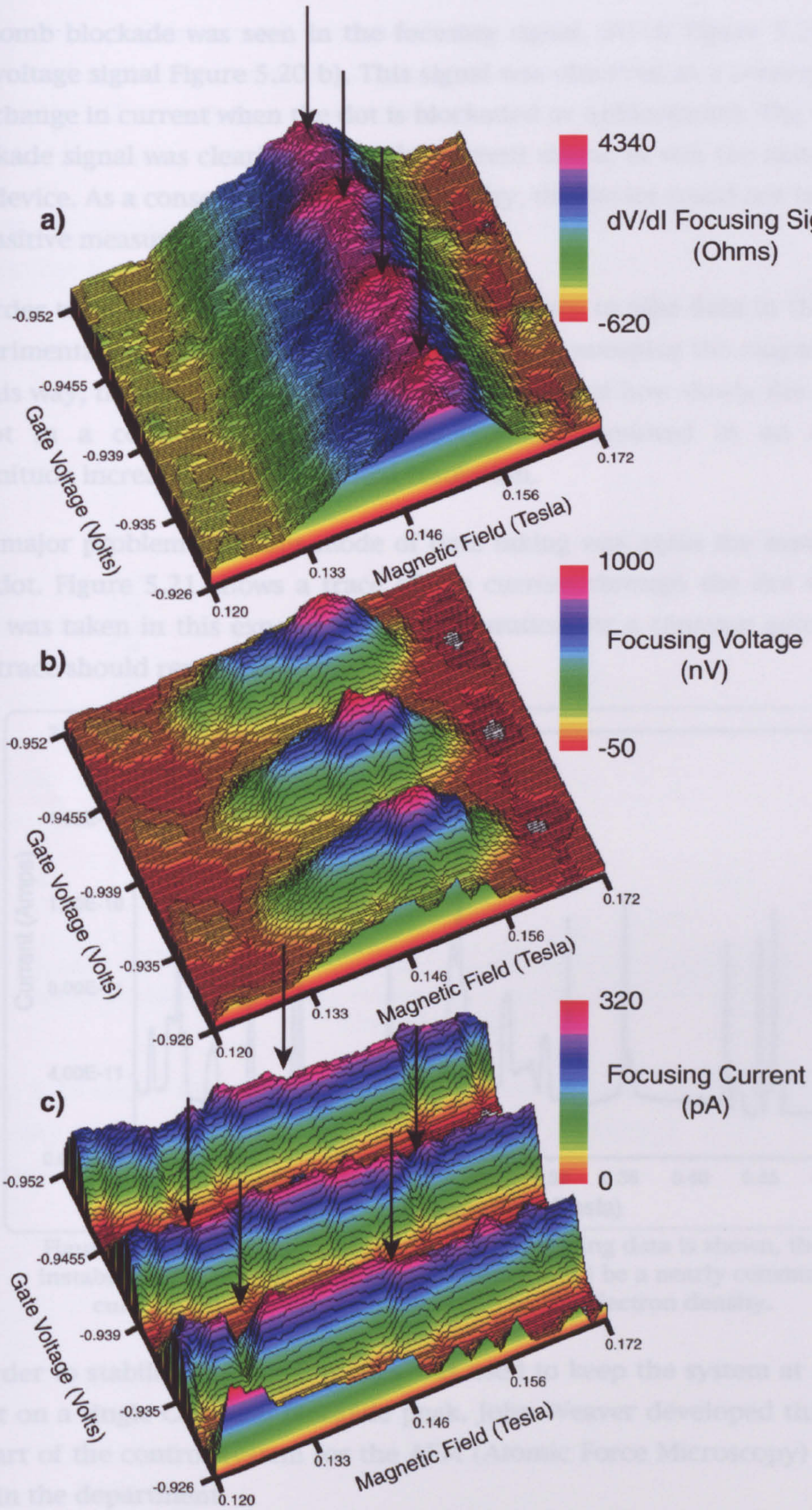

Figure 5.20 3-D Surface Plots of focusing data over three Coulomb blockade peaks. a) dV/dI focusing signal b) the voltage signal which is the potential to which the reservoir behind the focusing point contact is raised c) the current through the dot showing the Coulomb blockade structure and the instability of the device.

Coulomb blockade was seen in the focusing signal, dV/dI Figure 5.20 a) and the voltage signal Figure 5.20 b). This signal was observed as a consequence of the change in current when the dot is blockaded or unblockaded. The Coulomb blockade signal was clearly seen in the current signal, as was the instability of the device. As a consequence of this instability, the device could not be used as a sensitive measurement of energy.

In order to increase the resolution it was necessary to take data in the second experimental mode i.e. fixing the gate voltage and sweeping the magnetic field. In this way, the field resolution was now a function of how slowly the field was swept in a continuous manner and, typically, resulted in an order of magnitude increase in magnetic field resolution.

The major problem with this mode of data taking was again the instability of the dot. Figure 5.21 shows a trace of the current through the dot when the data was taken in this experimental configuration. At a constant gate voltage, this trace should represent a constant current.

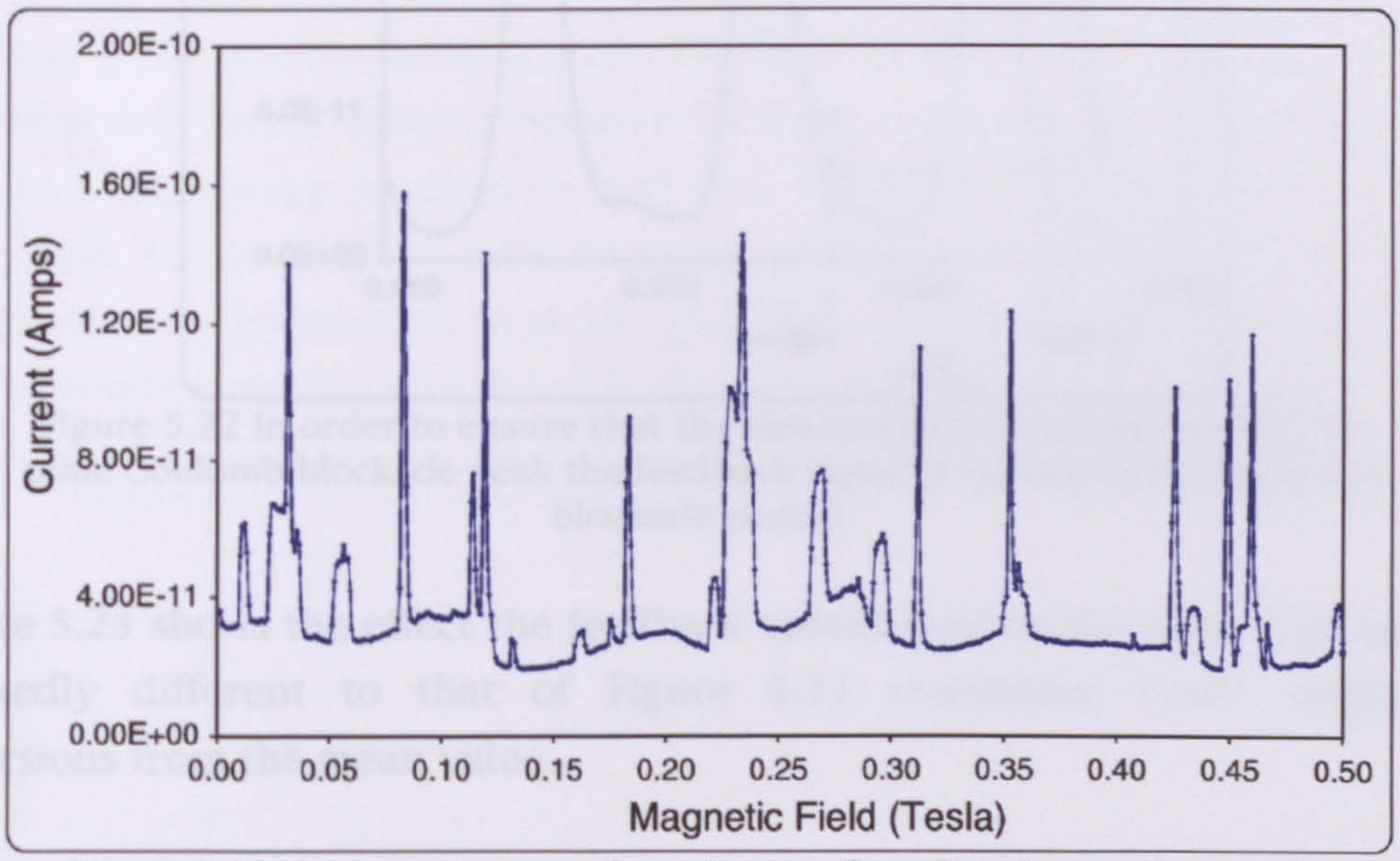

Figure 5.21 the current part of an electron focusing data is shown, the instability of the dot is clearly visible. This should be a nearly constant current, modulo the small effect of B on the electron density.

In order to stabilise the dot feedback was used to keep the system at the same point on a single Coulomb blockade peak. John Weaver developed this system as part of the control system for the AFM (Atomic Force Microscopy) research within the department.

A signal from the lockin amplifier, which was used to measure the current, provided the input signal to the feedback system. This generated an error signal which was inserted into the gate voltage line. If the current signal

deviated from a pre-set value the feedback system generated an error signal which was applied to the plunger gate causing the current signal to return to the pre-set value. In this way, the dot was continuously adjusted to maintain a constant current.

Due to the periodic nature of blockade, the error signal needed to be limited. Restricting the error signal ensured that it was impossible for the stabilisation to occur on a different conductance peak with the same magnitude and slope. This is illustrated in Figure 5.22

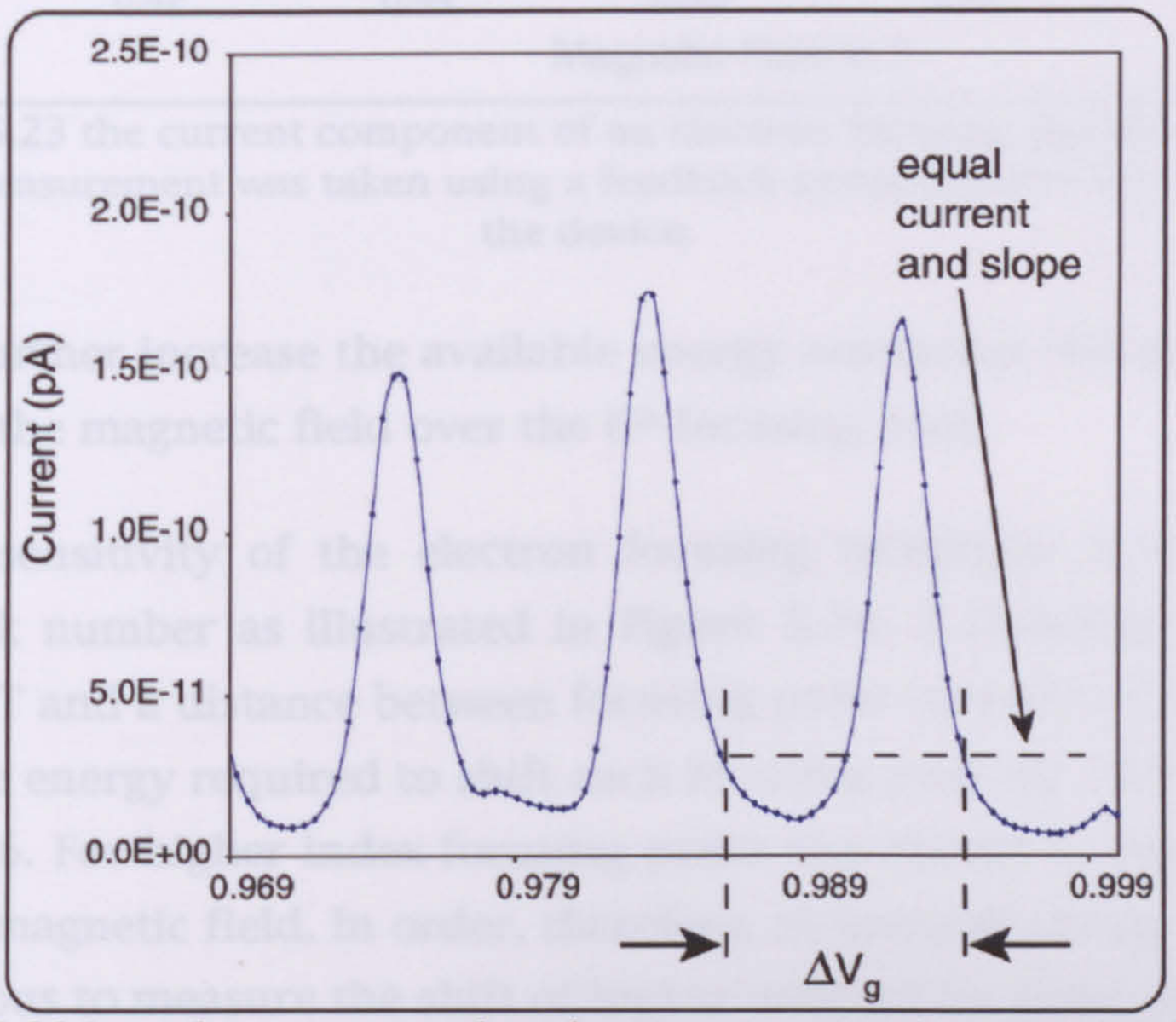

Figure 5.22 In order to ensure that the measurement is maintained on the same Coulomb blockade peak the feedback signal is limited to less than one blockade period.

Figure 5.23 shows the effect the feedback system had on the data. The trace is markedly different to that of Figure 5.21 containing lower magnitude excursions from the mean value.

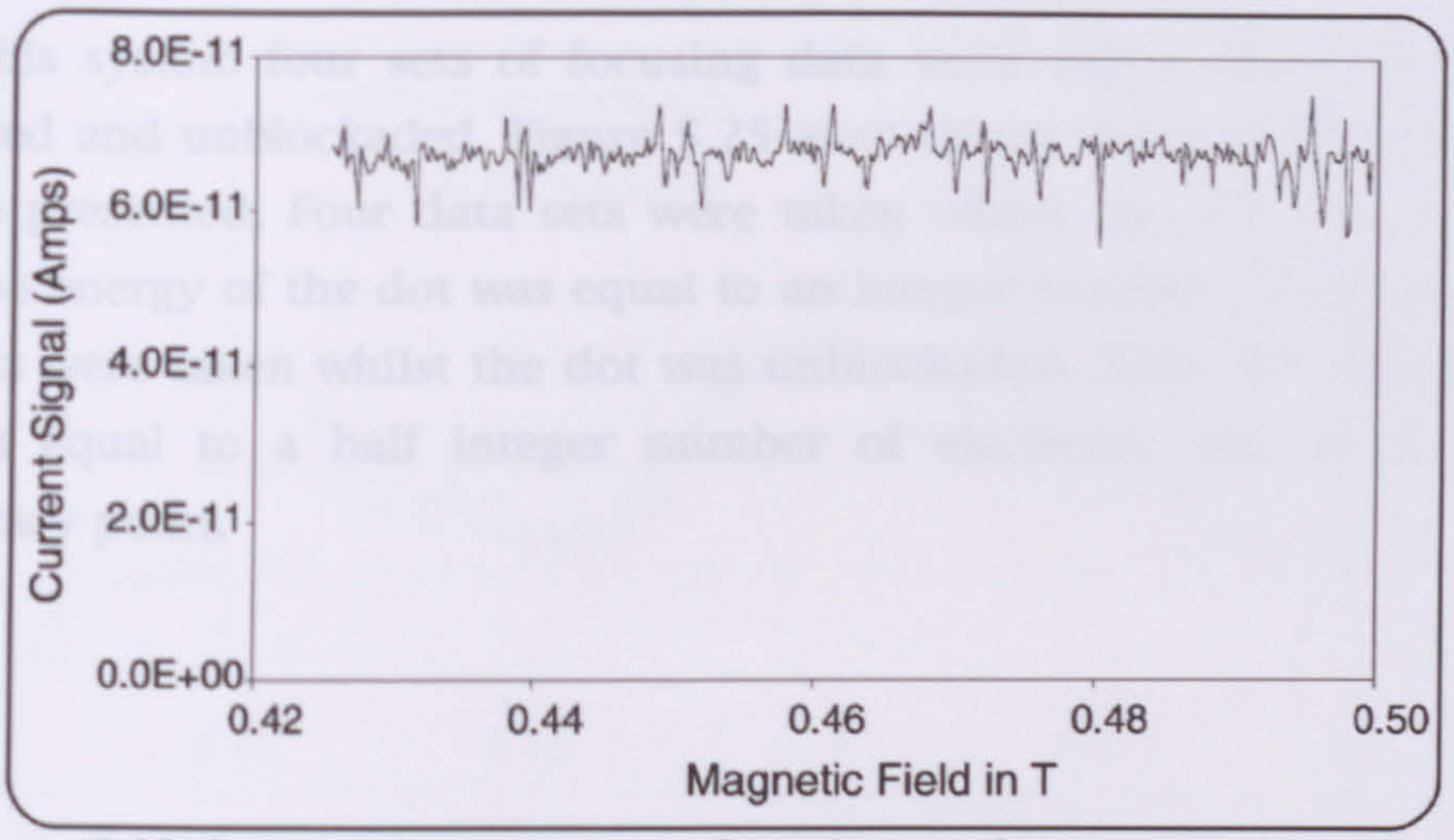

Figure 5.23 the current component of an electron focusing signal is shown. This measurement was taken using a feedback system to actively stabilise the device.

In order to further increase the available energy resolution this data was taken by sweeping the magnetic field over the 6th focusing peak.

The energy sensitivity of the electron focusing technique is related to the focusing peak number as illustrated in Figure 5.24. A focusing signal with a period of 0.1T and a distance between focusing point contacts of 2μm has been assumed. The energy required to shift each focusing peak by 1mT is calculated using Eqn. 5.6. For higher index focusing peaks less energy is required to shift that peak in magnetic field. In order, therefore, to increase energy resolution it is advantageous to measure the shift of higher indexed focusing peaks.

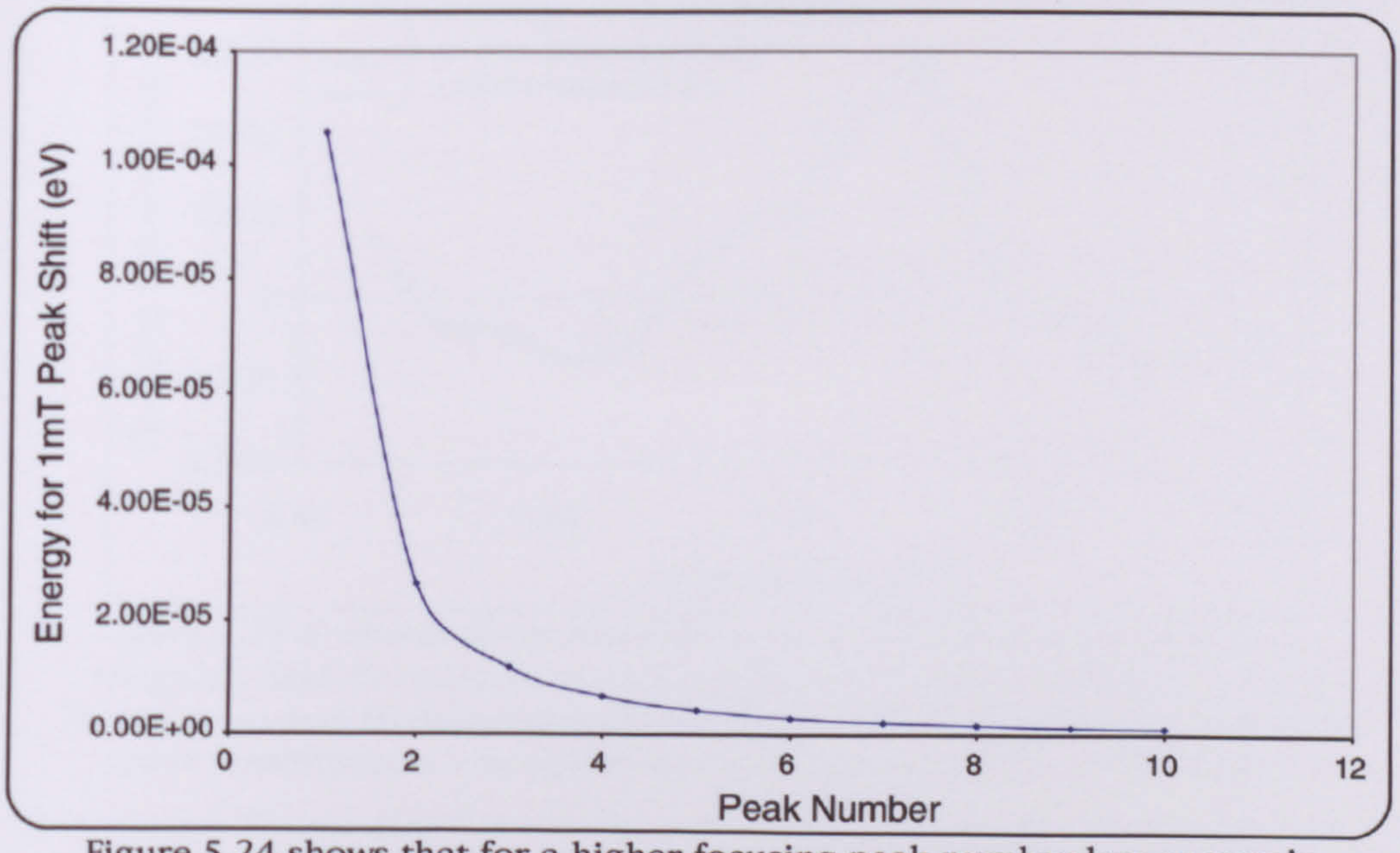

Figure 5.24 shows that for a higher focusing peak number less energy is required to shift a peak by 1mT.

Using this system four sets of focusing data were taken whilst the dot was blockaded and unblockaded. Figure 5.25 a)-c) shows three graphs. Eight data sets are presented. Four data sets were taken whilst the dot was blockaded. Here, the energy of the dot was equal to an integer number of electrons. Four data sets were taken whilst the dot was unblockaded. Here, the energy of the dot was equal to a half integer number of electrons, and at the charge degeneracy point.

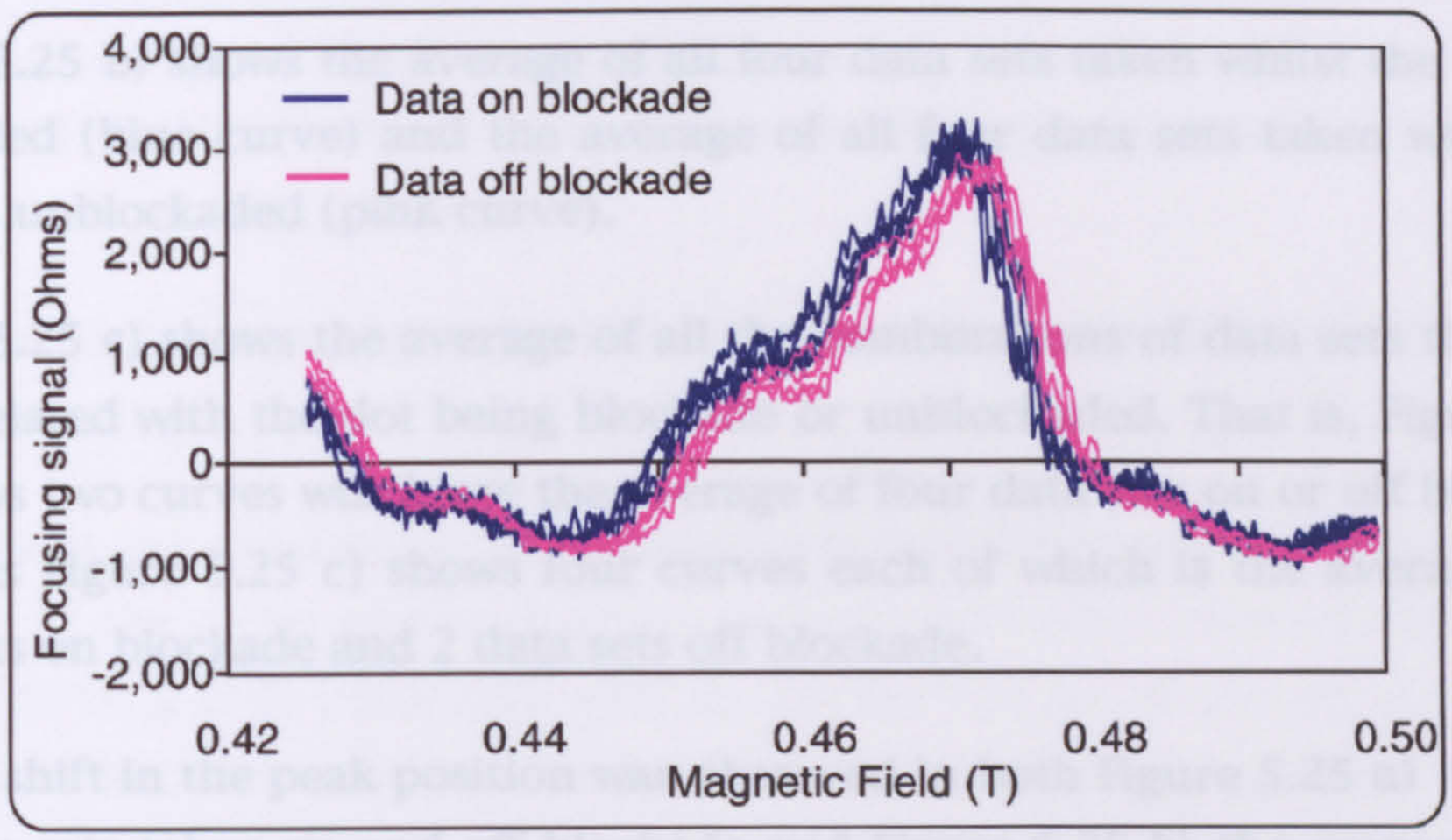

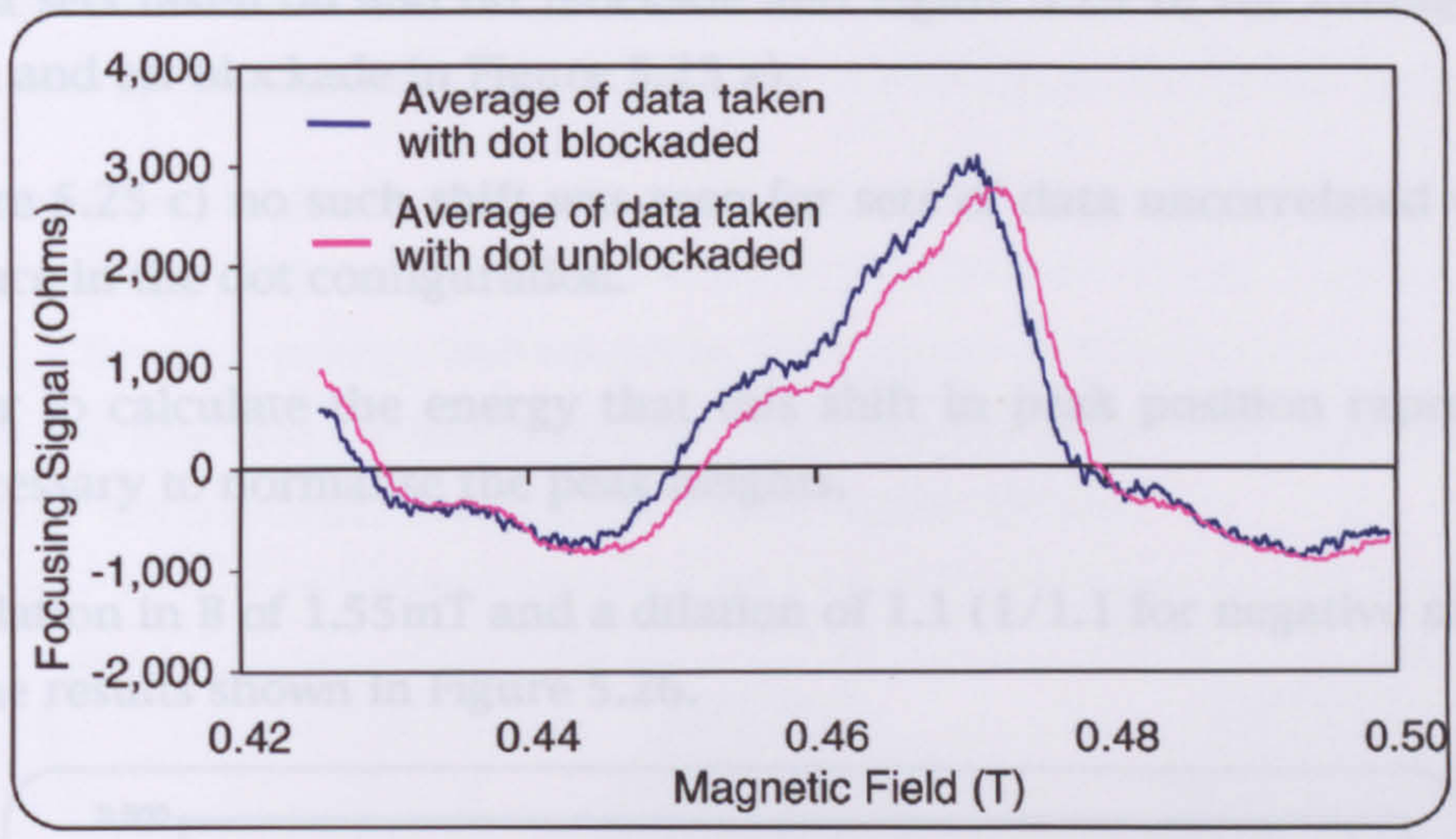

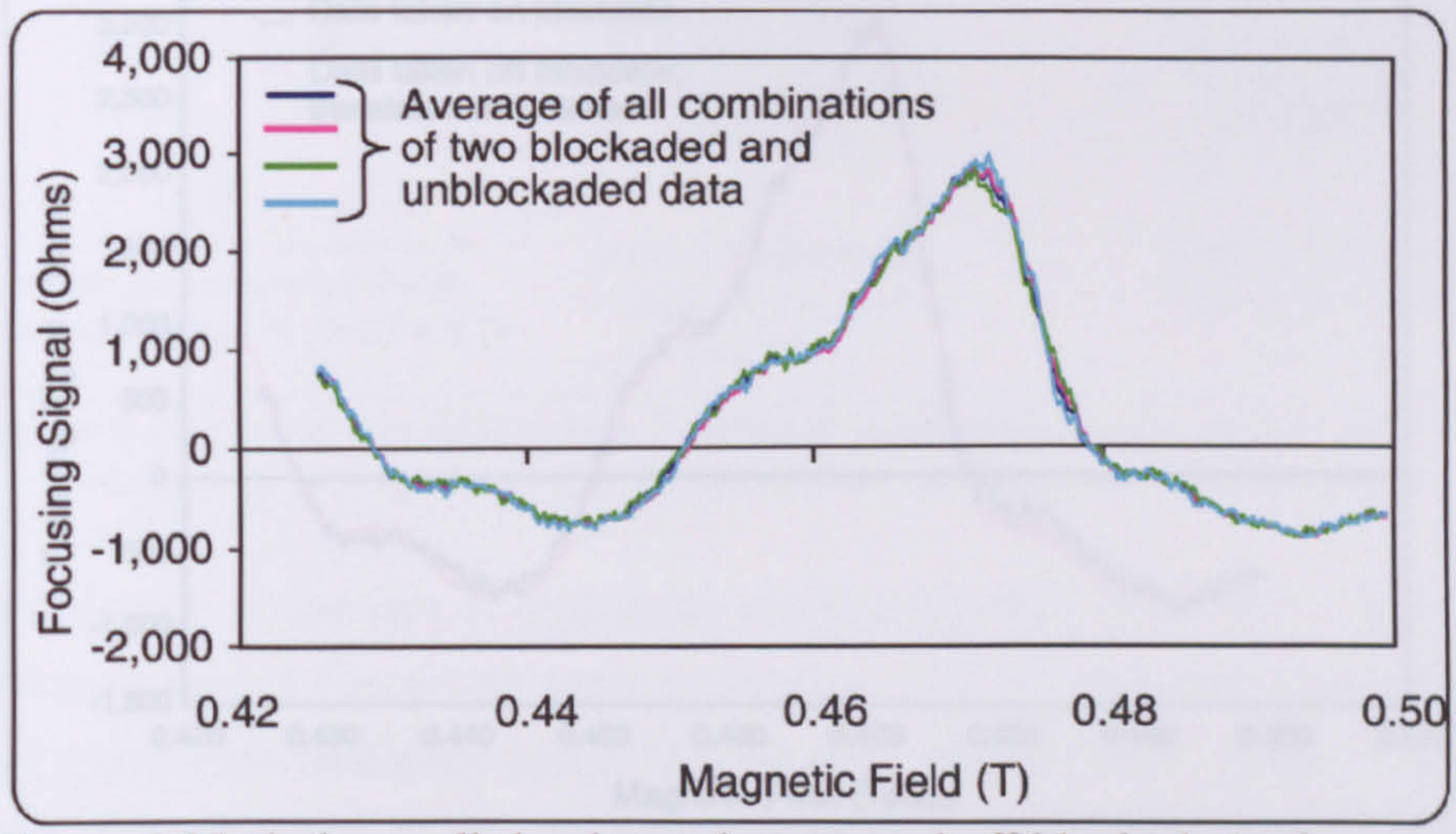

Figure 5.25 a) shows all the data taken on and off blockade in the same magnetic field direction b) averages together all data taken on blockade (blue curve) and all data taken off blockade (red curve) with c) showing all other combinations containing two data sets on and two off blockade.

Figure 5.25 a) shows all the data taken whilst the dot was blockaded (blue curves) and all the data taken whilst the dot was unblockaded (pink curves).

Figure 5.25 b) shows the average of all four data sets taken whilst the dot was blockaded (blue curve) and the average of all four data sets taken whilst the dot was unblockaded (pink curve).

Figure 5.25 c) shows the average of all the combinations of data sets that were uncorrelated with the dot being blockade or unblockaded. That is, Figure 5.25 b) shows two curves which are the average of four data sets on or off blockade. Whereas Figure 5.25 c) shows four curves each of which is the average of 2 data sets on blockade and 2 data sets off blockade.

A clear shift in the peak position was observed in both Figure 5.25 a) between the data sets taken on and off blockade and Figure 5.25 b) the average of the data on and off blockade in Figure 5.25 a).

In Figure 5.25 c) no such shift was seen for sets of data uncorrelated with the difference in the dot configuration.

In order to calculate the energy that this shift in peak position represents it was necessary to normalise the peak heights.

A translation in B of 1.55mT and a dilation of 1.1 (1/1.1 for negative numbers) gives the results shown in Figure 5.26.

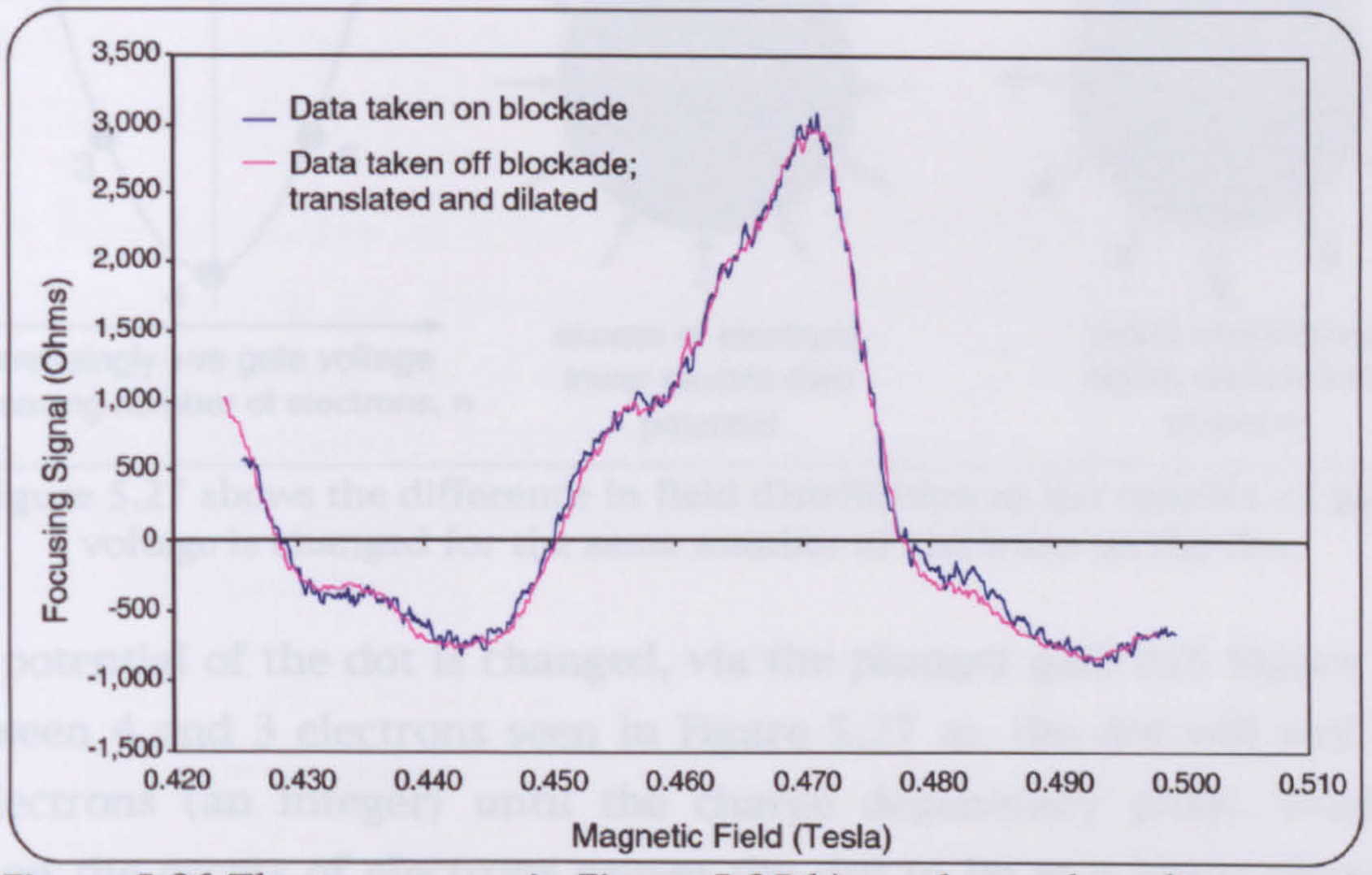

Figure 5.26 The two curves in Figure 5.25 b) can be made to lie on each other by translating the curve taken off blockade by -1.55mT and dilating the peak height 1.1 (1/1.1 for negative values).

Using Eqn. 5.6 it was possible to calculate the energy associated with the shift in peak position.

For a peak shift of 1.55mT on the sixth peak the period B=0.470/6≈80mT and δB=1.55mT/6≈260μT which led to an energy change between the two peaks of ≈55μeV.

This was of the same order as that obtained in section 5.2.2 for the single particle spacing.

Throughout the experiment, no evidence was found for a shift in focusing peak position of the order of the charging energy (≈480μeV). There does, though, appear to be a shift consistent with an energy change of almost an order of magnitude less than the charging energy. An interesting question resulting from these observations is why this measurement should be sensitive to the smaller energy changes, and yet seem to be oblivious to the larger ones?

The observation of peak shift with single particle energy spacing and not with charging energy may be due to an essential difference in the nature of these energies. Charging energy derives from the change in electric field distribution between the dot and its environment. Whereas the single particle energy is a function of the quantum mechanical states within the dot

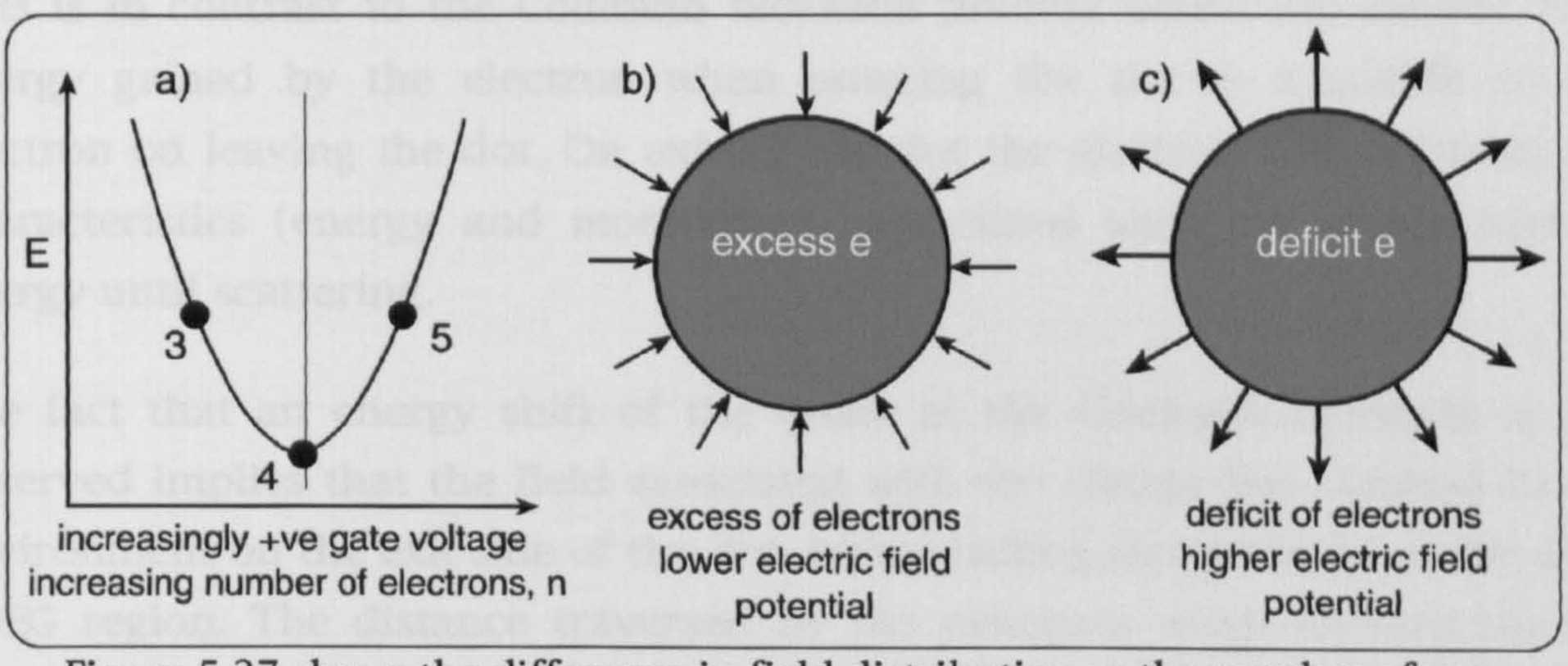

Figure 5.27 shows the difference in field distribution as the number of gate voltage is changed for the same number of electrons on the dot.

As the potential of the dot is changed, via the plunger gate (G5 Figure 5.1), to be between 4 and 3 electrons seen in Figure 5.27 a), the dot will still contain four electrons (an integer) until the charge degeneracy point. During this transition the excess of electrons causes the dot to be at a lower electric field potential than the surroundings, an illustration of the field lines is given in Figure 5.27 b). Similarly when the gate voltage is adjusted so the dot potential is between 4 and 5 electrons, the dot will still contain four electrons until the charge degeneracy point. During this transition the deficit of electrons causes the dot to be raised to a higher electric field potential than the surroundings. The energy associated with the excess or deficit is the same in both cases as the free energy function has a quadratic relationship.

Eqn. 5.7 $$E = \frac{1}{2}\varepsilon \int \vec{E}^2 dr$$

The Coulomb blockade energy is associated with the electrons charge and capacitive coupling with the environment. When the dot is maximally blockaded the electrons electric field is maximally contained within the dot. As the electron moves out less field is contained within the dot and more distributed to the environment. This process is essentially elastic.

The single particle energy spacing derives from a very different source. An electron residing on the dot has an energy characteristic of the quantum state. This state is a function of the wavelength of the electron. Electrons entering the dot will, assuming a low tunnelling probability and therefore long dwell time, take the lowest available quantum state within the dot. This process defines the electrons wavelength and hence energy. An important point to note is that this is an inelastic energy selection process. In order for the electron entering the dot to change wavelength in order to occupy the lowest available energy state excess energy must be distributed the environment as heat. This energy is therefore unavailable to the electron on leaving the dot. This is in contrast to the Coulomb blockade process where the electric field energy gained by the electron when entering the dot is available to the electron on leaving the dot. On exiting the dot the electron will maintain the characteristics (energy and momentum) associated with the single particle energy until scattering.

The fact that an energy shift of the order of the Coulomb blockade is not observed implies that the field associated with the charge has coupled to the environment on the exit side of the dot, hence raising the potential of the wide 2DEG region. The distance traversed by the electrons when focused for the sixth peak was 3μm which was well within the mean free path of $\approx$11μm (see Section 3.1) for this material.

5.5 Summary

In order to ascertain quantifiable information about the performance of the redesigned measurement system, temperature dependent conductance measurements of a large quantum dot structure were performed. This temperature dependent data set suffered from significant induced excess heating from the temperature control electronics. This was quantified, by taking data at the same lattice temperature in the presence and absence of the temperature control electronics, and then extracted from the original data in

quadrature. The resulting temperature dependence, plotted as FWHM, failed to drop below ≈250mK. This was taken to be the effective electron temperature of the system. It was shown, however, in section 4.7 that a substantial proportion of this effective electron temperature may be attributed to the excitation imposed across the sample during these experiments. When this contribution is accounted for the effective electron temperature decreases to 170mK. Additionally the line shape of the conductance peak taken at the lowest temperature suggested that this data was taken within the quantum blockade regime with strong coupling to the lead reservoirs. This coupling may lead to increased broadening of the peaks compared to the case where the dot is highly isolated.

In order to estimate a value for the total capacitance the width of the 400mK peak, once corrected for the effect of the temperature control electronics, was assumed to be an accurate reflection of the lattice temperature. This was justified by a straight-line fit of the last two high temperature points of the corrected width curve that passed close to the origin.

In order to estimate the separation of single particle states two models were used. One simply scales the electron density in the wide 2DEG to the size of the dot which results in a single number for the average single particle spacing. The other model uses a 2D parabolic confinement potential in order to investigate the distribution of eigenstates with deformation from circular symetric. This model gives a range of energies over which the separation between single particle states may exists.

Measurements of the quantum dot with a novel magnetic spectrometer device were also presented. Electron focusing techniques were used in order to investigate the energy of electrons leaving the dot before this energy was degraded by scattering. The focusing peak shifts were measured that were consistent with the estimated magnitude of separation between the single particle energy states within the dot. No evidence was seen for a shift in peak position which corresponded to the Coulomb blockade energy.

5.6 References

(1) Personal Communication, M. Holland, "Heterostructure Specifications" (1995).

(2) T. J. Thornton, M. Pepper, H. Ahmed *et al.*, "One-Dimensional Conduction in the 2D Electron-Gas of a GaAs-AlGaAs Heterojunction" Physical Review Letters 56 (11), 1198-1201 (1986).

(3) U. Meirav and E. B. Foxman, "Single-electron phenomena in semiconductors" Semiconductor Science and Technology 11 (3), 255-284 (1996).

(4) L. P. Kouwenhoven, C. M. Marcus, P. L. McEuen *et al.*, "Electron Transport in Quantum Dots" in Mesoscopic Electron Transport, edited by L. L. Sohn, L. P. Kouwenhoven, and G. Schon (Kluwer Academic Press, Dordrecht, 1997), Vol. 345.

(5) E. B. Foxman, P. L. McEuen, U. Meirav *et al.*, "Effects of Quantum Levels On Transport Through a Coulomb Island" Physical Review B-Condensed Matter 47 (15), 10020-10023 (1993).

(6) A. T. Johnson, L. P. Kouwenhoven, W. Dejong *et al.*, "Zero-Dimensional States and Single Electron Charging In Quantum Dots" Physical Review Letters 69 (10), 1592-1595 (1992).

(7) R. J. Haug, H. Pothier, J. Weis *et al.*, "Single-Electron Transistors Realized In In-Plane-Gate and Top-Gate Technology" Solid State Electronics 37 (4-6), 995-999 (1994).

(8) J. A. Nixon and J. H. Davies, "Potential Fluctuations in Heterostructure Devices" Physical Review B Condensed Matter 41 (11), 7929-7932 (1990).

(9) Thesis, L. P. Kouwenhoven, "Transport of Electron-Waves and Single-Charges in Semiconductor Nanostructures" , Delft University Of Technology, 1992.

(10) E. B. Foxman, U. Meirav, P. L. McEuen *et al.*, "Crossover From Single-Level to Multilevel Transport in Artificial Atoms" Physical Review B-Condensed Matter 50 (19), 14193-14199 (1994).

(11) M. A. Kastner, E. B. Foxman, P. L. McEuen *et al.*, "Transport Spectroscopy of a Coulomb Island" presented at the Nanostructures and Mesoscopic Systems, Santa Fe, New Mexico, 1991.

(12) L. Wang, J. K. Zhang, and A. R. Bishop, "Microscopic theory for Conductance Oscillations of electron tunneling through a Quantum Dot" Physical Review Letters 73 (4), 585-588 (1994).

(13) N. F. Johnson, "Quantum Dots - Few-Body, Low-Dimensional Systems" Journal Of Physics Condensed Matter 7 (6), 965-989 (1995).

(14) S. Tarucha, D. G. Austing, T. Honda *et al.*, "Shell filling and spin effects in a few electron quantum dot" Physical Review Letters 77 (17), 3613-3616 (1996).

(15) C. W. J. Beenakker and H. Van Houten, "Quantum Transport In Semiconductor Nanostructures" Solid State Physics Advances In Research And Applications 44, 1-228 (1991).

(16) H. Van Houten, C. W. J. Beenakker, and A. A. M. Staring, "Coulomb Blockade Oscillations in Semiconductor Nanostuctures" in Single Charge Tunneling, edited by H. Grabert and M. H. Devoret (Plenum Press, New York and London, 1993), Vol. 294, pp. 167-212.

(17) J. G. Williamson, H. Van Houten, C. W. J. Beenakker *et al.*, "Hot-Electron Spectrometry With Quantum Point Contacts" Physical Review B Condensed Matter 41 (2), 1207-1210 (1990).

(18) J. G. Williamson, H. Van Houten, C. W. J. Beenakker *et al.*, "Injection Of Ballistic Hot-Electrons and Cool Holes In a 2- Dimensional Electron-Gas" Surface Science 229 (1-3), 303-306 (1990).

(19) R. Landauer, "Spatial Variation Of Currents and Fields Due to Localized Scatterers In Metallic Conduction" IBM Journal Of Research And Development 32 (3), 306-316 (1988).

(20) M. Rahman, J. G. Williamson, K. Mathieson *et al.*, "Quantum Electron Beam Probe of Sidewall Dry Etch Damage" Microelectronic Engineering 1999 (1999 (accepted for publication)).

6 CONCLUSIONS

At the commencement of this work single electron, devices were being measured at 1.2K as this experimental arrangement offered a substantial reduction in electron temperature over the dilution unit. As a direct result of the work detailed in chapter 4, the temperature dependent data presented in chapter 5 suggests that the electron temperature is now of the order of 250mK. This temperature is low enough for well defined single particle states to exist in a quantum dot of lithographic diameter 500nm.

Initial noise measurements of the system, presented in section 4.2, identified numerous problem areas, all of which have been addressed within this work, resulting in a substantial improvement in measurement performance. Because of the painstaking attention to detail in the design and construction of the new measurement system a 20 fold increase in measurement resolution has been achieved,(1) see sections 4.2 and 5.2. A systems approach was adopted in order to make such a substantial improvement in measurement resolution. Subsystems were designed to work in conjunction with one another. As a result of the care taken in the choice of components and physical construction with regard to:

- Signal referencing; to minimise ground loops and common impedance signal paths (see section 4.4.3), and to separate the signal and shielding references (see section 4.4.1).
- Vibration isolation; to isolate ground vibration components from pumps, cooling fans and other plant equipment (sections 4.2 and 4.5.11).
- Bandwidth limiting; reducing the frequency range over which noise can couple into the system (see section 4.5.5).

The system is now capable of resolving fine structure information (see section 5.4.2) within experimental data which was previously severely compromised by temperature smearing.

Whilst an electron temperature of ≈ 250mK allows meaningful measurements of quantum dot devices further reductions in electron temperature may still be desirable. Limitations in heat extraction capability and the restrictions in physical space available make low temperature filtering a challenge in this dilution unit. Work that may lead to further improvement include:

- Internal shielding. An internal shield thermally anchored at base temperature would act as an additional level of both radiation and electromagnetic shielding.

- Cryogenic filtering. It may be necessary to filter signal lines at base temperature.

Fascinating data, presented in chapter 5 (see Figures 5.17 and 5.18), resulted immediately from the new measurement system. One of the initial devices measured, a novel magnetic spectrometer, suggested that it is possible to measure spin degenerate single particle energy directly and independently of the Coulomb blockade energy. The device, based on electron focusing techniques, was used in order to investigate the energy distribution of electrons local to the dot. This measurement was taken within an elastic mean free path of the electrons leaving the dot. Such an experimental arrangement allowed the electron to be measured whilst it retained well-defined information about the energy state it had previously occupied within the dot. This measurement technique appears to be insensitive to charging energy yet able to distinguish the smaller single particle spacing due to quantum confinement effects. It is proposed that this is due to the essential difference in the origin of these energies. Charging energy is a function of the classical interaction between the electron and the environment and is a function of the redistribution of electric field between the two. The single particle energy (see Figure 5.6) is a function of the confinement of the electron to the order of its wavelength, and is a quantum mechanical effect. The gain and loss of charging energy the electron experiences as it moves onto and off the dot is an elastic process. The energy loss associated with an electron occupying a quantum mechanical state on the dot is an inelastic process.

Future work may investigate smaller quantum dots in the few electron regime, Here, since the single particle spacing is much larger, more subtle detail may

become apparent that would otherwise become lost due to scattering events. Within the few electron regime quantum dots may be considered analogous to atoms and are found to exhibit shell filling structure but, unlike atoms, may be simply manipulated, with a single device being comparable to many different elements. It may be possible using this local energy measurement technique, to gain new insight into shell filling structure that has already been observed[2-5] within single quantum dots. Such devices may also providing an invaluable tool to investigate electron orbital behaviour in coupled quantum dots.

Since the completion of the system, it has been used extensively, particularly as an integral part of the research into strained layer superlattices. It has proved to be a highly accurate and precise measurement tool, without which the results presented in chapter 5 and the recent publications[6] as well as future proposed work would not be possible.

6.1 References

(1) Personal Communication, M. Rahman, "Electron Temperature of Dilution Refrigerator" (1995).

(2) L. P. Kouwenhoven, T. H. Oosterkamp, S. Tarucha *et al.*, "Coulomb Oscillations In Few-Electron Quantum Dot" Physica B 251, 191-196 (1998).

(3) S. Tarucha, D. G. Austing, T. Honda *et al.*, "Shell Filling And Spin Effects In A Few Electron Quantum Dot" Physical Review Letters 77 (17), 3613-3616 (1996).

(4) S. Tarucha, D. G. Austing, T. Honda *et al.*, "Atomic-Like Properties Of Semiconductor Quantum Dots" Japanese Journal of Applied Physics Part 1-Regular Papers Short Notes & Review Papers 36 (6B), 3917-3923 (1997).

(5) S. Tarucha, T. Honda, D. G. Austing *et al.*, "Electronic States In Quantum Dot Atoms And Molecules" Physica E 3 (1-3), 112-120 (1998).

(6) B. Milton, C. J. Emeleus, K. A. Lister *et al.*, "Modulation Of Landau Levels By A One-Dimensional Periodic Potential" Physica E (To Be Published).